Title
Investigation of Dynamic Behavior in Erbium-doped Yttrium Aluminum Garnet and Yttria

Author
Liu, Brad Chun-Ting

Publication Date
2015

Peer reviewed|Thesis/dissertation

UNIVERSITY OF CALIFORNIA

Los Angeles

Investigation of Dynamic Behavior in Erbium-doped Yttrium Aluminum Garnet and Yttria

A dissertation submitted in partial satisfaction
of the requirements for the degree Doctor of Philosophy
in Electrical Engineering

by

Brad Chun-Ting Liu

2015

ABSTRACT OF THE DISSERTATION

Investigation of Dynamic Behavior in Erbium-doped Yttrium Aluminum Garnet and Yttria

by

Brad Chun-Ting Liu

Doctor of Philosophy in Electrical Engineering
University of California, Los Angeles, 2015
Professor Oscar M. Stafsudd, Chair

Erbium-doped in YAG ($Y_3Al_5O_{12}$) and in yttira (Y_2O_3) are the most often used laser gain media for generation of 1.6 μm and 3 μm laser radiation. Of all the laser gain media studied, Er-based materials are the most complicated due to the presence of rich non-linear energy transfer kinetics processes. Energy transfer up-conversion (ETU) and excited state absorption (ESA) processes in Er-based laser gain materials has been investigated by many groups over the last four decades using the fluorescence decay time as an indirect measure of the ETU and ESA rates. The values reported for ETU and ESA vary two-to-three orders of magnitudes for the same materials. When attempting to model and prototype high power Er-based lasers, such a large uncertainty in the values for ETU and ESA coefficients leads to large (and sometimes unrealistic) predictions in terms of laser performance. To allow the laser community to better model and prototype high power Er-based lasers, a more accurate knowledge of ETU and ESA coefficients is needed. The objective of the present effort was to develop a faster and more accurate technique for quantifying, in absolute terms, the values for ETU and ESA coefficients in Er-based materials. The technique reported here emphasized measuring the rise and decay times of the fluorescence signal from the energy states that directly impact ETU and ESA as a function of pump wavelength and pump intensity. ETU and ESA was investigated in 0.5% and 50% single crystal and polycrystalline

(ceramic) Er:YAG and 1%, 15%, and 25% polycrystalline Er:Yttria with the fluorescence signal quantified for the $^4S_{3/2}$, $^4F_{9/2}$, $^4I_{9/2}$, $^4I_{11/2}$, and $^4I_{13/2}$ states. Results for the rise and fall time of the fluorescence signal in the case of 0.5% Er:YAG do not show any appreciable ETU component. This result is consistent with results already published in literature and thus validating that the technique developed in the present study. In the case of the 50% Er:YAG, measurements were made, which allowed the direct observation of the effects of ESA and ETU of the $^4I_{11/2}$, and $^4I_{13/2}$ energy states (laser states). This technique appears to be applicable to many other rare earth ion systems.

The dissertation of Brad Chun-Ting Liu is approved.

Chi On Chui

Warren S. Grundfest

Suneel Kodambaka

Oscar M. Stafsudd, Committee Chair

University of California, Los Angeles

2015

Dedication

To my parents and grandparents.

Contents

List of Figures

List of Tables

Acknowledgements

I extend my deepest gratitude to Professor Oscar Stafsudd, my advisor, for all his patience, guidance, and support throughout all these years. In addition to his brilliant insight on many scientific problems I encountered along the way, his enthusiasm, encouragement, and kindness has made my graduate student life wonderful and unforgettable. During tough times, in addition to Professor Stafsudd's support, Professor Stafsudd's wife Jacquie also provided tremendous help and offered great ideas on resolving many problems I had to deal with. It is no exaggeration to say that I couldn't have made it without their support and guidance. I sincerely thank them from the bottom of my heart for everything they have done for me!

I want to thank Dr. Ramesh Shori for advising me in various ways and things, the support of equipment, and other research opportunities outside of UCLA campus. The amount of time he has spent on helping me in my conference poster and paper well into past midnight, (especially when he is already so busy!) is much appreciated. Furthermore, I want to thank him for all the help he has provided with my dissertation. Given how busy he is, he still spent hours on it with me. On this note without going too much into detail, I want to indicate that, unfortunately, I was unable to put his name in front of my dissertation along with other committee members due to the new school system. Nevertheless, I want to acknowledge here, emphatically, that he is an invaluable advisor in my Ph.D. student life, and it was an honor to have him on my Ph.D. final defense committee.

It goes without saying that the Ph.D. committee members are extremely busy with their

own research groups. On top of that, they helped me in arranging a time to be present at both my oral qualifier and my final defense. I want to express my gratitude to my committee members Professor Chi On Chui, Professor Suneel Kodambaka, and Professor Warren Grundfest for their time and deep insight, which helped me formulate some of the potential future work and research.

Sometimes graduate students can potentially run into trouble with the school system such as almost missing potential school form submissions deadlines, and sometimes graduate students are just confused about the system. The people at graduate student office and the department staff office are truly wonderful to obtain help and suggestions from. I want to thank Jackie Trang, Gershwin Mason III, and Jose Cano, from The Electrical Engineering Department here at UCLA. I want to also thank Deeona Columbia, Mandy Smith, and Ryo Arreola.

There are several "key individuals" to me, who have shaped me into becoming an electrical engineer. I want to thank Tyler Johnson my high school physics tutor in giving me a solid appreciate of physics, Professor John A. Mallinckrodt from Cal Poly Pomona for further improving my understanding and appreciation of physics, and, finally, Professor Phyllis Nelson from Cal Poly Pomona for advising me for many years since my undergraduate days and for introducing me to a wonderful advisor at UCLA after I was accepted into the graduate program.

Finally, I want to thank all my family and friends for being part of my life all these years. Their support were indispensible to my journey along the way to completing my Ph.D. work.

VITA

2004–2008	B.S. Electrical Engineering California State Polytechnic University, Pomona
2008–2010	M.S. Electrical Engineering University of California, Los Angeles
2011–2015	Teaching Assistant University of California, Los Angeles Department of Electrical Engineering

Chapter 1

Introduction

Rare earth ions are a gift from nature to mankind due to their isolated f-shell energy levels. This isolation allows engineers to dope them into many material without changing much its optical absorption and emission wavelength processes within a solid. However, the benefit comes at the cost of complexity in the interaction within and among rare earth ions in solids. In general, the behavior of rare earth ions in host material is known to be difficult to predict. In the following sections, the development of energy transfer discover and schemes are discussed.

In this dissertation, the details of energy transfer of erbium ions doped in yttrium aluminum garnet (YAG, $Y_3Al_5O_{12}$) and yttria (Y_2O_3) is investigated. The energy transfer processes involve energy transfer up-conversion (ETU) and excited state absorption (ESA). This is investigated by using a technique that is perhaps first proposed and used in this study. The main goal of this study is to search for new and efficient ways of transferring energy and to determine their actual strengths through direct experimental techniques ultimately leading to creating more efficient laser systems. The engineering aspect of this study concerns the extreme interest in the two wavelength regions that are essentially only obtainable in erbium ions in insulating host[1]. The wavelengths of interests are 1.6 μm for

[1] semiconductor laser at 1.6 μm is available.

eye safe operation and $3\,\mu$m or more exact $2.94\,\mu$m for medical applications and materials processing. For the processes that are important to the two wavelengths, the cross sections of ESA and ETU are determined using this technique.

Unlike many other methods, This technique does not require single crystal. Powdered samples, which are easily and cheaply produced[2], with careful handling can produce sufficient information about sample transfer rates and concentration dependence, which are critical for making lasers. This technique, although tested only on erbium-doped in YAG and Erbium-doped in yttria, is not restricted to either erbium active ions only or YAG and Yttria hosts. It can be applied to other active ions doped in other hosting material. The only key lies in the time information as will be discussed in Section 2 in page 9.

1.1 History of Energy Transfer

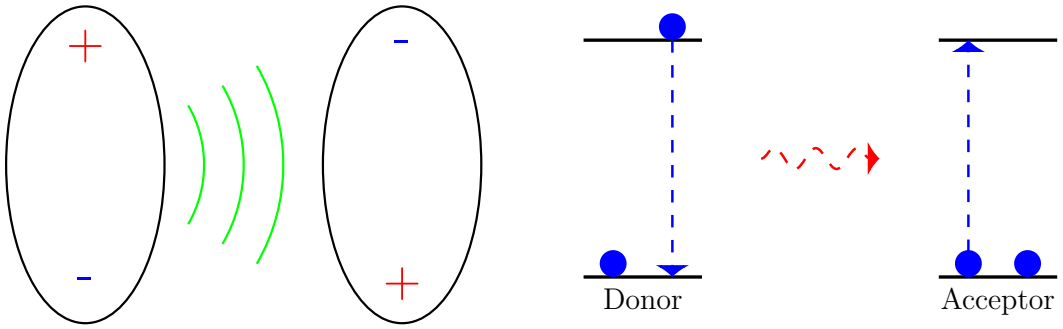

(a) Two ions in a dipole-dipole resonant energy transfer.

(b) Energy diagram of the dipole-dipole resonant energy transfer.

Figure 1.1: Forster energy transfer between ions.

Several energy transfer processes, which are critical to the operation of rare earth lasers, and schemes of engineering were discovered and developed over a long period of time. The complexity and challenges are observable by looking at the history of the discovery and engineering schemes of energy transfer.

[2]Essentially these processes can be done by wet chemistry and some furnace work.

In 1948, Forster published his experimental results regarding intermolecular energy transfer in his study of organic molecules in Tripaflavin and Rhodamin B. In the experiment, one of the molecules absorbs the energy and transfers the energy to the other molecule [9]. This phenomena was termed, at the time, "energy wondering". It was indicated that the interaction is that of a dipole-dipole, and the strength of the interaction is proportional to the inter-molecular distance to the inverse sixth power r^{-6}. This is illustrated in Figure 1.1 on page 2.

Forster energy transfer is a resonant or near resonant energy transfer between molecules. However, in many solids and inorganic compounds, the energy transfer theory depends on energy transfer via forbidden states. In other words, even though energy cannot be optically released via forbidden state, the state can still non radiatively transfer the energy by means of electronic exchange among molecules. In 1953, Dexter formulated the theory for such an effect and indicated that the range of this effect requires that the molecules be on the order of 1 nm apart or less, which, in contrast to Forster energy transfer, can occur up to an intermolecular distance on the order of 10 nm [6]. This effect accounts for much of the energy transfer up-conversion (ETU) with a strength of inter-molecular distance dependence of e^{-kr}, where r is again the intermolecular distance and k is a constant that depends upon van der Waals radius and several other factors. This is illustrated in Figure 1.2 on page 4. Later on, Inokuti and Hirayama generalized the Forster and Dexter theory in 1965 considering higher multipolar and exchange interactions such as dipole-quadruple and quadruple-quadruple interactions [27]. Their results showed the non-exponential behavior of fluorescence life times.

In addition to energy transfer, cooperative absorption was also observed. Cooperative absorption is the absorption of a photon by two or more ions such that each ion enter its own excited state and that the excited states' energy sum is equal to the energy of the absorbed photon. In short, a single photon can simultaneously excite more than one ion. In 1961, Varsony and Dieke [43] from John Hopkins University observed in $PrCl_3$ several "weak" absorption lines that belongs to only the sums of different energy levels in Praseodymium

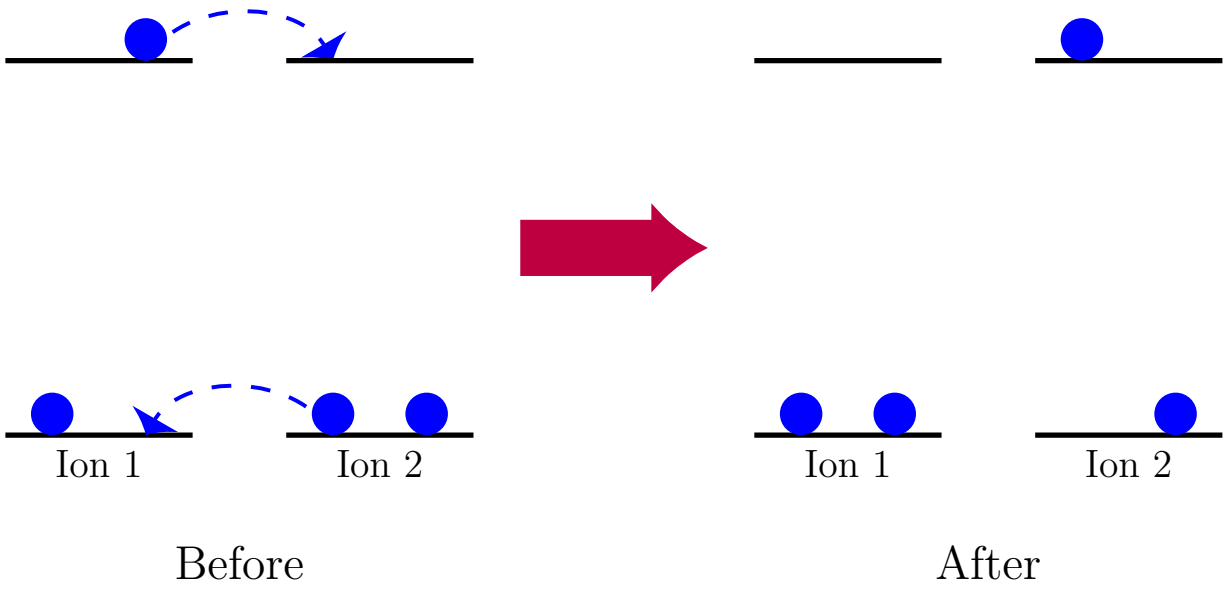

Figure 1.2: Dexter energy transfer

indicating that in addition to resonant energy transfer as worked out by Forster and Dexter, resonant optical absorption, or collaborative absorption, is also possible. In 1962, Dexter worked out the theoretical model of cooperative absorption [7].

As given in Dexter's work [7], cooperative absorption effect simply depends on the dipole-dipole resonance, it should not be ion specific. In other words, if the theory of collaborative absorption is true, A similar effect should be observable between dissimilar ions as well. In 1963, Wong et. al at UCLA observed exactly this in a Pr:$CeCl_3$ crystal, which the absorption lines can only be explained by the sums of Cerium and Praseodymium energy levels [33]. Cooperative Absorption is illustrated in Figure 1.3 on page 5.

Nearly 10 years later, cooperative luminescence was observed in ytterbium phosphate $YbPO_4$ [34]. Cooperative luminescence, as given in Figure 1.4 on page 5 is the reverse of cooperative absorption in the sense that a single photon is co-emitted by two or more excited ions. The emitted photon energy is equal to the sum of the energy released by the excited ions. Ytterbium has only energy level near 1 μm however, when excited by 1 μm excitation source, a dim green fluorescence is observed at 497 nm indicating the existence of the effect.

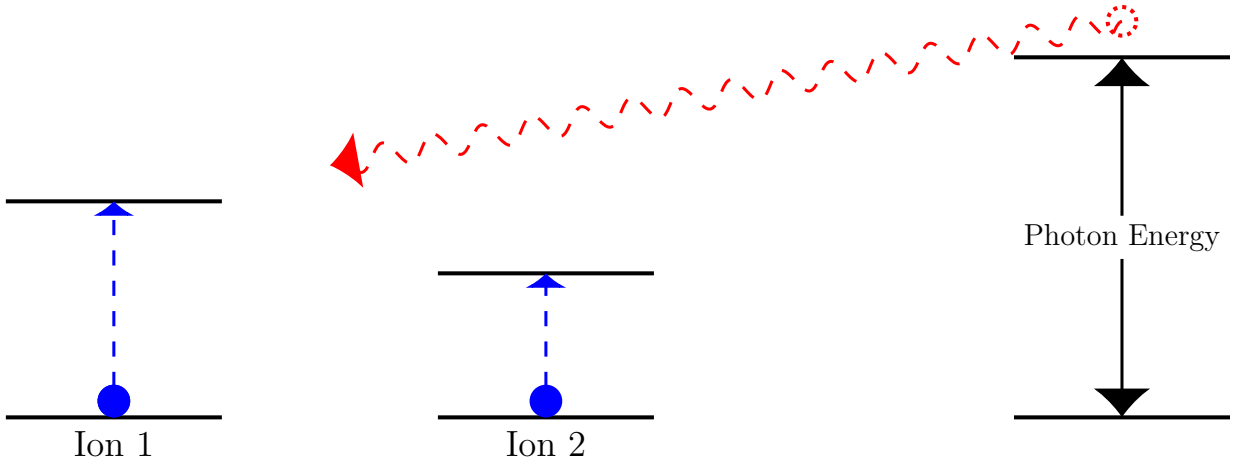

Figure 1.3: Cooperative Absorption

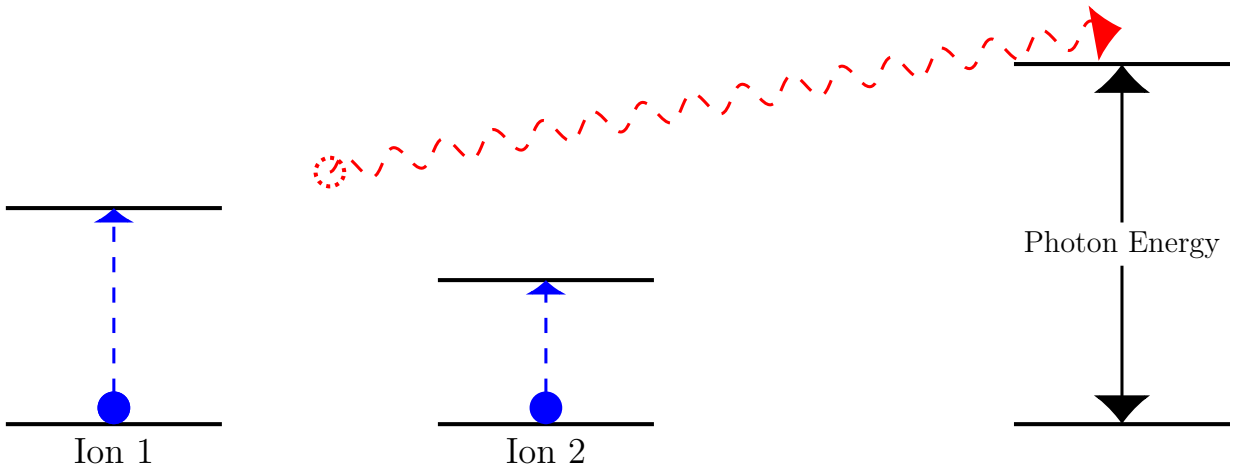

Figure 1.4: Cooperative luminescence

According to the theory of cooperative absorption and luminescence, the effect should not be ion specific. Therefore, this effect should occur in dissimilar ions as well. Furthermore, this effect could potentially be electronic Raman scattering. The only way to truly prove the existence of such an effect is by having two dissimilar ions exhibiting such an effect. However, it is to our knowledge that this effect has yet been observed in the afforementioned desired conditions. The difficulty lies in, perhaps, not in the fact the observation of the actual emission but in the indistinquishability of impurity fluorescence versus actual cooperative luminescence.

The above processes concludes all of the current understanding of energy transfer mechanism that can occur in materials. Excellent review papers of these processes were written by Grant, Auzel, and Wright [2, 5, 19, 46].

1.2 History of Laser Schemes

Based on the aforementioned background work on energy transfers, a race on developing new laser host and laser using various rare earth ions took place. Since rare earth ions naturally had long life times and narrow energy bands, they are potentially good laser materials. However, the narrow band also causes the material difficult to pump or excite; therefore, one particular interest was how to take advantage of the long life times and narrow bands and get around the pumping difficulty? Is it possible to utilize two different ions to make a laser system work? For example, many tried to take the advantage broad pump bands of Cr^{+3} (Sensitizer) and transfer energy into the rare earth Nd^{+3} (Acceptor) for lasing. This work was filled with great disappointment: energy transfer effects were observed. However the low efficiency of the transfer is simply not practical for laser systems in most cases. The pair Cr^{+3} and Nd^{+3} were tested by codoping them into virtually every known garnet crystal. Much of the energy absorbed ended up in heat. It was discovered that this ion pair in GSGG Gadolinium Scandium Gallium Garnet system showed an efficient energy transfer making it, particularly, applicable for arc-lamps excitation for broadband absorption [4]. It turned out to be not of practical use due to its poor thermal-optical properties [45, 47]. To some extent, the energy transfer interests were reduced from the surge of good semiconductor lasers that can efficiently pump energy into the narrow bands of rare earth doped material systems. However, these diode pumps are still difficult to operate and to wavelength-tune due to narrow absorption bands of rare earth ions.

Energy transfer processes are still of great interest for erbium in various oxide hosts. The reason in this case is the $3\,\mu$m transition has a 10x longer terminal state life time than the lasing upper state. In this case, the $3\,\mu$m terminal state is also the $1.6\,\mu$m transition,

which goes into the ground state manifold[3]. Under normal conditions, one would expect that the $3\,\mu$m operation would be very difficult and would terminate due to the filling of the final state. Somewhat surprising is that various authors [8, 44] and 1 commercial source have reported and are selling continuous wave (CW) $2.94\,\mu$m Er:YAG lasers. The commercial source accomplished this via energy transfer scheme first suggested by the work of Furtada et. al. [10], in which, the co-dopants of other rare earths are used to extract energy populations from the terminal $^4I_{13/2}$ level by cross relaxation to the counter doping ions. The work of Furtado et. al. [10] showed that small amounts of rare earths in the order of a few hundred parts per million in heavily doped crystals significantly change the life times. This led to the enhanced ability of engineers to produce CW $3\,\mu$m lasers. Prior to Furtado's work, neither the extreme variability of $3\,\mu$m laser crystals nor the difficulty to reproduce similar experimental laser result was understood.

1.3 Previous Studies of Erbium Systems

As indicated in the begining, erbium laser applications are of great interest. The energy levels in different materials are calculated and experimentally verified [21–23, 25, 26, 30, 37, 39]. The current two more promising hosting material are YAG and yttria. The erbium stark levels in these materials are well known [20, 24, 25, 36, 38]. Lots of effort were spent on obtaining a good model of erbium doped in YAG, yttria, and other systems.

In addition to fluorescence and absorption wavelengths information, the rate equation model of erbium-doped systems is also investigated and still is a topic of investigation today. As indicated in the begining, the energy transfer processes that go on inside erbium-doped systems are complicated. The difficulty in the rate equation model as worked out by Georgescu et. al., and many others is that there are at least 9 parameters embedded inside the system as shown in Figure 2.10 and Equations 2.24 [3, 11–18, 32, 35, 41, 42]. Excellent

[3]Typically $1.6\,\mu$m is doped at 1% in YAG and in the order of 50% for the 3um in YAG. The doping levels were found experimentally.

work has also been done by Huber et. al. for measuring excited state coefficients in low doped erbium-doped systems, which is an extremely important parameter for 1.6 μm and 3 μm laser operation [29].

Even though lots of information is obtained about erbium-doped systems, the system is still not completely known. In principle from absorption spectra, we can determine the oscillator strengths and or transition probability / Einstein coefficients. The fluorescent life times have been determined. However, the exact energy paths are not completely determined. The work of Joshi et. al. demonstrated a modulated dual wavelength pumping technique, in which the dominant paths for the upconversion can be determined. The complexity of the model is a reflection of the failure of simple models to correctly predict laser behavior. Some of the parameters in the model are determinable via experimental measurements and theoretical calculations. These include optical cross-sections from absorption spectra. The radiative rates, and measured fluorescent time and cross relaxation. However, cross relaxation and energy transfer terms typically are difficult to measure and many of them are unknown. They are used to fit data, in which more parameters than the number of data points are present. However, since there are so many undetermined parameters, this leads to ambiguities in the model.

Chapter 2

Population Density Rate Equation Model

2.1 Introduction

In typical classical laser formalism, the processes that occurs in a sample are Ground State Absorption (GSA), Spontaneous Emission (SpE), and Stimulated Emission (StE). GSA, as given in Figure 2.1[1] on page 10, occurs when the wavelength of optical excitation corresponds to the energy gap of its ground state energy level and one of its excited states. GSA is just stimulated absorption from the ground state. This is emphatically distinquished with the term GSA simply because another important effect called Excited State Absorption (ESA) to be discussed later also plays an important role in this work. In Figure 2.1, A photon is absorbed by an ion or atom, which leaves it in excited energy state. N_0 is the ground state population. E_0 is the ground state energy level. Ground state is named S_0. S_1, N_1, and E_1 are the name of the excited state, the state population and excited state energy level, respectively. SpE (Figure 2.2 on page 11) is the part of the radiative portion of the

[1]For convenience, the excited state population N_1 and, in later figures, N_2 as well are not drawn to physical reality. It is merely for convenience and clarity that the excited states have such large population unless the optical pumping mechanism and absorption coefficients are strong.

total decay phenomena, which includes both radiative and non-radiative. The other part of radiative decay is due to StE as in Figure 2.3 on page 11.

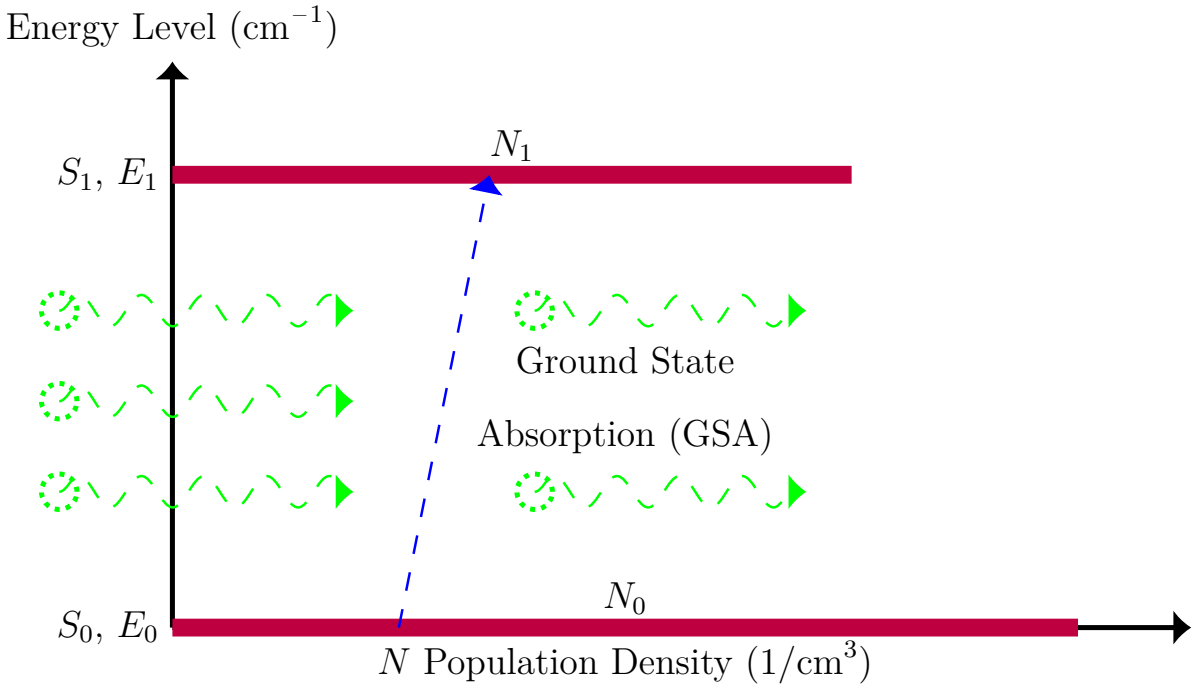

Figure 2.1: Population density diagram showing Ground State Absorption (GSA) process.

In Figure 2.4 on page 12 and given in Equation 2.1 on page 10, the optical pump has an intensity I_0 and is turned on and turned off at t_i and t_f, respectively. If the pump intensity is assumed to be low such that the ground state population density N_0 is roughly constant and that the stimulated emission (StE) effect can be ignored, then the population density rate equation model is as given in Equation 2.2 on page 10, where τ_1 is the natural life time of the state N_1 and α_0 is the absorption coefficient of the state S_0.

$$I(t) = \begin{cases} 0 & t < t_i \\ I_0 & t_i \leq t \leq t_f \\ 0 & t_f < t \end{cases} \tag{2.1}$$

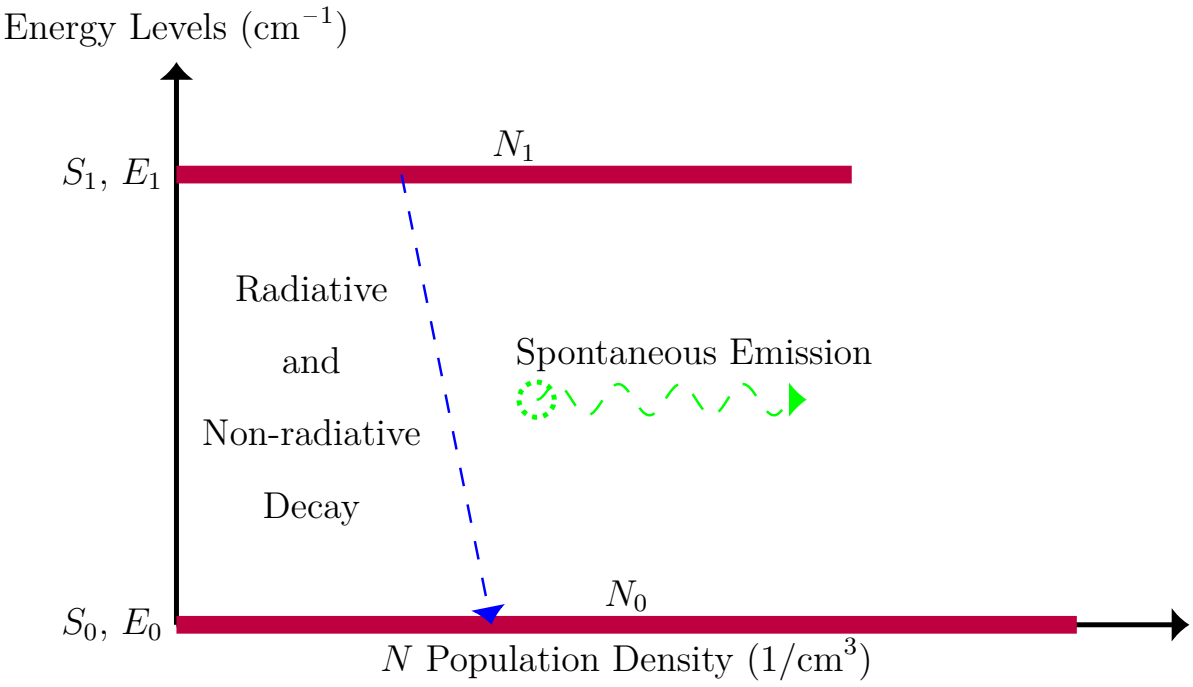

Figure 2.2: Population density diagram showing spontaneous emission and population decay mechanisms.

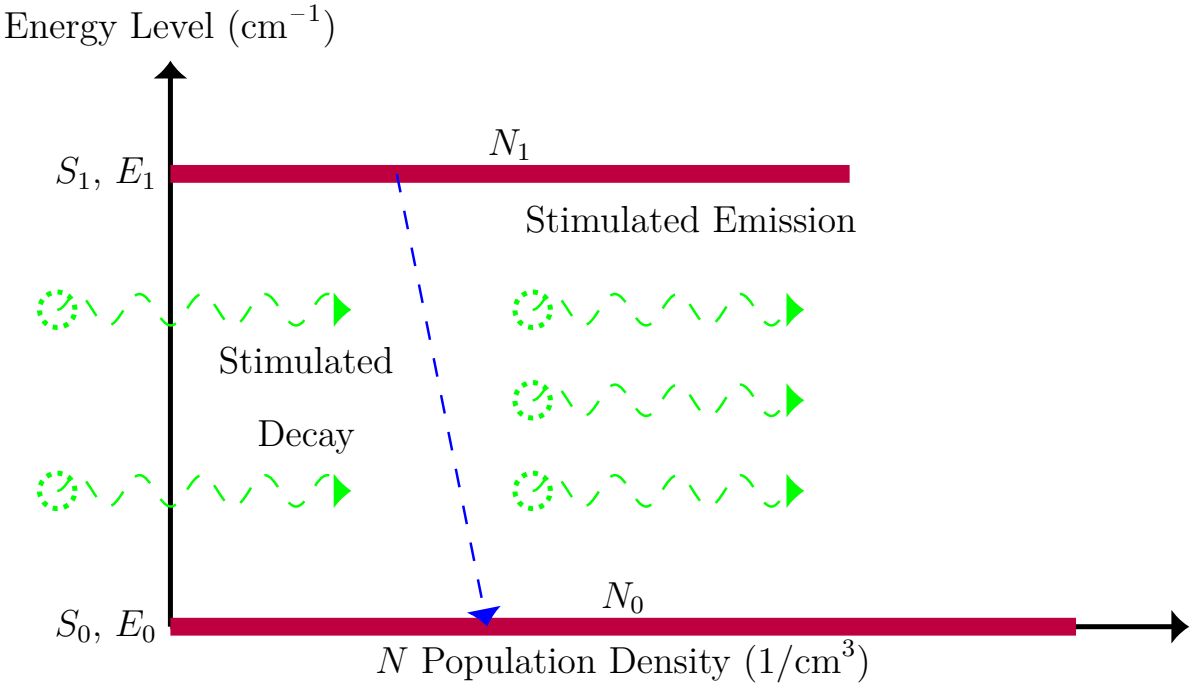

Figure 2.3: Population density diagram showing stimulated emission and decay due to optical stimulation.

$$\frac{dN_1}{dt} = \begin{cases} -\frac{N_1}{\tau_1} & t \leq t_i \\ -\frac{N_1}{\tau_1} + \alpha_0 I_0 N_0(t_i) & t_i < t \leq t_f \\ -\frac{N_1}{\tau_1} & t_f < t \end{cases} \tag{2.2a}$$

$$\frac{dN_0}{dt} = 0 \tag{2.2b}$$

$$N_1(t) = \begin{cases} 0 & t \leq t_i \\ \alpha_0 I_0 N_{0i} \tau_1 (1 - e^{-\frac{t-t_i}{\tau_1}}) & t_i < t \leq t_f \\ N_1(t_f) e^{-\frac{t-t_f}{\tau_1}} & t_f < t \end{cases} \tag{2.3a}$$

$$N_0(t) = N_{0i} \tag{2.3b}$$

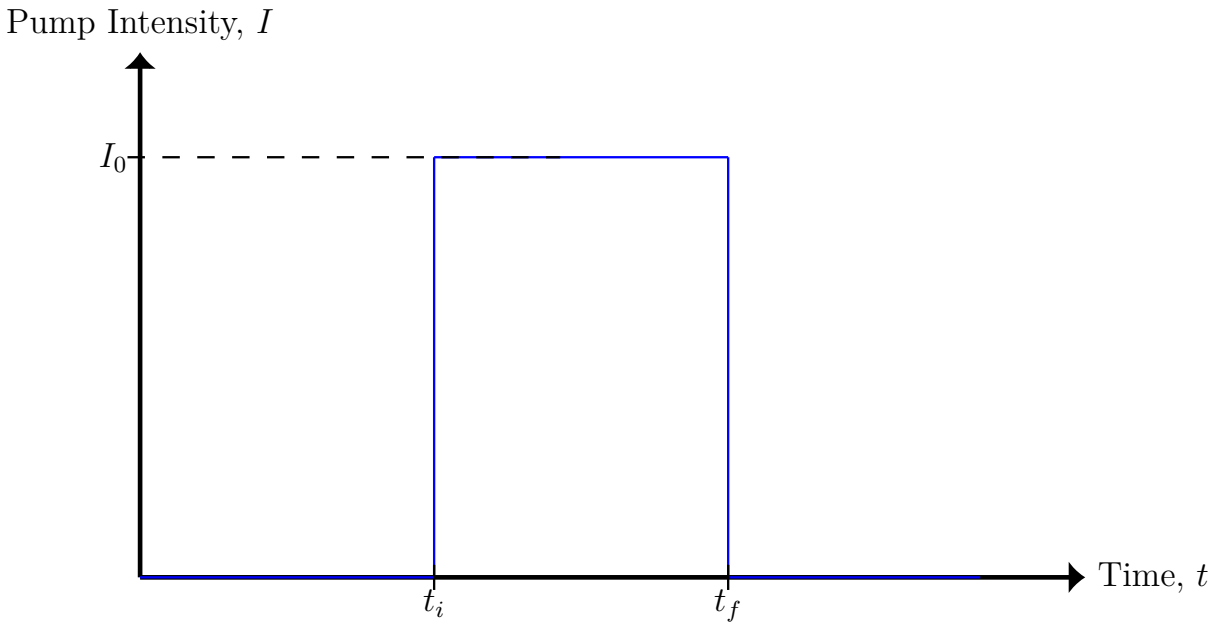

Figure 2.4: Pump Intensity versus Time. The pump is turned on only during t_i and t_f.

The natural life time τ_1 of the state S_1 is the invese of the total decay rate R_1 as given in Equation 2.4 on page 13. The total rate R_1 of state S_1 is the sum of radiative decay rate $R_{1,r}$ and non-radiative decay rate $R_{1,nr}$ as given in Equation 2.5 on page 13. The rate equation model in Equation 2.2 on page 10 will yield solution of population densities in Equation 2.3

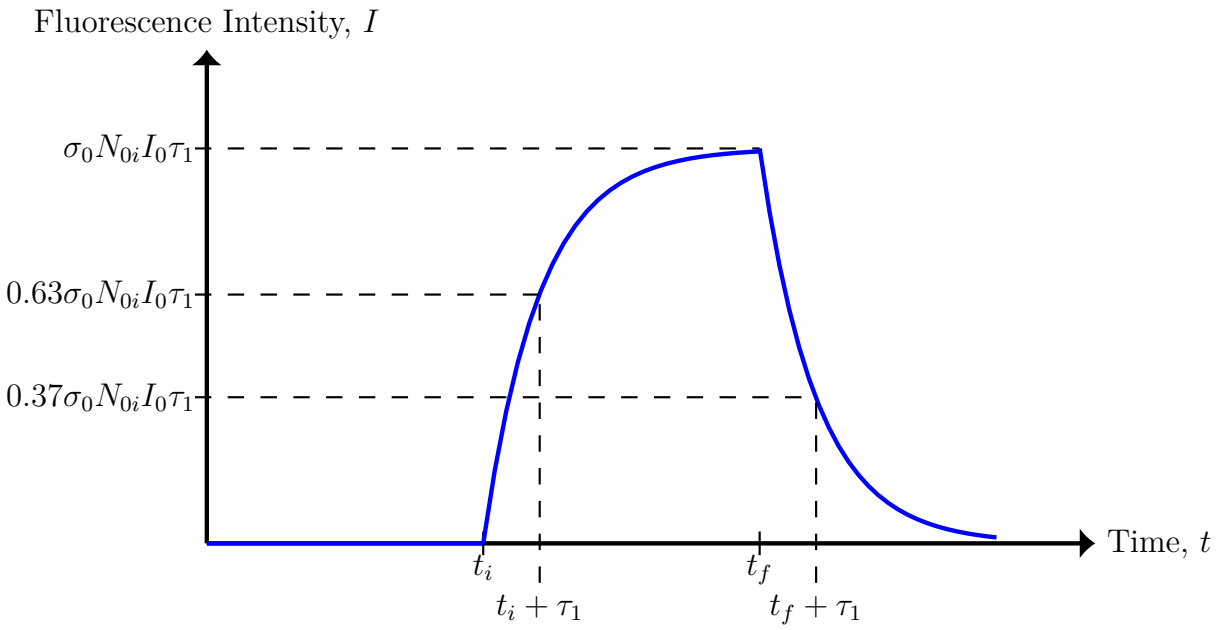

Figure 2.5: Fluorescence Intensity versus Time. The pump is as given on Figure 2.4 on page 12.

on page 12, where $N_0 i$ stands for the initial population density of the N_0 state. It is assumed that before pump is turned on, all ions or atoms are in ground state S_1 leavning the excited state S_1 with no population.

$$\tau_1 = 1/R_1 \tag{2.4a}$$

$$\tau_{1,r} = 1/R_{1,r} \tag{2.4b}$$

$$\tau_{1,nr} = 1/R_{1,nr} \tag{2.4c}$$

$$R_1 = R_{1,r} + R_{1,nr} \tag{2.5a}$$

$$\frac{1}{\tau_1} = \frac{1}{\tau_{1,r}} + \frac{1}{\tau_{1,nr}} \tag{2.5b}$$

The fluorescence intensity I_f observed then is only the portion that's radiatively decaying out as light or photon. This is given in Equation 2.6. Since we ultimately use photodetector

to capture the fluorescence. It is power, not intensity, we are capturing. However, since stimulated emission can usually be ignored unless the system is in laser action, it is safe to assume uniform radiation in all directions. All it turns out is that the photodetector captures part of the total fluorescence power, which is proportional to the fluorescence intensity. As long as the set up between the pump, the sample, and the detector remain unchanged, the fluorescence captured is always proportional to the sum of total intensity from the volumn that fluoresces.

$$I_f(t) = \frac{\frac{1}{\tau_{1,r}}}{\frac{1}{\tau_{1,r}} + \frac{1}{\tau_{1,nr}}} N_1(t) \tag{2.6a}$$

$$I_f(t) = \frac{R_{1,r}}{R_{1,r} + R_{1,nr}} N_1(t) \tag{2.6b}$$

Here we can easily see from Figure 2.5 on page 13 that during the pump turn on and after the pump turn off, after one time constant τ_1 the system will be only 37% away from its final state of the population. If we call the time to reach this point for during the rise and the fall rise time constant τ_{rise} and fall time constant τ_{fall}, we see that τ_{rise}, τ_{fall} and τ_1 are all the same. This, however, is no longer true when we remove the assumption that ground state population N_0 is "immutable" due to extremely large population and low pumping intensity. This assumption breaks when the pump intensity is high. In this work, the pump intensity goes up to a continuous wave (CW) of $10\,\mathrm{kW/cm^2}$, which according to calculated values, is to significantly change ground state population N_0.

As we remove the ideal or simplified assumption and start considering the possibilities of a changing ground state population N_0 and stimulated emission (StE) effects σ_1, the rate equation becomes Equation 2.7 on page 14. During the times when the pump is off, the solution is the same as Equation 2.3a on page 12. We next move on to solving the general case, which works whether the high intensity pump is turned on or off.

$$\frac{dN_1}{dt} = \begin{cases} -\frac{N_1}{\tau_1} & t < t_i \\ -\frac{N_1}{\tau_1} - \sigma_1 I_0 N_1 + \alpha_0 I_0 N_0 & t_i \le t \le t_f \\ -\frac{N_1}{\tau_1} & t_f < t \end{cases} \tag{2.7a}$$

$$\frac{dN_0}{dt} = \begin{cases} +\frac{N_1}{\tau_1} & t < t_i \\ +\frac{N_1}{\tau_1} + \sigma_1 I_0 N_1 - \alpha_0 I_0 N_0 & t_i \le t \le t_f \\ +\frac{N_1}{\tau_1} & t_f < t \end{cases} \tag{2.7b}$$

To solve the general case, eigenvalue and eigenvector techniques in linear algebra can be used. First the equations are put into matrix form with a column vector $\mathbf{x}$ and a two-by-two matrix A defined in Equation 2.8 in page 15 and Equation 2.9 on page 15. The rate equation model then becomes Equation 2.10 on page 15.

$$\mathbf{x}(t) = \begin{bmatrix} N_1(t) \\ N_0(t) \end{bmatrix} \tag{2.8}$$

$$A = \begin{bmatrix} -\frac{1}{\tau_1} - \sigma_1 I_0 & \alpha_0 I_0 \\ \frac{1}{\tau_1} + \sigma_1 I_0 & -\alpha_0 I_0 \end{bmatrix} \tag{2.9}$$

$$\frac{d}{dt}\mathbf{x} = A\mathbf{x} \tag{2.10}$$

To solve the equation, we apply the solution in Equation 2.11 on page 16 to this differential equation as discussed in Strang's work [40]. The t_m in this equation is meant to be substituted by the proper initial condition. The general solution then is given in 2.12 on page 16. With the right initial conditions, we can obtain the population density $N_0(t)$ and $N_1(t)$ with the pump condition as given earlier in Figure 2.4 on page 12. We assume before pump is turned on the ions are all in ground state S_0 as before, which yields the following population density in Equation 2.13 and page 16.

$$\mathbf{x}(t) = e^{A(t-t_m)}\mathbf{x}(t_m) \tag{2.11}$$

$$N_1(t) = \frac{1}{(\alpha_0+\sigma_1)I_0+\frac{1}{\tau_1}}\Bigg(N_1(t_m)\{\alpha_0 I_0 + (\sigma_1 I_0 + \frac{1}{\tau_1})e^{-[(\alpha_0+\sigma_1)I_0+\frac{1}{\tau_1}](t-t_m)}\} + N_0(t_m)\alpha_0 I_0\{1 - e^{-[(\alpha_0+\sigma_1)I_0+\frac{1}{\tau_1}](t-t_m)}\}\Bigg) \tag{2.12a}$$

$$N_0(t) = \frac{1}{(\alpha_0+\sigma_1)I_0+\frac{1}{\tau_1}}\Bigg(N_1(t_m)\{\sigma_1 I_0 + \frac{1}{\tau_1}\}\{1 - e^{-[(\alpha_0+\sigma_1)I_0+\frac{1}{\tau_1}](t-t_m)}\} + N_0(t_m)\{\sigma_1 I_0 + \frac{1}{\tau_1} + \alpha_0 I_0 e^{-[(\alpha_0+\sigma_1)I_0+\frac{1}{\tau_1}](t-t_m)}\}\Bigg) \tag{2.12b}$$

$$N_1(t) = \begin{cases} 0 & t \le t_i \\ \frac{N_0(t_i)\alpha_0 I_0}{(\alpha_0+\sigma_1)I_0+\frac{1}{\tau_1}}(1 - e^{-[(\alpha_0+\sigma_1)I_0+\frac{1}{\tau_1}](t-t_i)}) & t_i < t \le t_f \\ N_1(t_f)e^{-\frac{t-t_f}{\tau_1}} & t_f < t \end{cases} \tag{2.13a}$$

$$N_0(t) = \begin{cases} N_{0i} & t \le t_i \\ \frac{N_0(t_i)}{(\alpha_0+\sigma_1)I_0+\frac{1}{\tau_1}}\{(\sigma_1 I_0 + \frac{1}{\tau_1}) + \alpha_0 I_0 e^{-[(\alpha_0+\sigma_1)I_0+\frac{1}{\tau_1}](t-t_i)}\} & t_i < t \le t_f \\ N_1(t_f)(1 - e^{-\frac{t-t_f}{\tau_1}}) + N_0(t_f) & t_f < t \end{cases} \tag{2.13b}$$

From Equation 2.13a, it is clear that the rise time constant τ_{rise} and τ_{fall} are different from one each other as given in Equation 2.14. the rise time constant is smaller or faster than the fall time constant in this case and depends on the pump I_0 and the coefficients of StE σ_1 of the state S_1 and SpE α_0 of the state S_0. Furthermore, Equation 2.13a shows that having a bigger stimulated coefficient σ_1 from excited state S_1 will reduce the steady state population and a bigger absorption coefficient α_0 from ground state S_0 will increase the steady state population. This is as expected.

$$\tau_{rise} = [(\alpha_0 + \sigma_1)I_0 + \frac{1}{\tau_1}]^{-1} < \tau_1 \tag{2.14a}$$

$$\tau_{fall} = \tau_1 \tag{2.14b}$$

2.2 Excited State Absorption

Since the system in our case is not in laser action, the stimulated emission effect is often ignored. In other word, we assume that $\sigma_1 I_0 \approx 0$. This may seem a bit time wasting to find the most general solution then return to special case and ignore some terms in the solution; however, by working this part out, the effect of Excited State Absorption (ESA) on rise time constant τ_{rise} and the final steady state population can easily be deduced. Here the state diagram is increased by 1 more state called S_2, with its population density denoted as N_2 as given in Figure 2.6 on page 20. The energy gap between S_2 and S_1 is purposely introduced to be equal to that of S_1 to S_0. ESA occurs when the pump wavelength coincides with the energy gap between two excited states (in our case S_2 and S_1 with the energy gap as $E_2 - E_1$) with non-zero population in the lower excited state S_1. However, as clearly illustrated in Equation 2.16[2] it is only observable when the product of the pump intensity I_0 and the ESA coefficient α_1 of the state S_1 is around the same order of magnitude as the natural decay rate τ_1 of the state S_1. The state S_2 will have a total decay rate of $1/\tau_2$. This is the sum of the decay rate $1/\tau_{21}$ from S_2 to S_1 and decay rate $1/\tau_{20}$ from S_2 to S_0. Comparing the results from Equation 2.7, Equation 2.13 and Equation 2.14, the ESA coefficient will make rise time constant $\tau_{1,rise}$ of the state S_1 shorter or faster than the fall time constant $\tau_{1,fall}$ of the state S_1 while affecting the steady state population.

[2]The equation has been simplified by not having piecewise functions anymore. The piecewise information is contained in the pump intensity I, which has been defined earlier in Equation 2.1 on page 10.

$$\frac{1}{\tau_2} = \frac{1}{\tau_{21}} + \frac{1}{\tau_{20}} \tag{2.15}$$

$$\frac{dN_2}{dt} = -\frac{N_2}{\tau_2} + \alpha_1 I N_1 \tag{2.16a}$$
$$\frac{dN_1}{dt} = \frac{N_2}{\tau_{21}} - (\alpha_1 I - \frac{1}{\tau_1})N_1 + \alpha_0 I N_0 \tag{2.16b}$$
$$\frac{dN_0}{dt} = \frac{N_2}{\tau_{20}} + \frac{N_1}{\tau_1} - \alpha_0 I N_0 \tag{2.16c}$$
$$\tag{2.16d}$$

An interesting way to look at rate equation is that, based on the earlier 2-level result as given in Equation 2.13a the steady state population density in Equation 2.16b of N_1 is proportional to the pump intensity I_0 such that $N_1 \propto I_0$; However, looking at Equation 2.16a, the final steady state population density of N_2 is proportional to the pump intensity I_0 again, and is multiplied by the population density N_1 of state S_1. We know N_1 is again proportional to I_0; therefore, the state population S_2 is proportional to the square of the pump intensity such that $N_2 \propto I_0^2$, and is a 2 photon process. By 2 photon process, we mean that it takes 2 photons to excite an ion consecutively up into the S_2 state. Generalizing this result, an n-photon absorption process will mean the process is proportional to I_0^n. This result as verified by many other researchers is illustrated again in Chapter 4 on page 34.

Up to this point, even the three level system as given in Equation 2.16 can be, even though cumbersome and difficult, theoretically, solved using linear systems theory of eigenvalue and eigenvector method as given in Equation 2.11. Everything here in the rate equation are linear terms and the rate equations dN_0/dt, dN_1/dt, and dN_2/dt should be labeled as $dN_{0,l}/dt$, $dN_{1,l}/dt$, and $dN_{2,l}/dt$, respectively, indicating that they are linear part of the rate equations. This indicates that there is a non-linear part of rate equation $dN_{0,nl}/dt$, $dN_{1,nl}/dt$, and $dN_{2,nl}/dt$, such that the total rate of the states $dN_{0,t}/dt$, $dN_{1,t}/dt$, and $dN_{2,t}/dt$ become Equation 2.17

$$\frac{dN_{2,t}}{dt} = \frac{dN_{2,l}}{dt} + \frac{dN_{2,nl}}{dt} \tag{2.17a}$$
$$\frac{dN_{1,t}}{dt} = \frac{dN_{1,l}}{dt} + \frac{dN_{1,nl}}{dt} \tag{2.17b}$$
$$\frac{dN_{0,t}}{dt} = \frac{dN_{0,l}}{dt} + \frac{dN_{0,nl}}{dt} \tag{2.17c}$$

2.3 Energy Transfer Up-conversion (ETU) and Cross Relaxation (XR)

Energy Transfer Up-Conversion (ETU) and Cross Relaxation (XR) are processes explained by Dexter and Forster energy transfer schemes in as discussed in Section 1.1. As shown in Figure 2.7 and Figure 2.8, both ETU and XR involves an ion transfering its enery to another ion. Based on Figure 2.9, the non-linear portion of the rate equation has been given in Equation 2.18 and Equation 2.19. As described by Equation 2.17, is the sum of the linear part of the processes and non-linear part of the processes. For the three level system then, by combining Equation 2.17, Equation 2.16 (this is the linear part), Equation 2.18, Equation 2.19, and Equation 2.20, the total rate is given explicitly by Equation 2.21. A 2 is multiplied by the terms going into or out of the state S_1 because the state either loses or gains 2 ions to produce the effect. Furthermore, just as ESA has an I^2 term for two photon "ladder jumps", ETU and XR have N^2 dependence. There are also 3 ion processes not discussed here; however, the idea is similar. The general model of this is treated and discussed by Zuegel et. al. [48].

$$\frac{dN_{2,ETU}}{dt} = W_{11}N_1^2 \tag{2.18a}$$
$$\frac{dN_{1,ETU}}{dt} = -2W_{11}N_1^2 \tag{2.18b}$$
$$\frac{dN_{0,ETU}}{dt} = W_{11}N_1^2 \tag{2.18c}$$

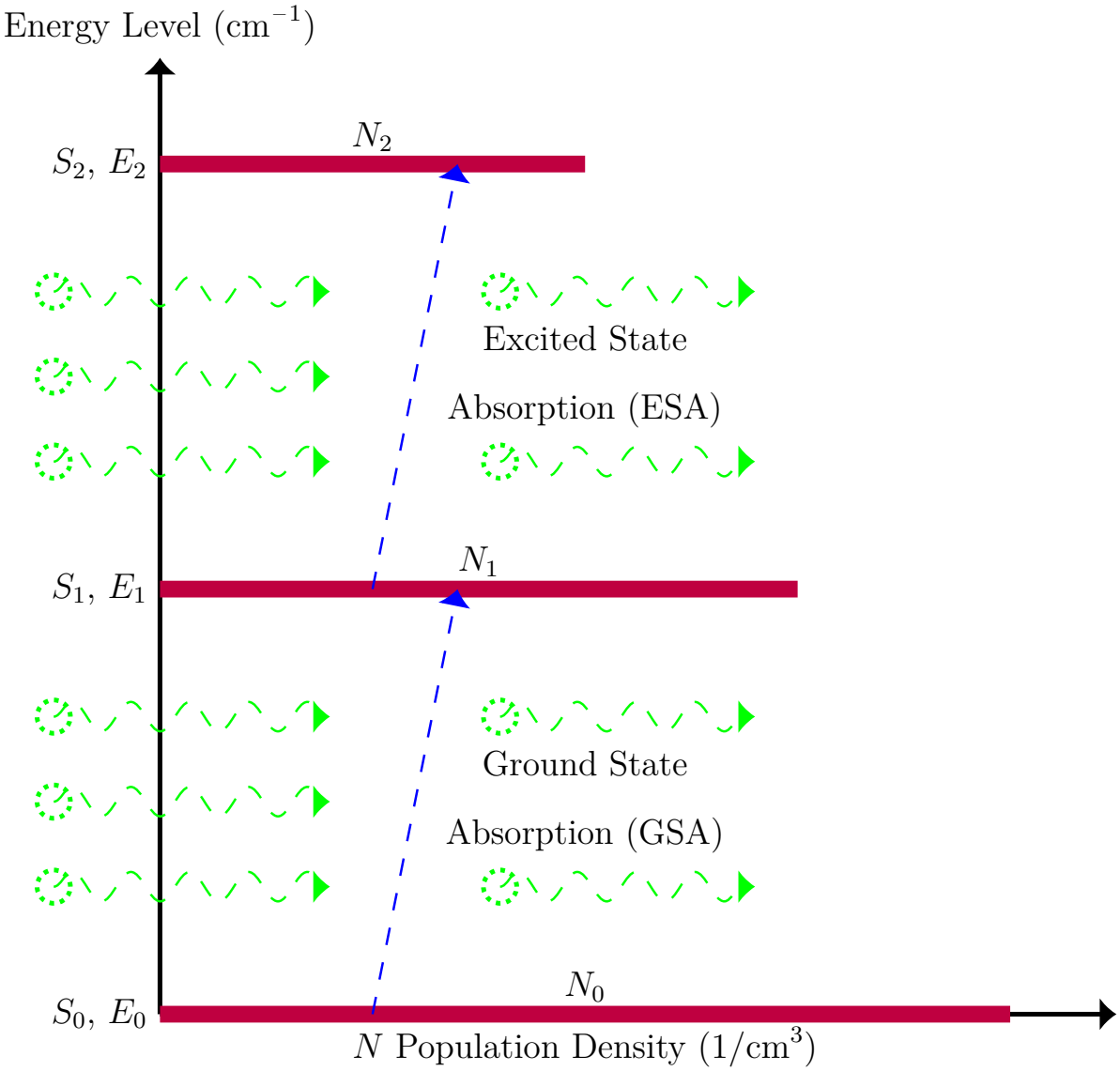

Figure 2.6: Simple 3 level population density diagram showing Ground State Absorption (GSA) and Excited State Absorption (ESA). This N_2 level will have its own stimulated emission down to N_1 and radiative and non-radiative decays as well as spontaneous emissions down to N_1 and N_0.

$$\frac{dN_{2,XR}}{dt} = -W_{20}N_2N_0 \tag{2.19a}$$

$$\frac{dN_{1,XR}}{dt} = 2W_{20}N_2N_0 \tag{2.19b}$$

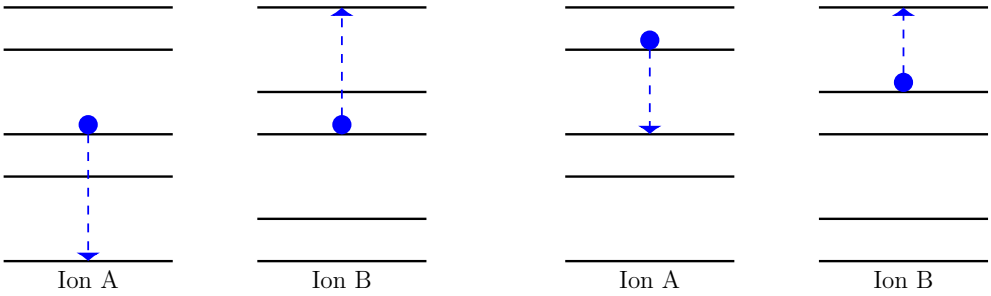

(a) ETU causing one ion coming back to ground state.

(b) ETU process ending in both ions in excited state.

Figure 2.7: Energy Transfer Up-conversion (ETU) of Ion A transfering energy to Ion B.

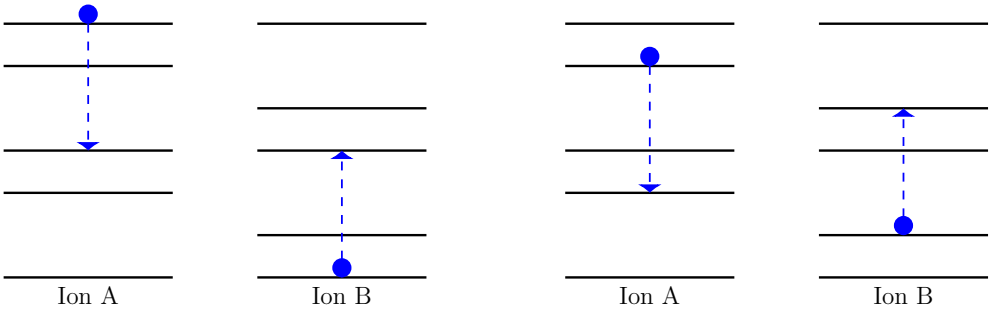

(a) XR leaving both ions in the same state.

(b) XR leaving both ions at some mid-energy level.

Figure 2.8: Cross Relaxation (XR) of Ion A transfering energy to Ion B.

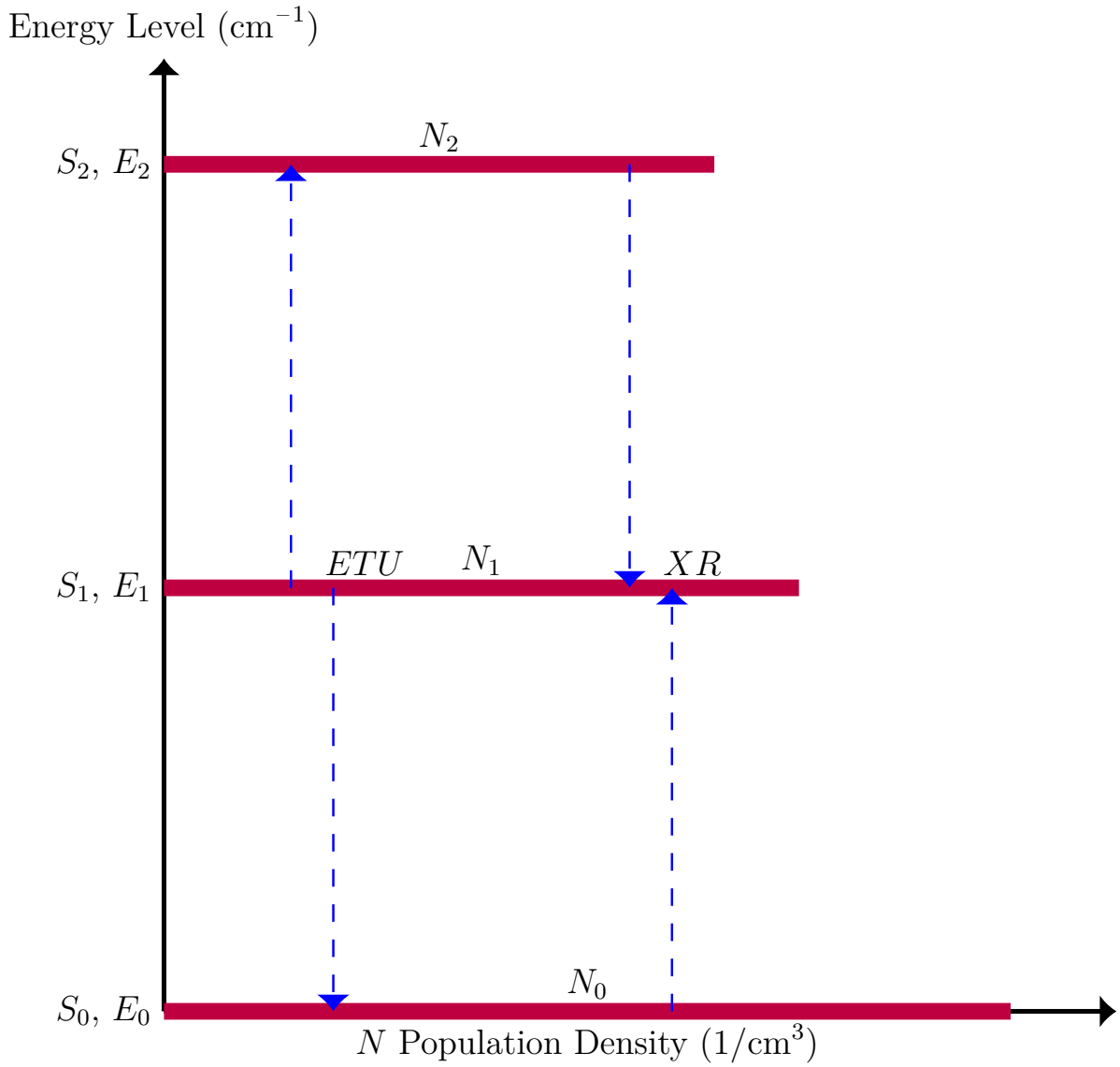

Figure 2.9: An example of simple 3 level population density diagram showing Energy Transfer Up-conversion (ETU) and Cross Relaxation (XR).

$$\frac{dN_{0,XR}}{dt} = -W_{20}N_2N_0 \tag{2.19c}$$

$$\frac{dN_{2,nl}}{dt} = \frac{dN_{2,ETU}}{dt} + \frac{dN_{2,XR}}{dt} \tag{2.20a}$$
$$\frac{dN_{1,nl}}{dt} = \frac{dN_{1,ETU}}{dt} + \frac{dN_{1,XR}}{dt} \tag{2.20b}$$
$$\frac{dN_{0,nl}}{dt} = \frac{dN_{0,ETU}}{dt} + \frac{dN_{0,XR}}{dt} \tag{2.20c}$$

$$\frac{dN_2}{dt} = -\frac{N_2}{\tau_2} + \alpha_1 I N_1 + W_{11}N_1^2 - W_{20}N_2N_0 \tag{2.21a}$$
$$\frac{dN_1}{dt} = \frac{N_2}{\tau_{21}} - (\alpha_1 I - \frac{1}{\tau_1})N_1 + \alpha_0 I N_0 - 2W_{11}N_1^2 + 2W_{20}N_2N_0 \tag{2.21b}$$
$$\frac{dN_0}{dt} = \frac{N_2}{\tau_{20}} + \frac{N_1}{\tau_1} - \alpha_0 I N_0 + W_{11}N_1^2 - W_{20}N_2N_0 \tag{2.21c}$$

2.4 Erbium Systems

Rare earth ions, because of its isolated 4f shell of electron, allow it to be doped in virtually anything without much change in its energy levels. Furthermore, erbium, in particular, is just right for making 1.6 μm and 3 μm lasers because of its energy gaps between different energy levels. However, the system is not problem free. For example, in lightly doped Erbium Yttrium Aluminum Garnet of 0.5% (0.5%Er:YAG) the life time ratio between the laser terminal state and the laser upper state of 3 μm laser has a ratio of 10 leaving Continuous Wave (CW) operation nearly impossible. This has been resolved, though inefficiently due to large quantity of phonon generation, by energy transfer scheme worked out by Furtado et. al. as given in Section 1.1 [10]. Furthermore, ESA and ETU effects are strongly exhibited in erbium due to the right energy gaps between levels making the system extremely complex. This complexity due to ESA and ETU is a double edged sword. If exploited correctly, this will help the laser action. On the other hand, if this process is used incorrectly, the result is detrimental to laser action.

To show the complexity of the system, we include the model used by Georgescu et. al. as given in Figure 2.10 on page 26 [11, 32]. In this figure, all processes that is associated with $^4I_{15/2}$, $^4I_{13/2}$, $^4I_{11/2}$, $^4I_{9/2}$, $^4F_{9/2}$, $^4S_{3/2}$ will contain a subscript 0, 1, 2, 3, 4, and 5, respectively. For example, the ground state $^4I_{15/2}$, $^4I_{13/2}$, $^4I_{11/2}$, $^4I_{9/2}$, $^4F_{9/2}$, $^4S_{3/2}$ has a population density of N_0, N_1, N_2, N_3, N_4, and N_5, respectively. Each state has been labeled by that number in the figure as well. R is the natural decay rate as discussed in Equation 2.4. As an example, R_5 is the total natural decay rate from $^4S_{3/2}$. R_5 includes R_{54}, R_{53}, R_{52}, R_{51}, and R_{50} as given in Equation 2.22, where R_{54}, R_{53}, R_{52}, R_{51}, and R_{50} are natural decay rates from $^4S_{3/2}$ to $^4F_{9/2}$, $^4I_{9/2}$, $^4I_{11/2}$, $^4I_{13/2}$, and $^4I_{15/2}$. This convention is true for other states as well. The inverse of R_5 is the natural fluorescence life time τ_5 as given in Equation 2.23. The cooperative effects such as ETU and XR will have coefficients W with subscripts of the involved states at the beginning of the process. The number of subscripts also indicates the number of ions required for a process. For example, W_{11} indicates that two ions from $^4I_{13/2}$ are required for the process, where as W_{511} requires three ions: one from $^4S_{3/2}$ and two from $^4I_{13/2}$. The pump wavelength of 965 nm corresponds to the gaps shown in the figure for GSA and ESA's. The absorption coefficient α of various states will carry the subscript by the similar convention. For example, the absorption coefficient from $^4I_{13/2}$ to $^4F_{9/2}$ is α_{14}.

From looking at Equation 2.24, it is clear that the non-linear differential equation of six coupled levels is extremely difficult if not impossible to solve analytically. To add to the problem, there are a lot of constants or parameters depending on the host material for the erbium ions. Most of these constants need experimental work to obtain. The natural life time constants τ of various levels are well known and can easily be measured as is done in Chapter 5. Many coefficients have been cleverly obtained such as ESA coefficients at $^4I_{13/2}$ $\alpha_1(\lambda)$, $^4I_{11/2}$ $\alpha_2(\lambda)$, and $^4F_{9/2}$ $\alpha_3(\lambda)$ for various materials by Koetke and Huber [29] via a clever dual pump technique. Several cooperative coefficients (ETU) and (XR) have been estimated by Georgescu et. al. and many others [12] using another technique. However, the path of energy that ions take and the coefficients were all estimated with many assumptions. Not one single method is able to obtain all the information. In Chapter 6, we present a

simple technique that can yield information about rare earth systems that are particularly useful to laser crystal makers.

$$R_5 = R_{54} + R_{53} + R_{52} + R_{51} + R_{50} \tag{2.22}$$

$$\tau_5 = \frac{1}{R_5} \tag{2.23a}$$

$$\tau_{54} = \frac{1}{R_{54}} \tag{2.23b}$$

$$\tau_{53} = \frac{1}{R_{53}} \tag{2.23c}$$

$$\tau_{52} = \frac{1}{R_{52}} \tag{2.23d}$$

$$\tau_{51} = \frac{1}{R_{51}} \tag{2.23e}$$

$$\tau_{50} = \frac{1}{R_{50}} \tag{2.23f}$$

$$\begin{aligned}
{}^4\mathrm{S}_{3/2}: \quad \frac{dN_5}{dt} =& -\frac{1}{\tau_5}N_5 + \alpha_{25} I N_2 + W_{22} N_2^2 \\
& - W_{50} N_5 N_0 - W_{500} N_5 N_0^2 + W_{111} N_1^3 && \text{(2.24a)} \\
{}^4\mathrm{F}_{9/2}: \quad \frac{dN_4}{dt} =& \frac{1}{\tau_{54}}N_5 - \frac{1}{\tau_4}N_4 + \alpha_{14} I N_1 && \text{(2.24b)} \\
{}^4\mathrm{I}_{9/2}: \quad \frac{dN_3}{dt} =& \frac{1}{\tau_{53}}N_5 + \frac{1}{\tau_{43}}N_4 - \frac{1}{\tau_3}N_3 + W_{11} N_1^2 + W_{500} N_5 N_0^2 + W_{50} N_5 N_0 && \text{(2.24c)} \\
{}^4\mathrm{I}_{11/2}: \quad \frac{dN_2}{dt} =& \frac{1}{\tau_{52}}N_5 + \frac{1}{\tau_{42}}N_4 + \frac{1}{\tau_{32}}N_3 - (\frac{1}{\tau_2} + \alpha_{25} I) N_2 - 2W_{22} N_2^2 + \alpha_{02} I N_0 && \text{(2.24d)} \\
{}^4\mathrm{I}_{13/2}: \quad \frac{dN_1}{dt} =& \frac{1}{\tau_{51}}N_5 + \frac{1}{\tau_{41}}N_4 + \frac{1}{\tau_{31}}N_3 + \frac{1}{\tau_{21}}N_2 - (\frac{1}{\tau_1} + \alpha_{14} I) N_1 \\
& + W_{50} N_5 N_0 - 2W_{11} N_1^2 + W_{500} N_5 N_0^2 - 3W_{111} N_1^3 && \text{(2.24e)} \\
{}^4\mathrm{I}_{15/2}: \quad \frac{dN_0}{dt} =& \frac{1}{\tau_{50}}N_5 + \frac{1}{\tau_{40}}N_4 + \frac{1}{\tau_{30}}N_3 + \frac{1}{\tau_{20}}N_2 + \frac{1}{\tau_1}N_1 - \alpha_{02} I N_0 \\
& - W_{50} N_5 N_0 + W_{22} N_2^2 + W_{11} N_1^2 - W_{500} N_5 N_0^2 + 2W_{111} N_1^3 && \text{(2.24f)}
\end{aligned}$$

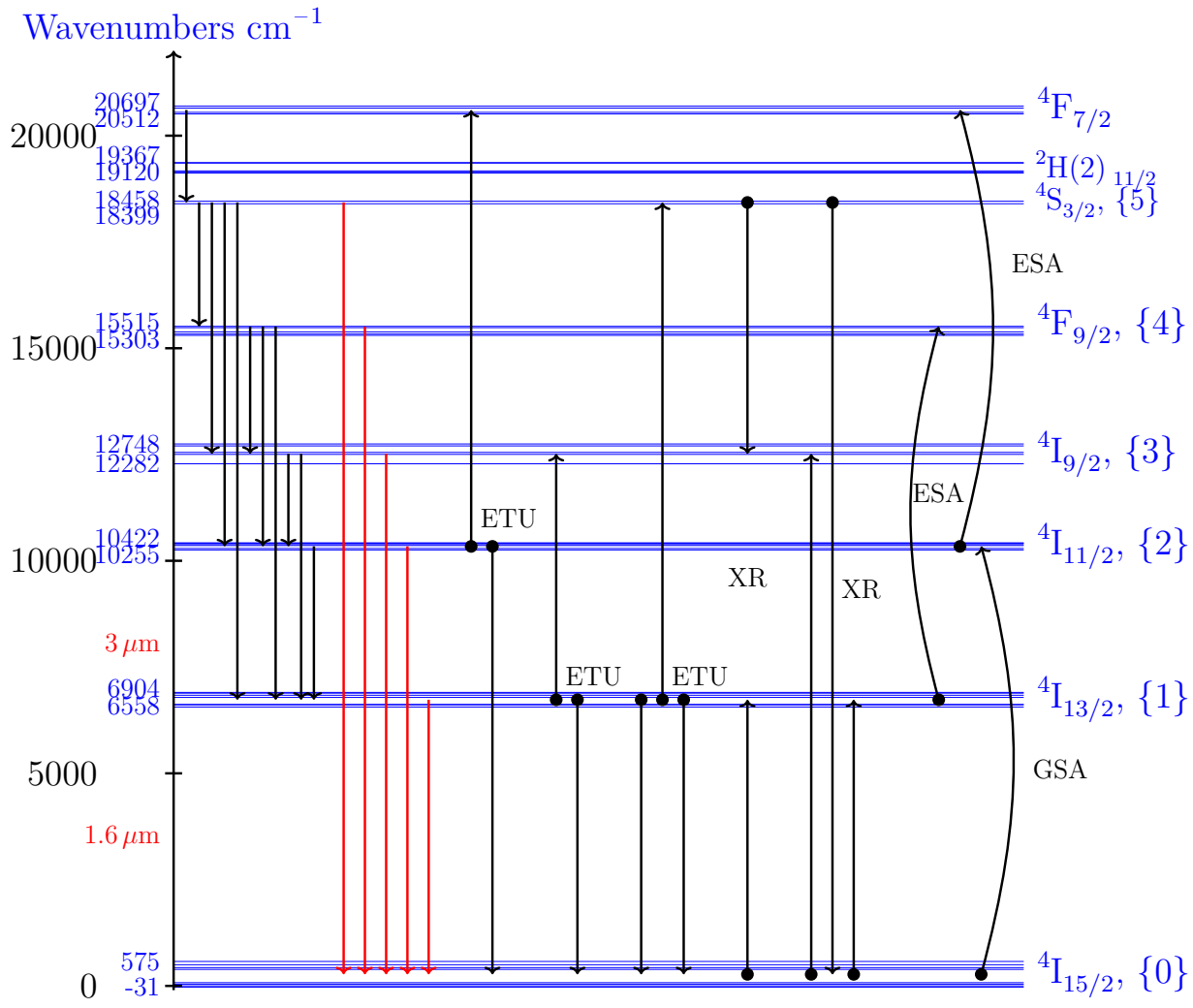

Figure 2.10: Calculated energy Levels of Er:YAG. The lighter color (red) downward arrows are the observed wavelengths of fluorescence as given in Figure 3.6 on page 31. ETU: Energy Transfer Upconversion, ESA: Excited State Absorption, XR: Cross Relaxation.

Chapter 3

Spectra of Erbium Under High Intensity Pumping

The present chapter elaborates on the emission spectra of erbium doped in both YAG and yttria under 960 nm high pump intensity (up to 10 kW/cm^2). The emission spectra is given to illustrate the relevant energy levels and to indicate the existence of the typical assumed unobservable $^4I_{9/2}$ fluorescence.

3.1 Setup of Spectral Investigation

A 960 nm fiber coupled laser diode at 7 W optical output is sent through a 2" focal length and 2" in diameter lens at 4" away from the laser. The laser beam is focused down to roughly 100 μm in diameter and directed onto an erbium-doped sample, which is placed 4" away from the lens. The erbium-samples are held in a heatsink to reduce thermal stress under high power pump. Ocean optics spectrometer is positioned 90° relative to the direction of the incoming laser beam. The actual laser power after going through the lens and onto the sample is 5 W. The schematic is given in Figure 3.1 on page 29.

The equipment list is given as follows.

1. 960nm fiber-coupled laser diode Model#: Sheaumann Lasers Inc.
2. Ceramic (Cer) Erbium-doped YAG samples
   (a) 1%
   (b) 3%
   (c) 50%
3. Ceramic (Cer) Erbium doped yttria samples
   (a) 1%
   (b) 15%
   (c) 25%
4. Ocean Optics UV-NIR4000
5. 2" focal length and 2" diameter convex lens x 2

3.2 Results on Spectra of Erbium-doped Samples

First, the spectra of the input pump is given in Figure 3.2 and Figure 3.3. The rest are the spectra of the samples listed above. This indicates what optical bandpass filters are needed or fluorescence or state population observation for future experiments.

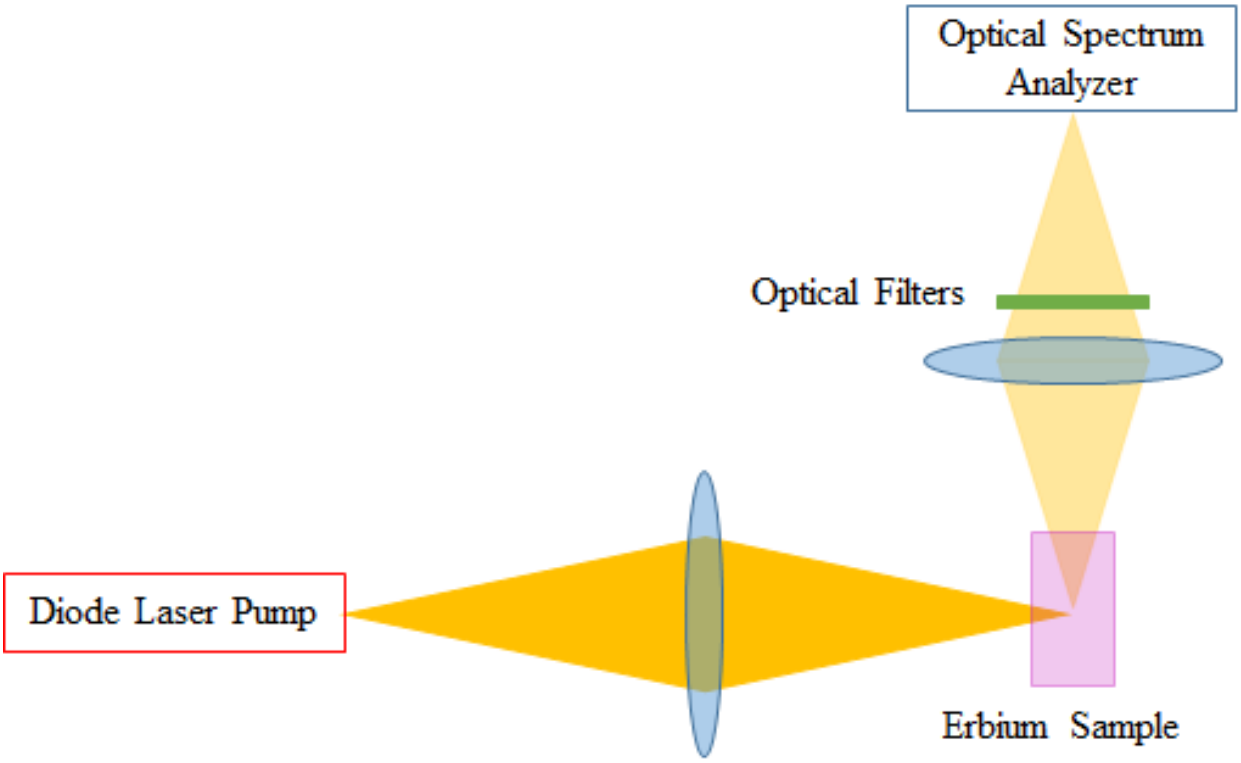

Figure 3.1: Experimental setup of optical spectra under high intensity 965 nm diode laser pumping.

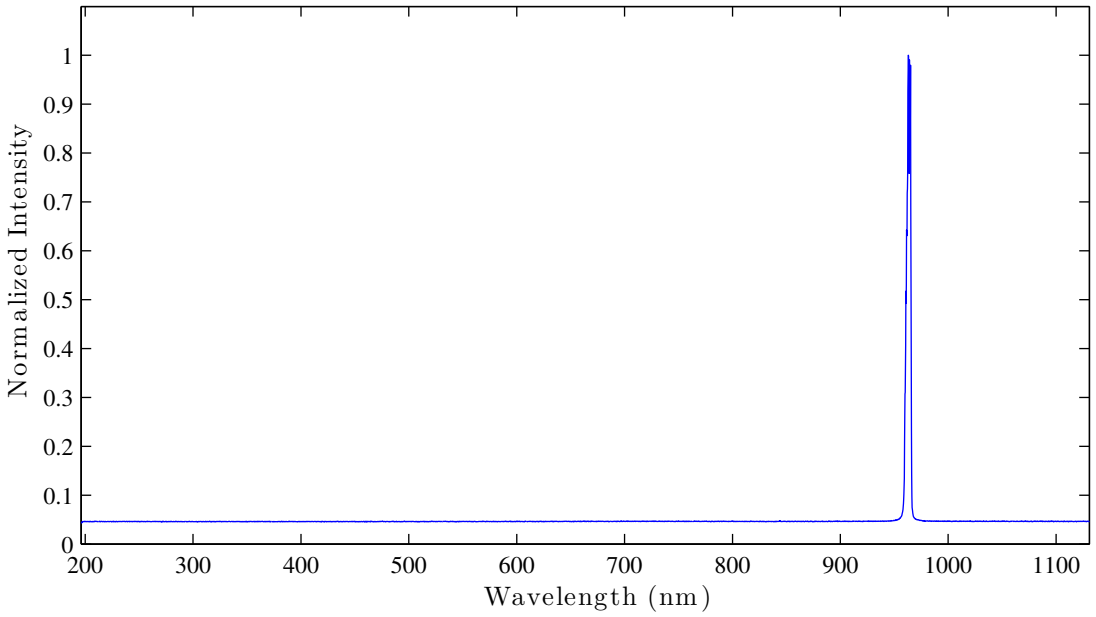

Figure 3.2: Fiber coupled 960 nm laser diode pump wavelength information.

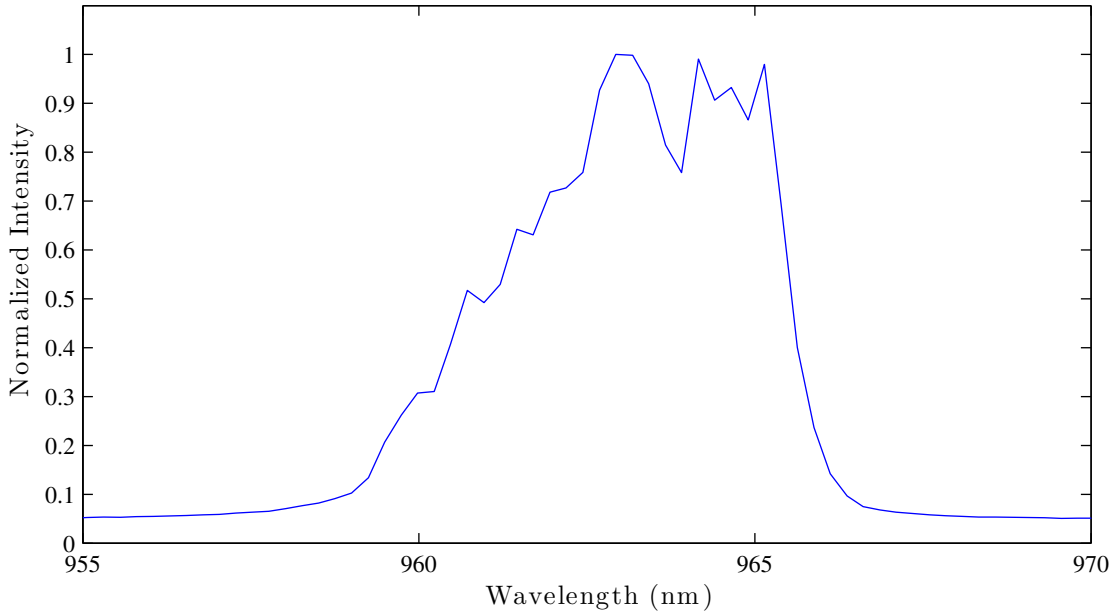

Figure 3.3: Fiber coupled 960 nm laser diode pump wavelength information zoomed in around 960 nm region.

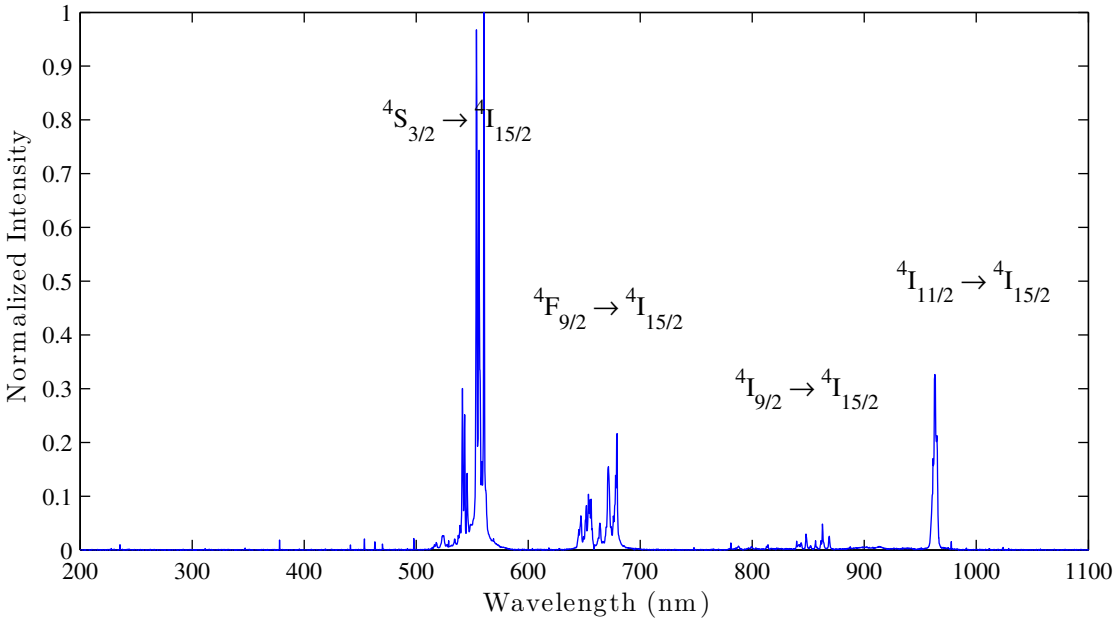

Figure 3.4: Fluorescence spectra of 1% Er:YAG under high intensity pumping.

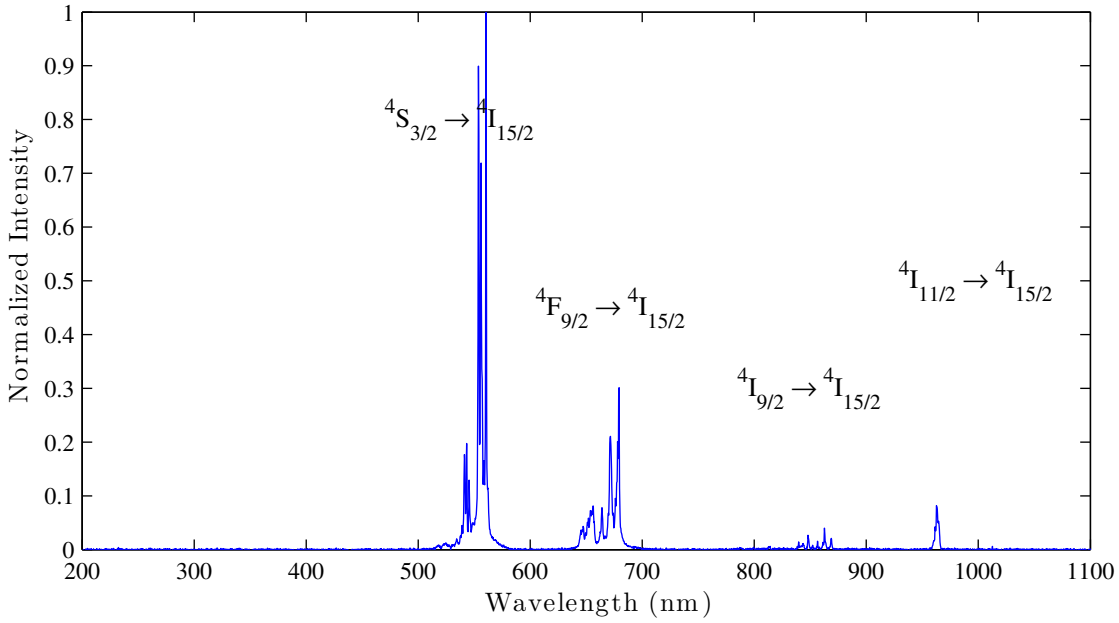

Figure 3.5: Fluorescence spectra of 3% Er:YAG under high intensity pumping.

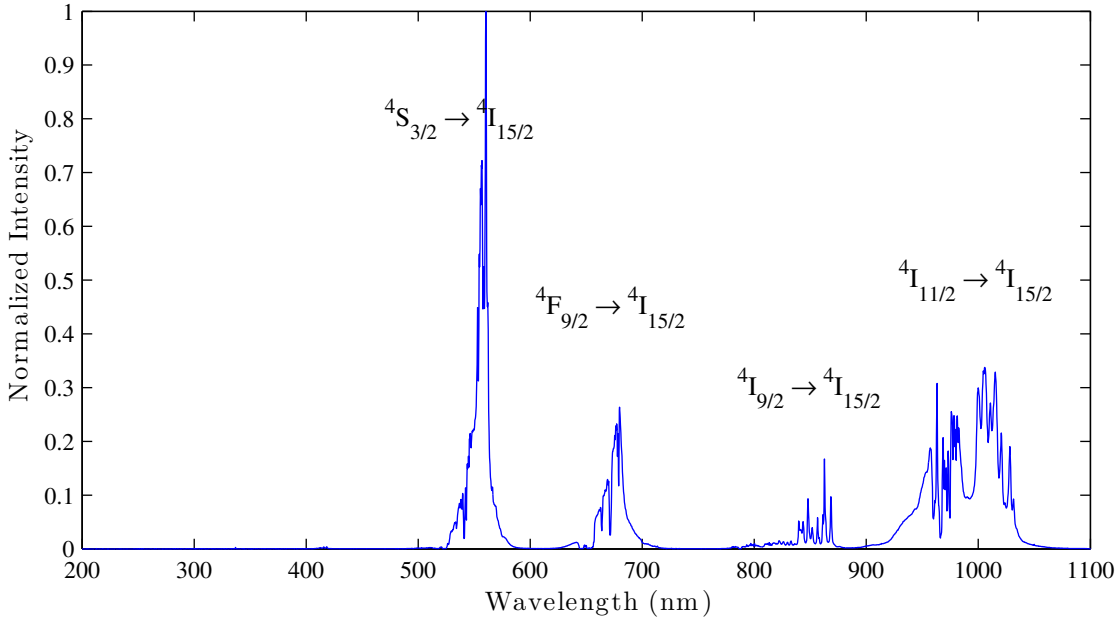

Figure 3.6: Fluorescence spectra of 50% Er:YAG under high intensity pumping.

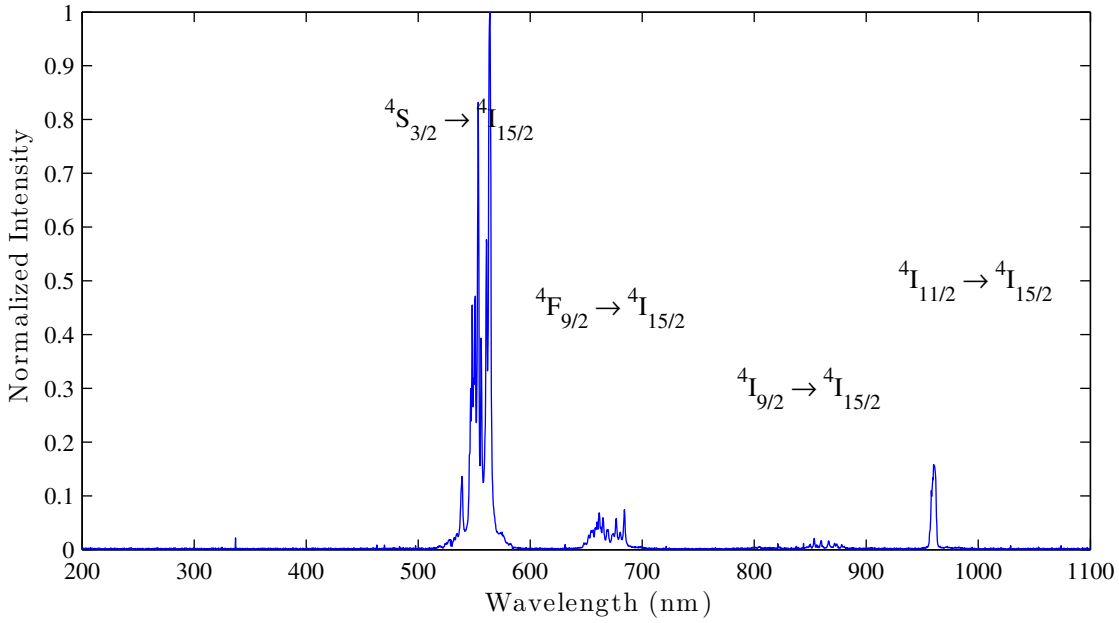

Figure 3.7: Fluorescence spectra of 1% Er:Y_2O_3 under high intensity pumping.

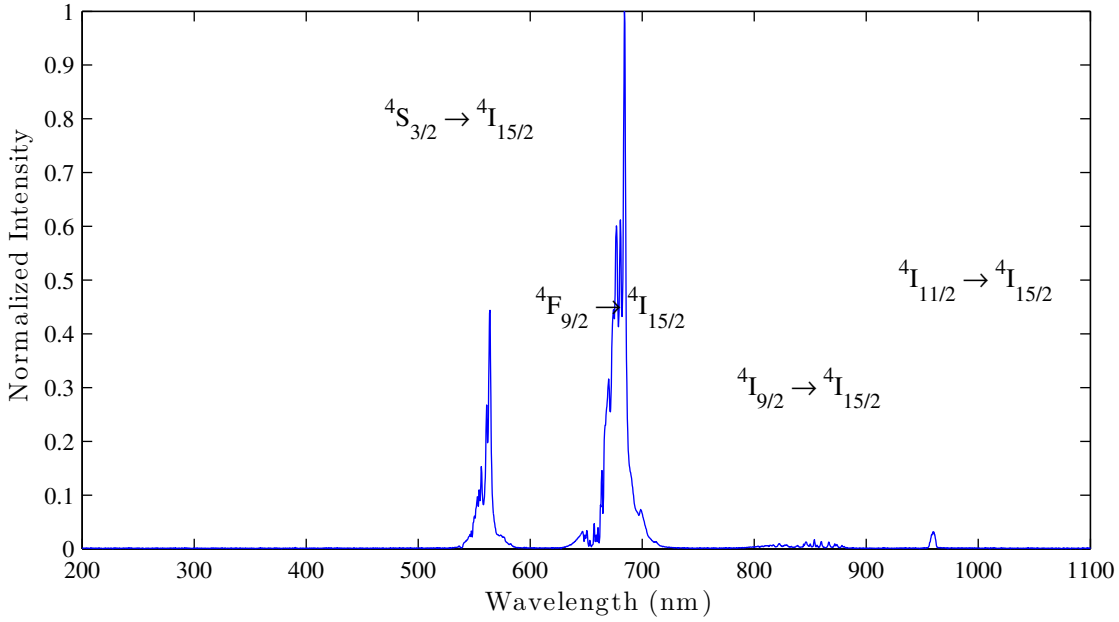

Figure 3.8: Fluorescence spectra of 15% Er:Y_2O_3 under high intensity pumping.

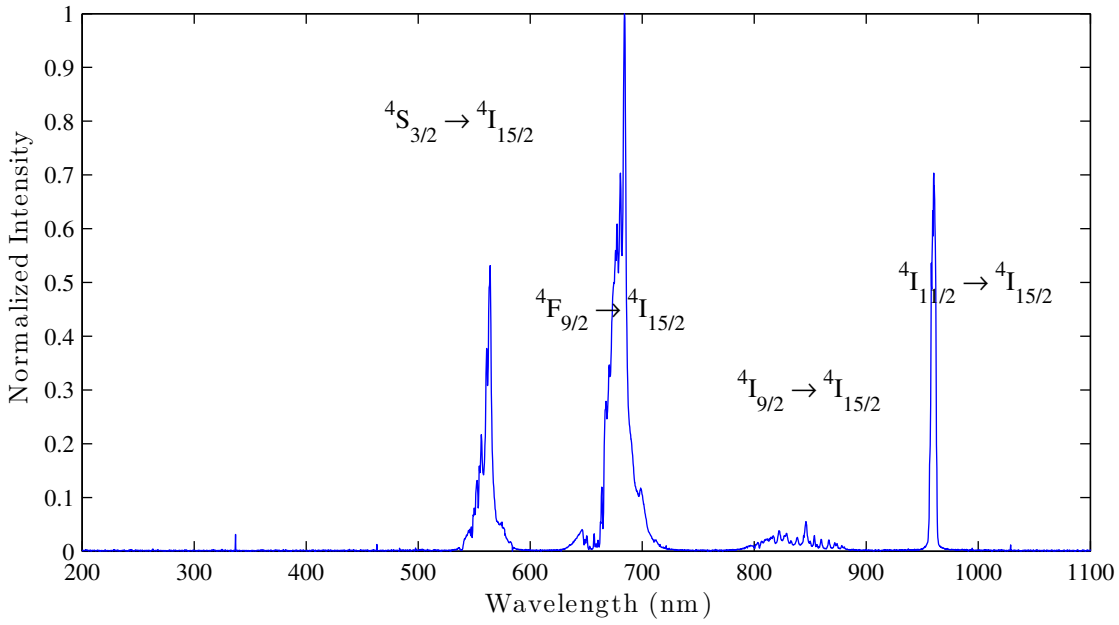

Figure 3.9: Fluorescence spectra of 25% Er:Y_2O_3 under high intensity pumping.

Chapter 4

Intensity Dependence

As given in the work of Auzel et. al. [1], the fluoresnce intensity has a power of n-dependence on input/excitation intensity, where n is the number of photons involved in the process, as given in Equation 4.1 on page 36. This is true for both ESA and ETU. For ETU, this relationship is obtainable as there are terms in the rate equation dependent of population-squared N^2 and even cubed N^3. Since the population of any state N is proportional to the input pump intensity I, then N^n indicates that the relationship is proportional to I^n. For ESA, this can also be obtained by looking at the rate equation and seeing that a state's population density rate of change is dependent of a lower excited state population density multiplied by the pump IN_l. Since the lower state population N_l is dependent of the input pump intensity itself, then substitute the upper state rate equation's N_l term with intensity times a constant then the upper state is also proportional to intensity squared. This can go higher to the third power or n^{th} power. However, the intensity would have to be incredibly high for third order effects to become observable. For some of the experimental results taken below, the numbers n aren't exactly to integer values due to other processes that are interfering with results such as thermal phonon decay [31].

4.1 Experimental Setup of Intensity Dependence

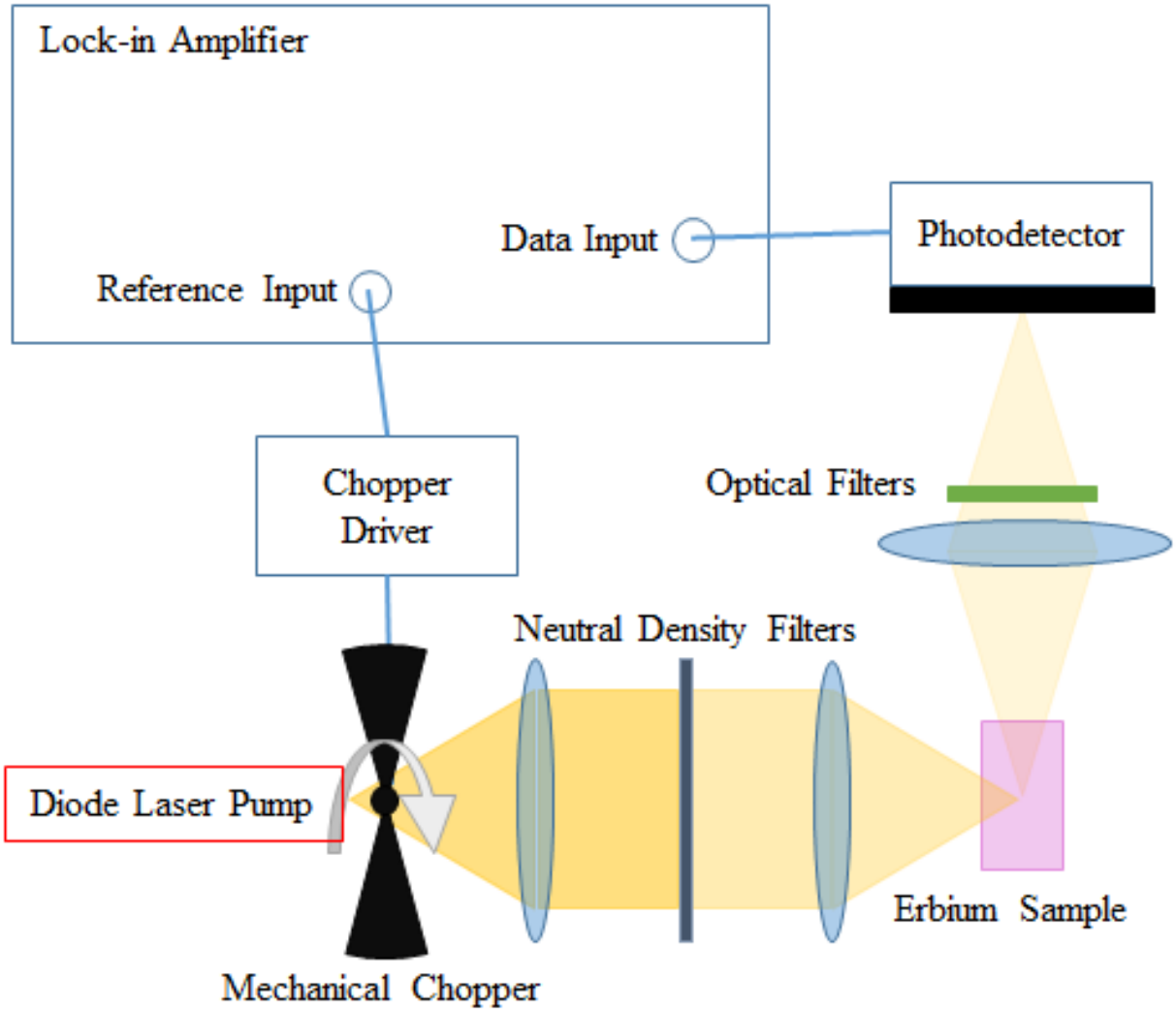

Figure 4.1: The experimental setup of Intensity Dependence.

$$I_{fluorescence} \propto I_{input}^{n} \tag{4.1}$$

A 965 nm fiber-coupled laser diode is used to excite the sample. First the laser beam is expanded and collimated through a lens before sending it through the ND-filter to change the total power of the beam. This reduce the chance of damaging the ND-filters from the high power laser beam. After the total power is changed to the desired level, the beam is then refocused to create the desired intensity incident upon the sample. The input laser beam is chopped for data collection through a lock-in amplifier for high signal-to-noise ratio. The data is collected through a PMT with the proper optical bandpass filter for the observation of the state of interest. The detailed equipment list is given below.

1. 7 W 965 nm fiber-coupled laser diode Model#: SNP-962-5-1022-6.5, Sheaumann Lasers Inc.
2. 50% erbium-doped YAG sample
3. Hamamatsu r955 Photomultiplier (PMT)
4. Stanford Research 810 Lockin Amplifier
5. Thorlabs chopper controller
6. Thorlabs 2 blade chopper blade
7. 2" focal length and 2" diameter convex lens x 2
8. Baltzer glass reflective type neutral density filter set
9. Thorlabs FB550-10 x2 bandpass filter
10. Thorlabs FB650-40 x2 bandpass filter

4.2 Results on Intensity Dependence

The results are plotted on log-log scale. The curve is fitted using power model $y = x^n$. By looking at the n value in the fitted curve, the number of photons n that is involved in the process can be obtained.

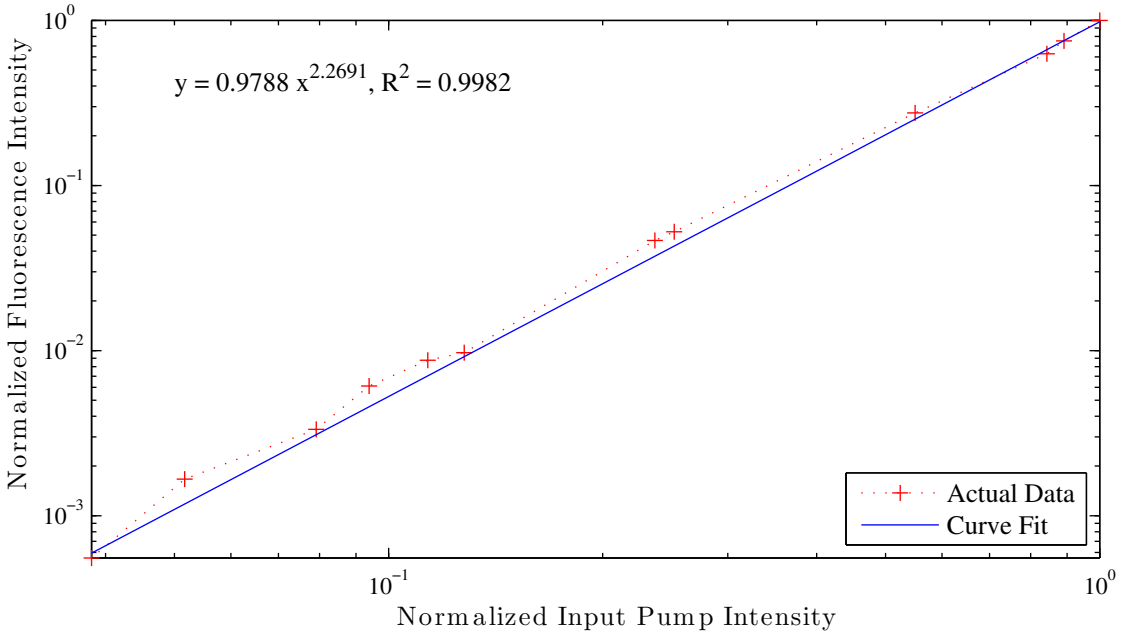

Figure 4.2: $^4S_{3/2}$ fluorescence intensity versus up to $10\,kW/cm^2$ of pump intensity of 50% Er:YAG. The fitted-curve information is given on top left corner of the plot.

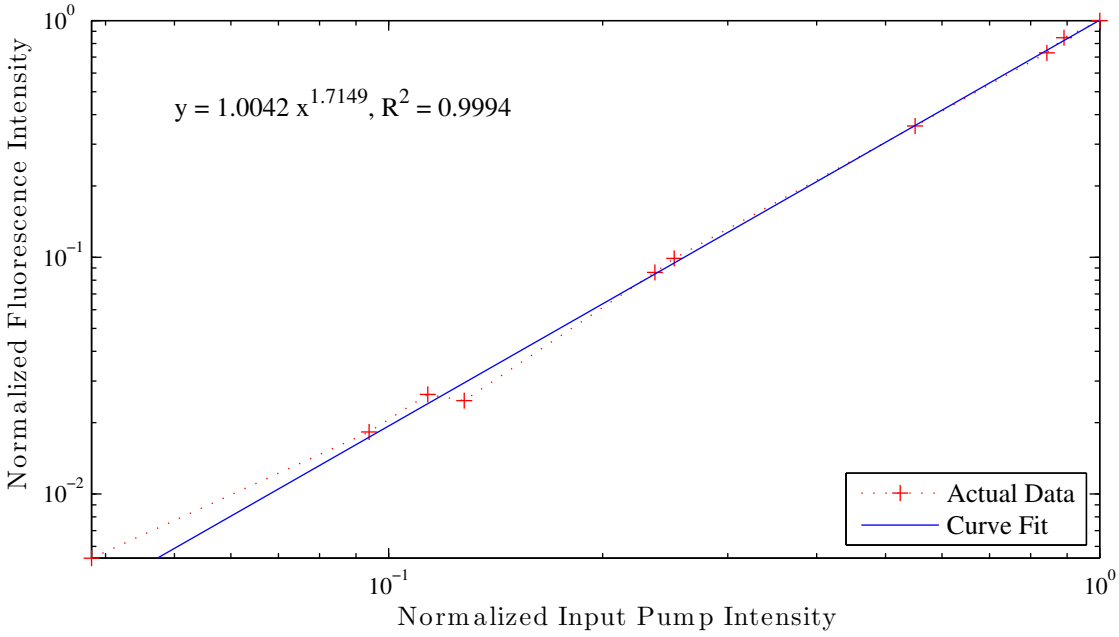

Figure 4.3: $^4F_{9/2}$ fluorescence intensity versus up to 10 kW/cm^2 of pump intensity of 50% Er:YAG. The fitted-curve information is given on top left corner of the plot.

Chapter 5

Low Pump Level Fluorescent Life Times

Under high intensity pumping, various nonlinear processes become important. However, under low intensity pumping and looking at only the decay, the ESA as well as nonlinear cooperative processes such as ETU and XR are negligible. This allows us to obtain the life times of the erbium systems of interest without much "contamination" of ESA, ETU, and XR. In other words, only the linear terms in the rate equations are present. The life time under low-pump levels (LTLP) τ_{nat} includes two rate component as was shown in Equation 2.5: the radiative decay rate from spontaneous emission R_{sp} and the non-radiative decay rate R_{nr}. This life time corresponds to the e^{-1} point of the fluorescence decay. If the decay follows that of exponential function, the plot of semilog-y would be a straight line. This is no longer true once the system contain non-linear cooperative effects such as ETU and XR. In this work, the low-pump life times are measured and tabulated in Section 5.3. Some of the results are plotted in both linear scale as well as semilog-y scale to demonstrate that the life time contains virtually no non-linear effects.

5.1 Experimental Setup for the Measurement of Fluorescent Life Times (Low-Pump Levels)

The experimental setup of low-pump fluorescent life time measurement consists of An electically modulated (square-wave) UV LED capable of 1 W of optical output used to excite the erbium samples with a set of two stacked 390 nm optical short pass filter (Semrock: FF01-390/SP-25) to block out any visible wavelength that can possibly come out of the UV LED. Next, a PMT with appropriate wavelength sensitivity and appropriate optical bandpass filter is used to collect desired energy level fluorescence life time of interest. The UV LED is driven by a square wave train. The life time information is collected during the off part of LED on-off cycle. The data is collected by Digital Phosphor Oscilloscope (DPO) DPO7000 series and averaged up to 10000 times. The DPO is synchronized to the LED driver's falling edge signal. The schematic is shown in Figure 5.1 on page 41. A list of equipment is given in the list below. The photodetector and optical filter combination is given in Table 5.1 on page 42.

$$\tau_{nat} = \frac{1}{R_{sp}} + \frac{1}{R_{nr}} \tag{5.1}$$

5.2 Results of Low-Pump Life Time

1. 1 W optical output LEDENGIN 365 nm UV-LED.
2. Erbium-doped YAG sample
   (a) 0.5%
   (b) 50%
3. Erbium-doped Yttria (Y2O3) sample
   (a) 1%

(b) 15%

(c) 25%

4. Hamamatsu r955 Photomultiplier (PMT)

5. Stanford Research 810 Lockin Amplifier

6. 2” focal length and 2” diameter convex lens x 1

7. Semrock: FF01-390/SP-25

8. Optical filter set.

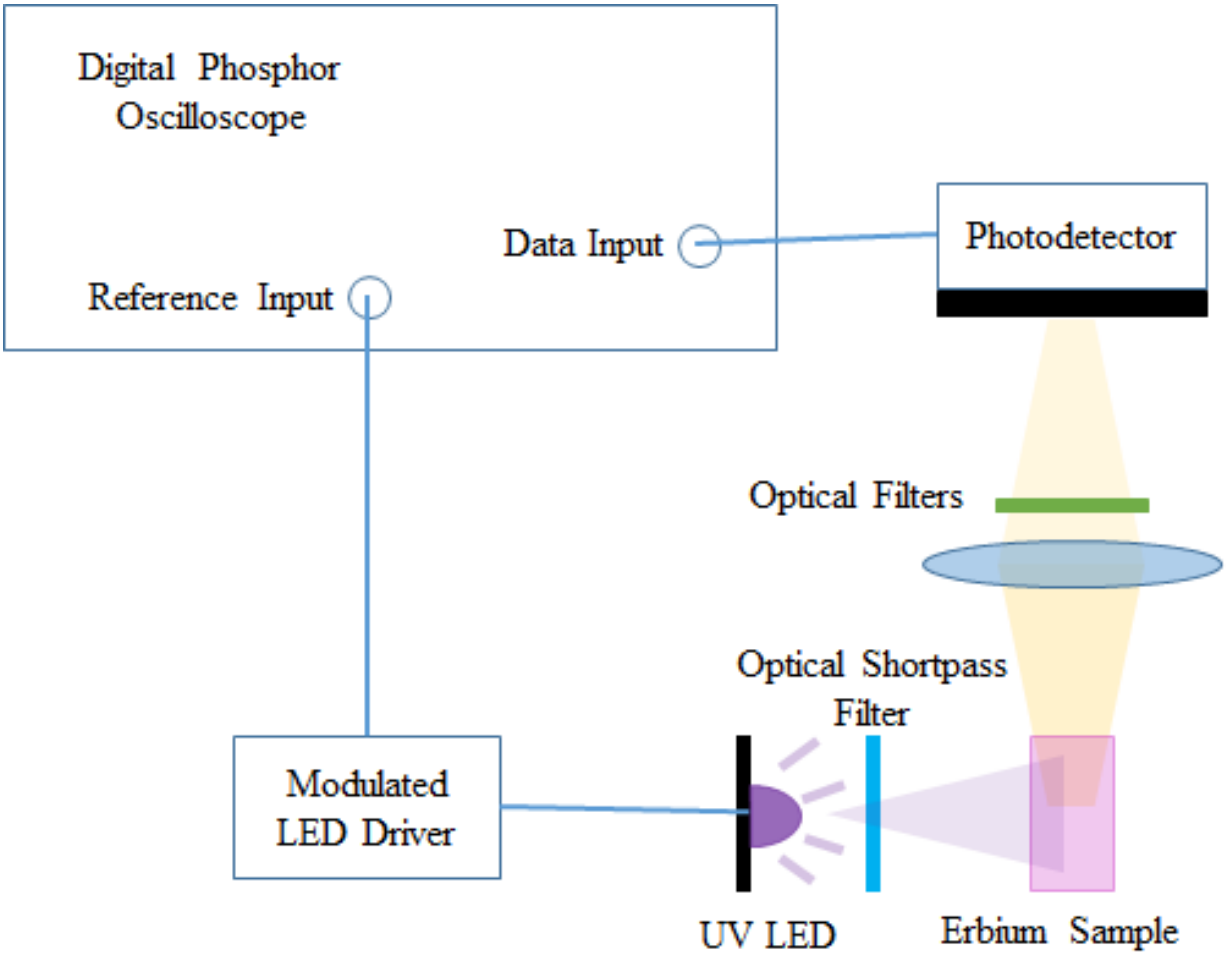

Figure 5.1: The experimental setup for Low life time measurements.

Table 5.1: This table contains the equipment pairing information for the observation of each fluorescence wavelength.

Energy Level	Wavelength	Filter Information	Photomultiplier
$^4S_{3/2}$	550 nm	Thorlabs FB550-10 x2	Hamamatsu R955
$^4F_{9/2}$	650 nm	Thorlabs FB650-40 x2	Hamamatsu R955
$^4I_{9/2}$	850 nm	Semrock FF01-857/30-25 x2	Hamamatsu R965
$^4I_{11/2}$	990 nm	Semrock BLP01-980R-25 x2	Hamamatsu R406
$^4I_{13/2}$	1500 nm	Semrock BLP01-980R-25 x2	Thorlabs PDA10CS

5.3 Result of Life Times (Low-Pump Level)

The life time under low-pump levels (LTLP) results are given tabulated in Table 5.2 on page 43 and Table 5.3 on page 43. The dynamics of the fluorescence is plotted on semilog-y scale to observe any non-exponential behavior. Should non-exponential behavior occur, which indicates ETU or XR effects become observable, the dynamics semilog-y plots will change from a straight line to a curved line. Fotunately, all plots are straight lines indicating the measurement is not too strongly affected by ETU and/or XR. Only some of the dynamic plots are given to illustrate the straight lines in contrast with the dynamic plots given in Chapter 6, which are all under high intensity pumping.

[1]Due to fast phonon decay to $^4I_{11/2}$

Table 5.2: Er:YAG Sample Life Times (Low-Pump Level) measured in µs

Energy Level	0.5% Er:YAG LPLT	50% Er:YAG LPLT
$^4S_{3/2}$	15	<3
$^4F_{9/2}$	< 15	< 3
$^4I_{9/2}$	Not observed[1]	Not observed
$^4I_{11/2}$	95	85
$^4I_{13/2}$	11200	1300

Table 5.3: Er:Y_2O_3 Life Time (Low-Pump Level) measured in µs

Energy Level	1% Er:Y_2O_3 LPLT	15% Er:Y_2O_3 LPLT	25% Er:Y_2O_3 LPLT
$^4S_{3/2}$	87	3.95	<2
$^4F_{9/2}$	85	22.5	< 14.6
$^4I_{9/2}$	87	10	16.5
$^4I_{11/2}$	2740	2550	295
$^4I_{13/2}$	13400	7700	770

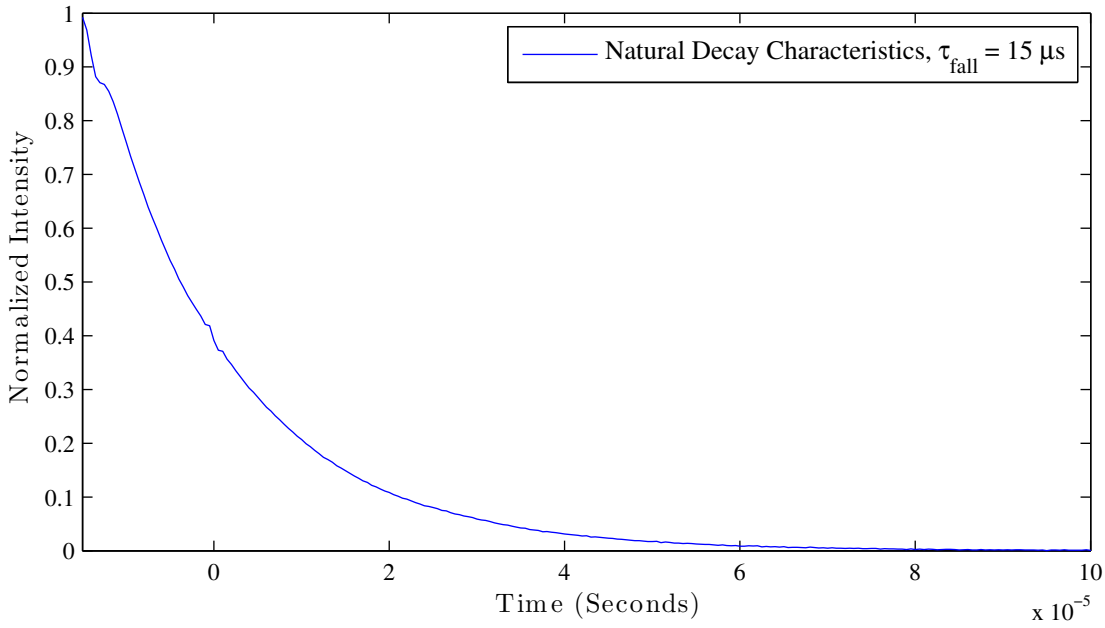

Figure 5.2: The decay characteristics of $^4S_{3/2}$ fluorescence intensity versus time for 1% Er:YAG under UV LED low intensity pumping is given on linear plot.

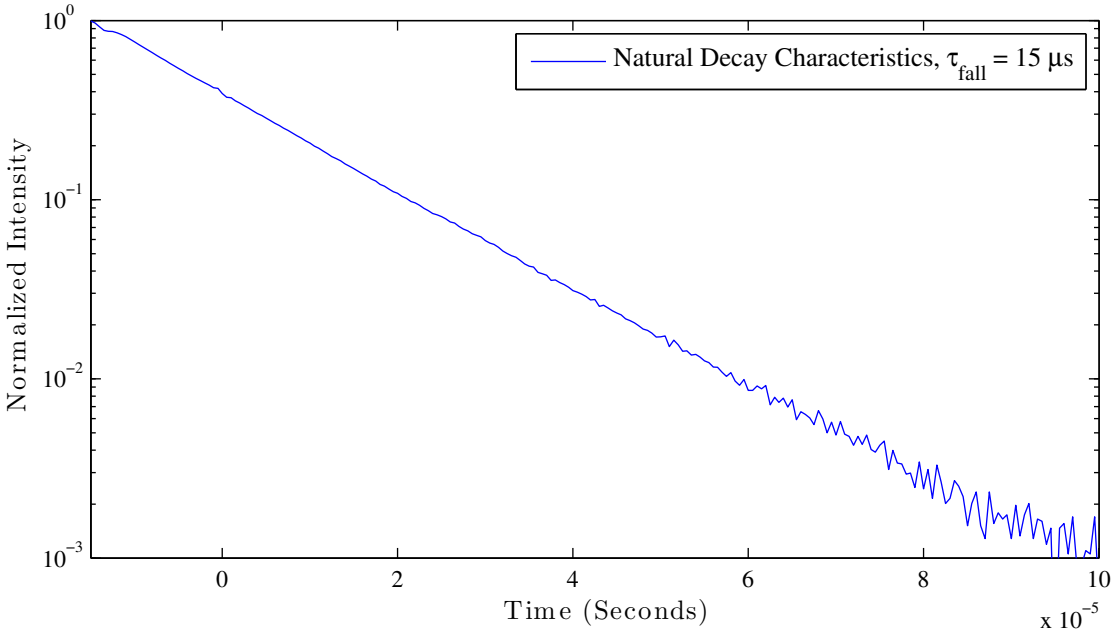

Figure 5.3: The decay characteristics of $^4S_{3/2}$ fluorescence intensity versus time for 1% Er:YAG under UV LED low intensity pumping is given on semilog-y plot.

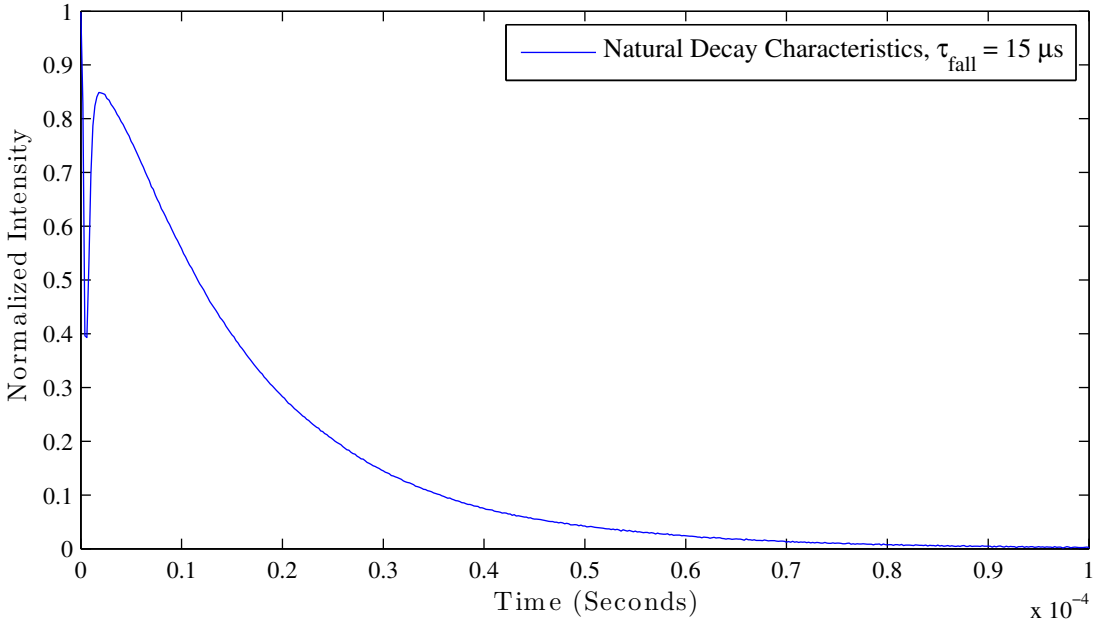

Figure 5.4: The decay characteristics of $^4F_{9/2}$ fluorescence intensity versus time for 1% Er:YAG under UV LED pumping is given on linear plot.

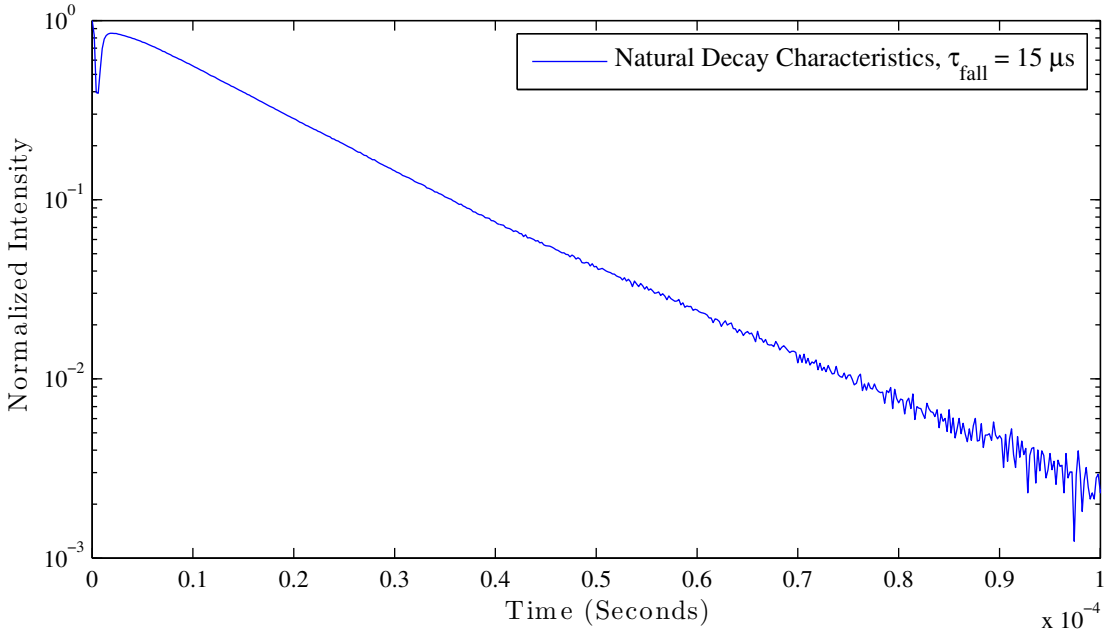

Figure 5.5: The decay characteristics of $^4F_{9/2}$ fluorescence intensity versus time for 1% Er:YAG under UV LED pumping is given on semilog-y plot.

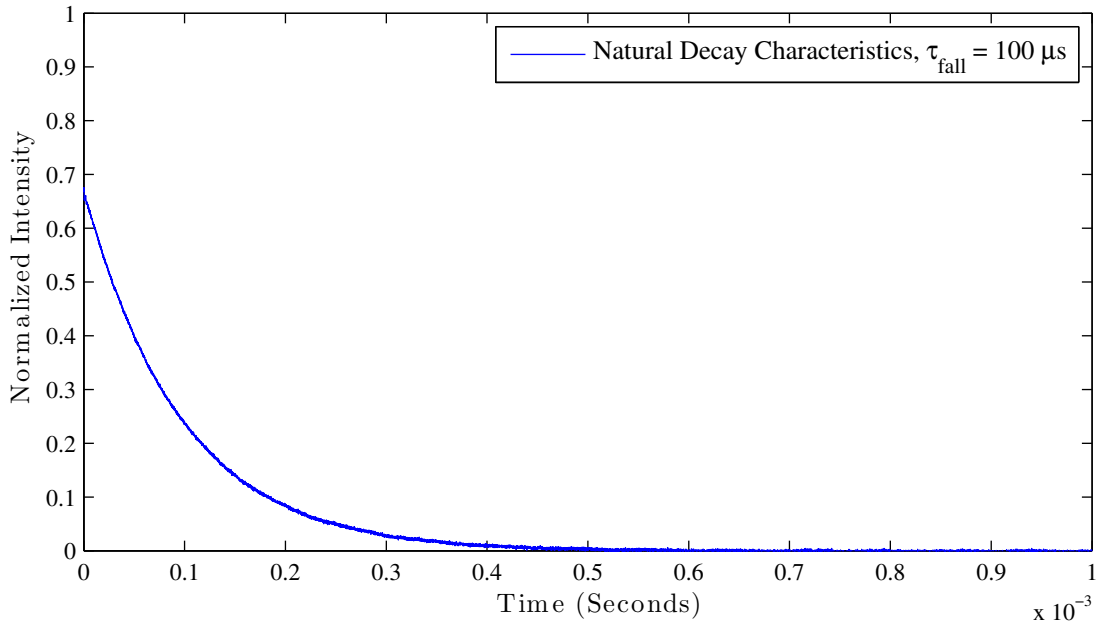

Figure 5.6: The decay characteristics of $^4I_{11/2}$ fluorescence intensity versus time for 0.5% Er:YAG under UV LED pumping is given on linear plot.

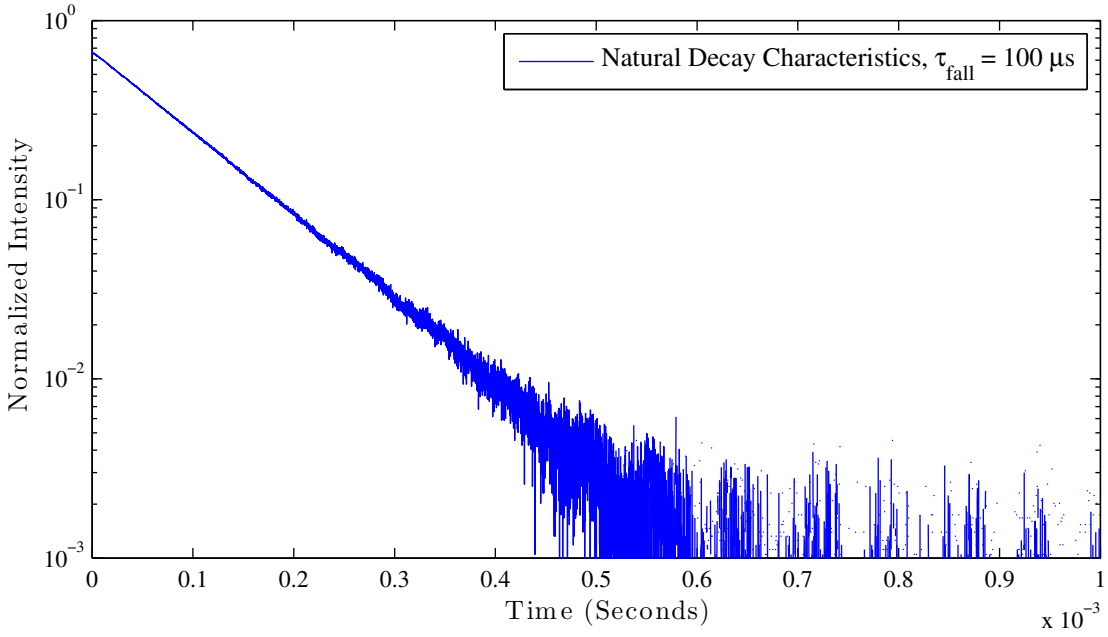

Figure 5.7: The decay characteristics of $^4I_{11/2}$ fluorescence intensity versus time for 0.5% Er:YAG under UV LED pumping is given on semilog-y plot.

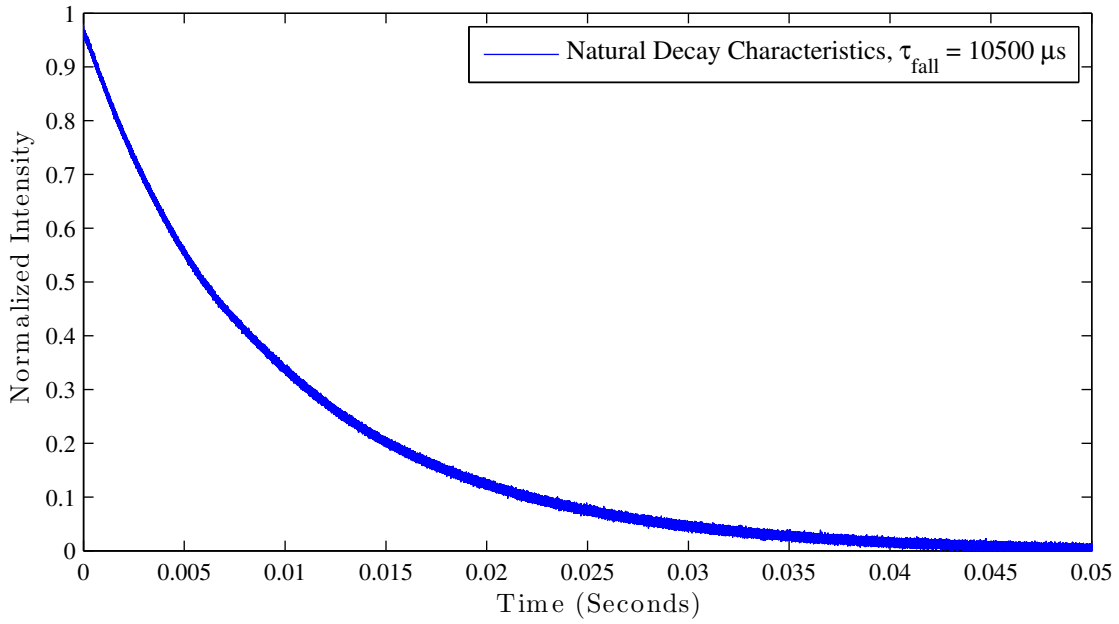

Figure 5.8: The decay characteristics of $^4I_{13/2}$ fluorescence intensity versus time for 0.5% Er:YAG under UV LED pumping is given on linear plot.

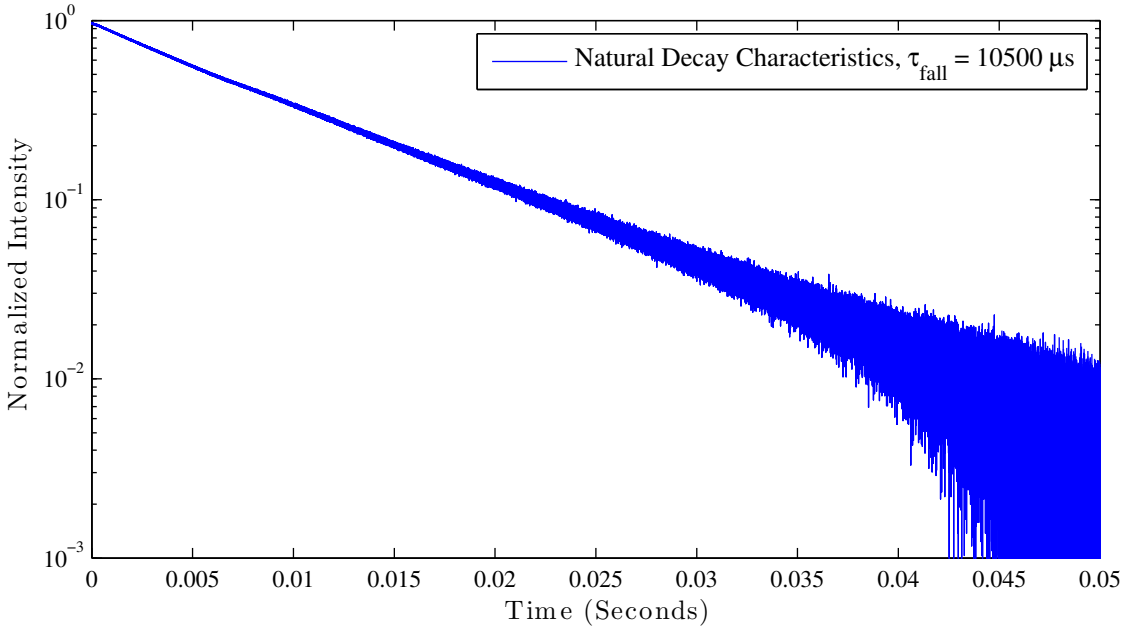

Figure 5.9: The decay characteristics of $^4I_{13/2}$ fluorescence intensity versus time for 0.5% Er:YAG under UV LED pumping is given on semilog-y plot.

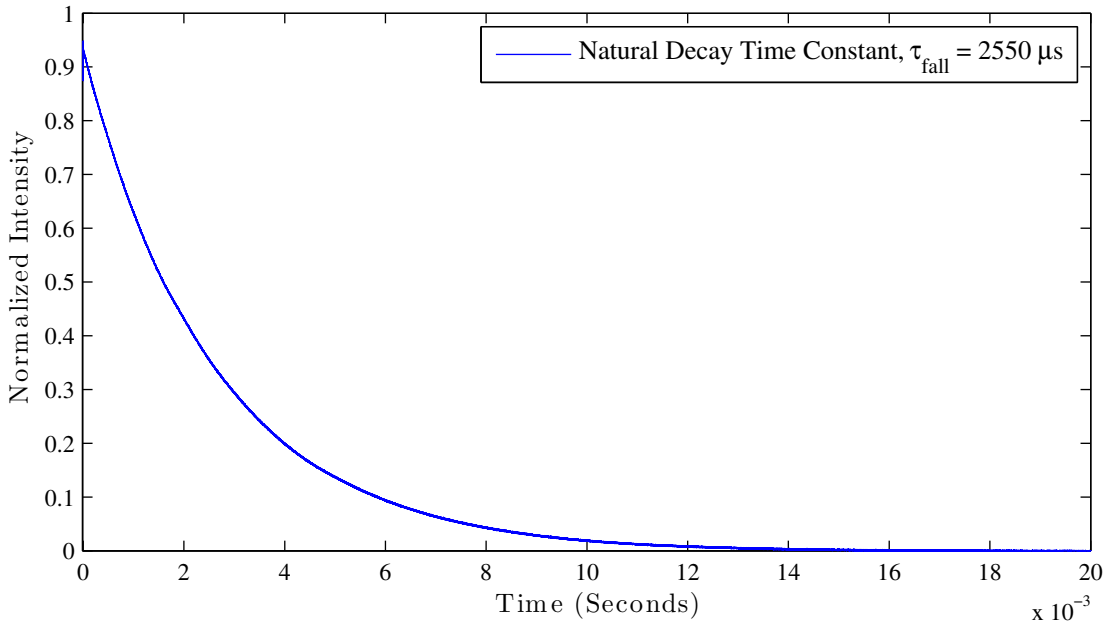

Figure 5.10: The decay characteristics of $^4I_{11/2}$ fluorescence intensity versus time for 15% Er:Yttria under UV LED pumping is given on linear plot.

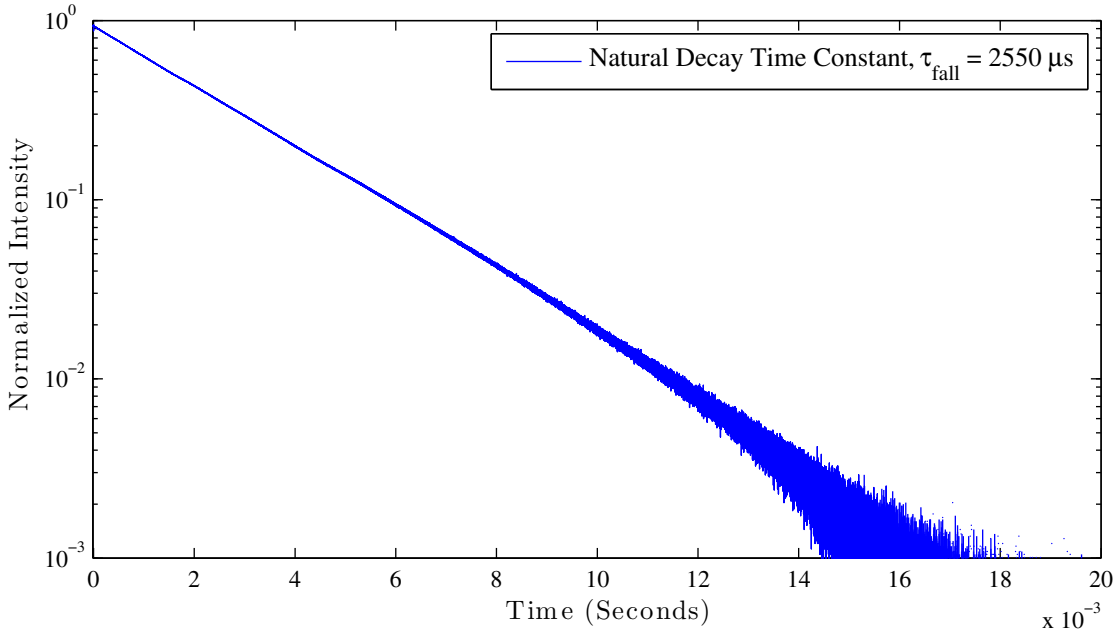

Figure 5.11: The decay characteristics of $^4I_{11/2}$ fluorescence intensity versus time for 15% Er:Yttria under UV LED pumping is given on semilog-y plot.

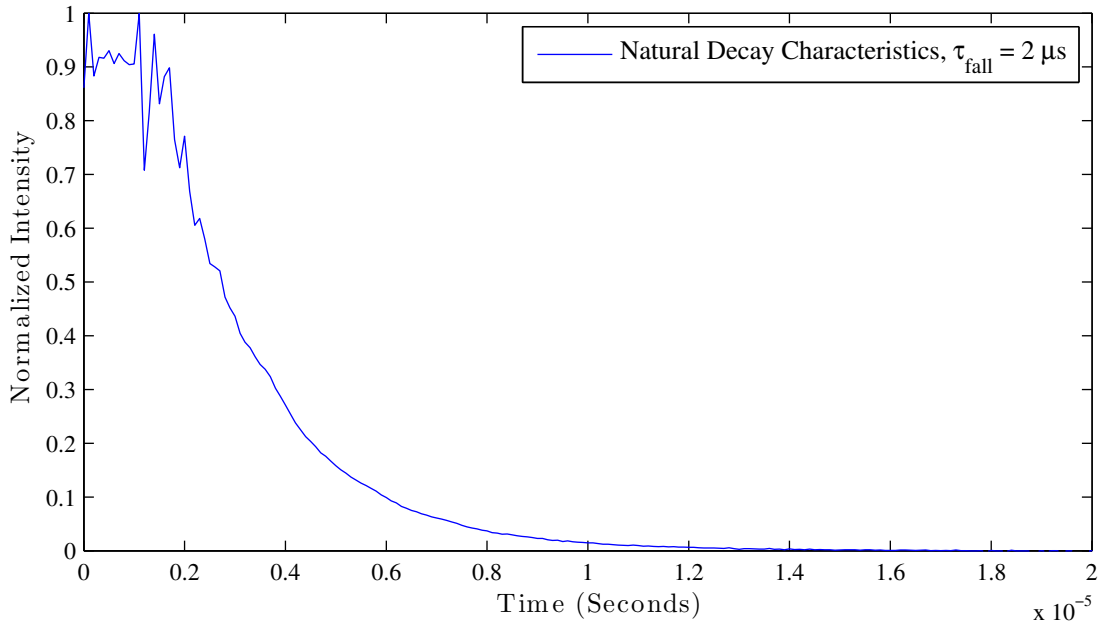

Figure 5.12: The decay characteristics of $^4S_{3/2}$ fluorescence intensity versus time for 25% Er:Yttria under UV LED pumping is given on linear plot.

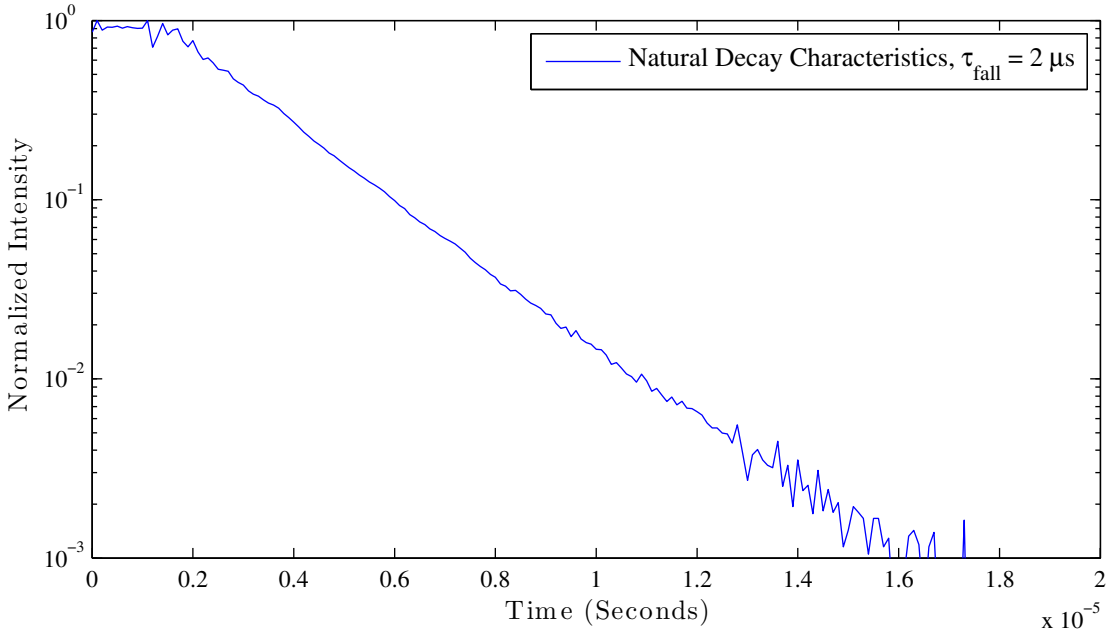

Figure 5.13: The decay characteristics of $^4S_{3/2}$ fluorescence intensity versus time for 25% Er:Yttria under UV LED pumping is given on semilog-y plot.

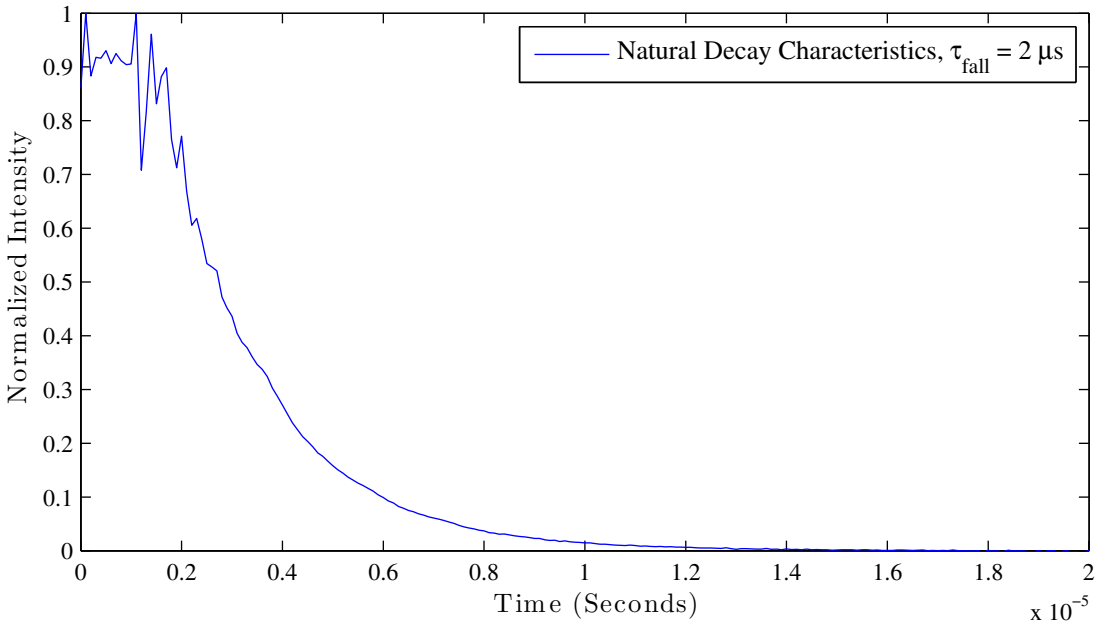

Figure 5.14: The decay characteristics of $^4S_{3/2}$ fluorescence intensity versus time for 25% Er:Yttria under UV LED pumping is given on linear plot.

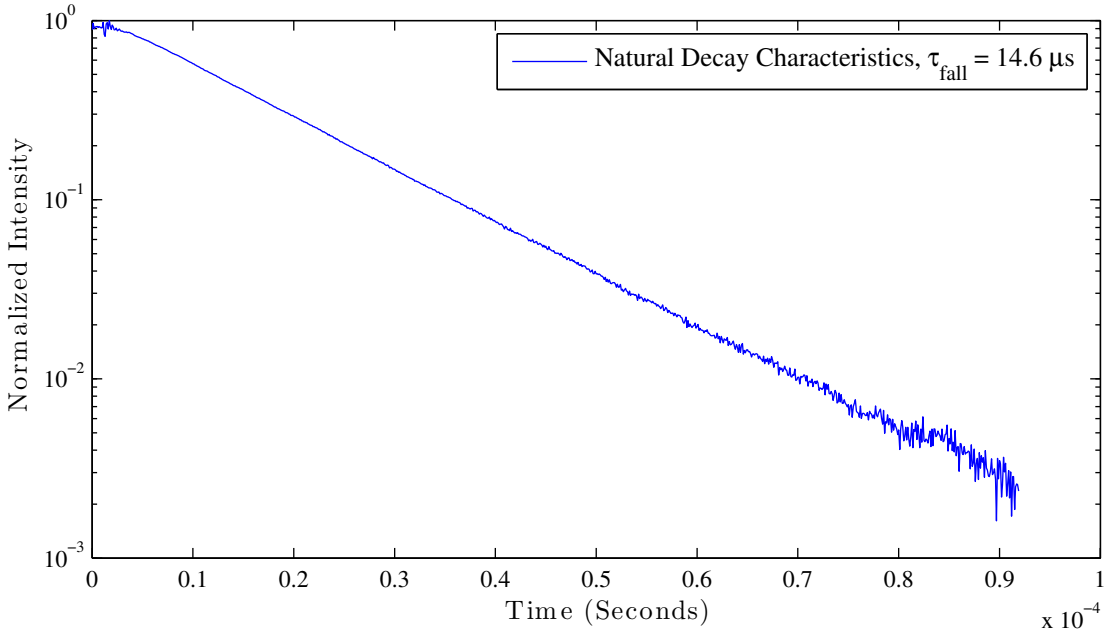

Figure 5.15: The decay characteristics of $^4F_{9/2}$ fluorescence intensity versus time for 25% Er:Yttria under UV LED pumping is given on semilog-y plot.

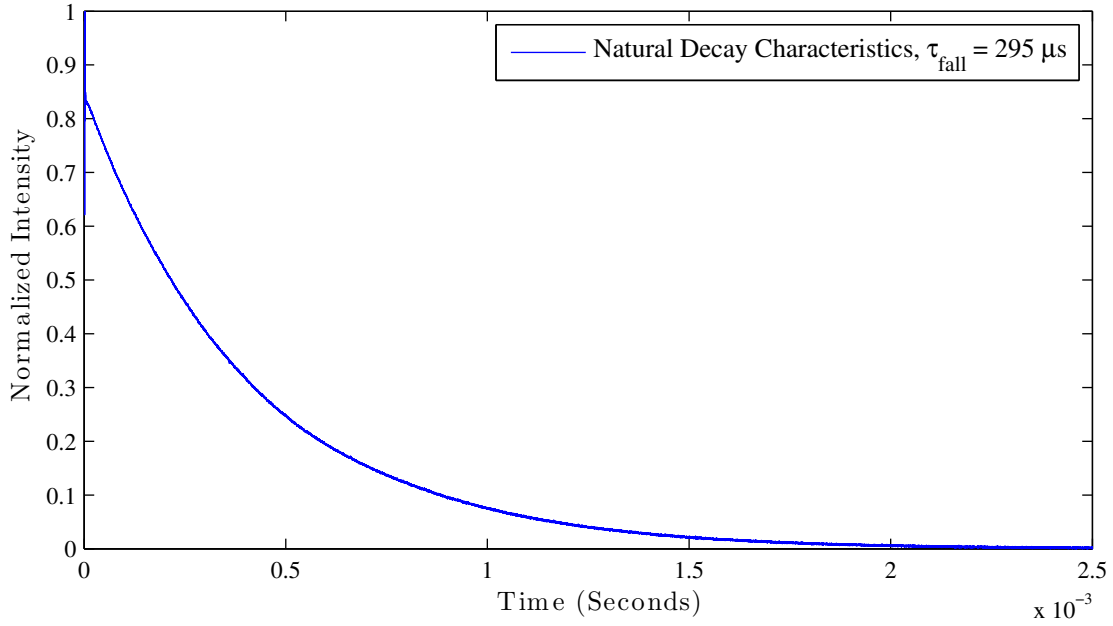

Figure 5.16: The decay characteristics of $^4I_{11/2}$ fluorescence intensity versus time for 25% Er:Yttria under UV LED pumping is given on linear plot.

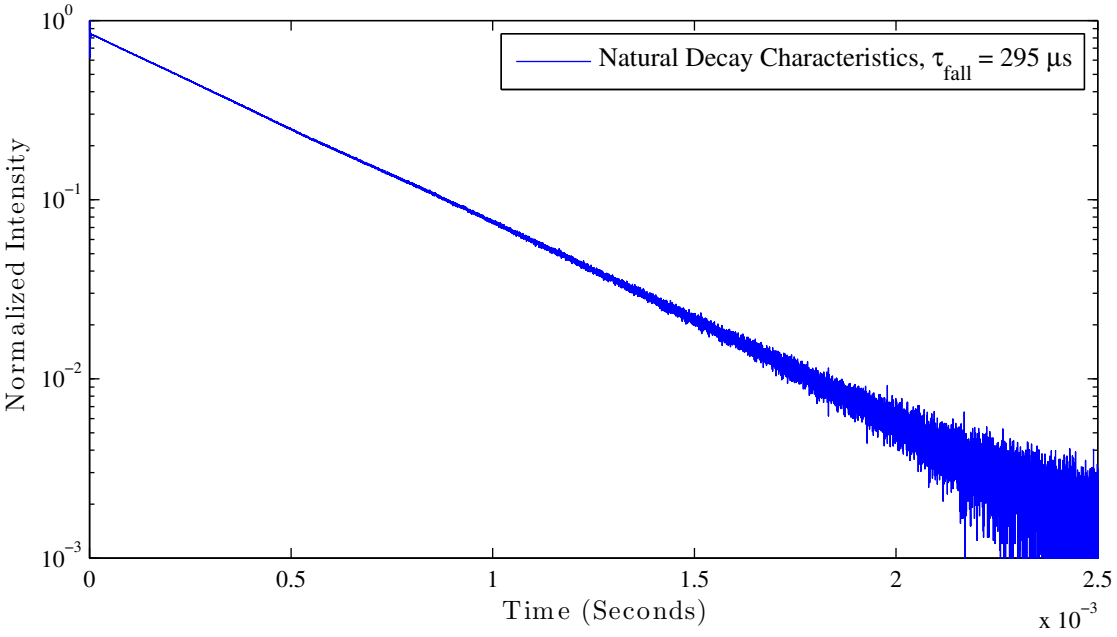

Figure 5.17: The decay characteristics of $^4I_{11/2}$ fluorescence intensity versus time for 25% Er:Yttria under UV LED pumping is given on semilog-y plot.

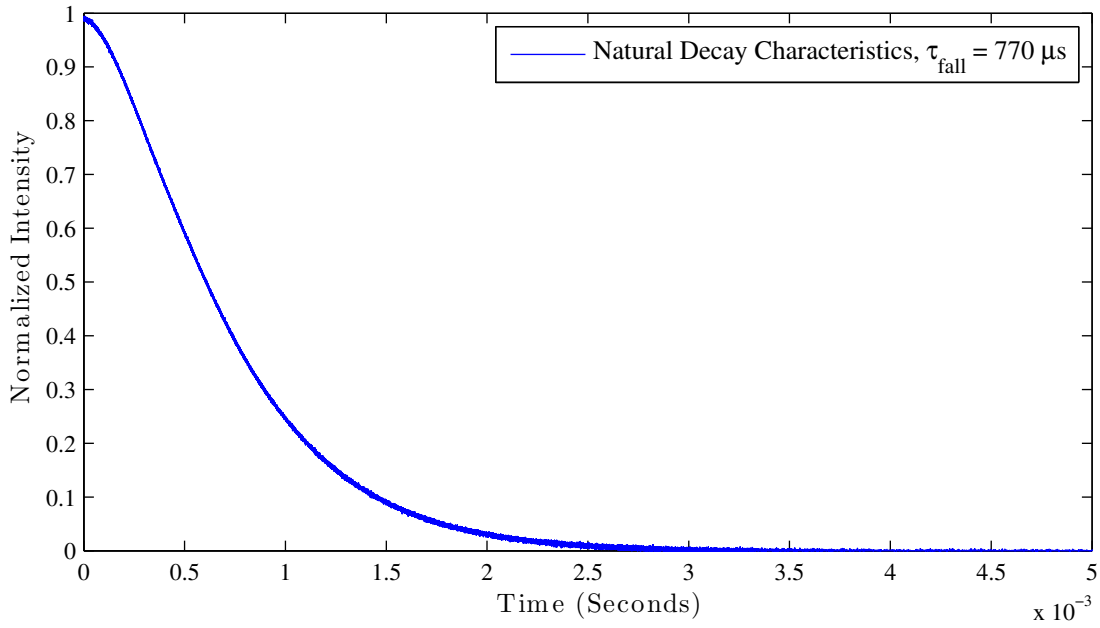

Figure 5.18: The decay characteristics of $^4I_{13/2}$ fluorescence intensity versus time for 25% Er:Yttria under UV LED pumping is given on linear plot.

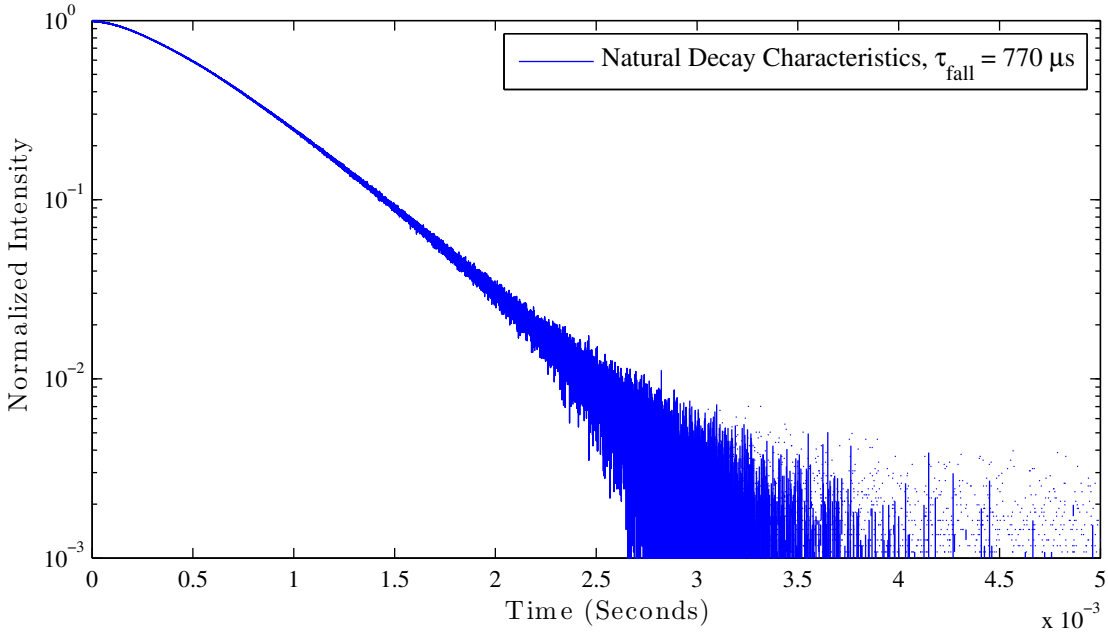

Figure 5.19: The decay characteristics of $^4I_{13/2}$ fluorescence intensity versus time for 25% Er:Yttria under UV LED pumping is given on semilog-y plot.

Chapter 6

Dynamic Life Time Measurement of Up-conversion Processes

In this chapter, the dynamics of the response of the erbium-doped samples to energy pumping is investigated. By dynamics, it is specifically referring to the fluorescence intensity versus time. As indicated in Chapter 2, The life times will change depending on the additional pump (ESA) effects and high population (ETU) effects. From these effects several physical processes such as ion clumping, energy path of ions, and the ETU coefficients can be obtained for the levels that are of particular interest to 1.6 μm and 3 μm lasers. Furthermore, by using this method on powdered samples, one can obtain information on the possibility of lasing without actually making a laser quality crystal rod, which is much more time consuming and expensive. First, experimental setup is given.

6.1 Theory of Dynamic Life Time Measurement

As given in Chapter 2, under high intensity pumpingThe rise characteristic time constant will be different from the fall characteristics due to the additional ESA effects assuming there are no cooperative effects such as ETU and XR. In this case, the rise time constant wil be

shorter than that of the fall time constant. The fall time constant is equal to natural decay or natural fluorescence time constant. The time constant is defined below.

$$\tau_m = \int_{t_0}^{\infty} t\Phi(t)\, dt \tag{6.1}$$

If non-linear terms from ETU and XR are included, the decay will no longer be exponential as is given in the semilog-y plots of Section 6.3. Since the characteristic is no longer exponential, the characteristic time τ will mean different things as given by the works of Inokuti and Hirayama [27].

As given in the work of Inokuti and Hirayama [27], "it is customary and convenient for practical purposes to introduce a 'decay time' which characterizes the behavior of the decay function." In their work, it is mentioned that two different convenient numbers can be used to characterize this decay parameter: the mean time τ_m as given in Equation 6.1, where $\Phi(t)$ is the fluorescence power defined in Inokuti's work, and the typical e^{-1} τ_e. If the decay function were exponential, then the two times τ_m and τ_e will be the same number. However, as indicated in Chapter 2, the rate equations are non-linear, the decay functions or fluorescence dynamics are not exponential decays. In this work, the e^{-1} or τ_e is used to characterize the time costants. For every energy level, both the rise and fall characteristics are looked at. By the rise time constant τ_{rise}, it is referring to the time it takes to reach 63% ($(1 - e^{-1}$ point) of the maximum intensity. The fall time constant τ_{fall} refers to the time for fluorescence intensity to reach 37% (e^{-1} point) of the maximum or initial fluorescence. If there are no nonlinear processes such as ETU and XR, then the apparent fall time constant is equal to the natural fluorescence decay. In the following discussion, Figure 2.10 on page 26 and Equation 2.24 on page 2.24 in Chapter 2 is reproduced here as Figure 6.1 on page 55 and Equation 6.2 on page 54, respectively, for convenience.

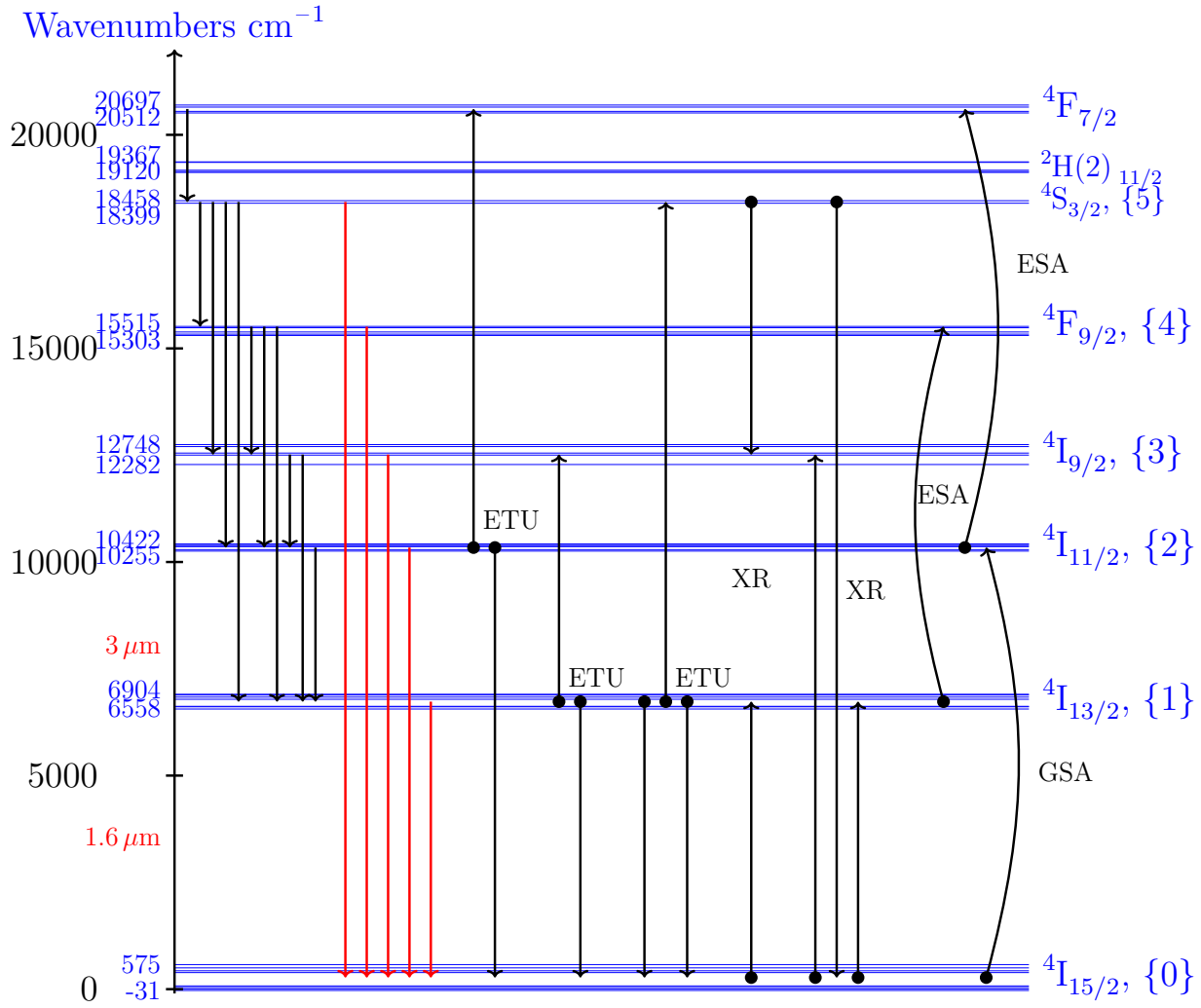

Figure 6.1: Calculated energy Levels of Er:YAG. The lighter color (red) downward arrows are the observed wavelengths of fluorescence as given in Figure 3.6 on page 31.

$$
\begin{aligned}
^4\mathrm{S}_{3/2}: \quad \frac{dN_5}{dt} &= -\frac{1}{\tau_5}N_5 + \alpha_{25} I N_2 + W_2 N_2^2 \\
&\quad - W_{50} N_5 N_0 - W_{500} N_5 N_0^2 + W_{111} N_1^3 && \text{(6.2a)} \\
^4\mathrm{F}_{9/2}: \quad \frac{dN_4}{dt} &= \frac{1}{\tau_{54}}N_5 - \frac{1}{\tau_4}N_4 + \alpha_{14} I N_1 && \text{(6.2b)} \\
^4\mathrm{I}_{9/2}: \quad \frac{dN_3}{dt} &= \frac{1}{\tau_{53}}N_5 + \frac{1}{\tau_{43}}N_4 - \frac{1}{\tau_3}N_3 + W_1 N_1^2 + W_{500} N_5 N_0^2 + W_{50} N_5 N_0 && \text{(6.2c)} \\
^4\mathrm{I}_{11/2}: \quad \frac{dN_2}{dt} &= \frac{1}{\tau_{52}}N_5 + \frac{1}{\tau_{42}}N_4 + \frac{1}{\tau_{32}}N_3 - (\frac{1}{\tau_2} + \alpha_{25} I) N_2 - 2W_2 N_2^2 + \alpha_{02} I N_0 && \text{(6.2d)} \\
^4\mathrm{I}_{13/2}: \quad \frac{dN_1}{dt} &= \frac{1}{\tau_{51}}N_5 + \frac{1}{\tau_{41}}N_4 + \frac{1}{\tau_{31}}N_3 + \frac{1}{\tau_{21}}N_2 - (\frac{1}{\tau_1} + \alpha_{14} I) N_1 \\
&\quad + W_{50} N_5 N_0 - 2W_{11} N_{11}^2 + W_{500} N_5 N_0^2 - 3W_{111} N_1^3 && \text{(6.2e)} \\
^4\mathrm{I}_{15/2}: \quad \frac{dN_0}{dt} &= \frac{1}{\tau_{50}}N_5 + \frac{1}{\tau_{40}}N_4 + \frac{1}{\tau_{30}}N_3 + \frac{1}{\tau_{20}}N_2 + \frac{1}{\tau_1}N_1 - \alpha_{02} I N_0
\end{aligned}
$$

When a system is under pump, several effects are changing the population of each state. For any state, the natural decay rate τ of the state, the absorption from lower state pumping into the state, the absorption from the state pumping out into higher energy state, and the ETU and XR non-linear terms are all affecting the population. All these effects will affect the earlier defined rise time τ_{rise}. When the pump is turned off, only the natural decay rate and the ETU and XR non-linear terms affect the population. This will have an impact on the fall time τ_{fall}. In a way, if we factor the ETU or XR term from Equation 6.2 so that it becomes either $(1/\tau + I\alpha + WN) \cdot N$ or $(1/\tau + WN) \cdot N$, we see that the time constants are evolving with population density N. This gives rise to the non-exponential results. In Section 6.3, the life times are investigated for both the purpose at looking at energy paths as well as up-conversion coefficients for some of the states.

6.2 Experimental Setup for Dynamic Life Time Measuerement

The experiment is similar to that of Chapter 5. Only this time the pump changed from an LED to a high powered laser diode, which is focused by a lens to increase the intensity incident upon the erbium-doped samples. The experimental setup is given in Figure 6.2 on page 58. A mechanically chopped laser diode pump is focused down in spot size by a lens to increase the intensity incident upon the erbium-doped sample. The fluorescence produced by the erbium-doped sample is collected by a lens and is optically filtered to yield only the fluorescence from the state of interest. Finally, this is collected the appropriate photodetetor for the wavelength of fluorescence. The data is sent into a digital oscilloscope. The list of equipment is given below:

1. Laser diode pump
   (a) 965 nm 7 W optical output laser diode pump Model#: SNP-962-5-1022-6.5, Sheaumann Lasers Inc. (focused down to give approximately 10 kW/cm^2 intensity).

(b) 800 nm 20 W optical output laser diode pump Model#: OPTO-PWR A020-8080-C (P/N: 4800-0033) (focused down to give approximately 1 kW/cm^2 intensity).

2. Erbium-doped YAG sample

   (a) 0.5%

   (b) 50%

3. Erbium-doped Yttria (Y_2O_3) sample

   (a) 1%

   (b) 15%

   (c) 25%

4. Photodetectors

5. Tektronix 7000 Series Digital Oscilloscope

6. 2" focal length and 2" diameter convex lens x 2

7. Baltzer reflective glass neutral density filter set.

8. optical filter set.

In addition to the list of items, the information of filter and photodetector combinations for observing each level's fluorescence is given in Table 6.1 on page 59. This table is identical to Table 5.1 in Chapter 5.

6.3 Results and Discussion of Dynamic Life Time Measurement

Table 6.2 on page 60 to Table 6.6 on page 61 is the summary of the characteristic life times obtained from the experiment. Some have two life times simply because two different

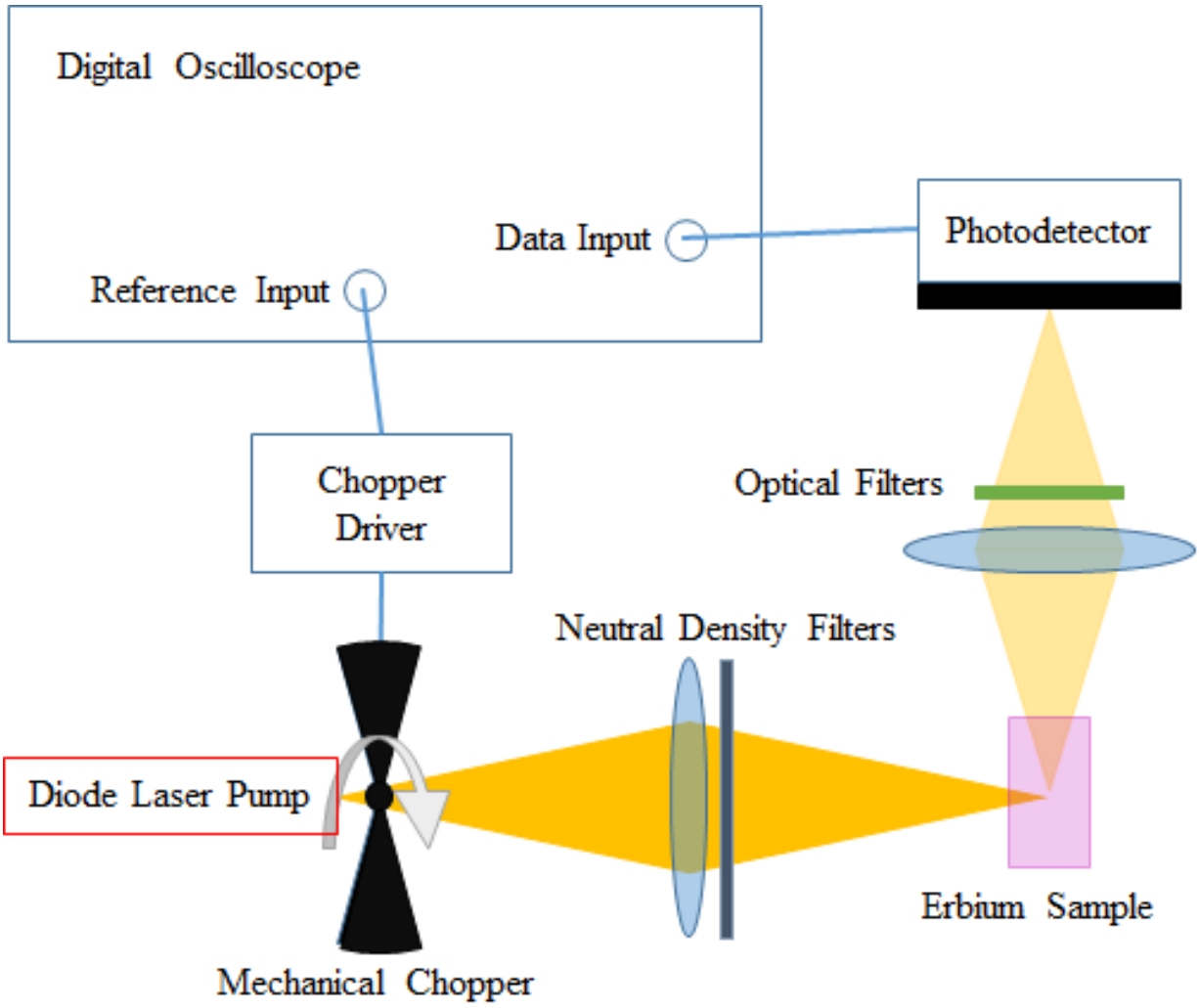

Figure 6.2: The experimental setup for fluorescence dynamics.

Table 6.1: This table contains the equipment pairing information for the observation of each fluorescence wavelength.

Energy Level	Wavelength	Filter Information	Photomultiplier
$^4S_{3/2}$	550 nm	Thorlabs FB550-10 x2	Hamamatsu R955
$^4F_{9/2}$	650 nm	Thorlabs FB650-40 x2	Hamamatsu R955
$^4I_{9/2}$	850 nm	Semrock FF01-857/30-25 x2	Hamamatsu R965
$^4I_{11/2}$	990 nm	Semrock BLP01-980R-25 x2	Hamamatsu R406
$^4I_{13/2}$	1500 nm	Semrock BLP01-980R-25 x2	Thorlabs PDA10CS

characteristics (a begining characteristic and a long term characteristic) are observed. This, as will be discussed later, is due to up-conversion from different energy states. Since some of the energy states have drastically different life time, one can observe the ratio of up-conversion bewtween states from the dynamics or time evolution of this experiment. The rows of the Tables are showing the life time characteristics (natural, rise, and fall) of each state. The columns indicating (the source) whether it is the natural life time pumped by UV-LED at a low intensity, pumped at high intensity by 800 nm laser diode into $^4I_{9/2}$ from the ground state $^4I_{15/2}$ or pumped at high intensity by 965 nm laser diode into $^4I_{11/2}$ from the ground state $^4I_{15/2}$.

Table 6.7 on page 61, Table 6.8 on page 62, and Table 6.9 on page 62 illustrate that at different pump intensity levels the characteristic times and the up-conversion rates change.

Under high pump intensity, as indicated previously, the non-linear terms of ETU and XR and ESA become important. With the non-linear terms the rise and fall characteristics are no longer a simple exponential. In order to illustrate this for the rise and fall curves, the data are plotted on semilog-y graphs. If the plots are straight on semilog-y graphs, then the charateristics are exponential. If the plots are not straight on the semilog-y graphs, then the characteristics are affected by non-linear terms (ETU and XR). For the decay or

Table 6.2: SC 0.5% Er:YAG Times Measured in µs

En. Lv	LTLP[1]	$^4I_{11/2}$ Rise	$^4I_{11/2}$ Fall	$^4I_{9/2}$ Rise	$^4I_{9/2}$ Fall
$^4S_{3/2}$	22	110 & 4000	22	5850	17
$^4F_{9/2}$	≤ 16	110 & 4500	16	5850	18
$^4I_{9/2}$	Not Ob.	110 & 5600	25 & 2500	1010	1010
$^4I_{11/2}$	100	95	100	95	95
$^4I_{13/2}$	11200	6500	7500	11200	11200

Table 6.3: 50% Er:YAG Times Measured in µs

En. Lv	LTLP	$^4I_{11/2}$ Rise	$^4I_{11/2}$ Fall	$^4I_{9/2}$ Rise	$^4I_{9/2}$ Fall
$^4S_{3/2}$	≤ 3	154	62	505	95
$^4F_{9/2}$	≤ 3	162	82	545	160
$^4I_{9/2}$	Not Ob.	200	95	640	280
$^4I_{11/2}$	90	185	155	290	190
$^4I_{13/2}$	1300	475	800	880	1180

Table 6.4: 1% Er:Y_2O_3 Times Measured in µs

En. Lv	LTLP	$^4I_{11/2}$ Rise	$^4I_{11/2}$ Fall	$^4I_{9/2}$ Rise	$^4I_{9/2}$ Fall
$^4S_{3/2}$	87	3050	160	5550	1150
$^4F_{9/2}$	85	6000	770	7400	3600
$^4I_{9/2}$	87	3000	170	5350	660
$^4I_{11/2}$	2740	2450	2650	2800	2800
$^4I_{13/2}$	13400	11400	12400	12400	12900

Table 6.5: 15% Er:Y_2O_3 Times Measured in µs

En. Lv	LTLP	$^4I_{11/2}$ Rise	$^4I_{11/2}$ Fall	$^4I_{9/2}$ Rise	$^4I_{9/2}$ Fall
$^4S_{3/2}$	3.95	2400	950	1420	780
$^4F_{9/2}$	22.5	3750	1400	1720	940
$^4I_{9/2}$	10	3050	1350	1540	840
$^4I_{11/2}$	2550	2567	2567	2150	2700
$^4I_{13/2}$	7700	5900	7300	5000	6800

Table 6.6: 25% Er:Y_2O_3 Times Measured in µs

En. Lv	LTLP	$^4I_{11/2}$ Rise	$^4I_{11/2}$ Fall	$^4I_{9/2}$ Rise	$^4I_{9/2}$ Fall
$^4S_{3/2}$	2	400	154	340	170
$^4F_{9/2}$	14.6	520	200	355	165
$^4I_{9/2}$	16.5	370	230	300	170
$^4I_{11/2}$	295	350	360	330	390
$^4I_{13/2}$	770	560	640	270	350

Table 6.7: Fluorescence of $^4I_{11/2}$ 50% Er:YAG under 800 nm pump at various power levels.

	100%	55%	25%	11%
Rise Time	315	190	185	145
Fall Time	180	170	150	130

Table 6.8: Fluorescence of $^4I_{11/2}$ 50% Er:YAG under 965 nm pump at various power levels.

	100%	55%	25%	11%
Rise Time	190	170	145	125
Fall Time	160	155	135	125

Table 6.9: Fluorescence of $^4I_{13/2}$ 50% Er:YAG under 965 nm pump at various power levels.

	100%	55%	25%	11%
Rise Time	460	580	660	720
Fall Time	860	840	940	1080

fall characteristics, it is relatively easy to put onto the semilog-y graphs. For rise time characteristics, however, due to the fact that it is $1 - exp(-t/\tau)$ instead of $exp(-t/\tau)$, the rise data collected will have to be subtracted by 1 and then inverted so that it can be plotted for the "straight line" analysis. Therefore, at high intensity as the system reach steady state for rise, it is becoming closer to zero. This is unnatural, and so it is mentioned in advanced. Furthermore, because the closer to "zero" the data is on semilog-y plot, the more sensitive to small fluctuation the plots become, the noise one observe at the steady state of the rise is merely an artifact of the mathematical tool the plots were presented with. With that stated, first the data taken from 965 nm laser diode is presented with from low doped to high doped YAG, then low doped yttria to high doped yttria.

Before showing the actual results, the rise and fall of 50% Er:YAG under low intensity pumping are illustrated in Figure 6.3 on page 63 and in Figure 6.4 on page 64. The figures clearly illustrates that under low intensity pumping, because the populations in the upper states are not high enough, the non-linear terms from ETU and XR are not observed. Therefore, the rise and fall characteristics are straight on the semilog-y plot. In addition, even under low intensity pumping, the rise time characteristic τ_{rise} is already showing a difference

from the fall time characteristic τ_{fall}.

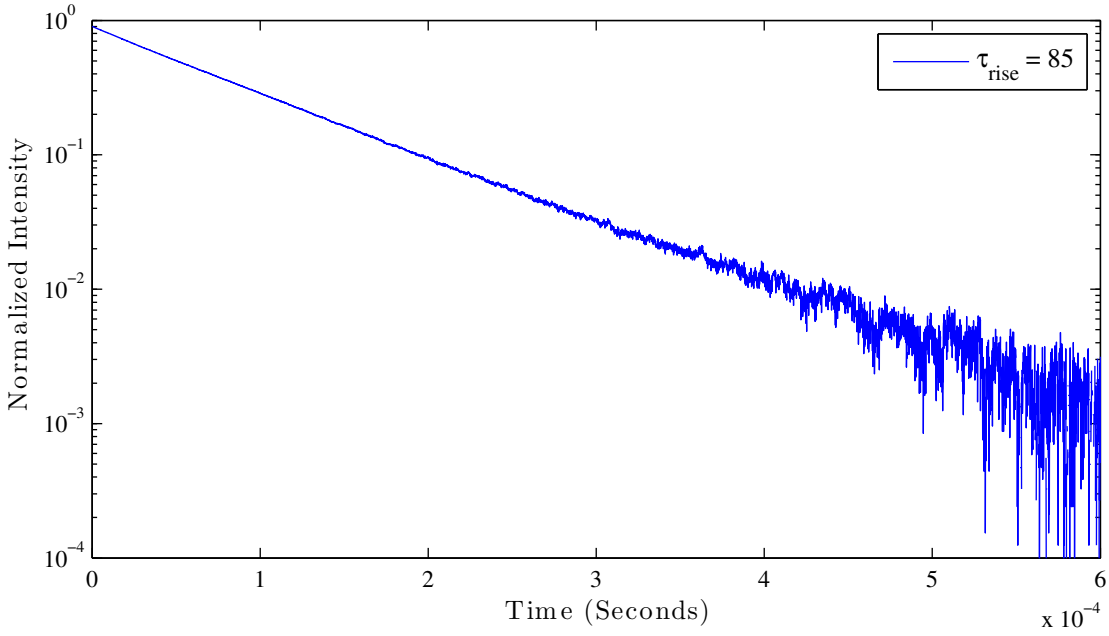

Figure 6.3: The rise characteristics of $^4I_{11/2}$ fluorescence intensity versus time for 50% Er:YAG under 965 nm low intensity pumping is given on semilog plot.

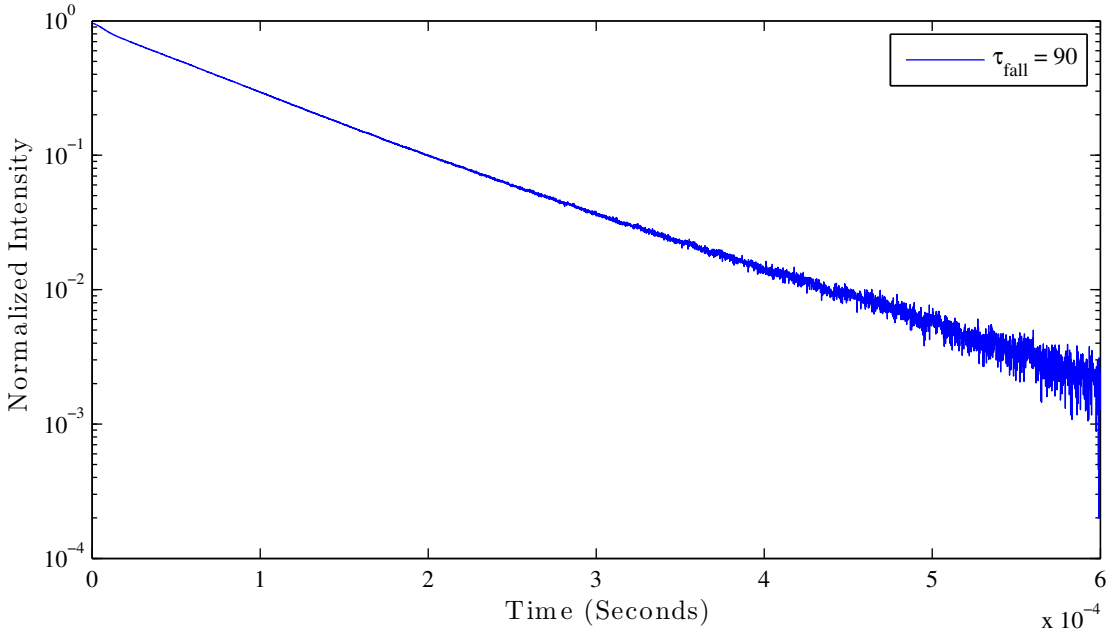

Figure 6.4: The fall characteristics of $^4I_{11/2}$ fluorescence intensity versus time for 50% Er:YAG under 965 nm low intensity pumping is given on semilog plot.

6.3.1 0.5% YAG under 965 nm Pump

First, the SC 0.5% YAG under 965 nm high intensity pumping is given. In Figure 6.5 on page 65 and In Figure 6.6 on page 66. One can clearly see the ESA occuring from both $^4I_{11/2}$ and $^4I_{13/2}$ on the rise distinctly from the semilog-y plot in the $^4S_{3/2}$. Due to the distinct life time difference among the 3 levels, the rise roughly follows the rise time characteristics of $^4I_{11/2}$ in the beginning and then it roughly follows that of $^4I_{13/2}$. From the semilog-y plot, one can estimate that roughly 10% of the up-converted population comes from $^4I_{13/2}$ and the other 90% of the population is from $^4I_{11/2}$. Furthermore, due to no up-conversion from ETU and XR, the fall time characteristics return to that of the natural decay.

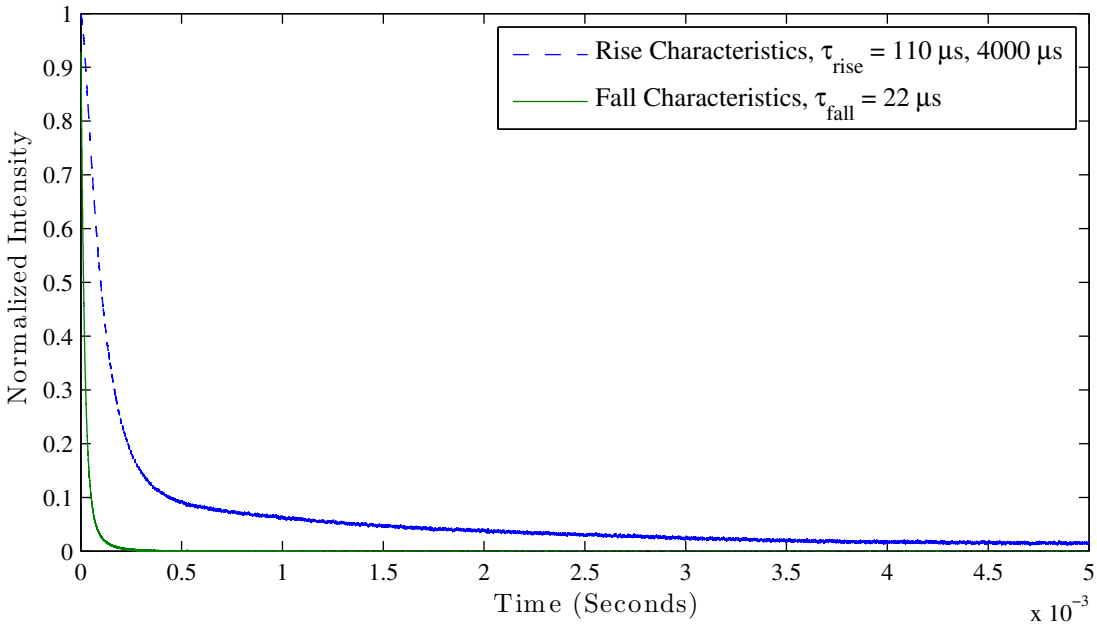

Figure 6.5: The dynamics of $^4S_{3/2}$ fluorescence intensity versus time for 0.5% Er:YAG under 965 nm up to 10 kW/cm^2 intensity puming on linear plot.

From Figure 6.7 on page 67 and Figure 6.8 on page 67, the red fluorescence from $^4F_{9/2}$ has both ESA and ETU coming from $^4I_{11/2}$ and $^4I_{13/2}$. Based on the semilog-y plot, around 50% of the population is contributed by $^4I_{13/2}$. In addition, on the decay or fall time characteristics in semilog-y plot, there is ETU still acting from $^4I_{13/2}$ in up-converting ions to $^4F_{9/2}$ but not from $^4I_{11/2}$. This is also true of the $^4I_{9/2}$ level as given in Figure 6.9 on page 68 and Figure 6.10 on

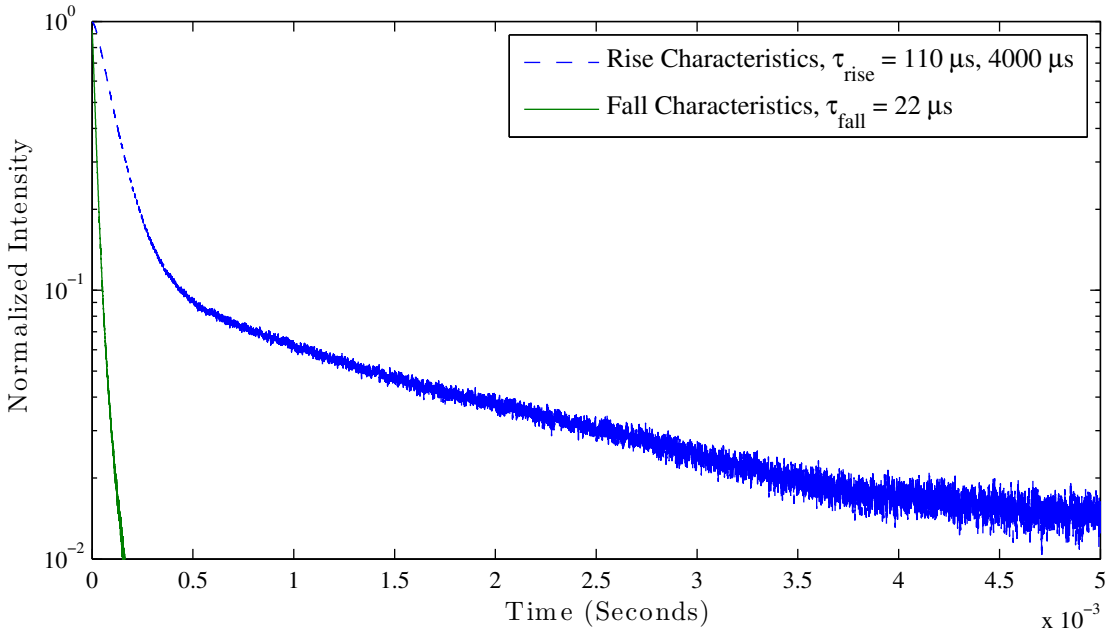

Figure 6.6: The dynamics of $^4S_{3/2}$ fluorescence intensity versus time for 0.5% Er:YAG under 965 nm up to 10 kW/cm^2 intensity puming on semilog-y plot.

page 68. The up-conversion due to ETU is especially worth mentioning because it is assumed that at a low doping of 0.5%, by the statistics of random ion substitution, there shouldn't be that many sites for erbium with two ions that are close enough to exhibit observable ETU effects, which indicates clumping occuring at even such a low doping of 0.5%. This is worth mentioning because there is no other known simple way of detecting ion clumping effects beside the electron paramagnetic resonance (EPR) method.

For $^4I_{11/2}$ level, a tiny amount (around 1%) of ETU up-conversion from $^4I_{13/2}$ is observed from the decay curve as given in Figure 6.11 on page 69 and Figure 6.12 on page 69. The life time is not changed by more than 5%. For $^4I_{13/2}$ level as given in Figure 6.13 on page 70 and Figure 6.14 on page 70, the ESA and ETU reduction of life time is observed, which correspond to the data from the upper-states.

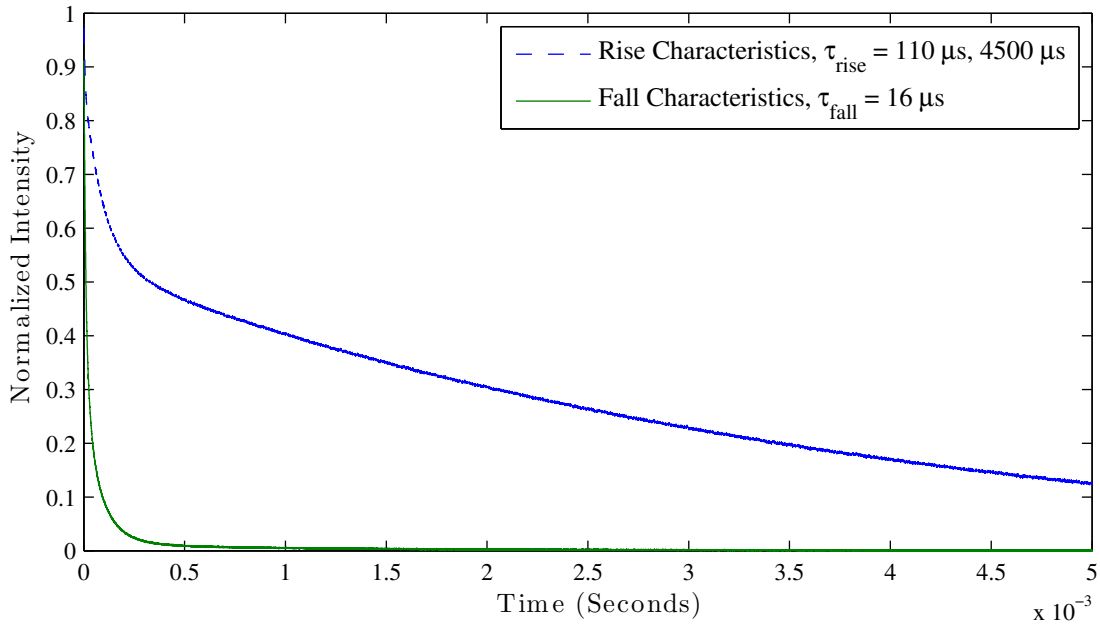

Figure 6.7: The dynamics of $^4F_{9/2}$ fluorescence intensity versus time for 0.5% Er:YAG under 965 nm up to 10 kW/cm^2 intensity puming.

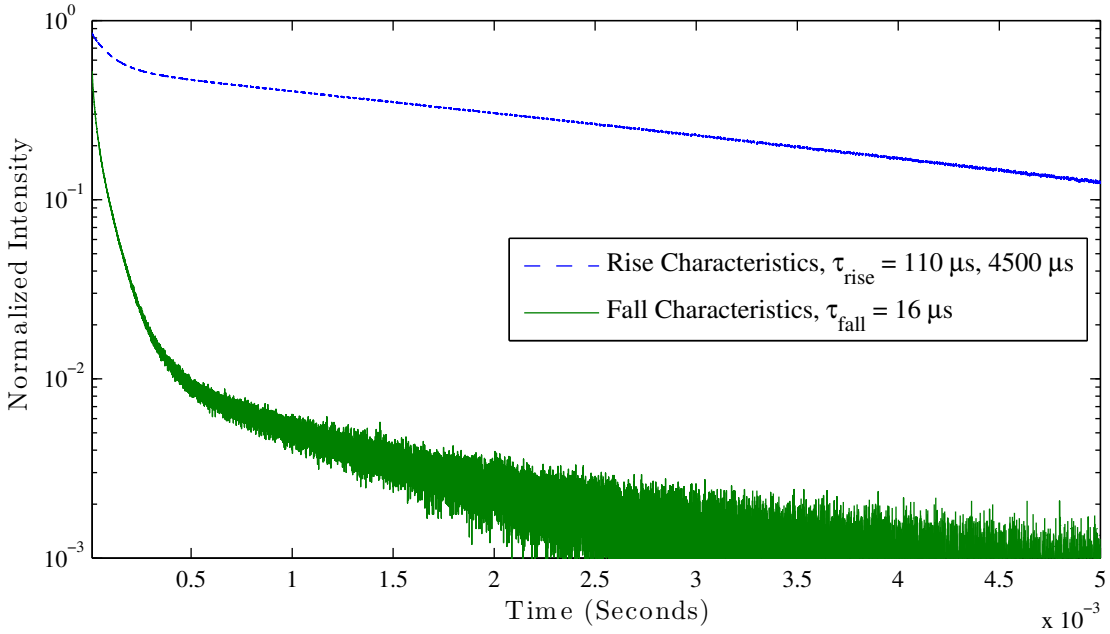

Figure 6.8: The dynamics of $^4F_{9/2}$ fluorescence intensity versus time for 0.5% Er:YAG under 965 nm up to 10 kW/cm^2 intensity puming on semilog-y plot.

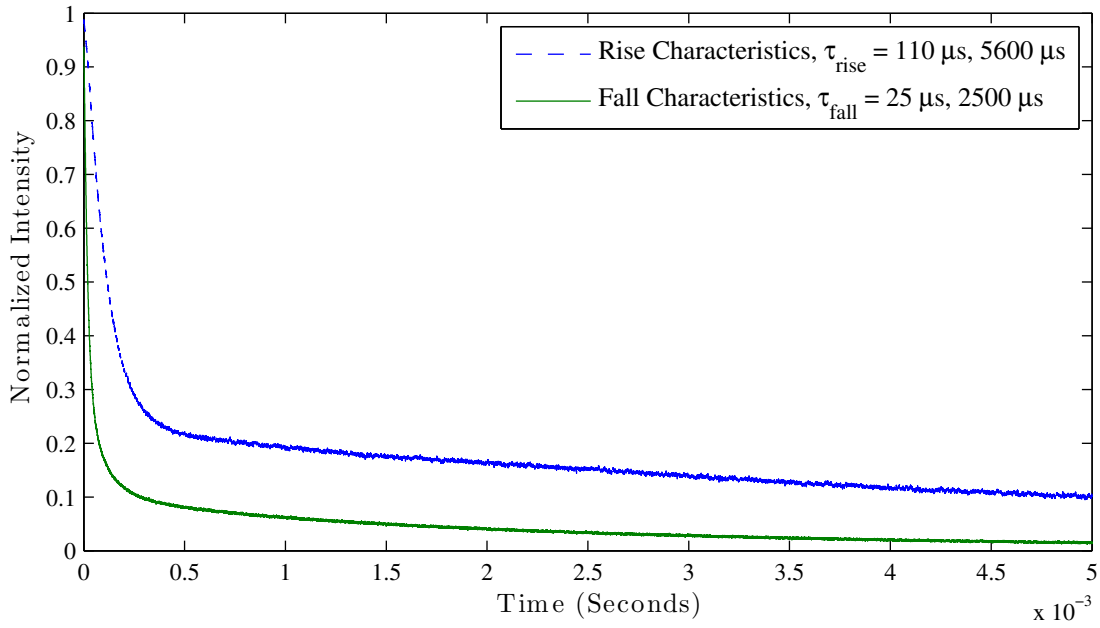

Figure 6.9: The dynamics of $^4I_{9/2}$ fluorescence intensity versus time for 0.5% Er:YAG under 965 nm up to 10 kW/cm^2 intensity puming.

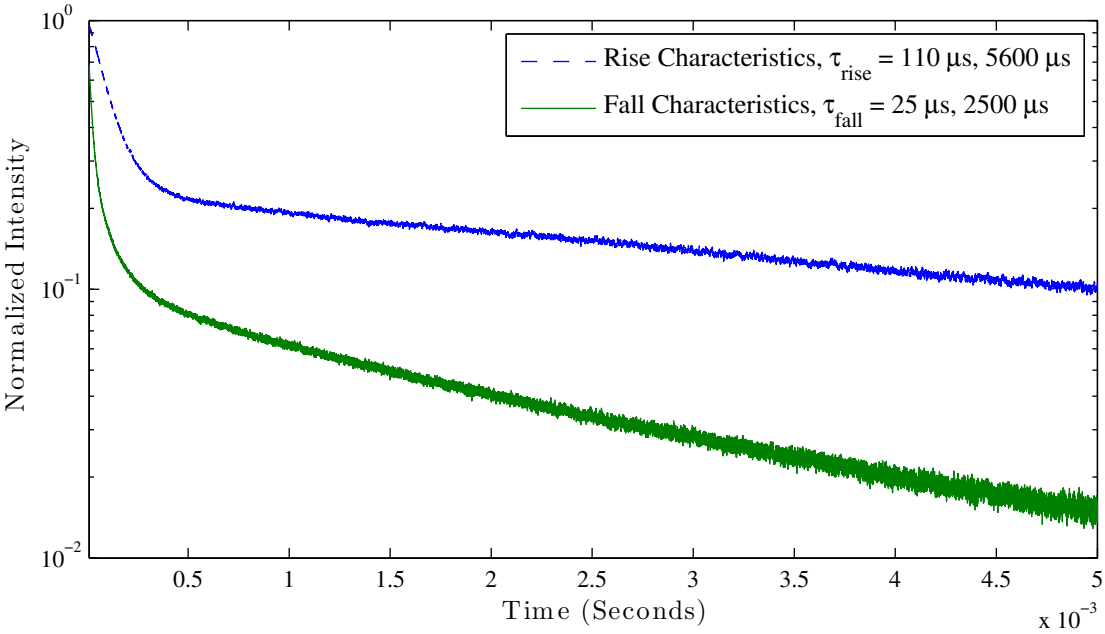

Figure 6.10: The dynamics of $^4I_{9/2}$ fluorescence intensity versus time for 0.5% Er:YAG under 965 nm up to 10 kW/cm^2 intensity puming on semilog-y plot.

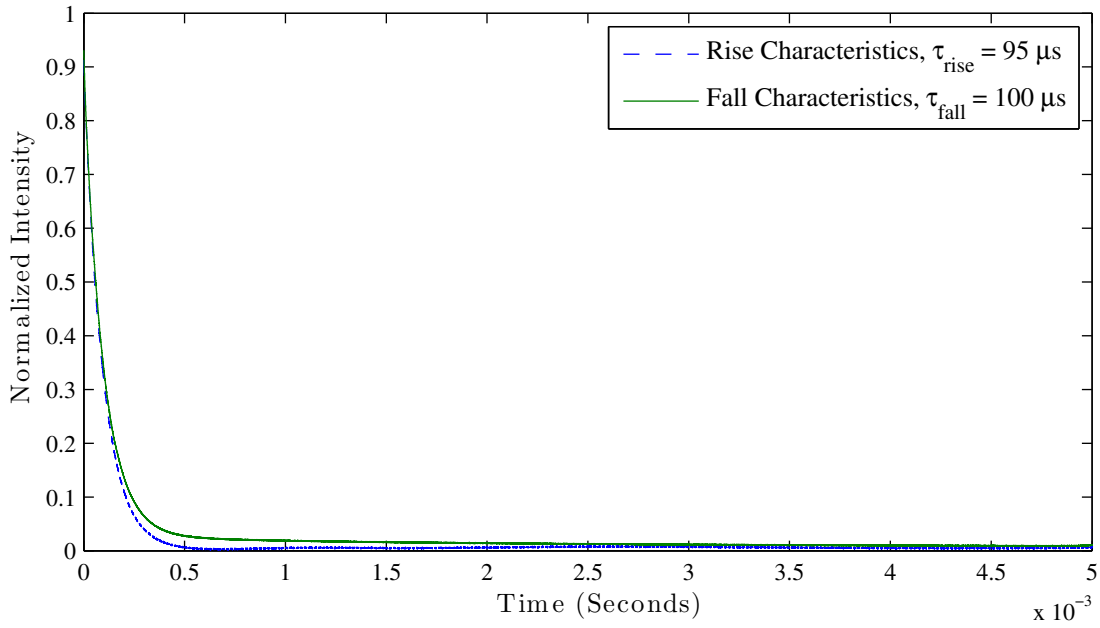

Figure 6.11: The dynamics of $^4I_{11/2}$ fluorescence intensity versus time for 0.5% Er:YAG under 965 nm up to 10 kW/cm^2 intensity puming.

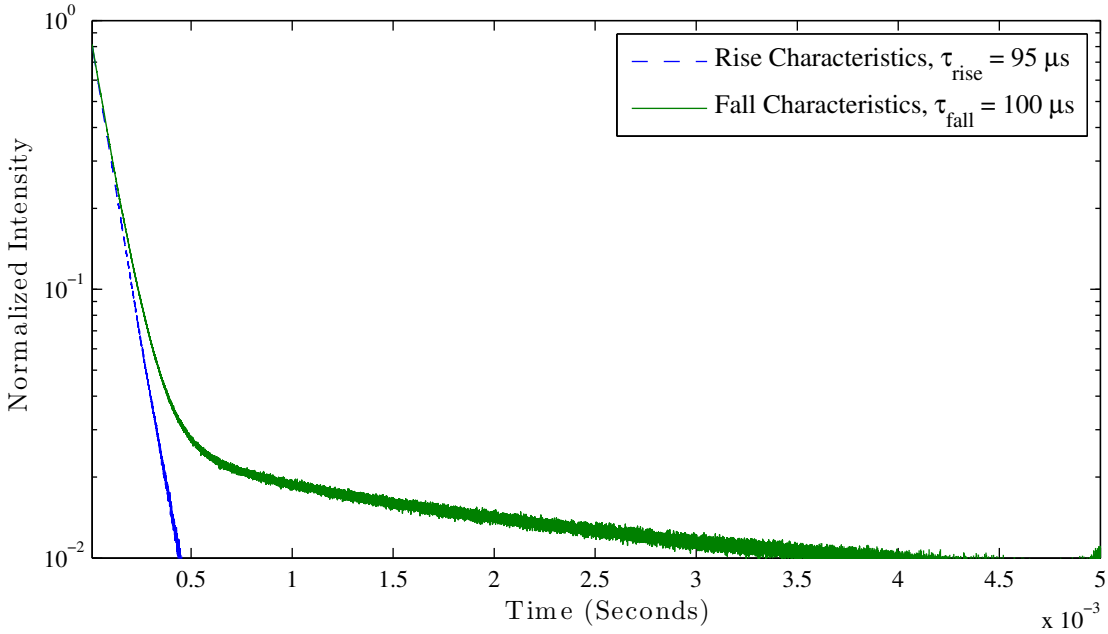

Figure 6.12: The dynamics of $^4I_{11/2}$ fluorescence intensity versus time for 0.5% Er:YAG under 965 nm up to 10 kW/cm^2 intensity puming on semilog-y plot.

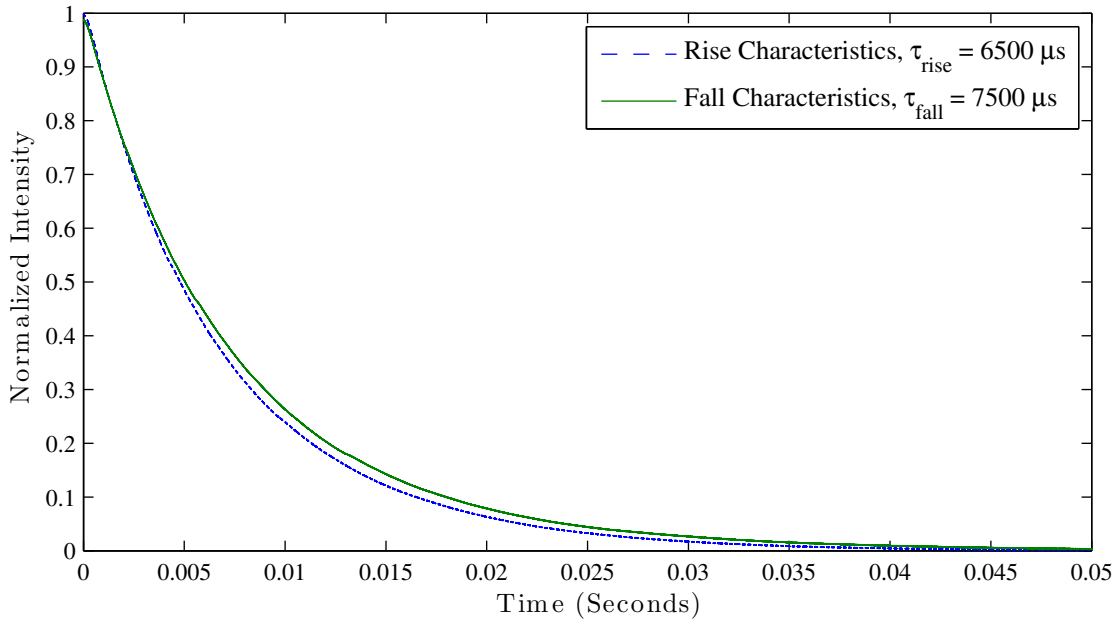

Figure 6.13: The dynamics of $^4I_{13/2}$ fluorescence intensity versus time for 0.5% Er:YAG under 965 nm up to 10 kW/cm^2 intensity puming.

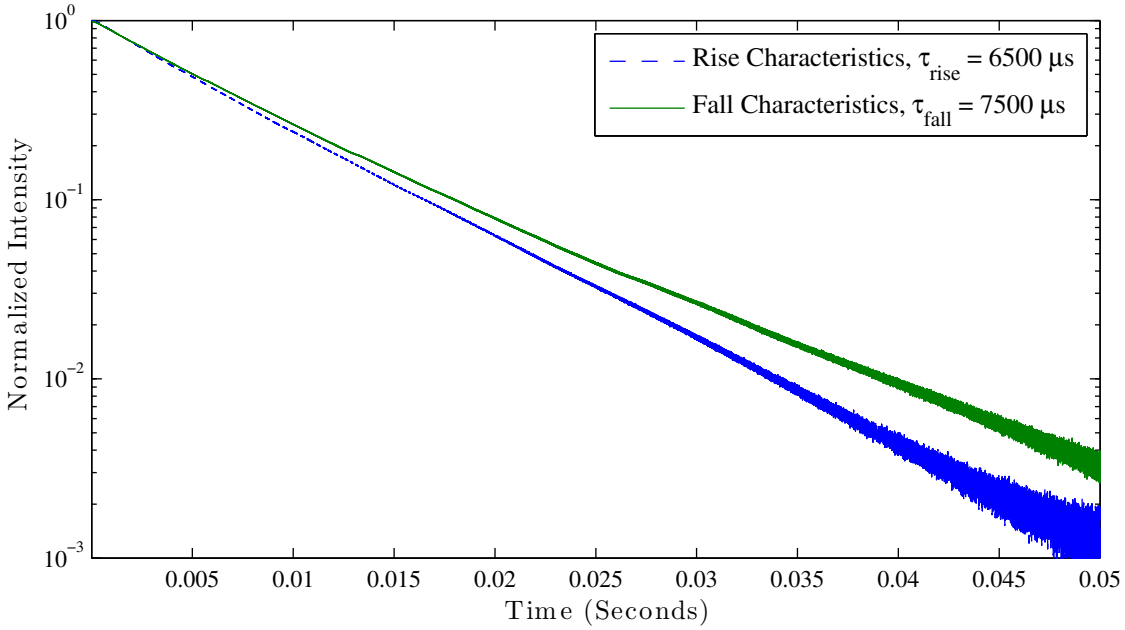

Figure 6.14: The dynamics of $^4I_{13/2}$ fluorescence intensity versus time for 0.5% Er:YAG under 965 nm up to 10 kW/cm^2 intensity puming on semilog-y plot.

6.3.2 50% Er:YAG under 965 nm Pump

In 50% Er:YAG, the situation is even more interesting. The states that above the pump state of $^4I_{11/2}$ such as $^4S_{3/2}$ (Figure 6.15 on page 71 and Figure 6.16 on page 72), $^4F_{9/2}$ (Figure 6.17 on page 73 and Figure 6.18 on page 73), and $^4I_{9/2}$ (Figure 6.19 on page 74 and Figure 6.20 on page 75) all exhibit non-exponential behavior on both the rise and fall. In addition, a lot of detail on the evolution of the up-conversion due to ETU and ESA rate are embedded in the plots. First, the rise on all these states exhibit an increase of up-conversion rate from less steep to more steep from looking at their log plots. This is because initially only ESA is affecting the up-conversion. As the population increases, the up-conversion due to ETU terms start to become more important and causes the slope to change. On the fall, the sharp drop into a less steep drop is due to the fact that the moment pump turns off, the steady state population from ESA portion of the up-conversion can no longer sustain itself. As it reaches quickly to the steady state population due to ETU portion, the ETU portion is also decreasing due to lower state depopulating ltself from the natural decay rate.

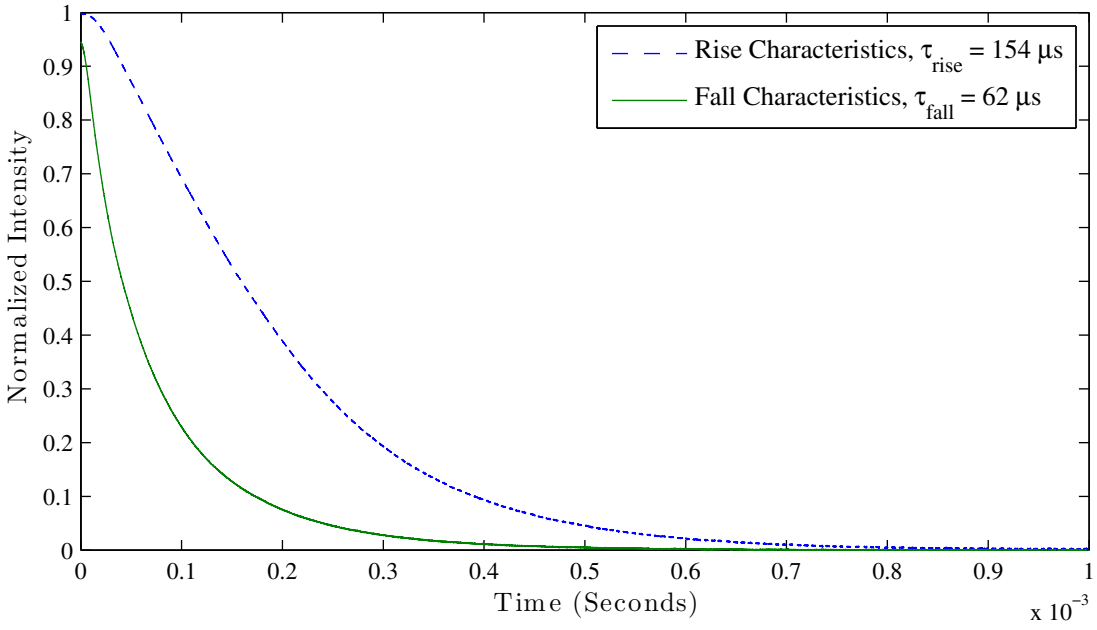

Figure 6.15: The dynamics of $^4S_{3/2}$ fluorescence intensity versus time for 50% Er:YAG under 965 nm up to 10 kW/cm^2 intensity puming.

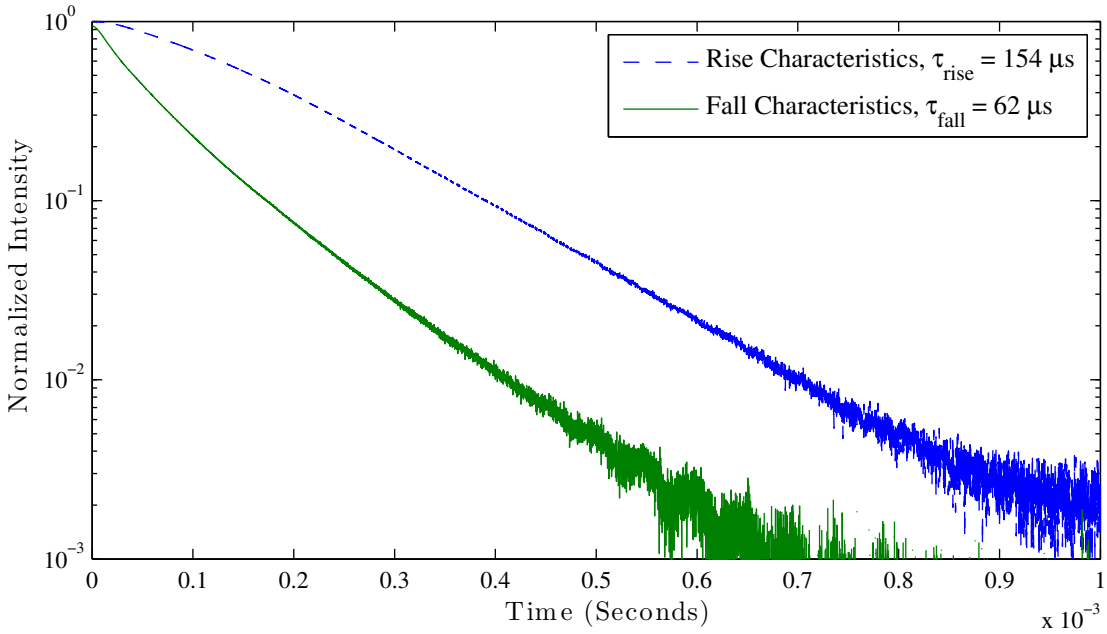

Figure 6.16: The dynamics of $^4S_{3/2}$ fluorescence intensity versus time for 50% Er:YAG under 965 nm up to 10 kW/cm^2 intensity puming on semilog-y plot.

From each state's semilog-y plot on the rise characteristics, the importance of up-conversion due to ESA and ETU from $^4I_{13/2}$ is observed from the slopes of the plots. For example, the state $^4S_{3/2}$ has very little importance as the $^4I_{13/2}$ only become dominant after close to 10^{-3}. From the end of the fall curve of $^4S_{3/2}$, no ETU is observed, this indicates that only ESA from $^4I_{13/2}$ is affecting the population in $^4S_{3/2}$. This is not true of of up-conversion of $^4I_{11/2}$ as from the rise curve the fluorescence characteristic time follows that of $^4I_{11/2}$ with a change of slope as the population in $^4I_{11/2}$ increases. Both ESA and ETU are important. On the fall, the ETU is strong enough to be observed that instead of showing sub-microseconds natural decay time, it is now reflecting the pump rate of ETU from $^4I_{11/2}$ as 62 μs.

First, usually the life time of $^4I_{9/2}$ in heavily doped is sub-microseconds. Here we observe a rise time of 200 μs and a fall time of 95 μs. this is because the fall curve is reflecting the up-conversion coming from lower states similar to the effects of $^4S_{3/2}$ and $^4F_{9/2}$. In addition to the similar results of $^4S_{3/2}$, the $^4F_{9/2}$ state population shows about 5% due to up-conversion from $^4I_{13/2}$. It is can be deduced that the 5% up-conversion is from ESA as the fall curve of

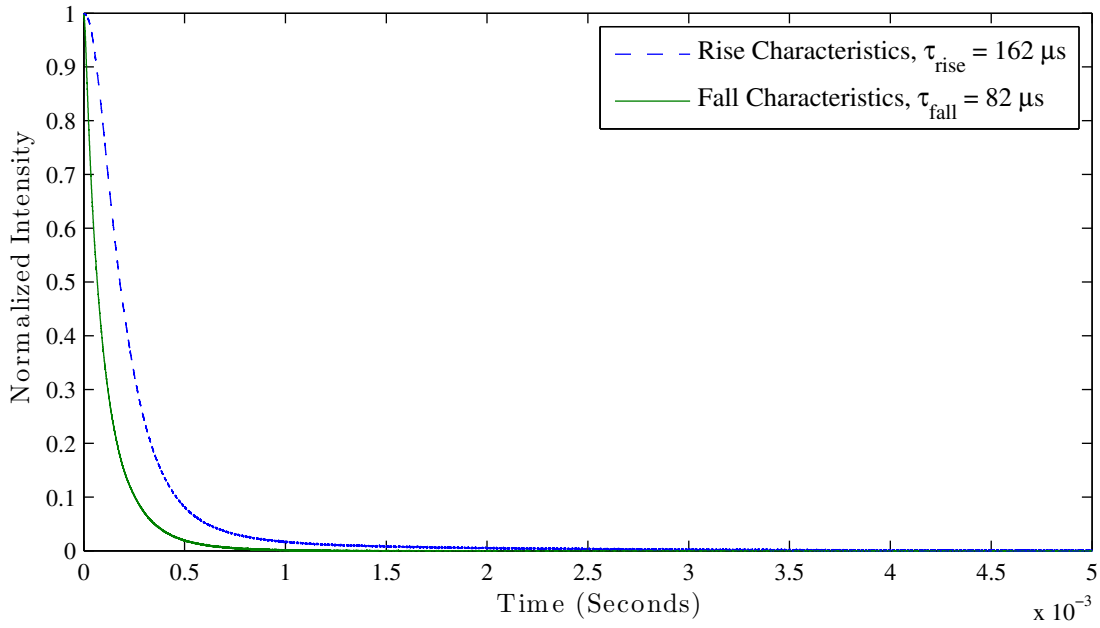

Figure 6.17: The dynamics of $^4F_{9/2}$ fluorescence intensity versus time for 50% Er:YAG under 965 nm up to 10 kW/cm^2 intensity puming.

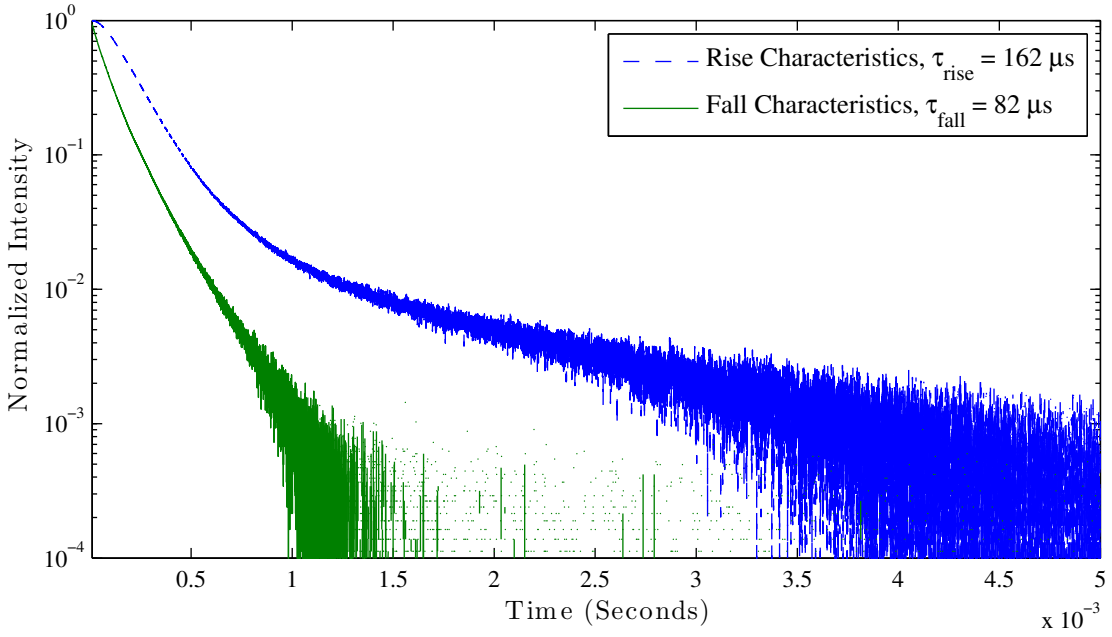

Figure 6.18: The dynamics of $^4F_{9/2}$ fluorescence intensity versus time for 50% Er:YAG under 965 nm up to 10 kW/cm^2 intensity puming on semilog-y plot.

this state shows no observable $^4I_{13/2}$ characteristics from ETU towards the end of the decay. The $^4I_{9/2}$ also show a similar effect; however, the characteristic fall time towards the end of the curve start to become less steep. This indicates the possibility of $^4I_{13/2}$ is affecting $^4I_{9/2}$ state population via ETU.

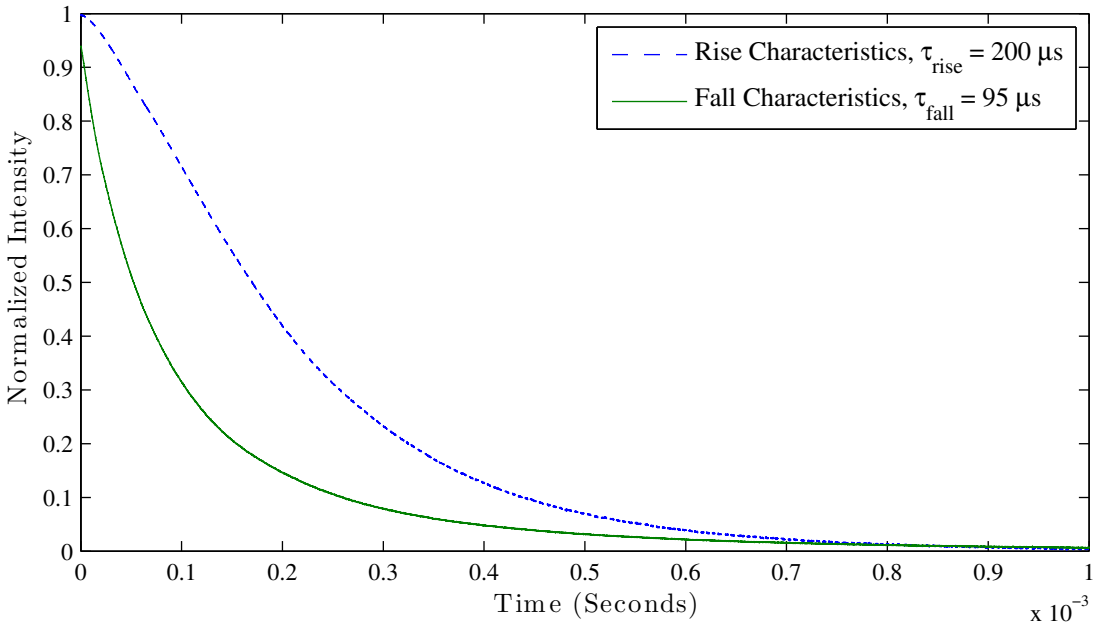

Figure 6.19: The dynamics of $^4I_{9/2}$ fluorescence intensity versus time for 50% Er:YAG under 965 nm up to 10 kW/cm^2 intensity puming.

For the pump state $^4I_{11/2}$ (Figure 6.21 on page 76 and Figure 6.22 on page 76) and the lower excited state $^4I_{13/2}$ (Figure 6.23 on page 77 and Figure 6.24 on page 78), they are the source states of up-conversion for the upper excited states $^4S_{3/2}$, $^4F_{9/2}$, and $^4I_{9/2}$. The information embedded in the pump state dynamics is nuanced. First, the rise time for this state increased roughly twice from the natural decay time of 90 μs to 185 μs. The fall time changed to 155 μs, which is an increase of slightly more than 50%. This is extremely awkward since on the rise, the ESA effects from $^4I_{11/2}$ should only cause the rise time to look shorter. However, what is obtained is the complete opposite by 100%. Furthermore, sine this is the pump state, this indicates that the lower excited state $^4I_{13/2}$ is strongly up-converting ions and dumping them into $^4I_{11/2}$ such that the lower excited state up-conversion masks the ESA

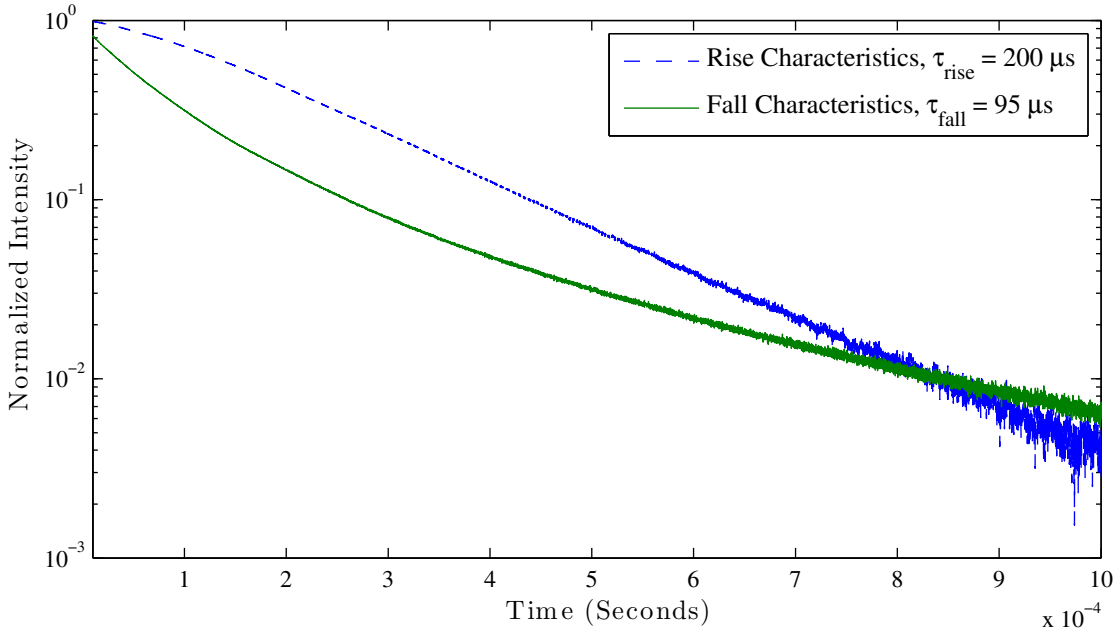

Figure 6.20: The dynamics of $^4I_{9/2}$ fluorescence intensity versus time for 50% Er:YAG under 965 nm up to 10 kW/cm^2 intensity puming on semilog-y plot.

effects on time on the pump state. The rise curve is not straight for the entire curve and the curve is becoming less steep. This indicates that as population becomes high, the ETU effects from the pump state is removing ions out of the state more effectively, which is in harmony with the afforementioned analysis of all the upper states above the pump become sharper on the rise after a certain point.

On the fall, it initially drops in population fast because of the up-conversion from ETU effects. After a certain point of slightly less than 10% of the maximum population, the curve returns to a straight line on the semilog-y plot indicating that the ETU effects from itself has become negligible. Furthermore, this should also imply when the $^4I_{13/2}$ stops up-converting via ETU.

For the lower excited state $^4I_{13/2}$, a rise time change of 1.3 ms to 475 μs a factor of roughly 2.7 between the two numbers, is observed. This indicates that ESA and ETU are both strongly up-converting to the upperstates. On the decay, a fall time of 800 μs is observed, which is about 2/3 of what the natural decay would be. In addition, the decay

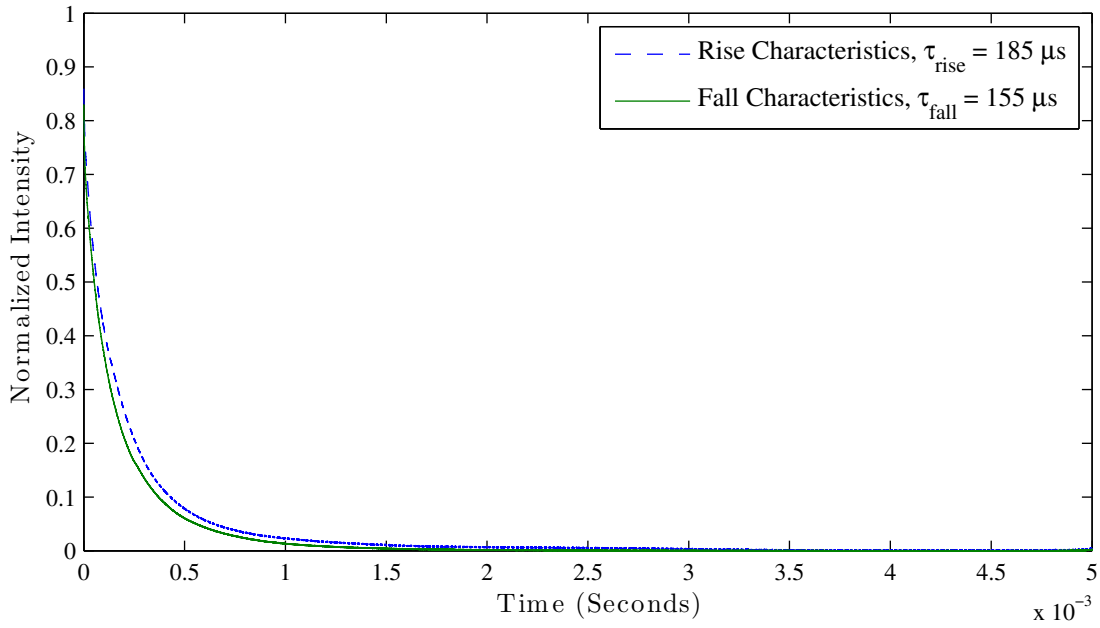

Figure 6.21: The dynamics of $^4I_{11/2}$ fluorescence intensity versus time for 50% Er:YAG under 965 nm up to 10 kW/cm^2 intensity puming.

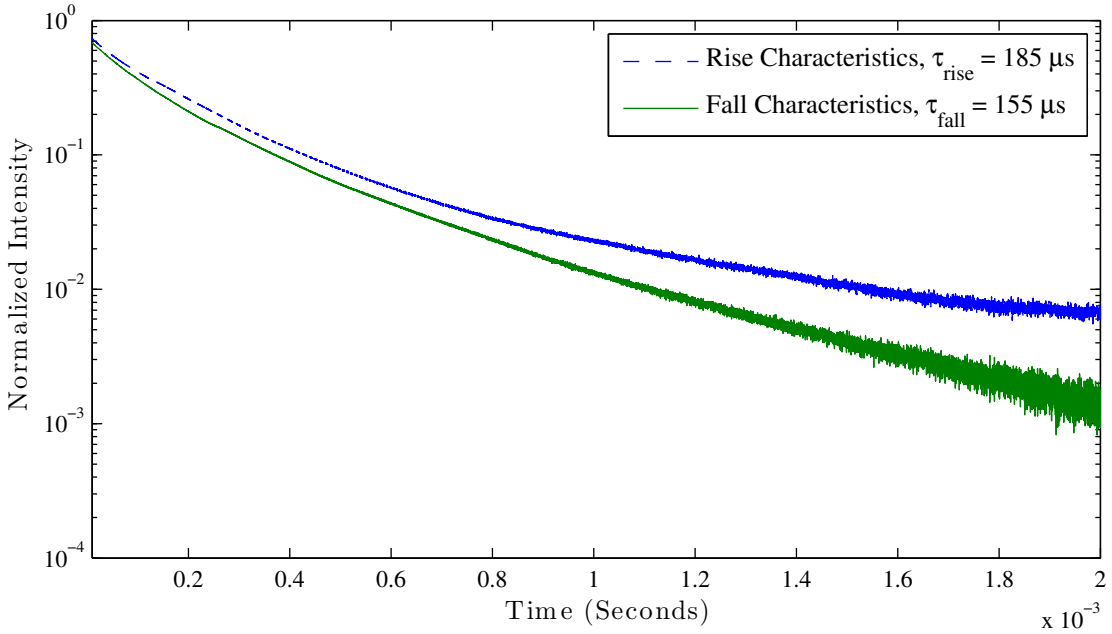

Figure 6.22: The dynamics of $^4I_{11/2}$ fluorescence intensity versus time for 50% Er:YAG under 965 nm up to 10 kW/cm^2 intensity puming on semilog-y plot.

curve becomes straight around the same point when the $^4I_{13/2}$ decay curve becomes straight.

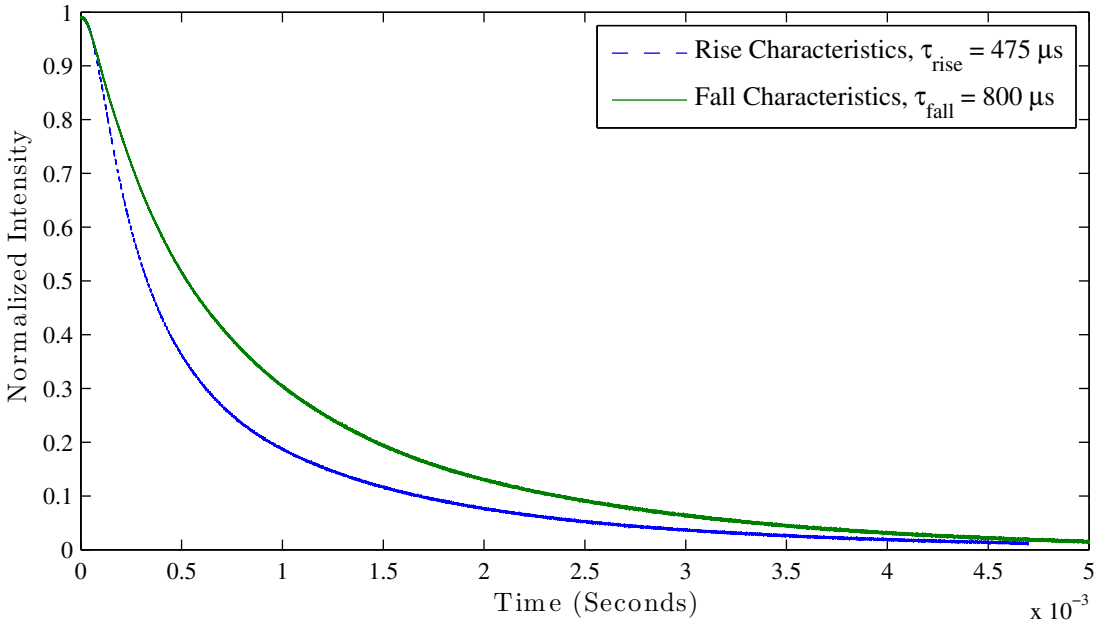

Figure 6.23: The dynamics of $^4I_{13/2}$ fluorescence intensity versus time for 50% Er:YAG under 965 nm up to 10 kW/cm^2 intensity puming.

At this point, it is important to mention that these characteristic times are all "lower bound" of the up-conversion strengths. The input pump intensity is not uniform every where; therefore, the center spot of the pump is much stronger than the outside. However, when fluorescence is observed, especially for the lower state, it is the overall population that is observed. This is important because as soon as a pinhole aperture of roughly 100 μm in diameter is added right in front of the sample, the rise time changed from 770 μs to 475 μs and the fall time changed from 1100 μs to 800 μs. The pinhole aperture allows the removal of the portion of the bean that is not high in intensity along the outer edge. Furthermore, after this correction, the numbers reported here especially for the high doped samples are still the "lower bound" for the fact that the sample are a bit too thick such that the green up-converted fluorescence along the beam propagation has a visually detectable change in intensity. Since the photodetector used captures all of the fluorescence by collecting the

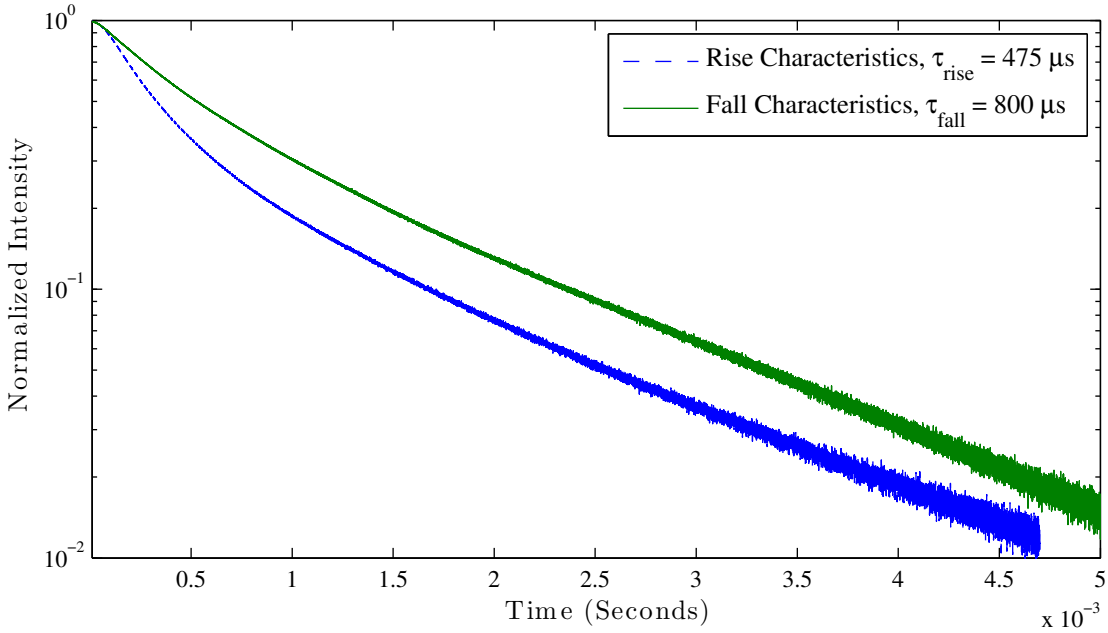

Figure 6.24: The dynamics of $^4I_{13/2}$ fluorescence intensity versus time for 50% Er:YAG under 965 nm up to 10 kW/cm^2 intensity puming on semilog-y plot.

fluorescence through a lens, it is capturing the sum of the high intensity portion of the fluorescence as well as the low intensity of the fluorescence. The low intensity portion of the fluorescence will have a much lower population as well as input pump intensity than the high intensity portion of the fluorescence region; therefore, the result is not purely the high up-conversion number. Therefore, for the low doped 0.5% Er:YAG, the $^4I_{13/2}$ has a rise time of 6000 μs is actually the "lower bound". The more accurate number should be closer to the 4000 μs or 4500 μs reported by the green fluorescence of $^4S_{3/2}$ or $^4F_{9/2}$. This is especially true for the low doped sample as there should be fewer ETU and XR effects that are affecting the population of $^4S_{3/2}$.

The fall time of the upper states above the pump such as $^4S_{3/2}$, $^4F_{9/2}$, and $^4I_{9/2}$ are changed due to ETU up-conversion. If the assumption of ETU effects from $^4I_{11/2}$ is relatively small is true, then the population of the lower state is not emptied too strongly by the ETU effects. Assume all other effects are ignored, then the rate equation of the upper state $^4S_{3/2}$ will have a natural decay and an ETU up-conversion term of Equation 6.3. Assuming N_2 is

something along the lines of Equation 6.4, then $N_2(t)$ is a convolution of the natural decay equation of N_2 with a life time of less than $1\,\mu$s with $N_2^2(t)$, which is roughly just $N_2^2(t)$ times a constant. The form is given in Equation 6.5, which is a time constant of half of that of $N_2(t)$ ($77.5\,\mu$s). The upper states of $^4S_{3/2}$, $^4F_{9/2}$, and $^4I_{9/2}$ all exhibit a life time around that range with slight variations, which may be due to other ETU and XR effects.

$$\frac{dN_5}{dt} = \frac{1}{\tau_5} + W_{22}N_2^2 \tag{6.3}$$

$$N_2(t) = e^{\frac{-t}{155\,\mu s}} \tag{6.4}$$

$$N_1(t) \approx W_{22} * N_2^2(t) = W_{22}e^{\frac{-2t}{155\,\mu s}} = W_{22}e^{\frac{-t}{77.5\,\mu s}} \tag{6.5}$$

6.3.3 1% Er:Yttria under 965 nm Pump

For 1% Er:Yttria, the behavior is in general similar to that of SC 0.5% Er:YAG. In $^4S_{3/2}$ (Figure 6.25 on page 80 and Figure 6.26 on page 81), the rise roughly follows that of $^4I_{11/2}$ (Figure 6.31 on page 84 and Figure 6.32 on page 84), which is roughly 3 ms instead of 87 μs of low-pump level decay time of the state. The fall time is 160 μs. This is different from the 87 μs because the fall does exhibit some up-conversion from $^4I_{11/2}$. $^4I_{9/2}$ (Figure 6.29 on page 82 and Figure 6.30 on page 83) has the same behavior as $^4S_{3/2}$ state on the dynamics.

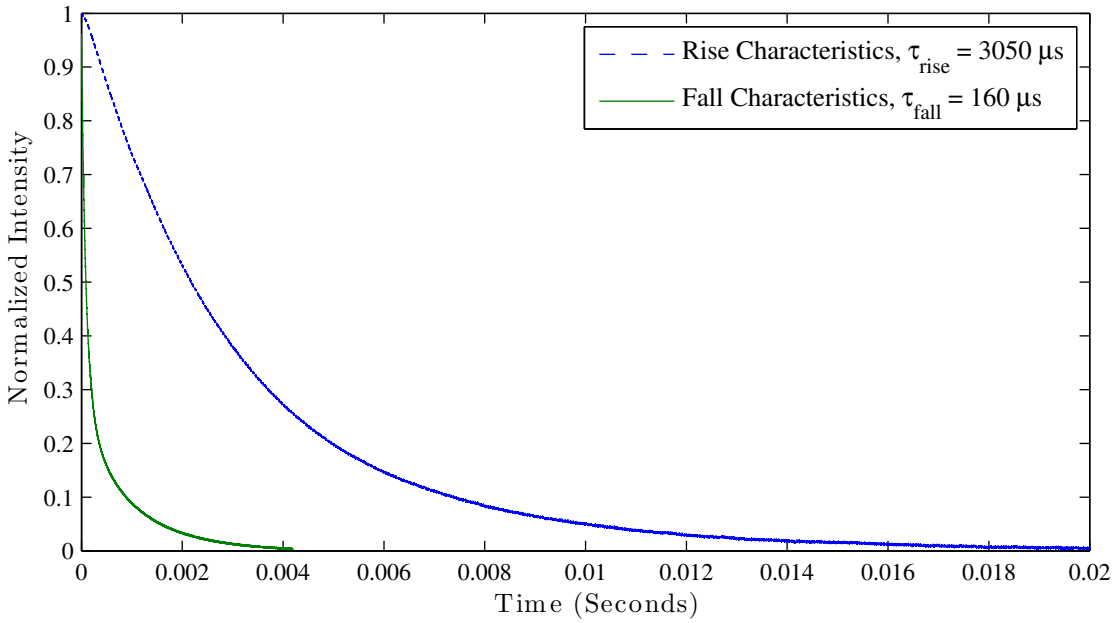

Figure 6.25: The dynamics of $^4S_{3/2}$ fluorescence intensity versus time for 1% Er:Y_2O_3 under 965 nm up to 10 kW/cm^2 intensity puming.

For the state $^4F_{9/2}$ (Figure 6.27 on page 81 and Figure 6.28 on page 82), it is unknown as to why the time on both the rise and fall become very different from other states. This suggests that there is should be another energy path added to the system. However, given how straight the curve is, it seems that a single exponential will do, which means it should be dependent of mainly only ESA coming from $^4I_{13/2}$. On the fall, it is not known as to what effects can cause a 770 μs on its fall time. Furthermore, from the data, of $^4S_{3/2}$, $^4F_{9/2}$, and $^4I_{9/2}$, the $^4F_{9/2}$ does not decay to $^4I_{9/2}$, at least not enough to be observed.

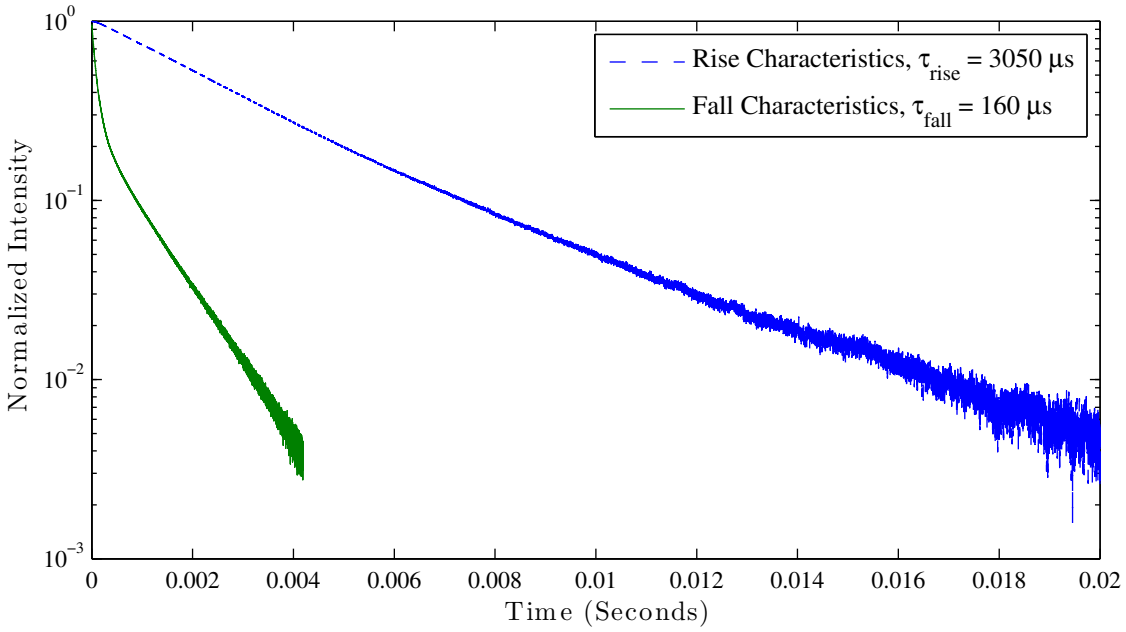

Figure 6.26: The dynamics of $^4S_{3/2}$ fluorescence intensity versus time for 1% Er:Y_2O_3 under 965 nm up to 10 kW/cm^2 intensity puming on semilog-y plot.

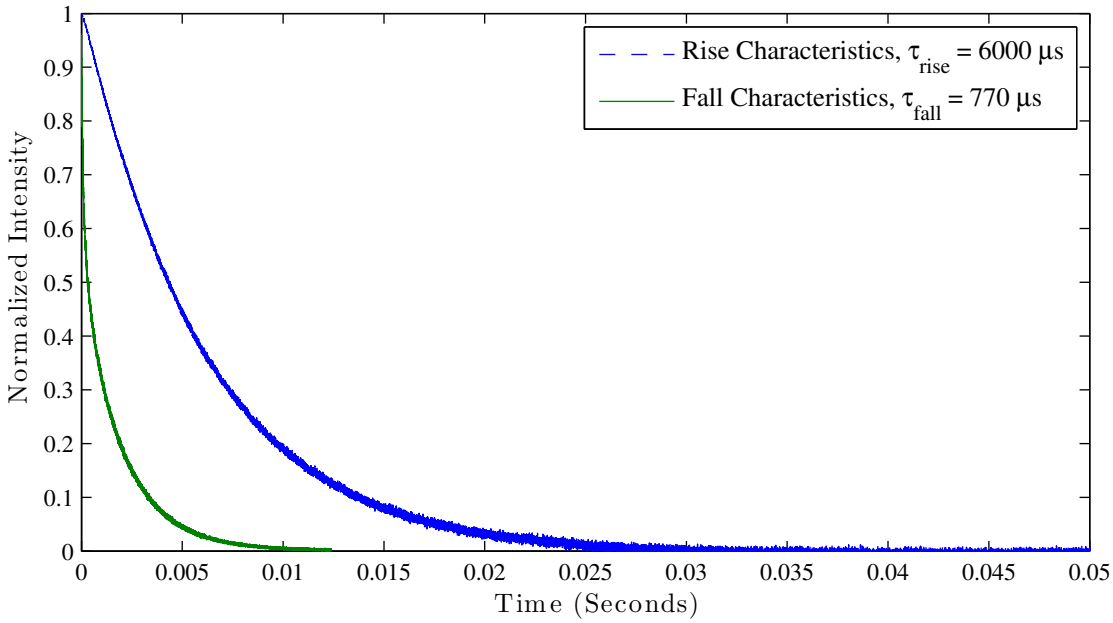

Figure 6.27: The dynamics of $^4F_{9/2}$ fluorescence intensity versus time for 1% Er:Y_2O_3 under 965 nm up to 10 kW/cm^2 intensity puming.

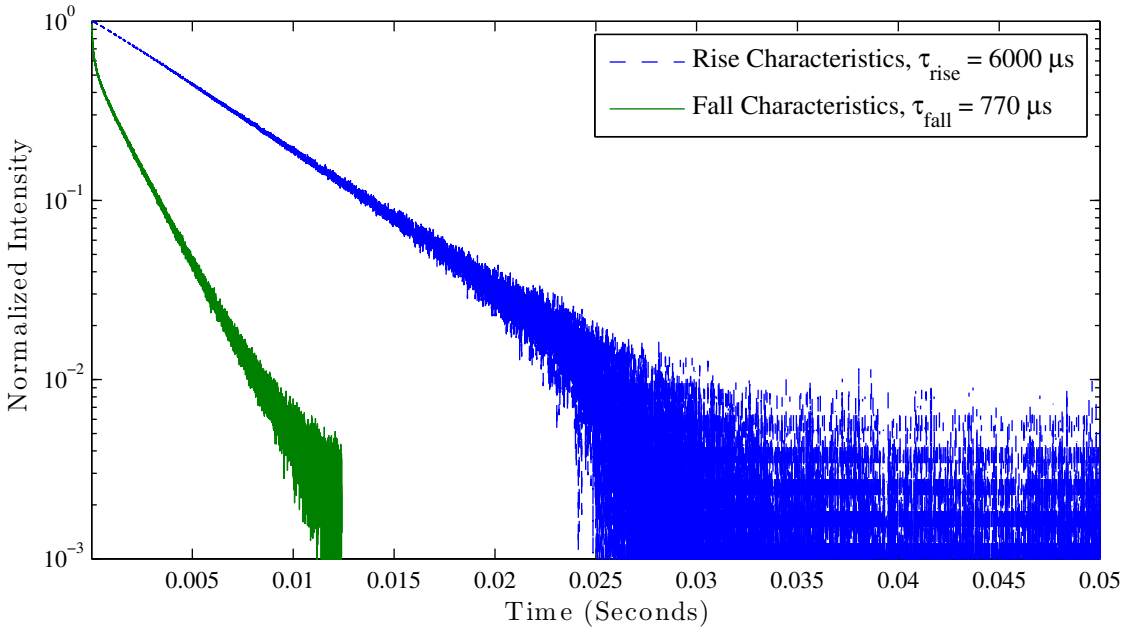

Figure 6.28: The dynamics of $^4F_{9/2}$ fluorescence intensity versus time for 1% Er:Y_2O_3 under 965 nm up to 10 kW/cm^2 intensity puming on semilog-y plot.

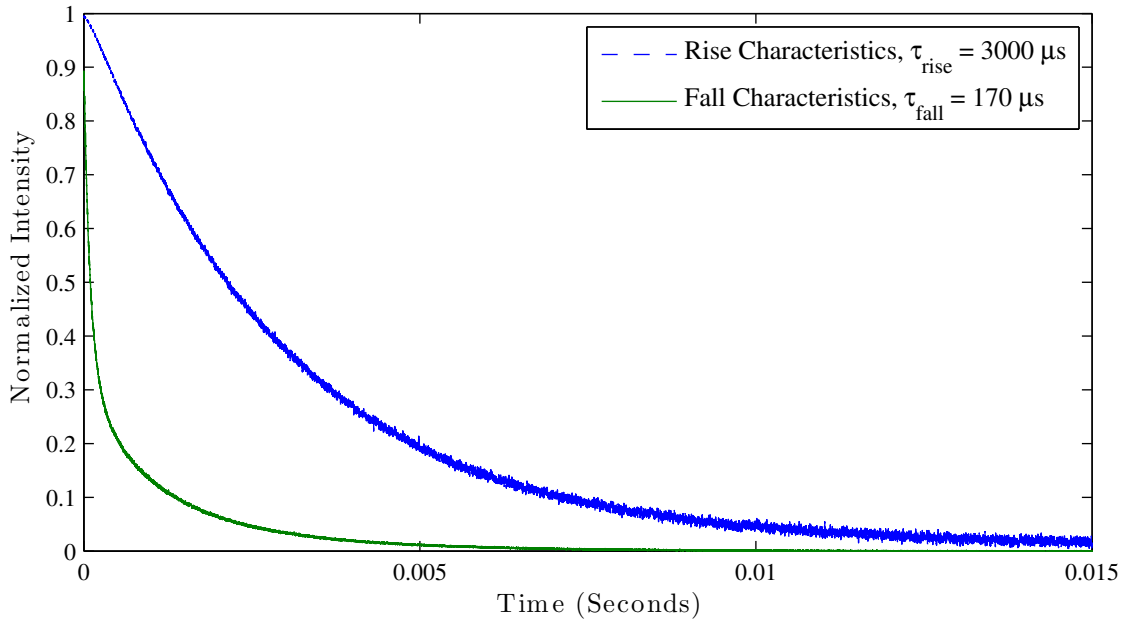

Figure 6.29: The dynamics of $^4I_{9/2}$ fluorescence intensity versus time for 1% Er:Y_2O_3 under 965 nm up to 10 kW/cm^2 intensity puming.

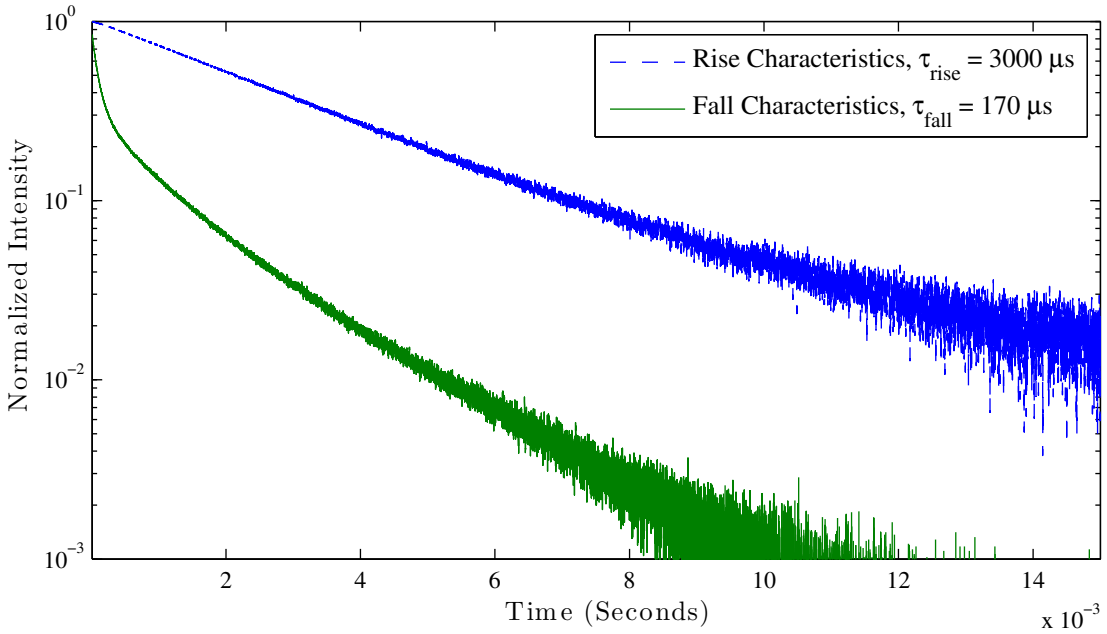

Figure 6.30: The dynamics of $^4I_{9/2}$ fluorescence intensity versus time for 1% Er:Y_2O_3 under 965 nm up to 10 kW/cm^2 intensity puming on semilog-y plot.

The $^4I_{11/2}$ (Figure 6.31 on page 84 and Figure 6.32 on page 84) does not change very much (around 10% on the rise 3% on the fall) as given on Table 6.4 with natural decay time of 2740, rise time of 2450, and fall time of 2650. However the results are lower bound as discussed in Section 6.3.2 indicating that the effects can only be this or higher.

The $^4I_{13/2}$ (Figure 6.33 on page 85 and Figure 6.34 on page 85) natural decay time is 13400, the rise time is 12400, and the fall time is 12900. The change for both are less than 10%, which, again, is a lower bound. However, on the dynamics side, it has an additional component that can be observed. The begining part of the rise is slow because it is waiting on the pump level $^4I_{11/2}$ to populate before the decay rate down to $^4I_{13/2}$ become steady state.

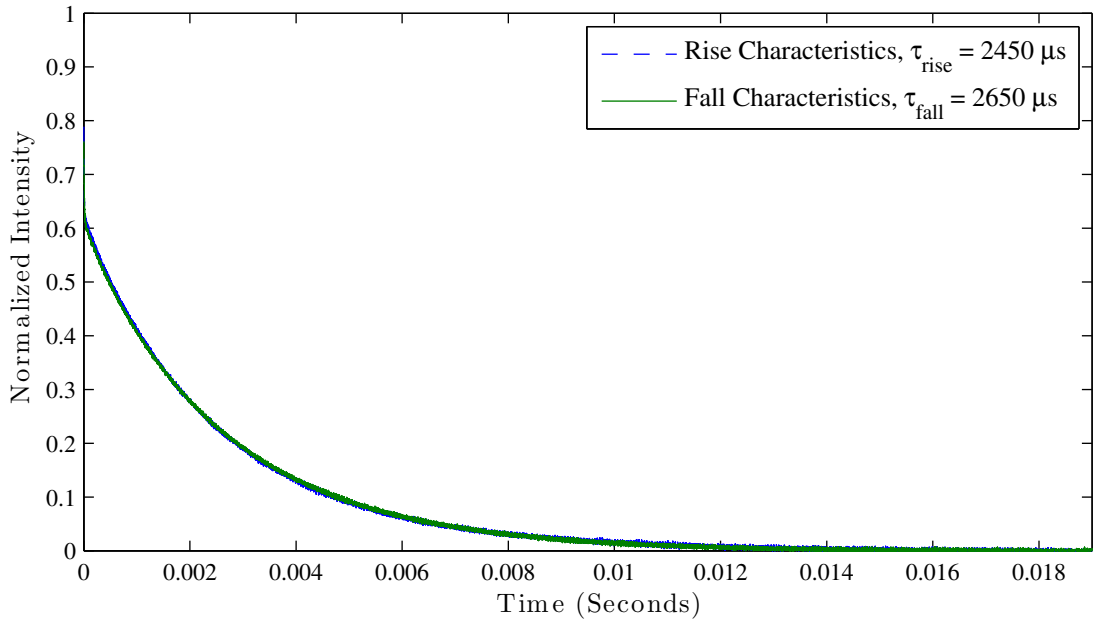

Figure 6.31: The dynamics of $^4I_{11/2}$ fluorescence intensity versus time for 1% Er:Y_2O_3 under 965 nm up to 10 kW/cm^2 intensity puming.

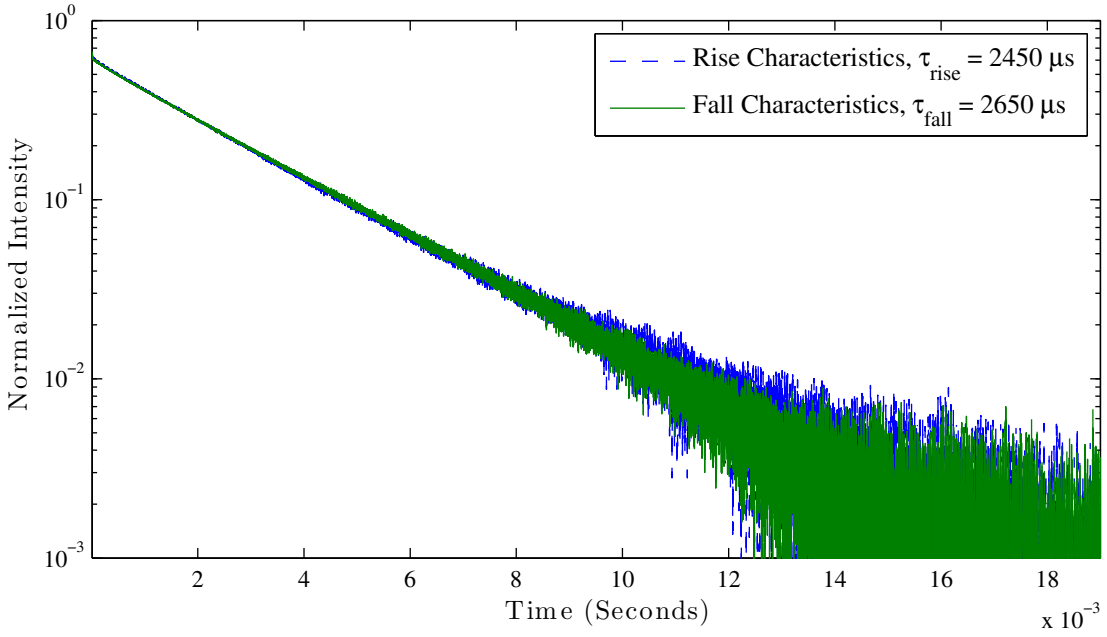

Figure 6.32: The dynamics of $^4I_{11/2}$ fluorescence intensity versus time for 1% Er:Y_2O_3 under 965 nm up to 10 kW/cm^2 intensity puming on semilog-y plot.

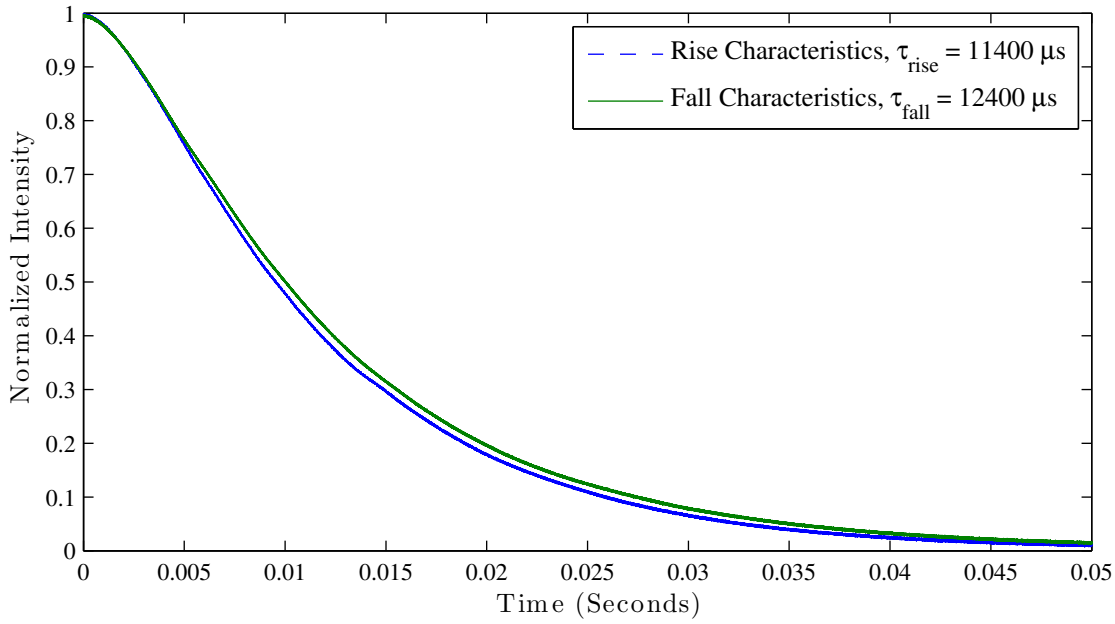

Figure 6.33: The dynamics of $^4I_{13/2}$ fluorescence intensity versus time for 1% Er:Y_2O_3 under 965 nm up to 10 kW/cm^2 intensity puming.

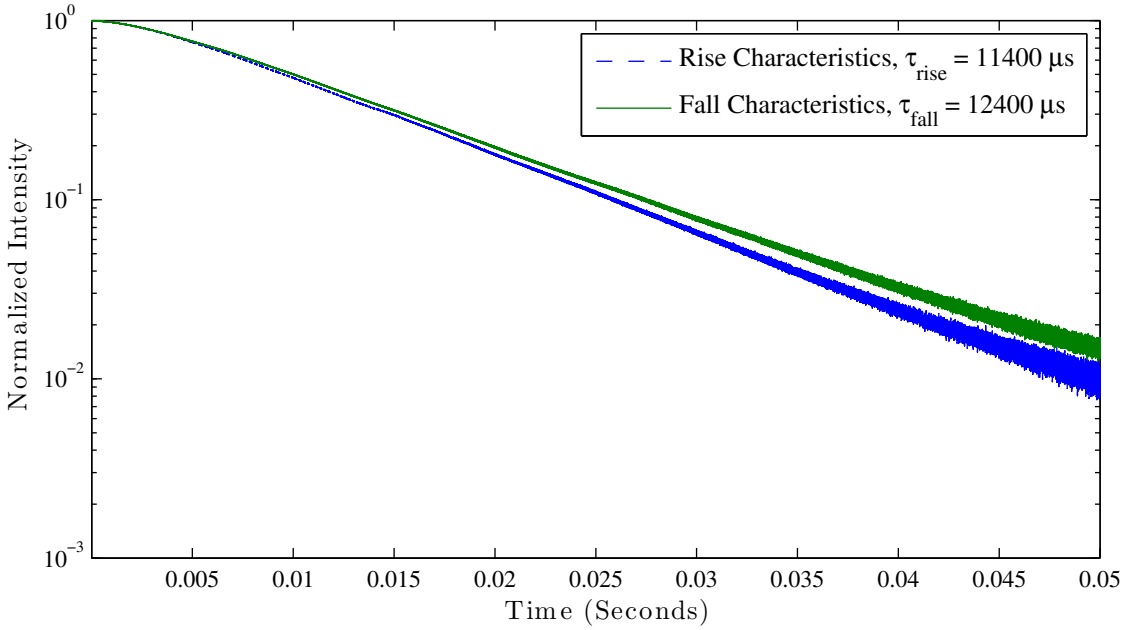

Figure 6.34: The dynamics of $^4I_{13/2}$ fluorescence intensity versus time for 1% Er:Y_2O_3 under 965 nm up to 10 kW/cm^2 intensity puming on semilog-y plot.

6.3.4 15% Er:Yttria under 965 nm Pump

The $^4S_{3/2}$ state (Figure 6.35 on page 87 and Figure 6.36 on page 87) rise time follows that of ESA from $^4I_{11/2}$ as the time are roughly the same. The fall time is also around half of that from $^4I_{11/2}$ ETU up-conversion as discussed in Equation 6.5 on page 79. The $^4F_{9/2}$ (Figure 6.37 on page 88 and Figure 6.38 on page 88) state is yet again an odd ball with perfectly straight line on semilog-y plot although the time should be a combination of ESA from $^4I_{11/2}$ and $^4I_{13/2}$. The $^4I_{9/2}$ (Figure 6.39 on page 89 and Figure 6.40 on page 89) is understandable as on the rise it shows a combination of $^4I_{11/2}$ ESA and ETU and $^4I_{13/2}$ ESA and ETU. The $^4I_{13/2}$ ESA and ETU dominates toward the end.

For the pump state $^4I_{11/2}$ (Figure 6.41 on page 90 and Figure 6.42 on page 90), even though the time does not change; however, toward the end of the rise at about last 10% from steady state, the ESA and ETU from lower state start to dominate the dynamics curve. The fall appear to be a straight line, which indicates that the ETU is negligible in comparison to ESA. For lower excited state $^4I_{13/2}$ (Figure 6.43 on page 91 and Figure 6.44 on page 91), the variation of the curve only indicates that the rate of change of the incoming population increases from one exponential characteristics to another due to the same reason as the $^4I_{13/2}$ of the 1% Er:Y2O3 as given in Section 6.3.4. For the similar reason then, the fall rate also increases from one exponential characteristics to another as the pump state $^4I_{11/2}$ is depopulated. The life time changes from the natural of 7700 μs to a rise time of 5900 μs and a fall time of 7300 μsṪhis is a change of 23% on the rise and a 5% change on the fall.

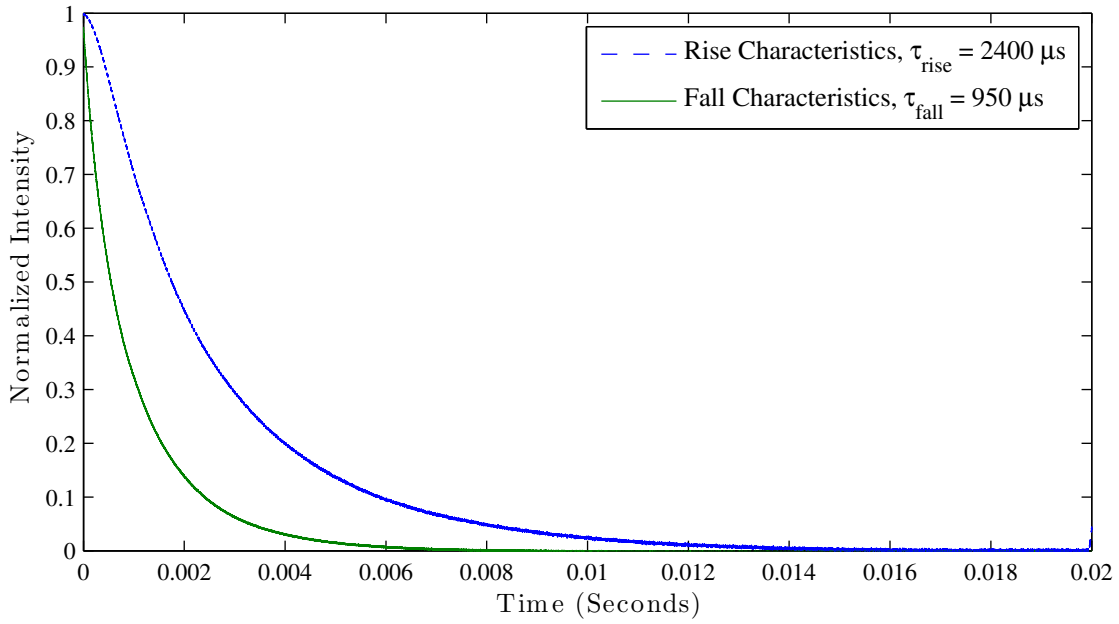

Figure 6.35: The dynamics of $^4S_{3/2}$ fluorescence intensity versus time for 15% Er:Y_2O_3 under 965 nm up to 10 kW/cm^2 intensity puming.

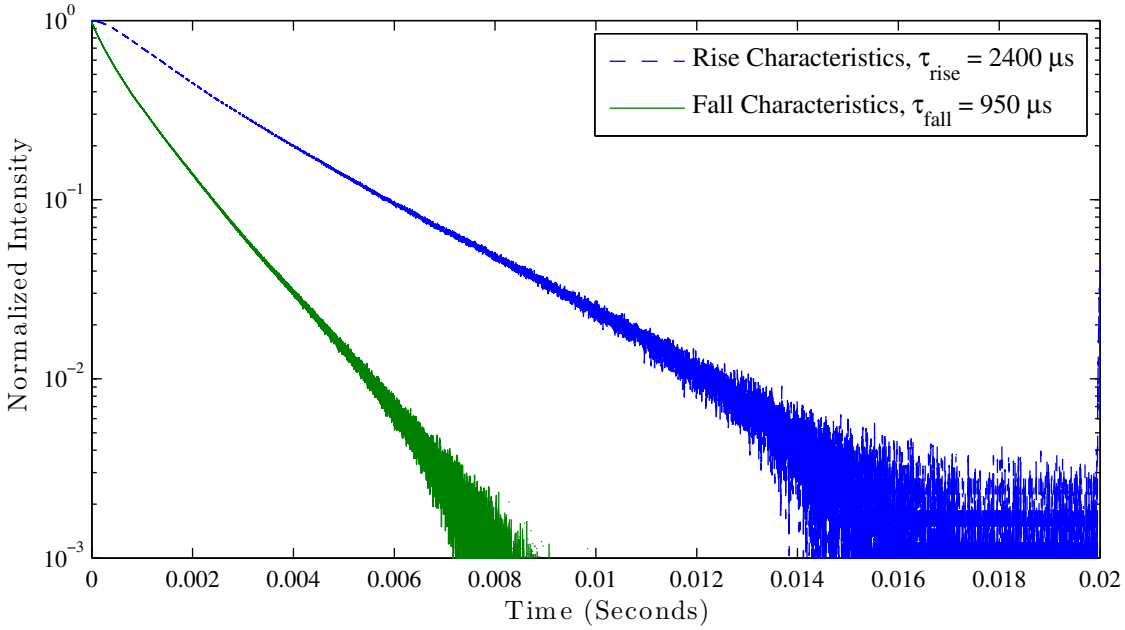

Figure 6.36: The dynamics of $^4S_{3/2}$ fluorescence intensity versus time for 15% Er:Y_2O_3 under 965 nm up to 10 kW/cm^2 intensity puming on semilog-y plot.

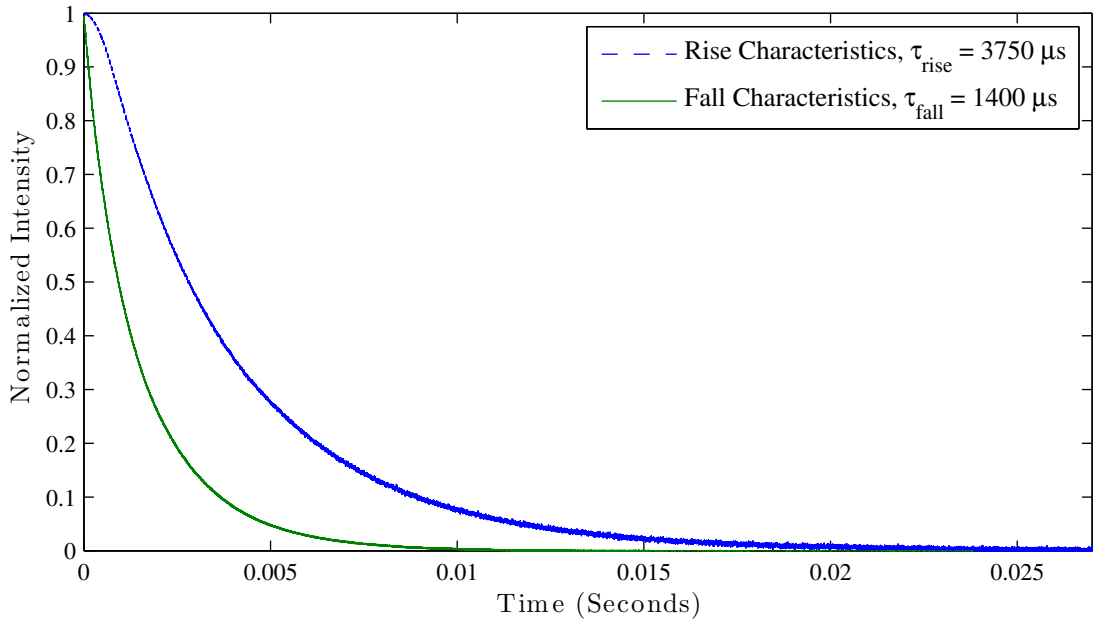

Figure 6.37: The dynamics of $^4F_{9/2}$ fluorescence intensity versus time for 15% Er:Y_2O_3 under 965 nm up to 10 kW/cm^2 intensity puming.

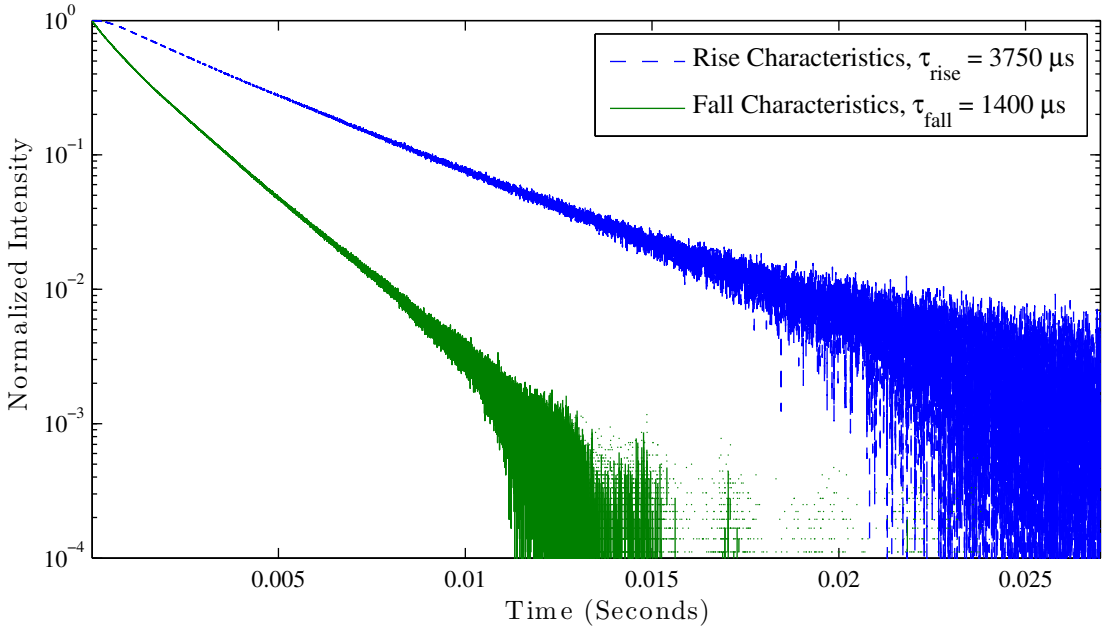

Figure 6.38: The dynamics of $^4F_{9/2}$ fluorescence intensity versus time for 15% Er:Y_2O_3 under 965 nm up to 10 kW/cm^2 intensity puming on semilog-y plot.

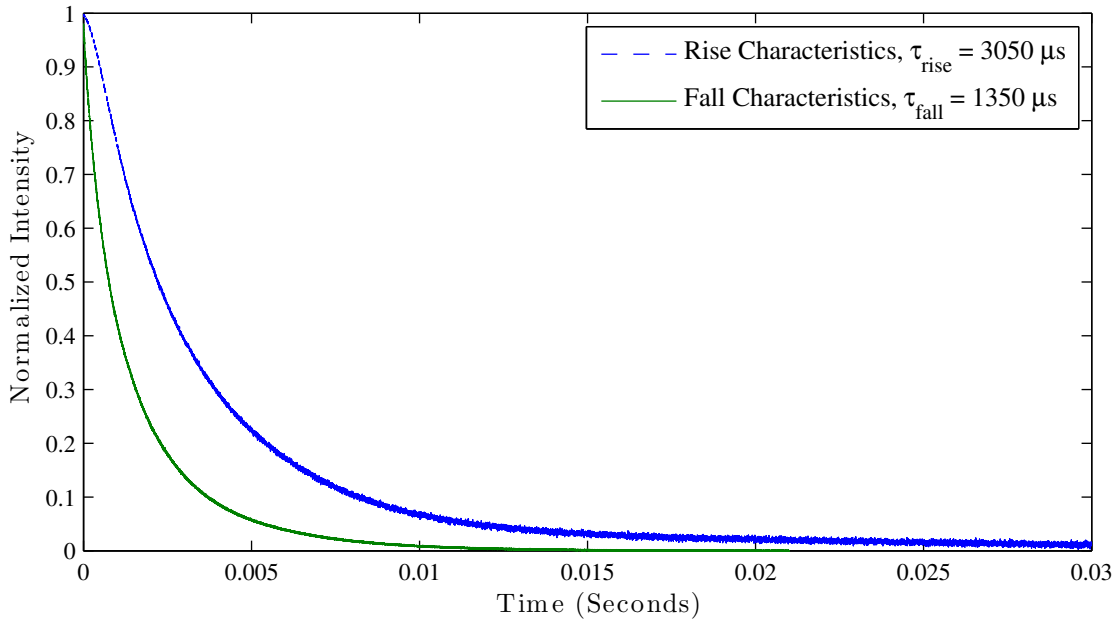

Figure 6.39: The dynamics of $^4I_{9/2}$ fluorescence intensity versus time for 15% Er:Y_2O_3 under 965 nm up to 10 kW/cm^2 intensity puming.

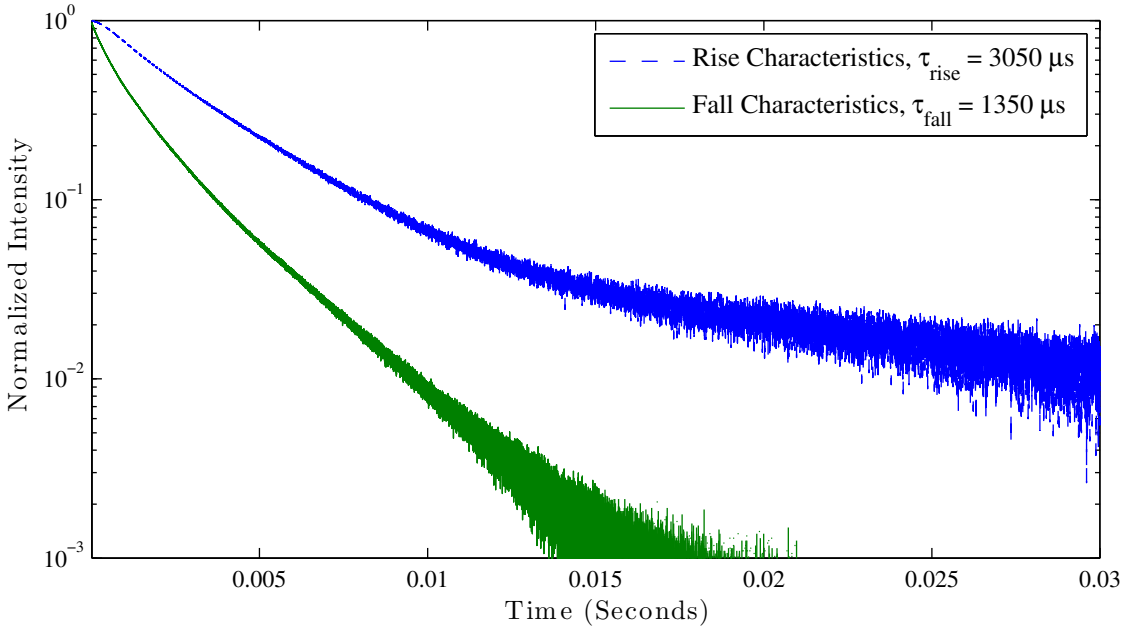

Figure 6.40: The dynamics of $^4I_{9/2}$ fluorescence intensity versus time for 15% Er:Y_2O_3 under 965 nm up to 10 kW/cm^2 intensity puming on semilog-y plot.

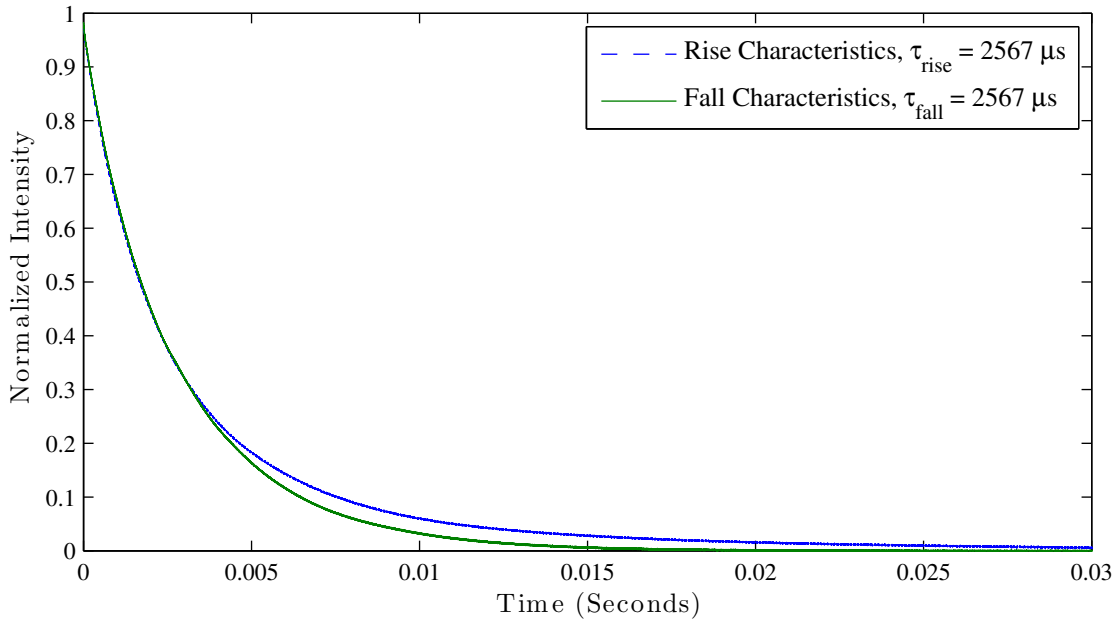

Figure 6.41: The dynamics of $^4I_{11/2}$ fluorescence intensity versus time for 15% Er:Y_2O_3 under 965 nm up to 10 kW/cm^2 intensity puming.

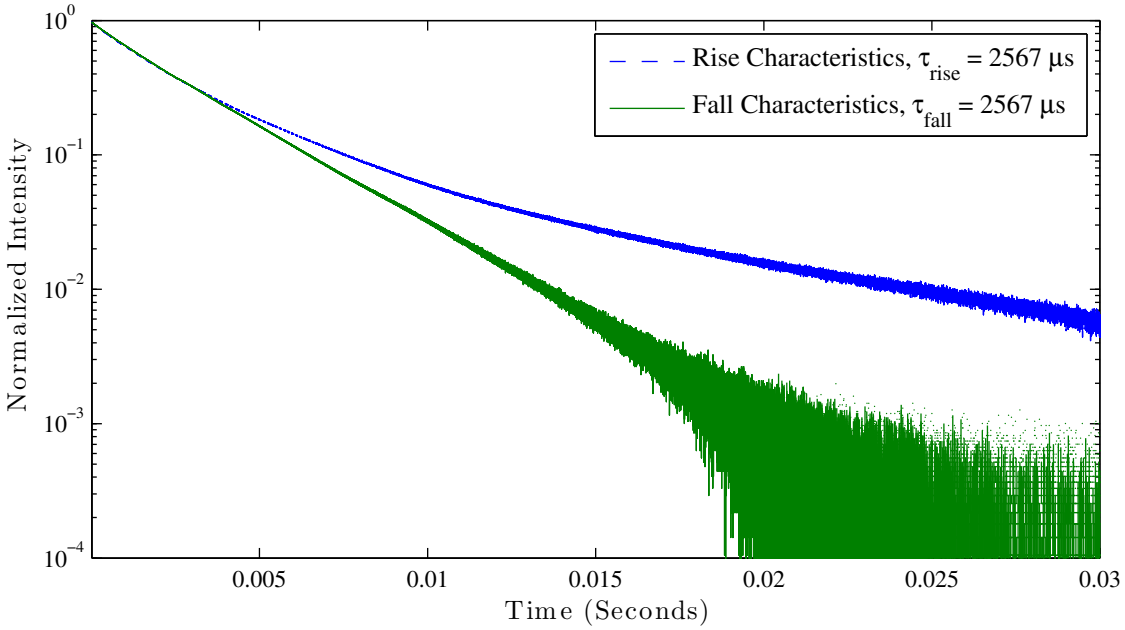

Figure 6.42: The dynamics of $^4I_{11/2}$ fluorescence intensity versus time for 15% Er:Y_2O_3 under 965 nm up to 10 kW/cm^2 intensity puming on semilog-y plot.

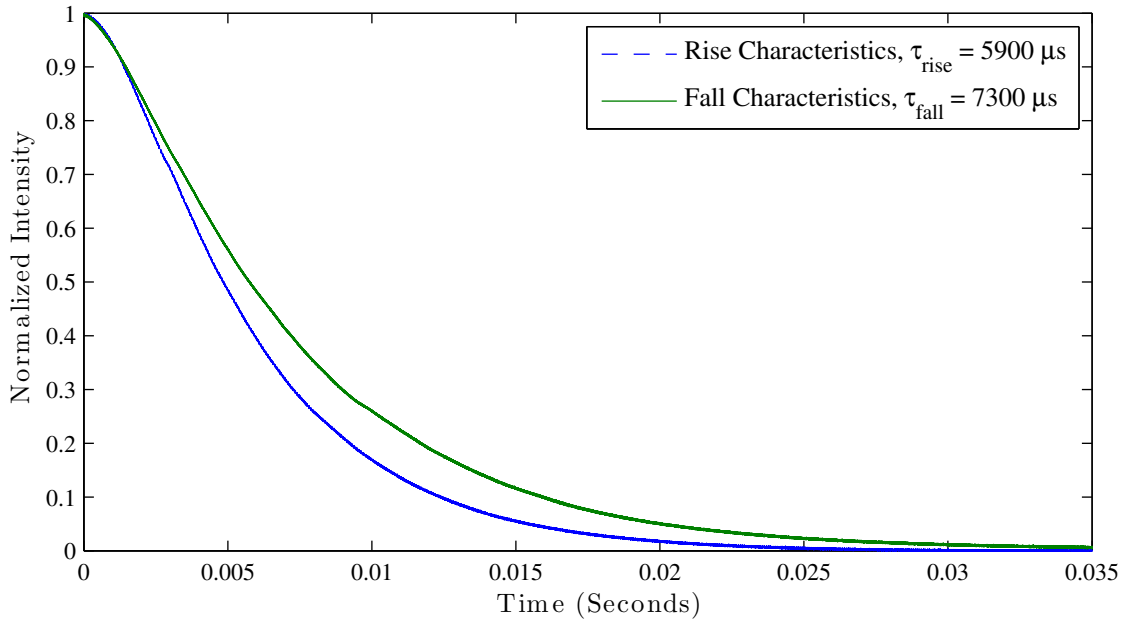

Figure 6.43: The dynamics of $^4I_{13/2}$ fluorescence intensity versus time for 15% Er:Y_2O_3 under 965 nm up to 10 kW/cm^2 intensity puming.

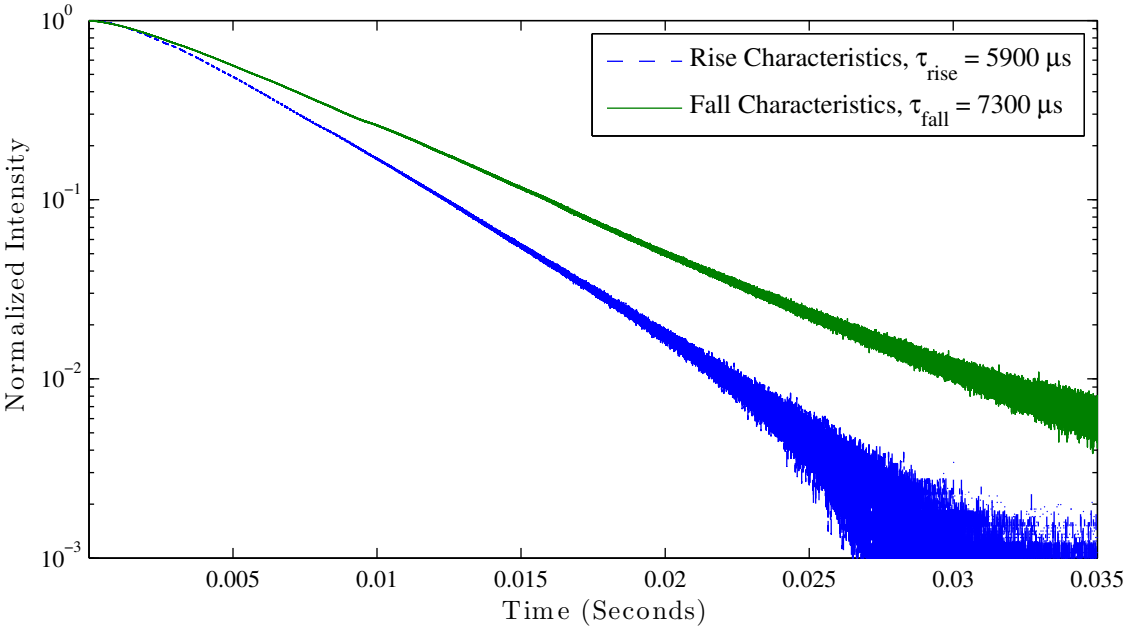

Figure 6.44: The dynamics of $^4I_{13/2}$ fluorescence intensity versus time for 15% Er:Y_2O_3 under 965 nm up to 10 kW/cm^2 intensity puming on semilog-y plot.

6.3.5 25% Er:Yttria under 965 nm Pump

For the 25% Er:Yttria, the upper excited state above the pump level $^4I_{11/2}$, they reflect roughly the rise time of the lower excited states of $^4I_{11/2}$ and $^4I_{13/2}$, and as the doping become higher, the ETU effects become visible as the slope on rise become sharper. For $^4S_{3/2}$ (Figure 6.45 on page 92 and Figure 6.46 on page 93), the rise changed from 2 μs of natural rate to 400 μs and the fall to 154 μs, which is roughly half of the fall time of $^4I_{11/2}$ under 965 nm high intensity pumping.

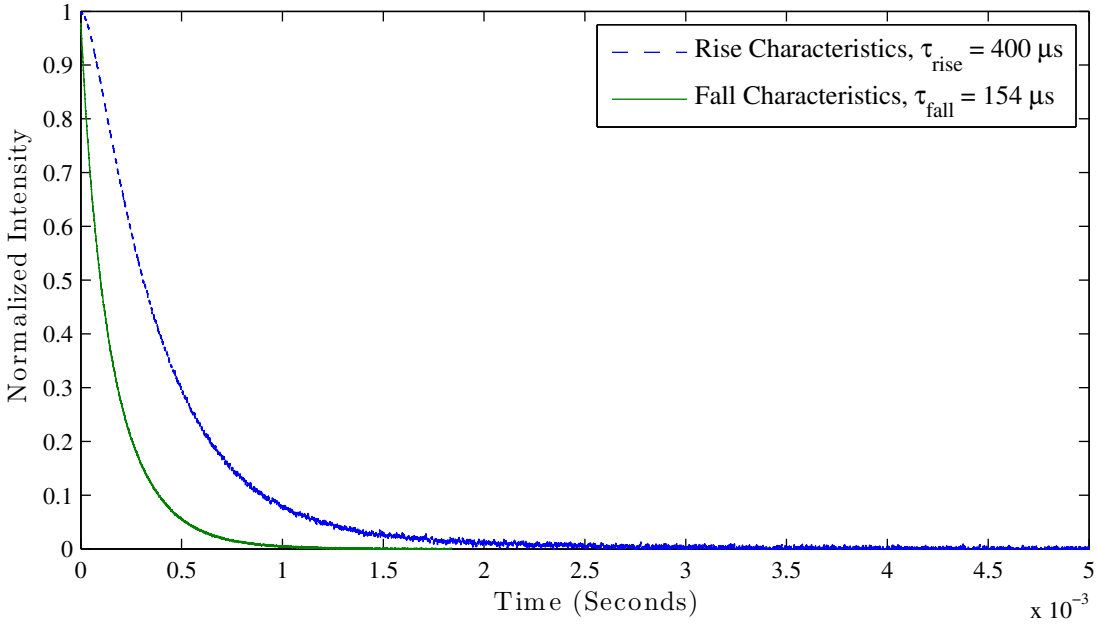

Figure 6.45: The dynamics of $^4S_{3/2}$ fluorescence intensity versus time for 25% Er:Y_2O_3 under 965 nm up to 10 kW/cm^2 intensity puming.

For $^4F_{9/2}$ (Figure 6.47 on page 93 and Figure 6.48 on page 94) the ESA from $^4I_{13/2}$ and the ESA and ETU from $^4I_{11/2}$ have a combined effect of 520 rise time and 230 fall time as opposed to the natural decay of 14.6 μs. The rise curve shows ETU becoming more dominant as the population become large. On the fall, it has virtually no change of exponential characteristics indicating that this up-conversion mainly depends on ETU. For the state of $^4I_{9/2}$ (Figure 6.49 on page 94 and Figure 6.50 on page 95), ETU and ESA effects can be observed in both the rise and fall.

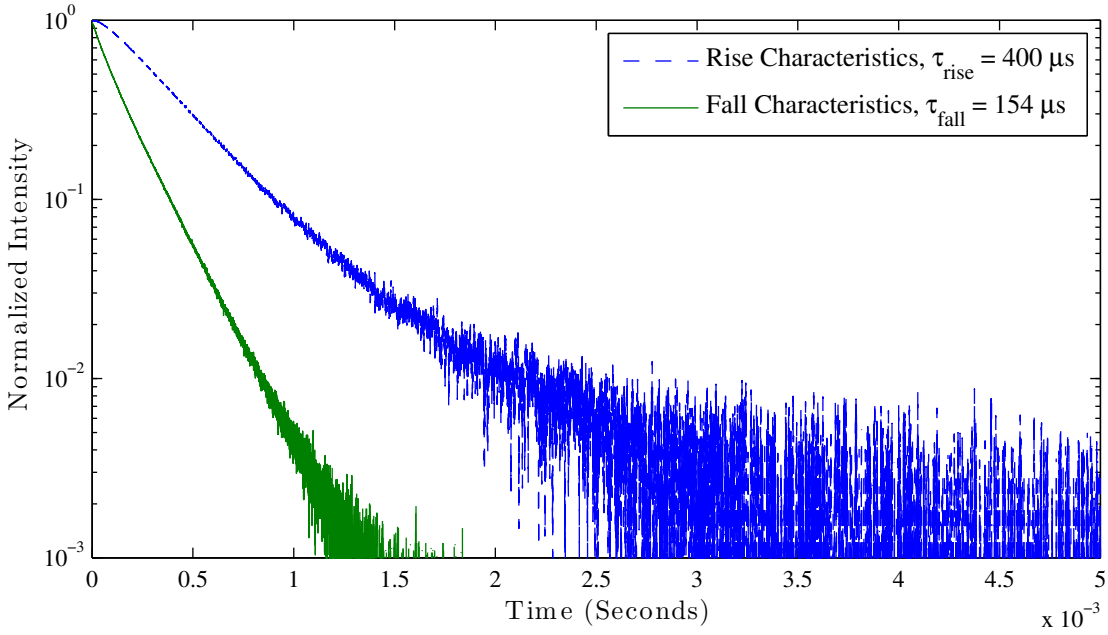

Figure 6.46: The dynamics of $^4S_{3/2}$ fluorescence intensity versus time for 25% Er:Y_2O_3 under 965 nm up to 10 kW/cm^2 intensity puming on semilog-y plot.

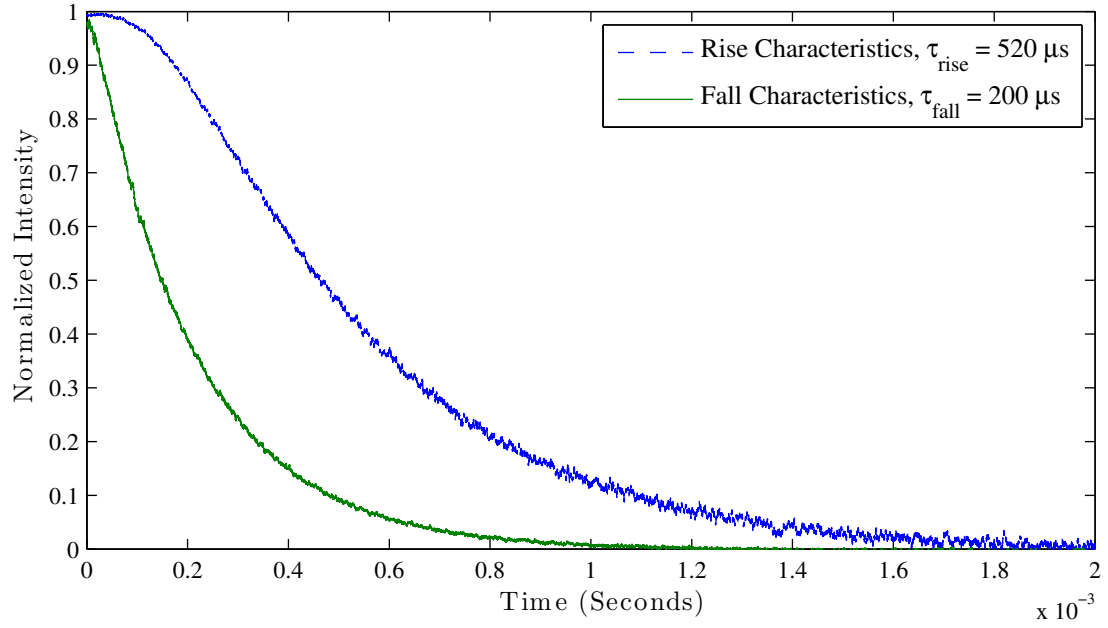

Figure 6.47: The dynamics of $^4F_{9/2}$ fluorescence intensity versus time for 25% Er:Y_2O_3 under 965 nm up to 10 kW/cm^2 intensity puming.

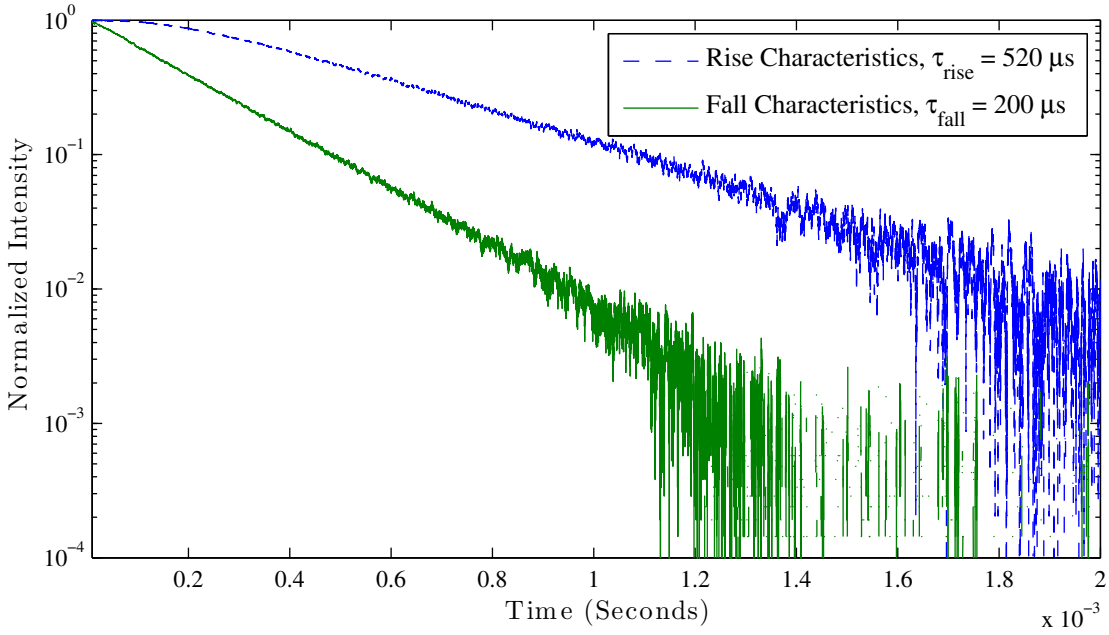

Figure 6.48: The dynamics of $^4F_{9/2}$ fluorescence intensity versus time for 25% Er:Y_2O_3 under 965 nm up to 10 kW/cm^2 intensity puming on semilog-y plot.

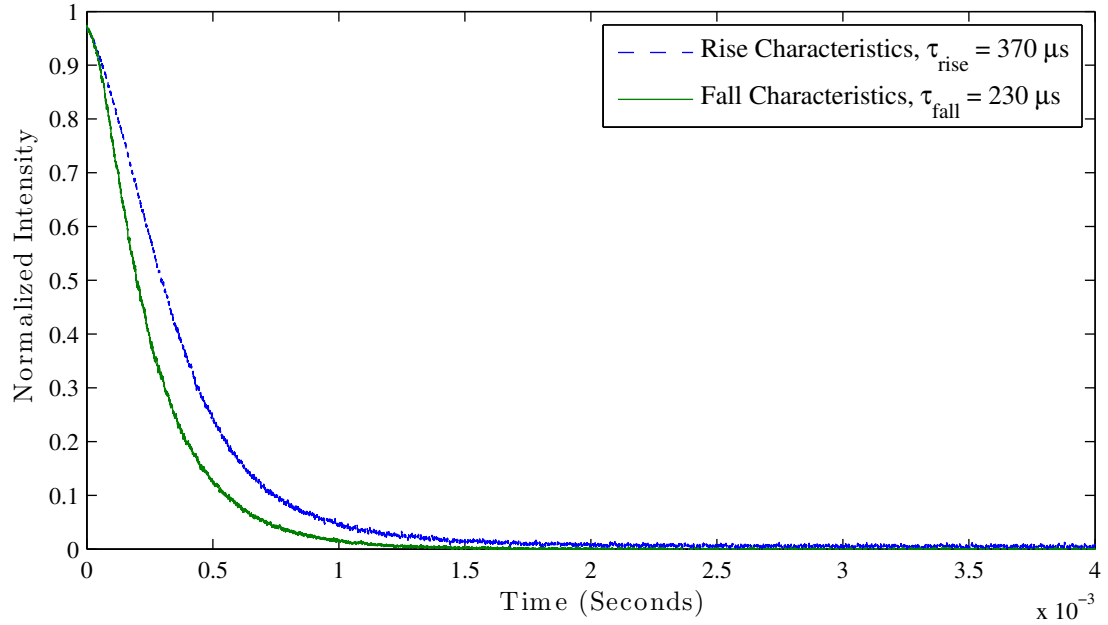

Figure 6.49: The dynamics of $^4I_{9/2}$ fluorescence intensity versus time for 25% Er:Y_2O_3 under 965 nm up to 10 kW/cm^2 intensity puming.

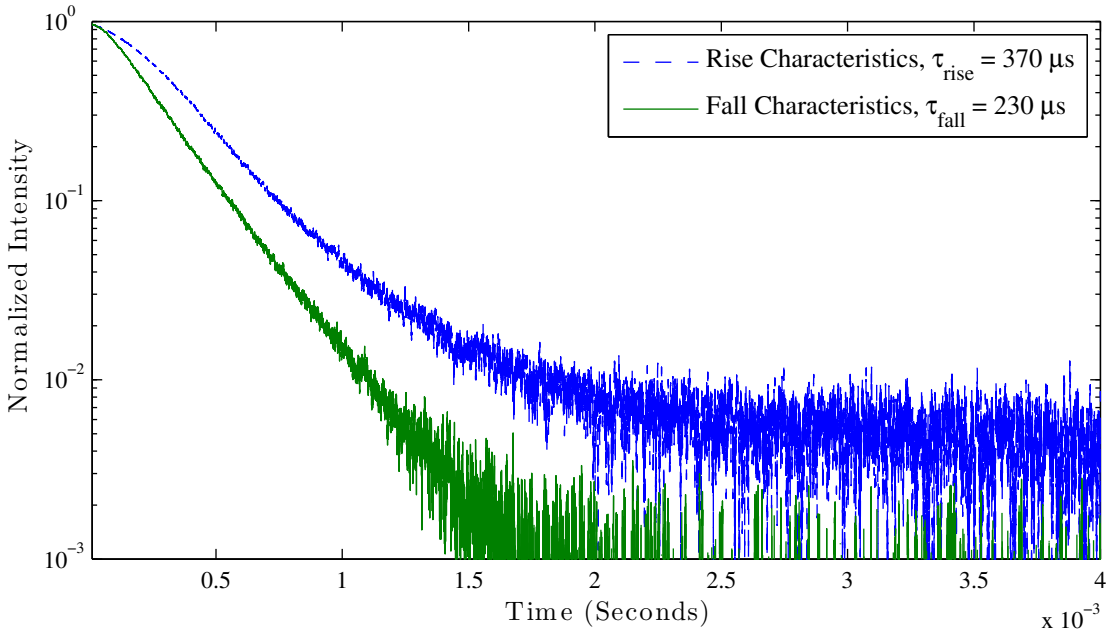

Figure 6.50: The dynamics of $^4I_{9/2}$ fluorescence intensity versus time for 25% Er:Y_2O_3 under 965 nm up to 10 kW/cm^2 intensity puming on semilog-y plot.

For the lower excited states, a low ESA coefficient is observed as the the rise and fall times are roughly the same for $^4I_{11/2}$ state (Figure 6.51 on page 96 and Figure 6.52 on page 96). The rise and fall life time are around 350 μs with natural decay at 295 μs, which is a 20% change in life time. Based on the changes in life time as well as the semilog-y plots of $^4I_{13/2}$ (Figure 6.53 on page 97 and Figure 6.54 on page 97), the ETU and ESA effects changed the rise time and fall time to 560 μs and 640 μs, respectively, from 770 μs natural decay time. This is a change of 27% and 17% for rise and fall, respectively.

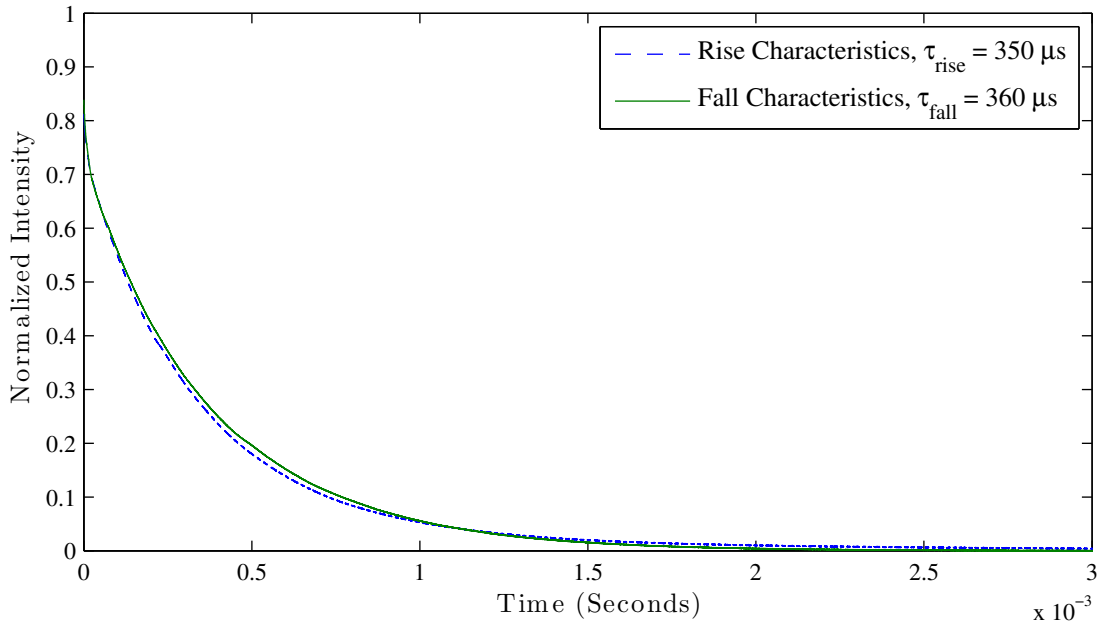

Figure 6.51: The dynamics of $^4I_{11/2}$ fluorescence intensity versus time for 25% Er:Y_2O_3 under 965 nm up to 10 kW/cm^2 intensity puming.

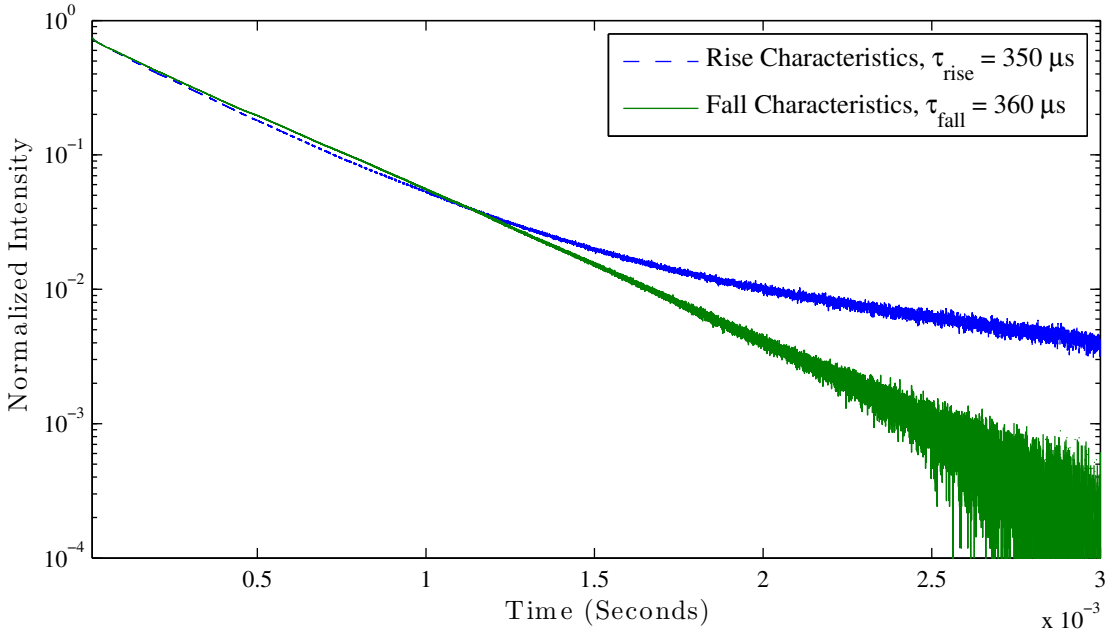

Figure 6.52: The dynamics of $^4I_{11/2}$ fluorescence intensity versus time for 25% Er:Y_2O_3 under 965 nm up to 10 kW/cm^2 intensity puming on semilog-y plot.

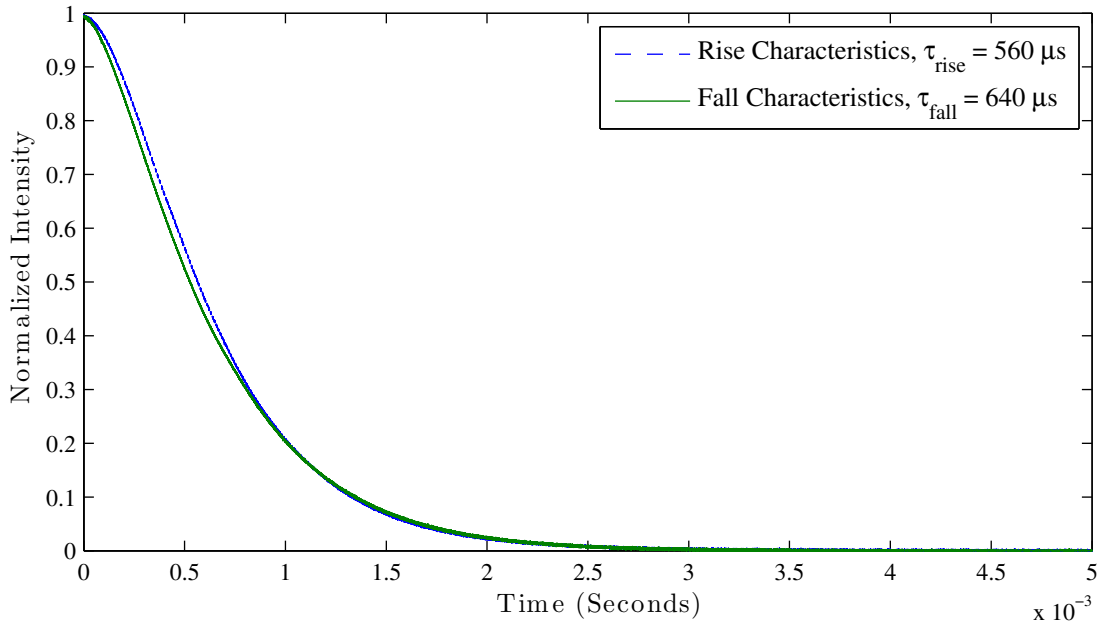

Figure 6.53: The dynamics of $^4I_{13/2}$ fluorescence intensity versus time for 25% Er:Y_2O_3 under 965 nm up to 10 kW/cm^2 intensity puming.

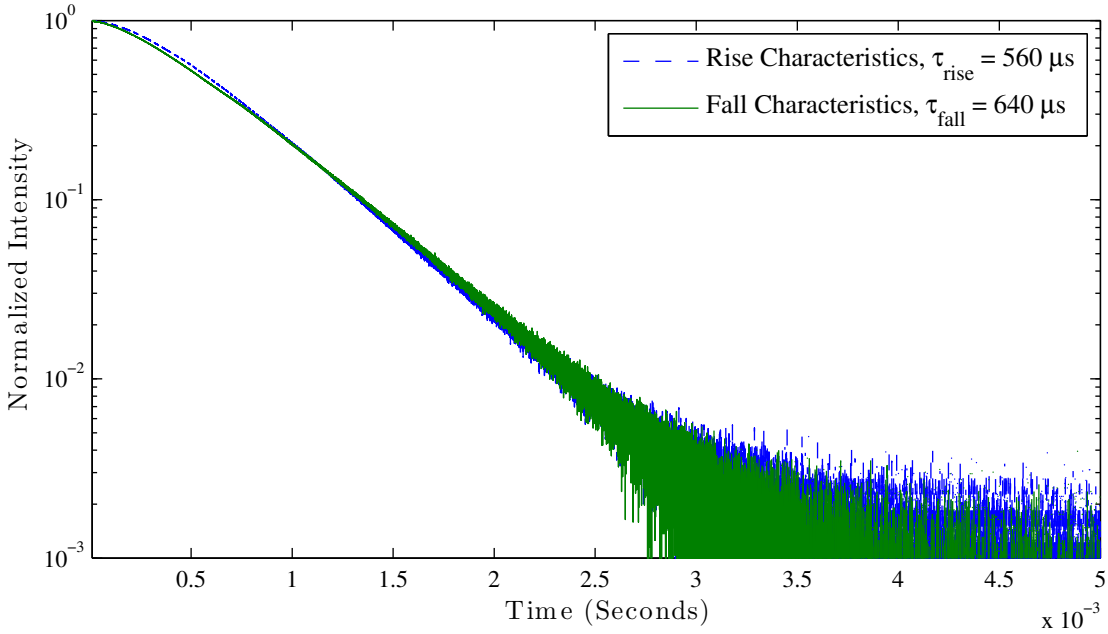

Figure 6.54: The dynamics of $^4I_{13/2}$ fluorescence intensity versus time for 25% Er:Y_2O_3 under 965 nm up to 10 kW/cm^2 intensity puming on semilog-y plot.

6.3.6 0.5% Er:YAG under 800 nm Pump

First of all, the pump at 800 nm is, unfortunately, ten times lower in intensity than what we have at 965 nm.For the 0.5% Er:YAG, the upper states above the pump state $^4I_{9/2}$ such as $^4S_{3/2}$ (Figure 6.55 on page 99 and Figure 6.56 on page 99) and $^4F_{9/2}$ (Figure 6.57 on page 100 and Figure 6.58 on page 100) all behave the same way with a rise time constant 5850 μs. On the fall, the time characteristics immediately returns to the natural decay of roughly 15 μs. For the pump state $^4I_{9/2}$ (Figure 6.59 on page 101 and Figure 6.60 on page 101), even under an intensity of 1 kW/cm^{-2} pumping into this state, which has a natural life time of sub-microseconds exhibits an additional rise time of 1000 μs, which has a connection with $^4I_{13/2}$. The $^4I_{11/2}$ (Figure 6.61 on page 102 and Figure 6.62 on page 102) is not affected by the pump at all. The $^4I_{13/2}$ (Figure 6.57 on page 100 and Figure 6.58 on page 100) is not affected by the pump either; however, this is the lower bound. Furthermore, because the pump power distribution, the fluorescence may be masked by the large area of the section of the pump that is not concentrated enough. It is suspected that the actual time should be closer to that of rise time in the $^4S_{3/2}$ and $^4F_{9/2}$ as they have a time of half of the pump.

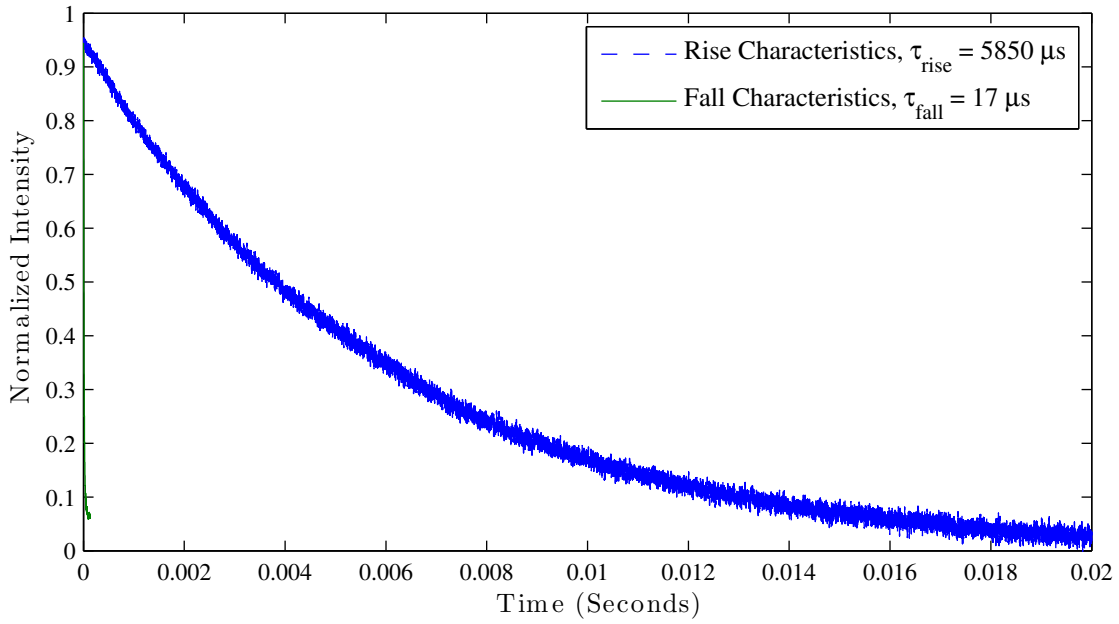

Figure 6.55: The dynamics of $^4S_{3/2}$ fluorescence intensity versus time for 0.5% Er:YAG under 800 nm up to 1 kW/cm^2 intensity puming on linear plot.

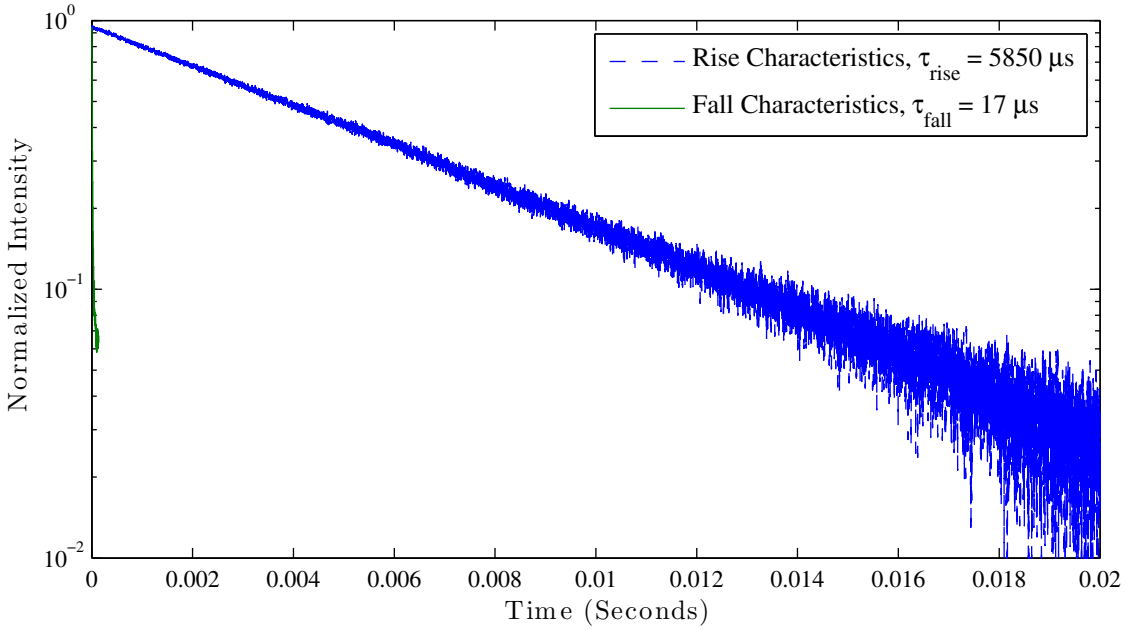

Figure 6.56: The dynamics of $^4S_{3/2}$ fluorescence intensity versus time for 0.5% Er:YAG under 800 nm up to 1 kW/cm^2 intensity puming on semilog-y plot.

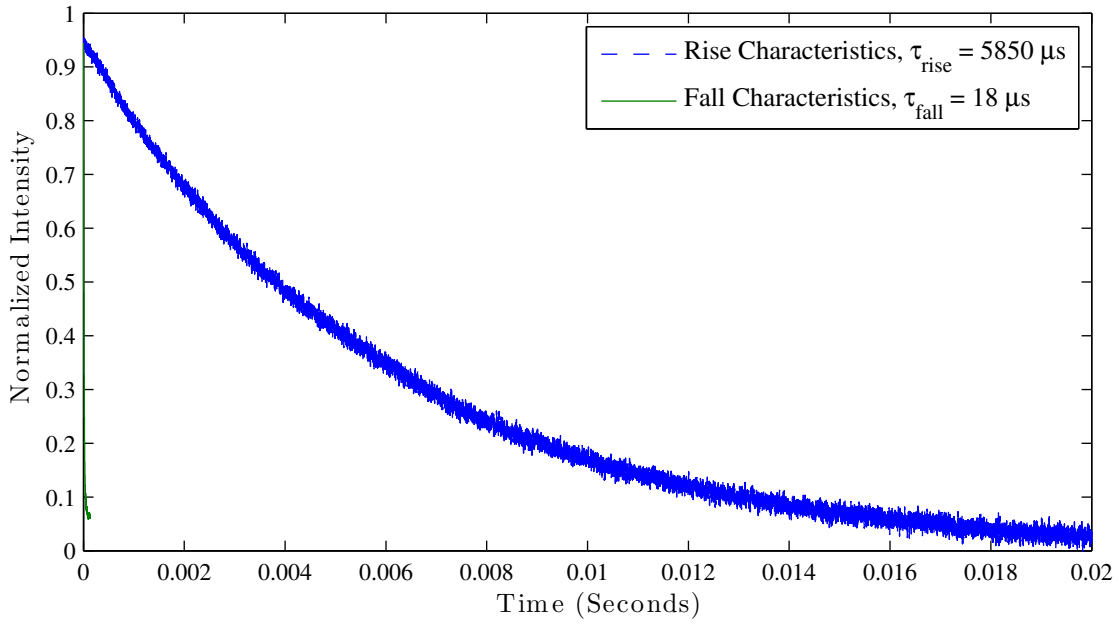

Figure 6.57: The dynamics of $^4F_{9/2}$ fluorescence intensity versus time for 0.5% Er:YAG under 800 nm up to 1 kW/cm^2 intensity puming.

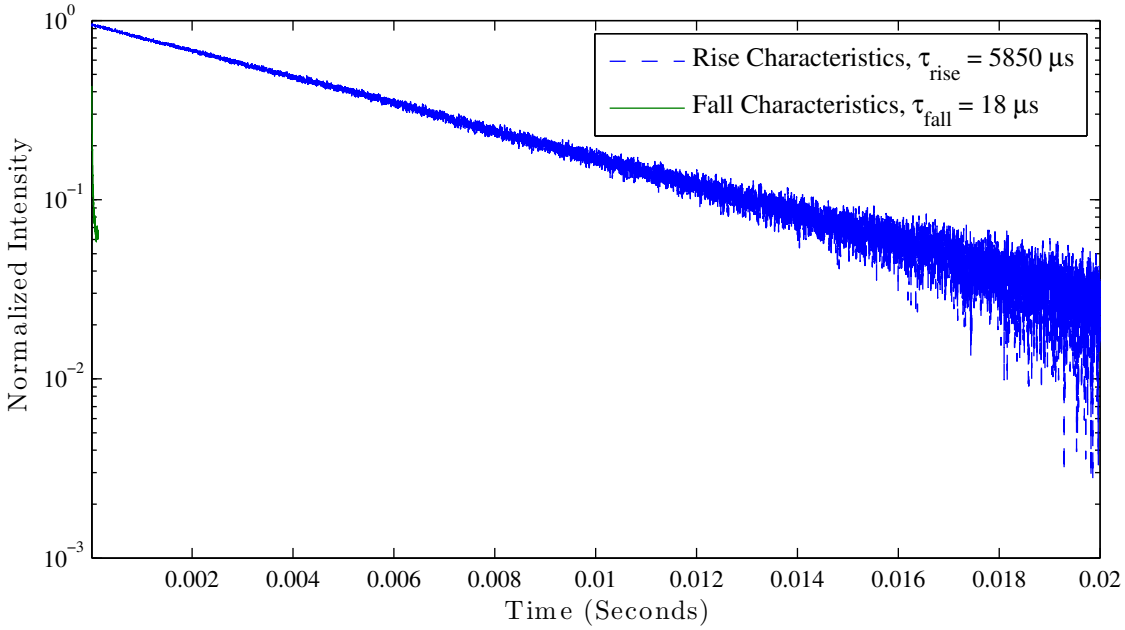

Figure 6.58: The dynamics of $^4F_{9/2}$ fluorescence intensity versus time for 0.5% Er:YAG under 800 nm up to 1 kW/cm^2 intensity puming on semilog-y plot.

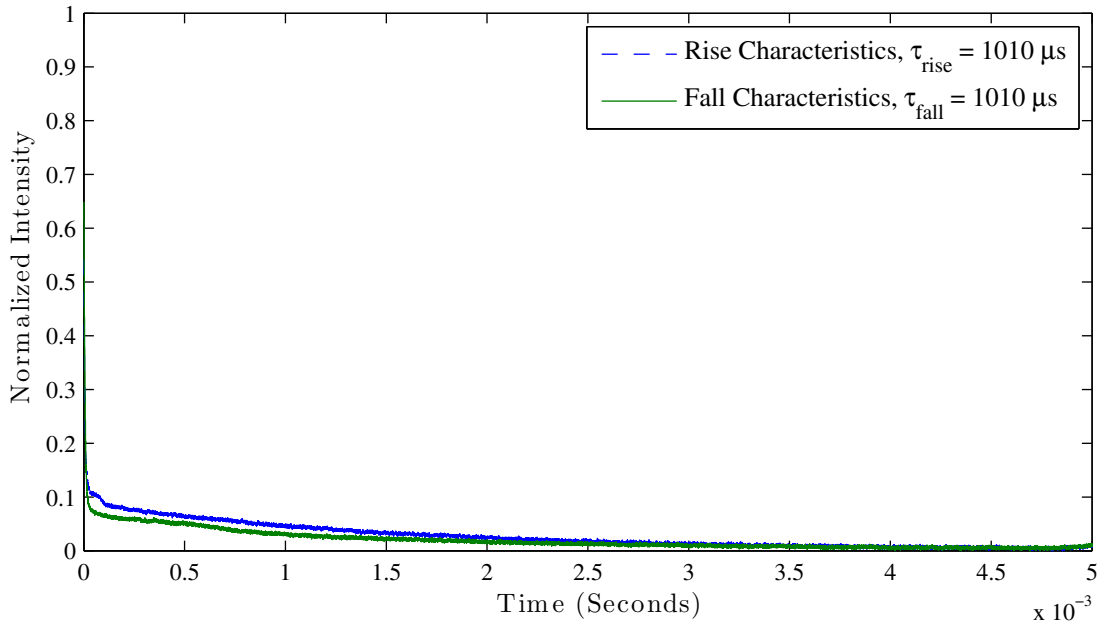

Figure 6.59: The dynamics of $^4I_{9/2}$ fluorescence intensity versus time for 0.5% Er:YAG under 800 nm up to 1 kW/cm^2 intensity puming.

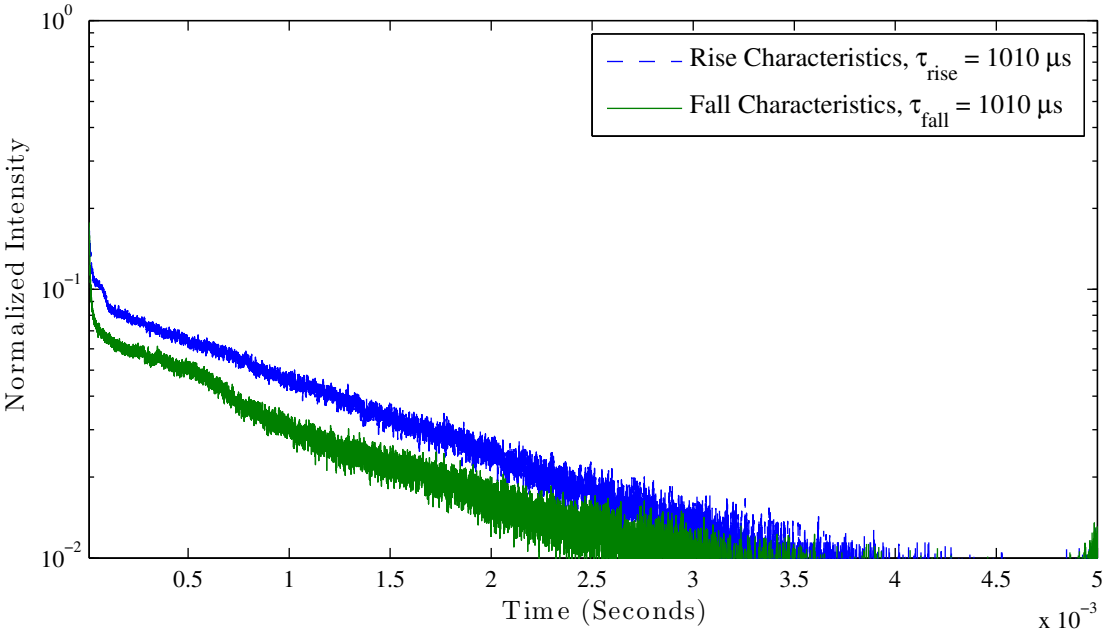

Figure 6.60: The dynamics of $^4I_{9/2}$ fluorescence intensity versus time for 0.5% Er:YAG under 800 nm up to 1 kW/cm^2 intensity puming on semilog-y plot.

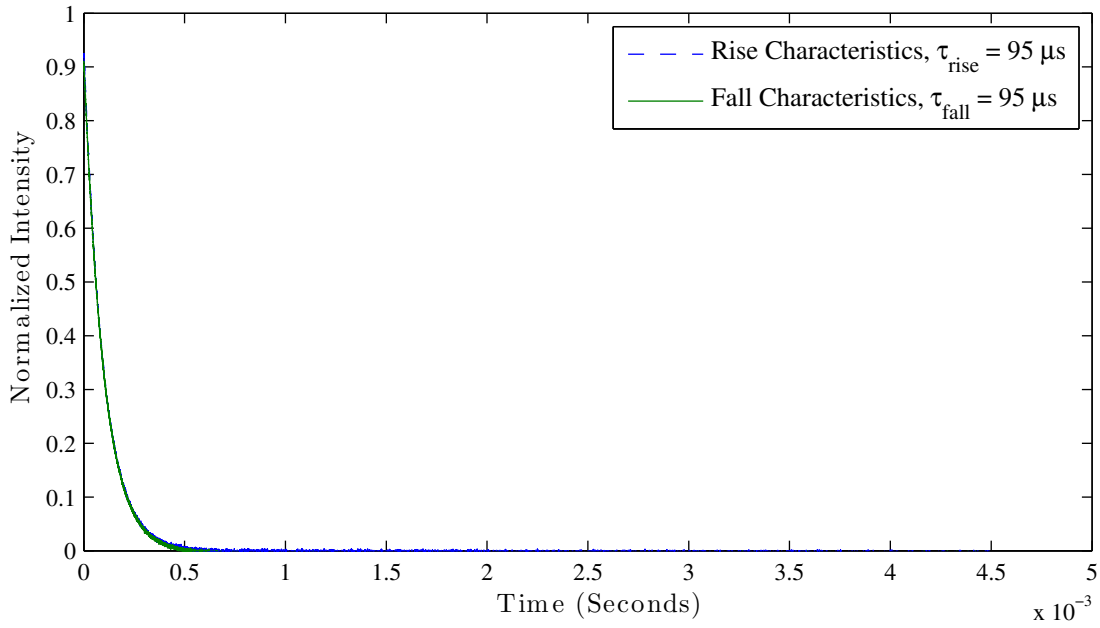

Figure 6.61: The dynamics of $^4I_{11/2}$ fluorescence intensity versus time for 0.5% Er:YAG under 800 nm up to 1 kW/cm^2 intensity puming.

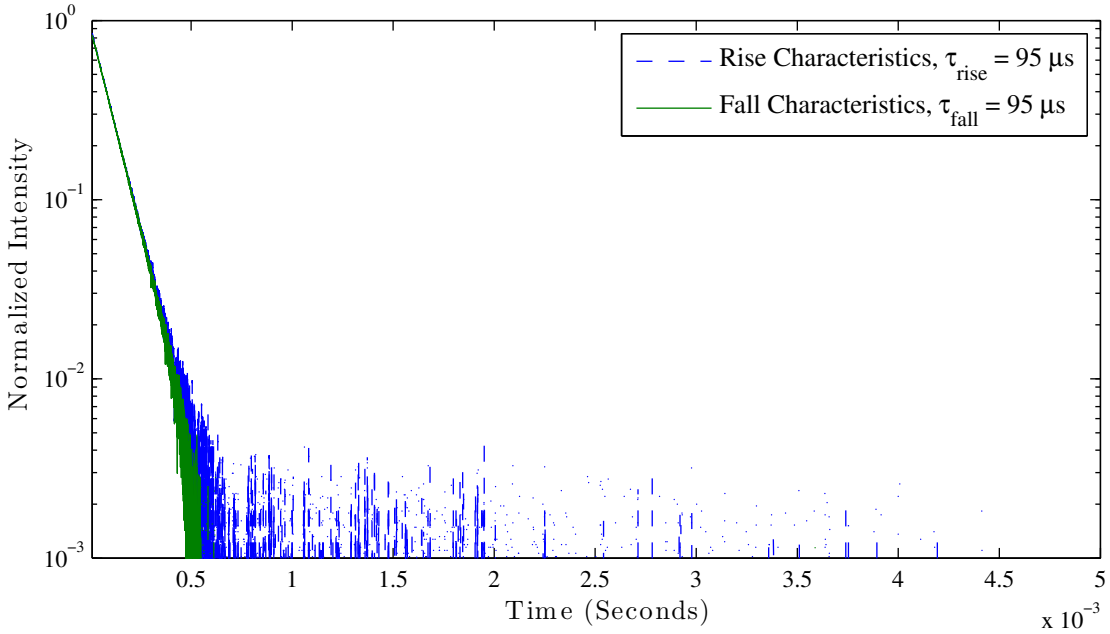

Figure 6.62: The dynamics of $^4I_{11/2}$ fluorescence intensity versus time for 0.5% Er:YAG under 800 nm up to 1 kW/cm^2 intensity puming on semilog-y plot.

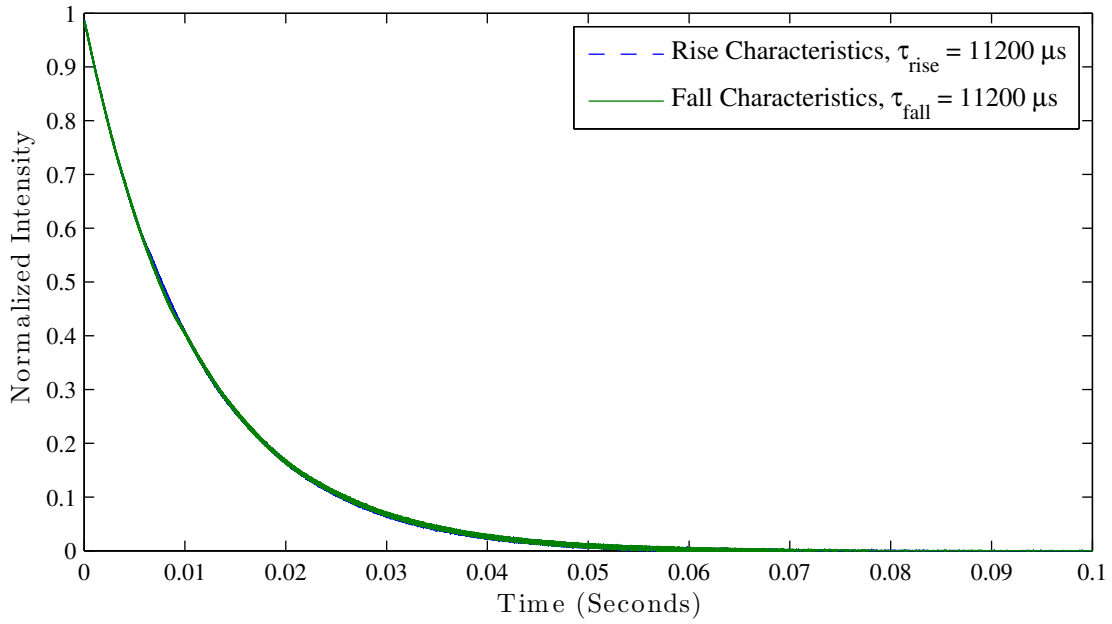

Figure 6.63: The dynamics of $^4I_{13/2}$ fluorescence intensity versus time for 0.5% Er:YAG under 800 nm up to 1 kW/cm^2 intensity puming.

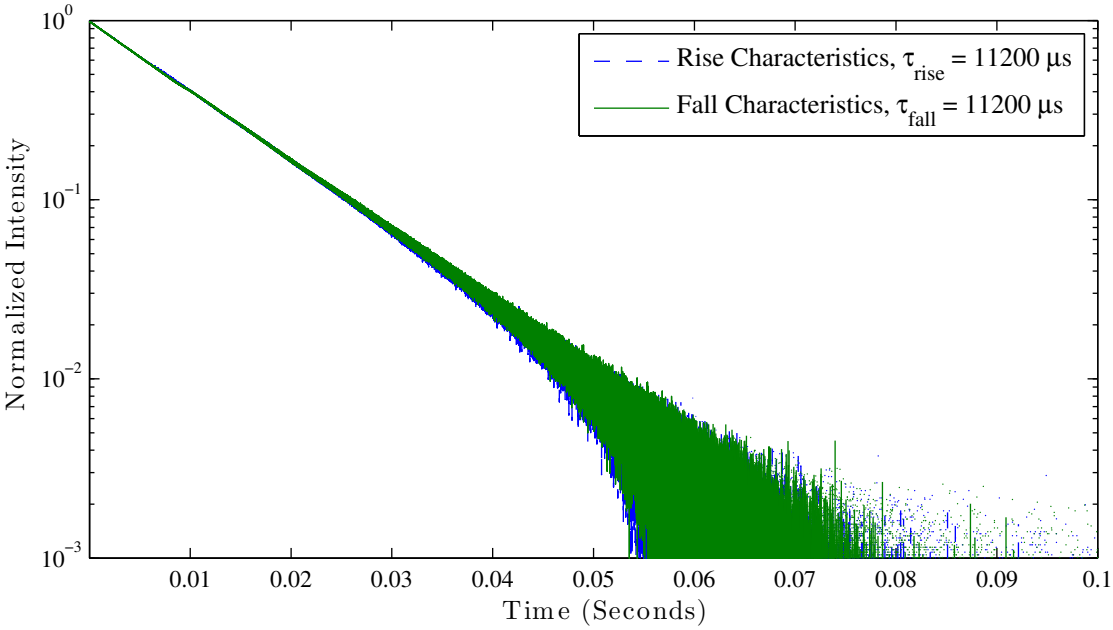

Figure 6.64: The dynamics of $^4I_{13/2}$ fluorescence intensity versus time for 0.5% Er:YAG under 800 nm up to 1 kW/cm^2 intensity puming on semilog-y plot.

6.3.7 50% Er:YAG under 800 nm Pump

For 50% Er:YAG, the $^4S_{3/2}$ level reflects mainly the ESA from $^4I_{13/2}$ leaving it with 505 μs on the rise time characteristics. The natural life time for this state is sub-microseconds. The fall time reflects the fall time of $^4I_{11/2}$ (Figure 6.65 on page 105 and Figure 6.66 on page 105) or roughly half of that as discussed in Equation 6.5. For the state $^4F_{9/2}$ (Figure 6.67 on page 106 and Figure 6.68 on page 106), the rise time is roughly also the same as $^4S_{3/2}$ at 545 μs reflecting the rise time of $^4I_{13/2}$. The natural decay or life time for this state is also sub-microseconds. The fall time is much longer than $^4S_{3/2}$ by almost two times at 160 μs. This indicates that there is some up-conversion from the $^4I_{13/2}$ and possibly some cooperative effects between $^4I_{11/2}$ and $^4I_{13/2}$. The $^4I_{9/2}$ (Figure 6.69 on page 107 and Figure 6.70 on page 107) even though it is the pump state, but it still exhibits an addition up-conversion observable in addition to the pump with a rise time of 640 μs. The decay or fall exhibit up-conversion primarily coming from the $^4I_{13/2}$ as well as $^4I_{11/2}$'s effects propagated down through $^4S_{3/2}$ onto $^4I_{9/2}$. The lower excited state of $^4I_{11/2}$ exhibits a strong response to $^4_{I13/2}$'s ESA from 800 nm as well as ETU coming from the $^4I_{13/2}$ that at a ten times lower intensity of a pump in comparison to the 965 nm pump the state's rise time increased to 290 μs from 95 μs. This is not a fair comparison; however, the strong conversion shows that it is worth further investigation, which is to be discussed in conclusions for future work. The fall time is 190 μs, which is 40 μslonger than the fall time under 965 nm pump. For $^4I_{13/2}$, even though the rise and the fall are 880 μs and 1180 μs, respectively, which is a much smaller effect in comparison to the results from $^4I_{13/2}$, the fall is expected to be small as the pump is much weaker than the 965 nm pump. However, unlike 965 nm pump case, it is done without a pinhole sitting in the front. This is still much lower than the actual effects. As the rise time of the upper excited states above the pump level of 550 μs indicates, the rise time should be around 550 μs.

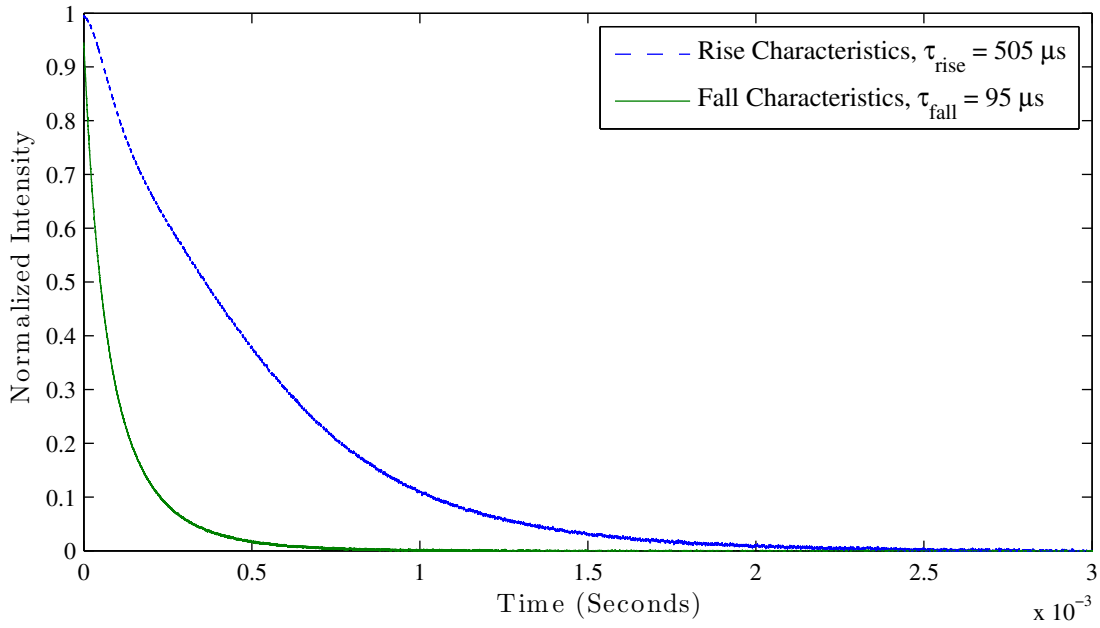

Figure 6.65: The dynamics of $^4S_{3/2}$ fluorescence intensity versus time for 50% Er:YAG under 800 nm up to 1 kW/cm^2 intensity puming on linear plot.

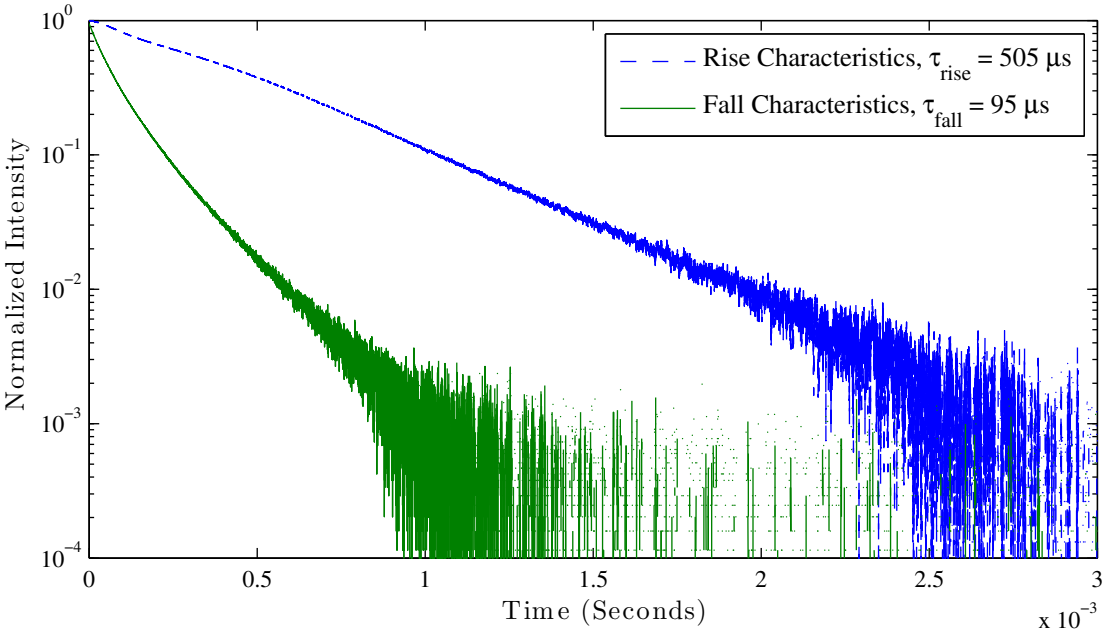

Figure 6.66: The dynamics of $^4S_{3/2}$ fluorescence intensity versus time for 50% Er:YAG under 800 nm up to 1 kW/cm^2 intensity puming on semilog-y plot.

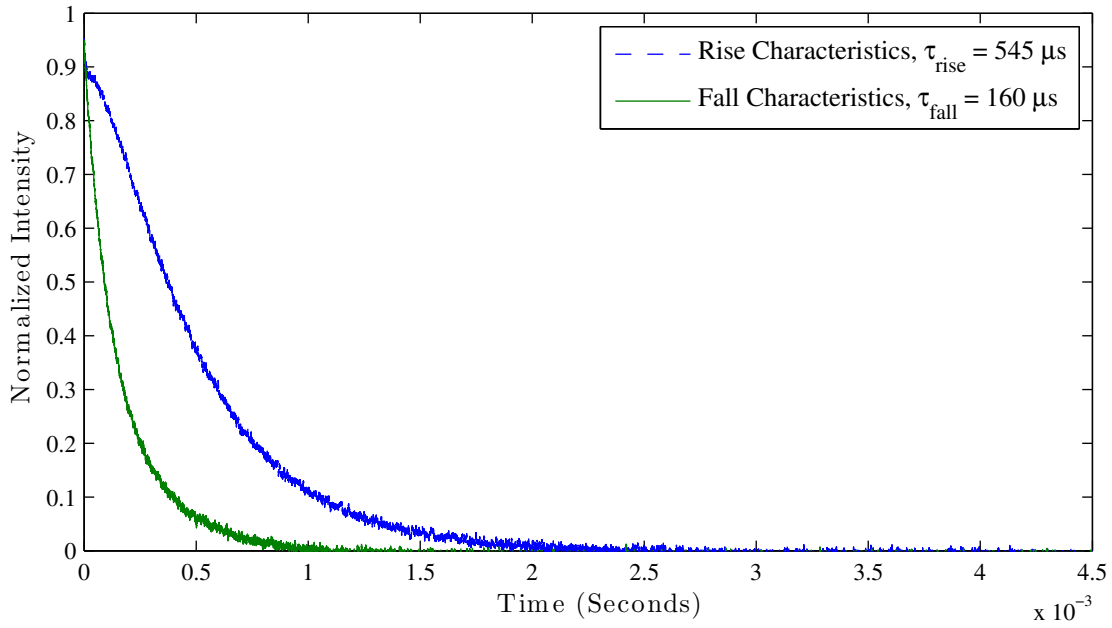

Figure 6.67: The dynamics of $^4F_{9/2}$ fluorescence intensity versus time for 50% Er:YAG under 800 nm up to 1 kW/cm^2 intensity puming.

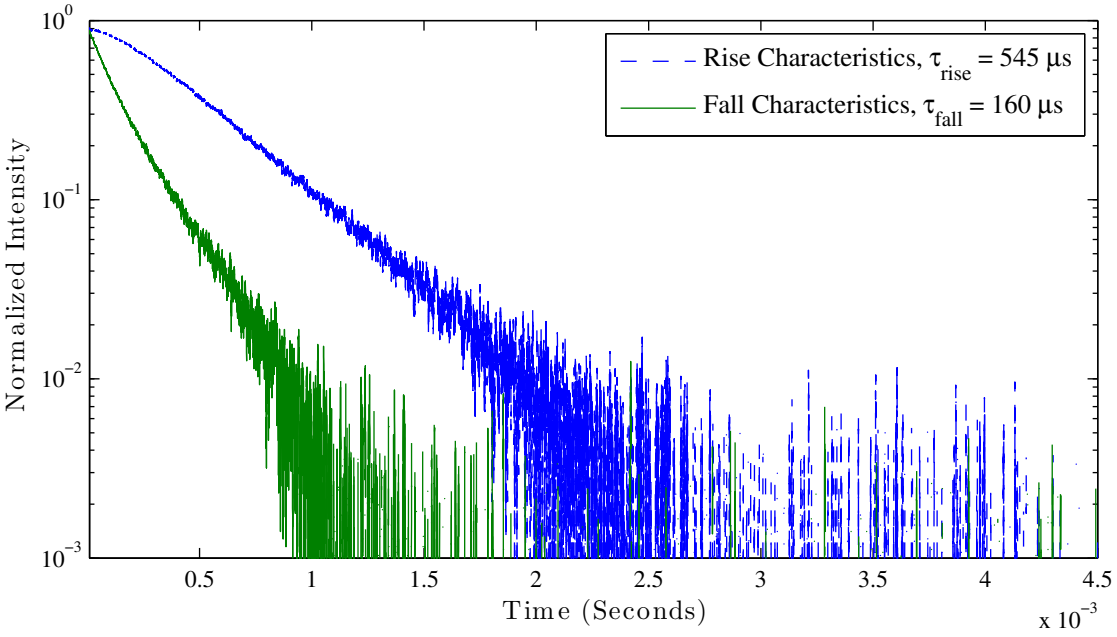

Figure 6.68: The dynamics of $^4F_{9/2}$ fluorescence intensity versus time for 50% Er:YAG under 800 nm up to 1 kW/cm^2 intensity puming on semilog-y plot.

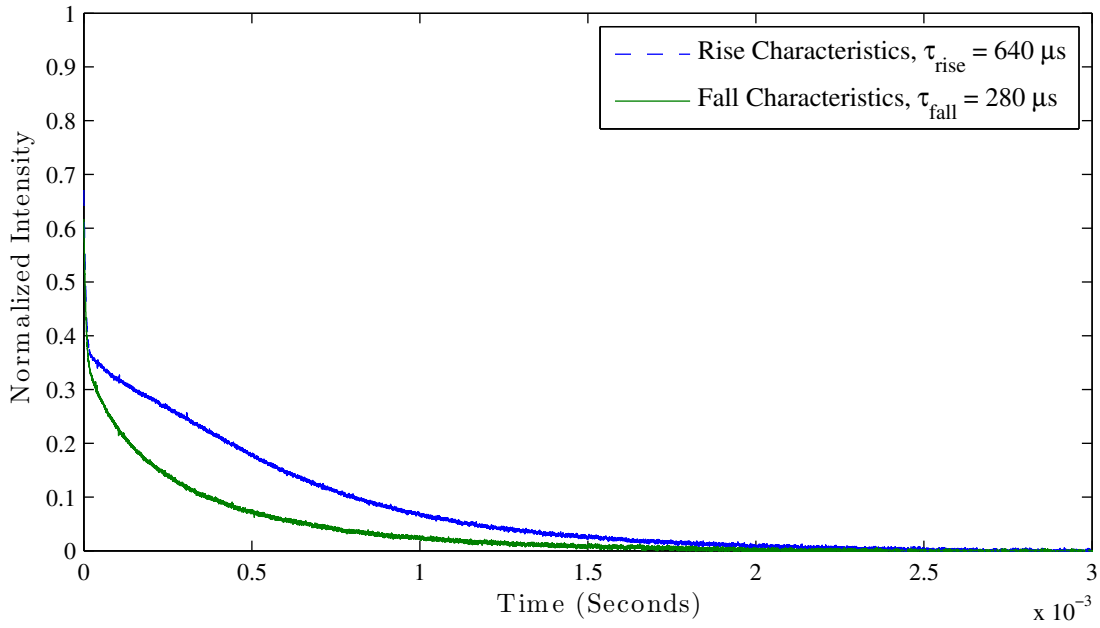

Figure 6.69: The dynamics of $^4I_{9/2}$ fluorescence intensity versus time for 50% Er:YAG under 800 nm up to 1 kW/cm^2 intensity puming.

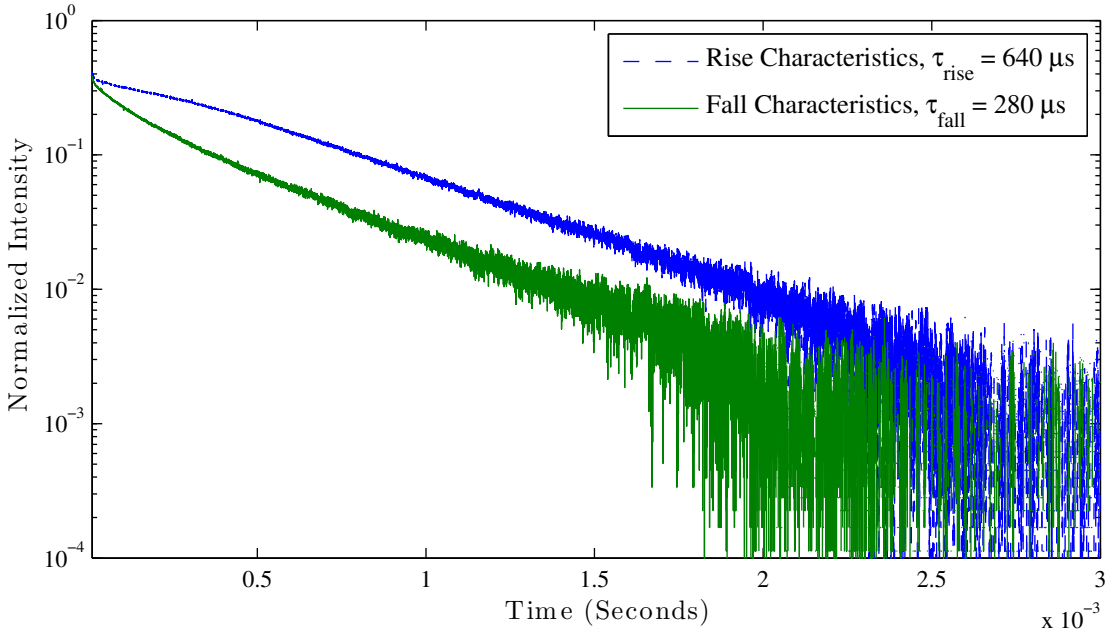

Figure 6.70: The dynamics of $^4I_{9/2}$ fluorescence intensity versus time for 50% Er:YAG under 800 nm up to 1 kW/cm^2 intensity puming on semilog-y plot.

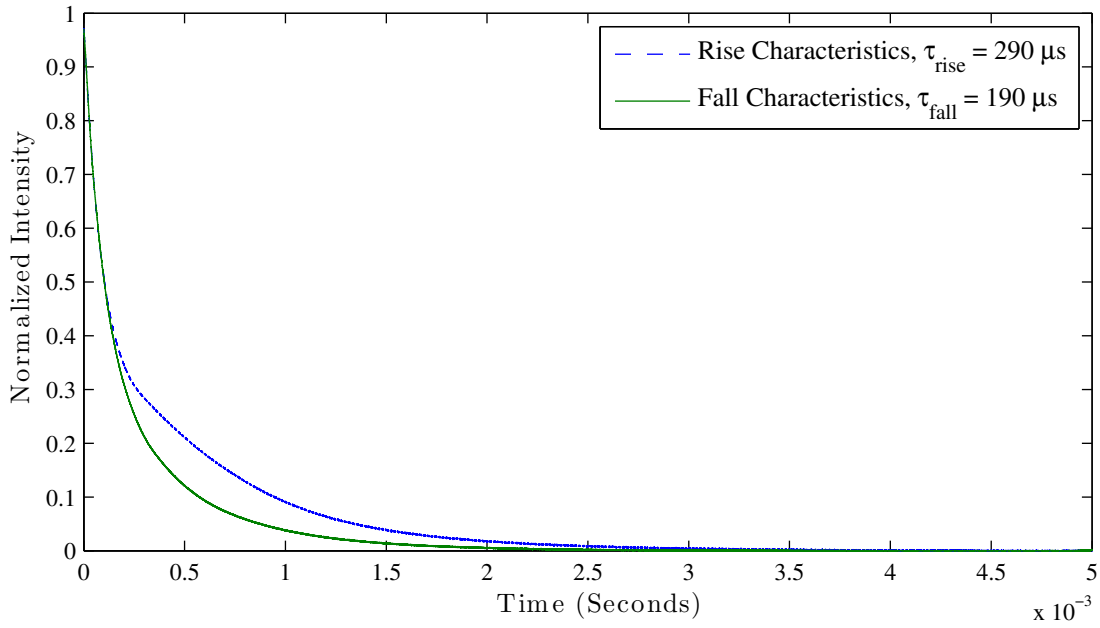

Figure 6.71: The dynamics of $^4I_{11/2}$ fluorescence intensity versus time for 50% Er:YAG under 800 nm up to 1 kW/cm^2 intensity puming.

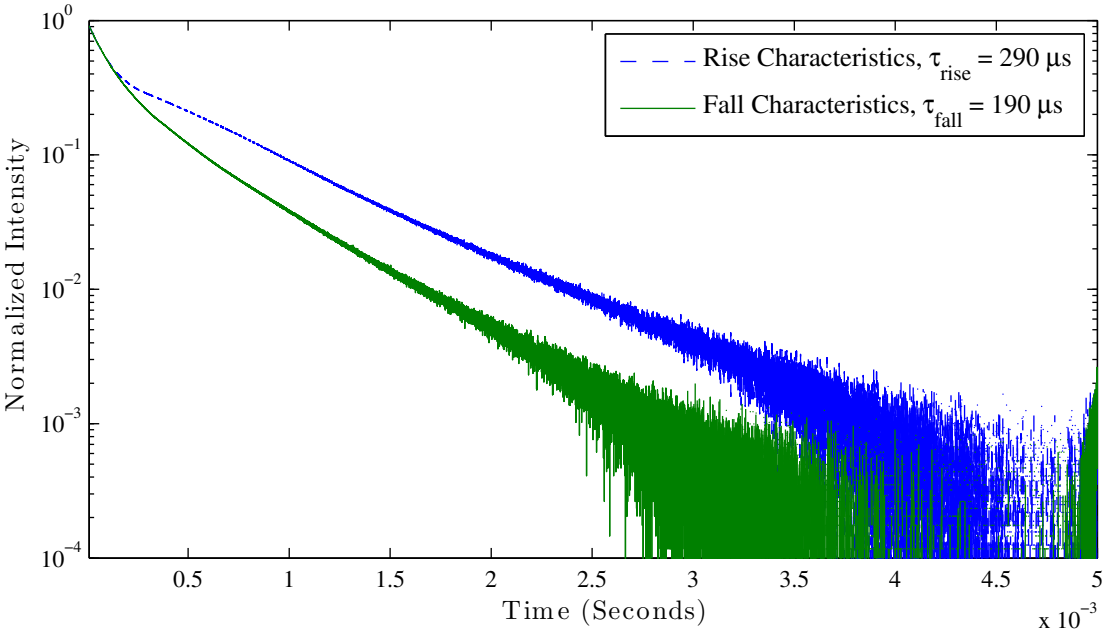

Figure 6.72: The dynamics of $^4I_{11/2}$ fluorescence intensity versus time for 50% Er:YAG under 800 nm up to 1 kW/cm^2 intensity puming on semilog-y plot.

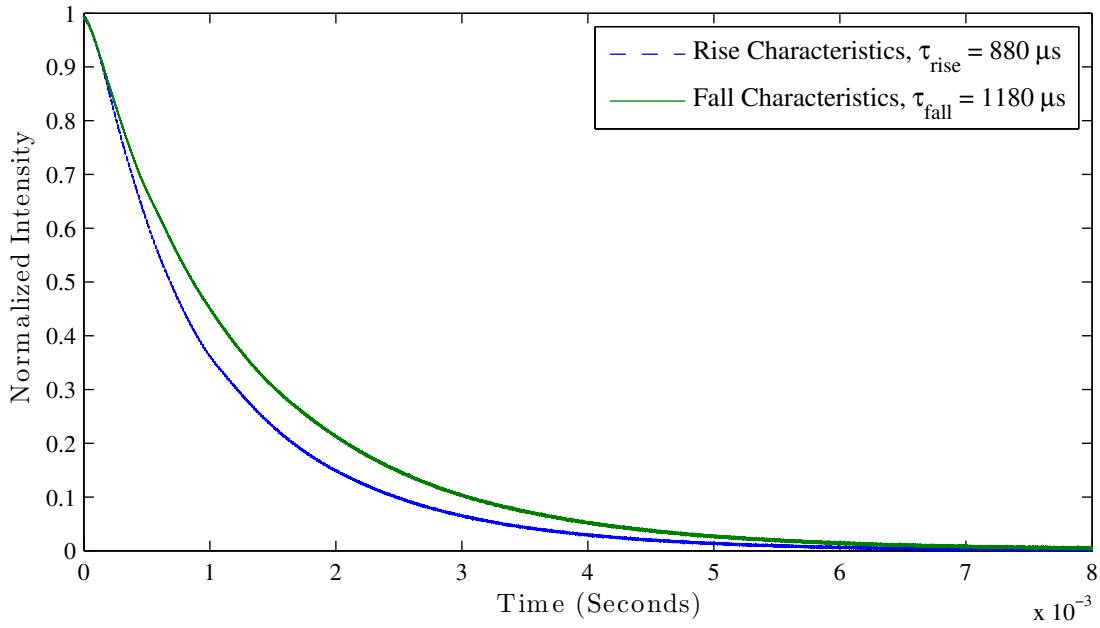

Figure 6.73: The dynamics of $^4I_{13/2}$ fluorescence intensity versus time for 50% Er:YAG under 800 nm up to 1 kW/cm^2 intensity puming.

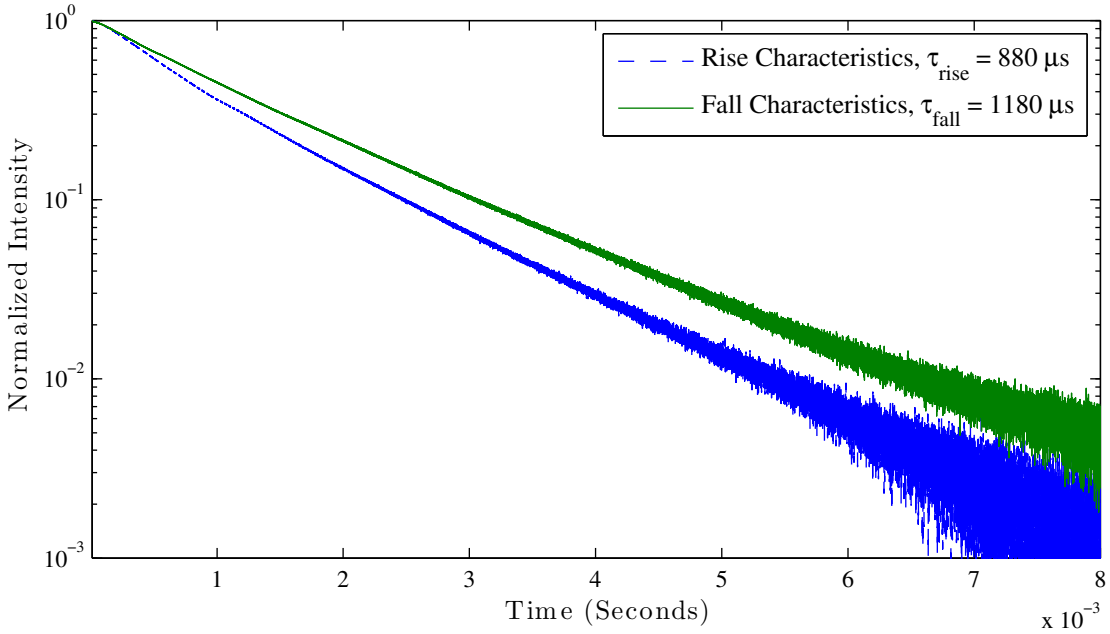

Figure 6.74: The dynamics of $^4I_{13/2}$ fluorescence intensity versus time for 50% Er:YAG under 800 nm up to 1 kW/cm^2 intensity puming on semilog-y plot.

6.3.8 1% Er:Yttria under 800 nm Pump

The state $^4S_{3/2}$ (Figure 6.75 on page 110 and Figure 6.76 on page 111) rise time reflects that of $^4I_{13/2}$ at 5550 μsThe fall reflects that of ETU up-conversion coming from $^4I_{11/2}$, which is roughly half of $^4I_{11/2}$'s decay time at 1150. The natural life time for the state is 87 μs.

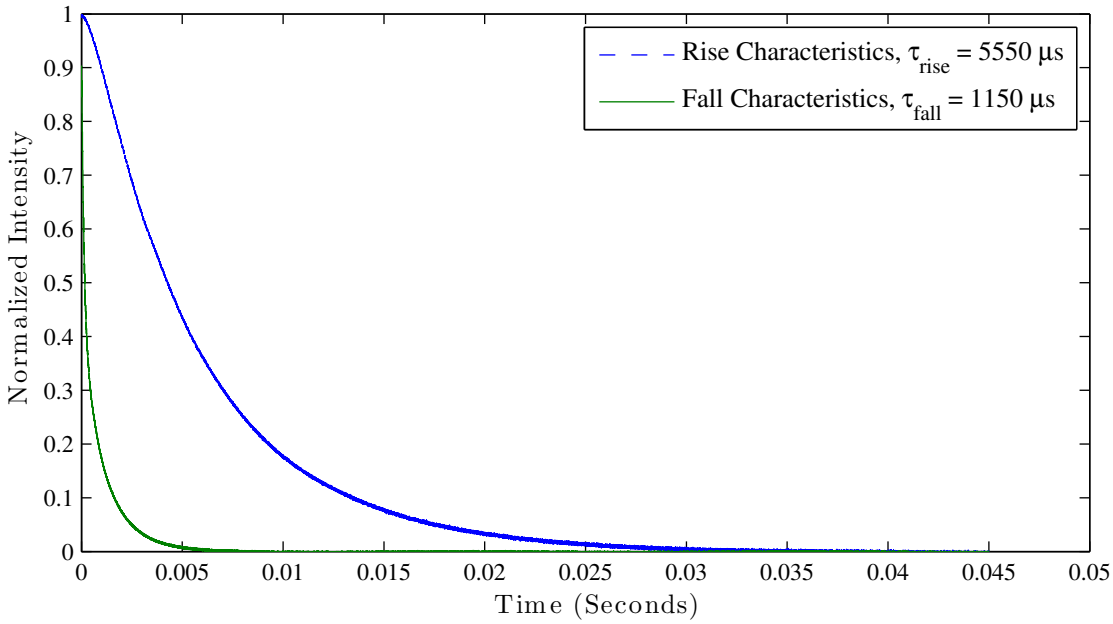

Figure 6.75: The dynamics of $^4S_{3/2}$ fluorescence intensity versus time for 1% Er:Y_2O_3 under 800 nm up to 1 kW/cm^2 intensity puming on linear plot.

The state $^4F_{9/2}$ (Figure 6.77 on page 111 and Figure 6.78 on page 112) shows a much longer life time coming in comparison to $^4S_{3/2}$ at 7400 μs. This suggests perhaps additional energy paths from the standard path assumption, such as cross ETU between $^4I_{11/2}$ and $^4I_{13/2}$. The fall too exhibit a longer time characteristics, which would also be resolved by this suggested path.

The state $^4I_{9/2}$ (Figure 6.79 on page 113 and Figure 6.80 on page 113) quickly reaches the first steady state point as its natural life time is extremely short (87 μs). As the state $^4I_{13/2}$ populates, a second slow rise takes over with a rise time of 5350 μssimilar to that of $^4S_{3/2}$. The fall is is much shorter simply due to the fact that the $^4S_{3/2}$ drops really quickly

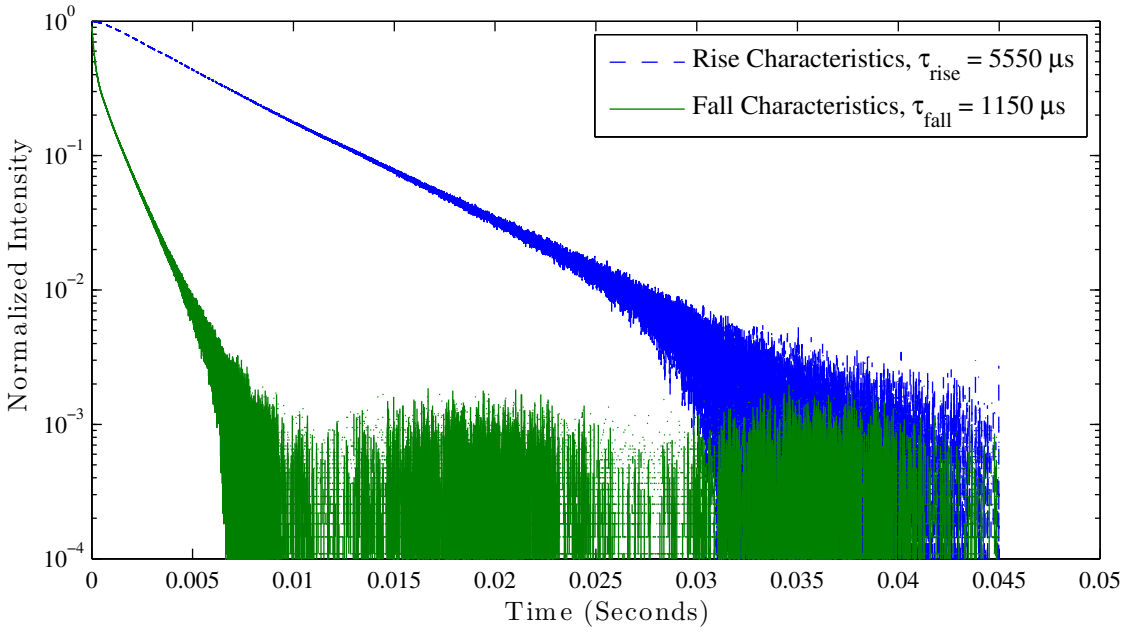

Figure 6.76: The dynamics of $^4S_{3/2}$ fluorescence intensity versus time for 1% Er:Y_2O_3 under 800 nm up to 1 kW/cm^2 intensity puming on semilog-y plot.

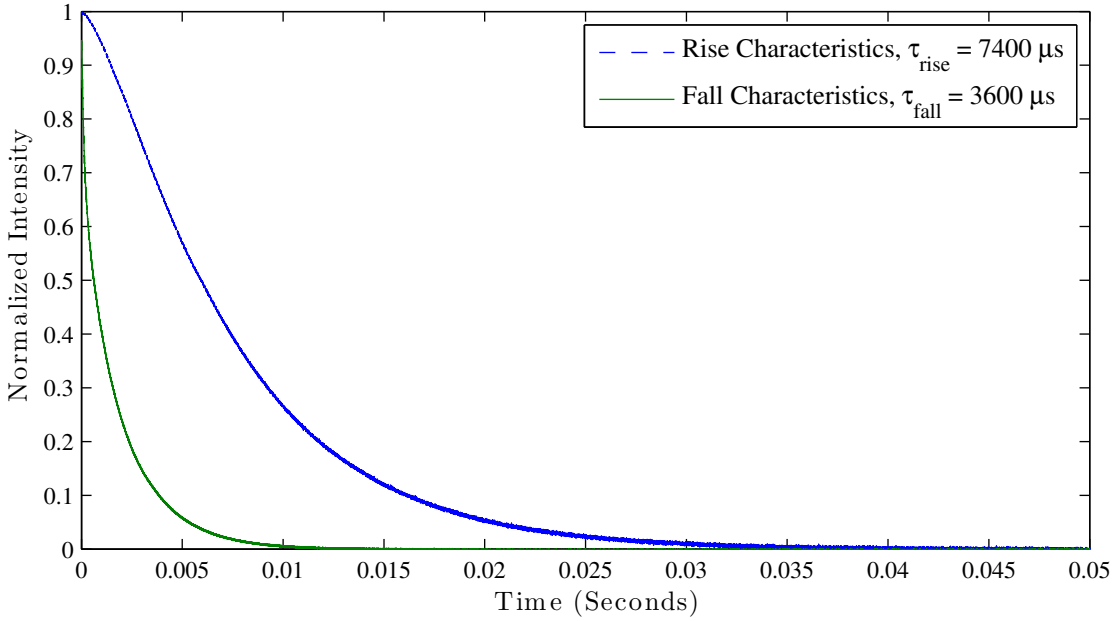

Figure 6.77: The dynamics of $^4F_{9/2}$ fluorescence intensity versus time for 1% Er:Y_2O_3 under 800 nm up to 1 kW/cm^2 intensity puming.

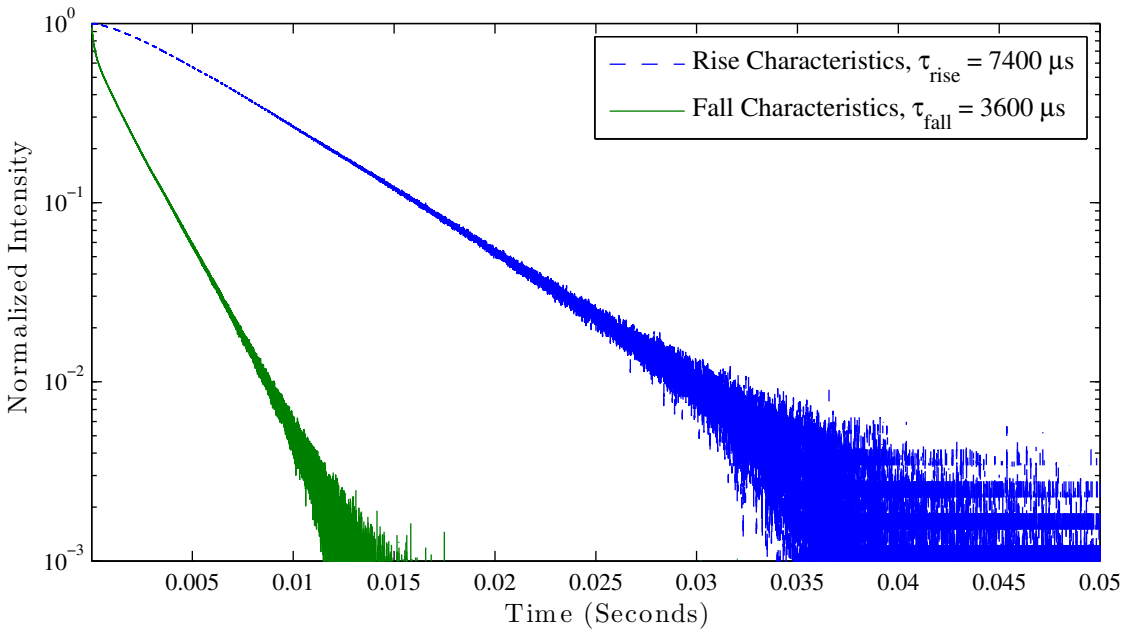

Figure 6.78: The dynamics of $^4F_{9/2}$ fluorescence intensity versus time for 1% Er:Y_2O_3 under 800 nm up to 1 kW/cm^2 intensity puming on semilog-y plot.

and the pump stopped feeding into this state. The up-conversion ETU from $^4I_{13/2}$ and the continued source feeding from $^4S_{3/2}$ does not become dominant until towards the end.

The lower excited state $^4I_{11/2}$ (Figure 6.81 on page 114 and Figure 6.82 on page 114) did not exhibited life time changes. The $^4I_{13/2}$ (Figure 6.83 on page 115 and Figure 6.84 on page 115) rise and fall experienced a change of 8% on the rise and 4% on the fall.

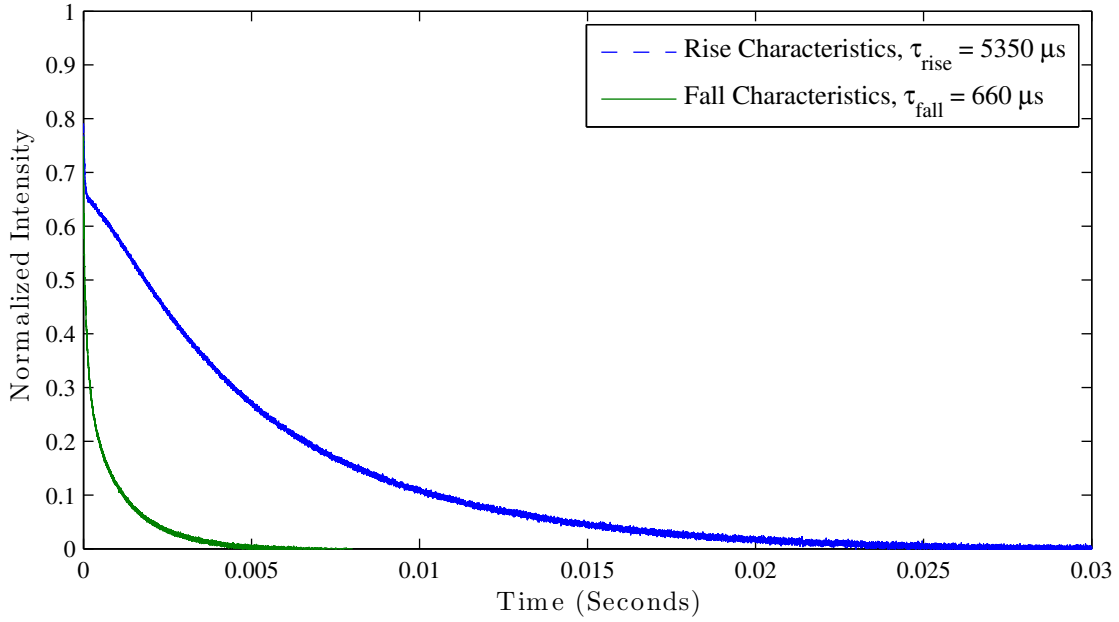

Figure 6.79: The dynamics of $^4I_{9/2}$ fluorescence intensity versus time for 1% Er:Y_2O_3 under 800 nm up to 1 kW/cm^2 intensity puming.

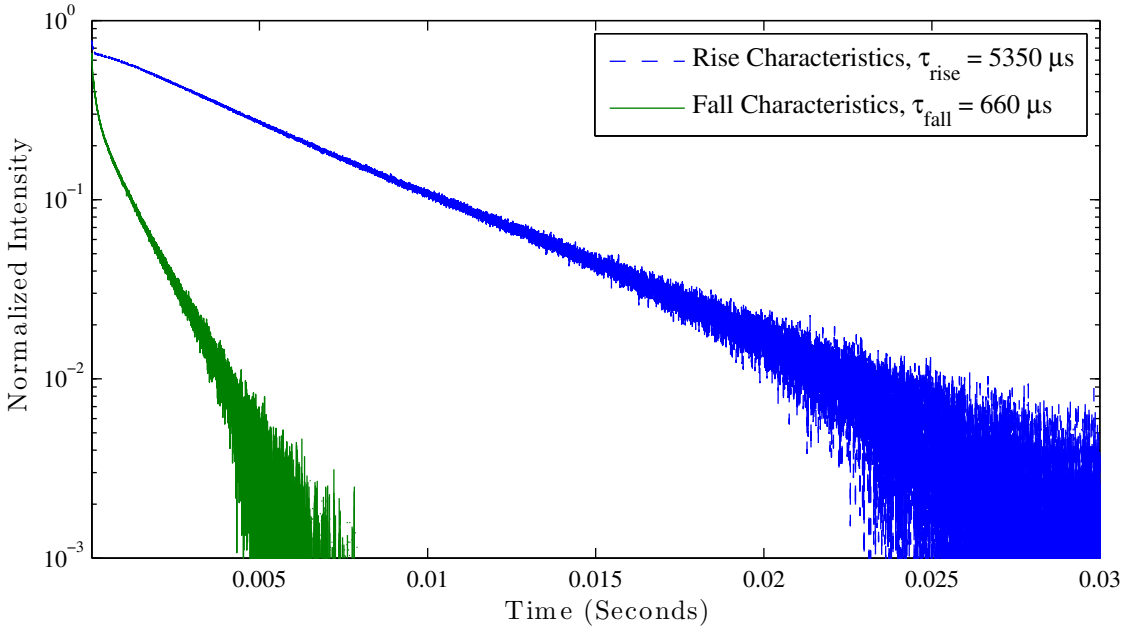

Figure 6.80: The dynamics of $^4I_{9/2}$ fluorescence intensity versus time for 1% Er:Y_2O_3 under 800 nm up to 1 kW/cm^2 intensity puming on semilog-y plot.

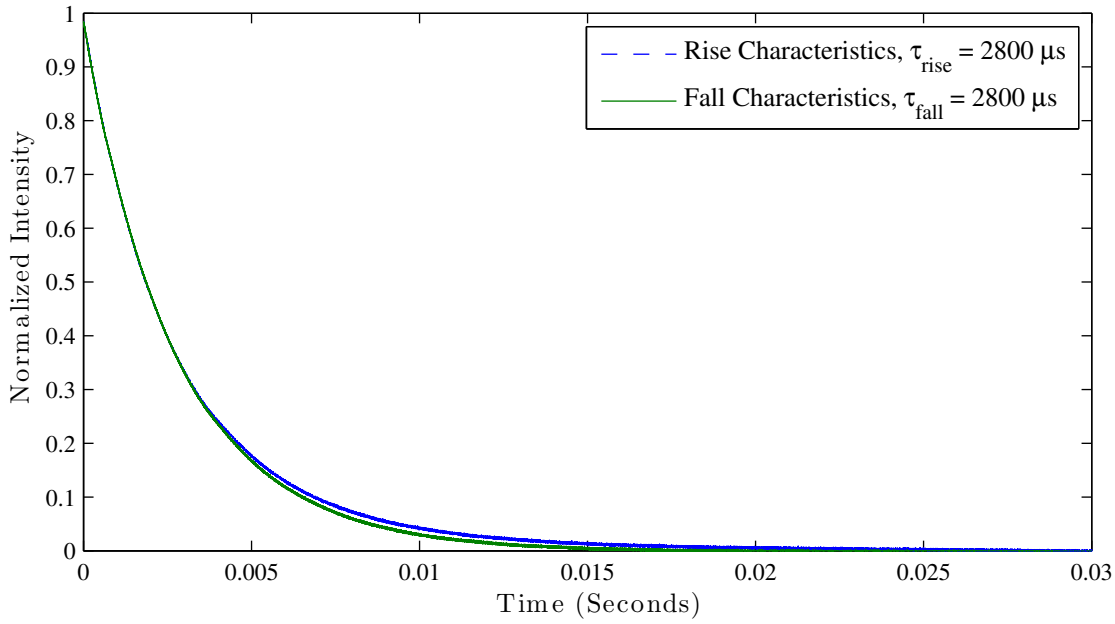

Figure 6.81: The dynamics of $^4I_{11/2}$ fluorescence intensity versus time for 1% Er:Y_2O_3 Er:YAG under 800 nm up to 1 kW/cm^2 intensity puming.

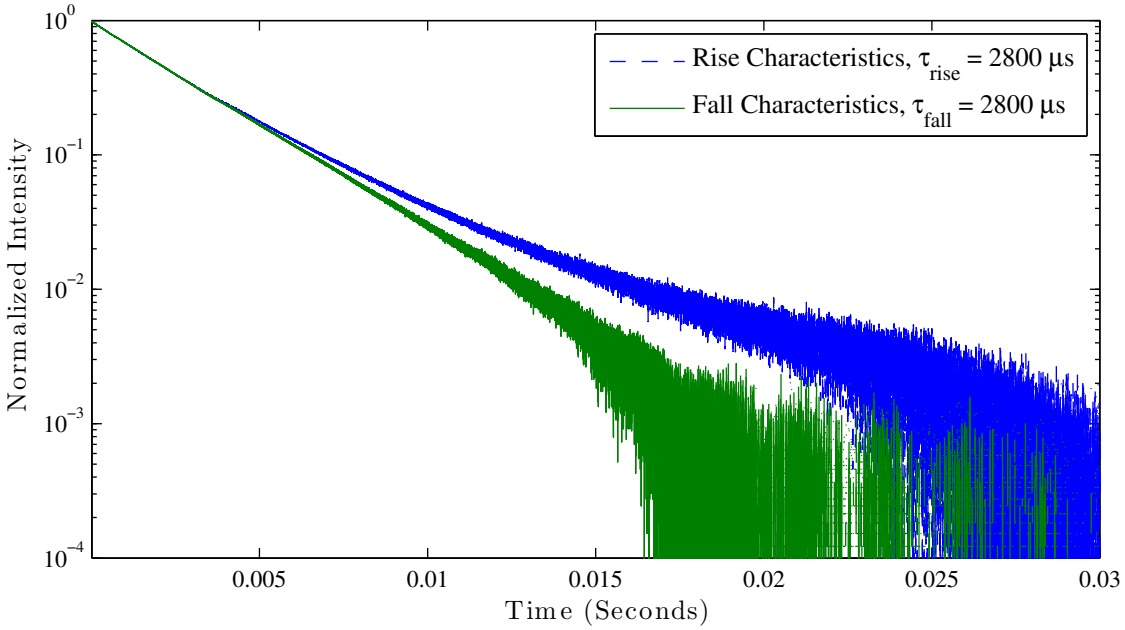

Figure 6.82: The dynamics of $^4I_{11/2}$ fluorescence intensity versus time for 1% Er:Y_2O_3 under 800 nm up to 1 kW/cm^2 intensity puming on semilog-y plot.

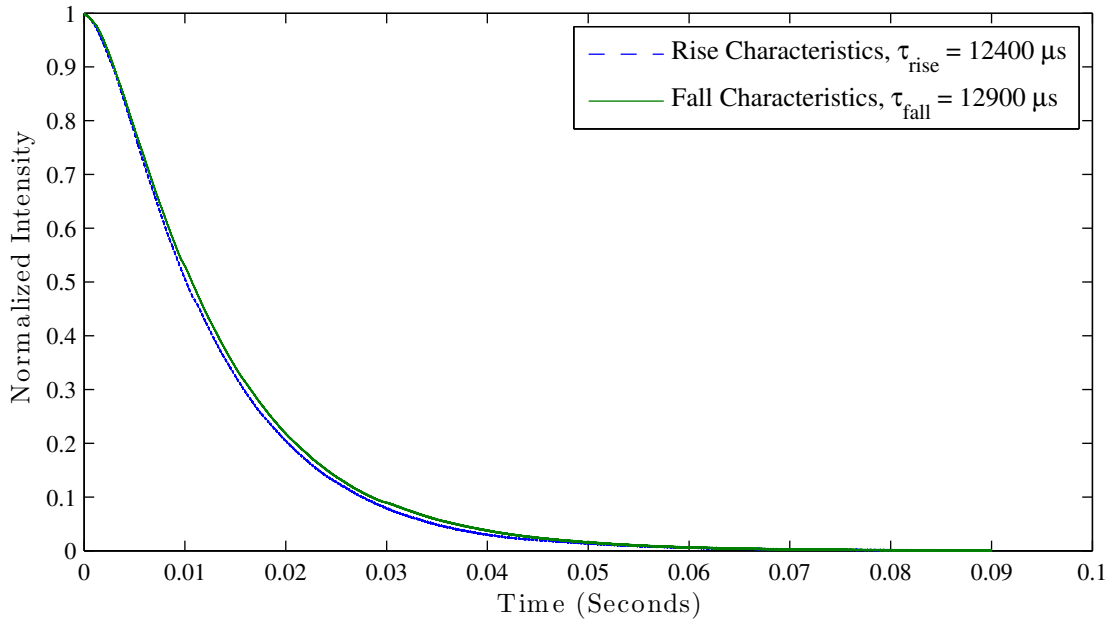

Figure 6.83: The dynamics of $^4I_{13/2}$ fluorescence intensity versus time for 1% Er:Y_2O_3 under 800 nm up to 1 kW/cm^2 intensity puming.

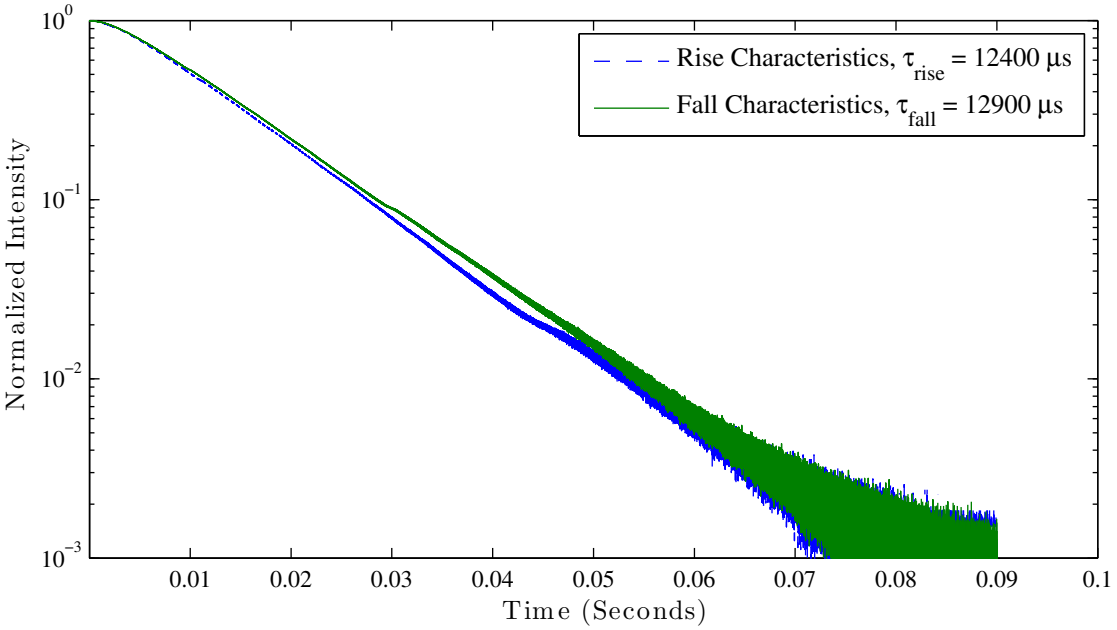

Figure 6.84: The dynamics of $^4I_{13/2}$ fluorescence intensity versus time for 1% Er:Y_2O_3 under 800 nm up to 1 kW/cm^2 intensity puming on semilog-y plot.

6.3.9 15% Er:Yttria under 800 nm Pump

For this sample, the rise and fall follows a similar trend on the states that are above the pump state of $^4I_{9/2}$ such as $^4S_{3/2}$ (Figure 6.85 on page 116 and Figure 6.86 on page 117) and $^4F_{9/2}$ (Figure 6.87 on page 117 and Figure 6.88 on page 118). The lower excited states below the pump state show some changes exhibiting the lower bound. The $^4I_{11/2}$ (Figure 6.91 on page 119 and Figure 6.92 on page 120) has a decrease on the rise time versus the natural decay from 2550 down to 2150, a decrease of 16%, and an increase in the fall time to 2700, an increase of 6%. This indicates that the ESA and ETU coming from $^4I_{13/2}$ (Figure 6.93 on page 120 and Figure 6.94 on page 121) is not enough to mask over the ESA and ETU decrease on time from $^4I_{11/2}$. An additional interesting fact is that about 75% of the population that ends up in $^4I_{9/2}$ (Figure 6.89 on page 118 and Figure 6.90 on page 119) experiences up-conversion through the lower excited states.

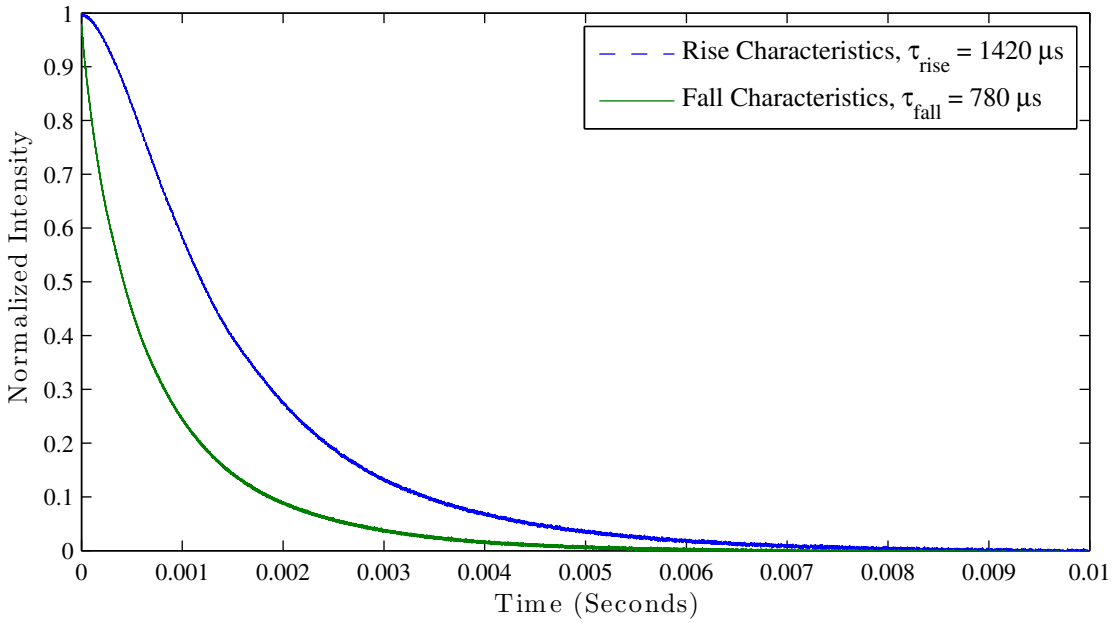

Figure 6.85: The dynamics of $^4S_{3/2}$ fluorescence intensity versus time for 15% Er:Y_2O_3 under 800 nm up to 1 kW/cm^2 intensity puming on linear plot.

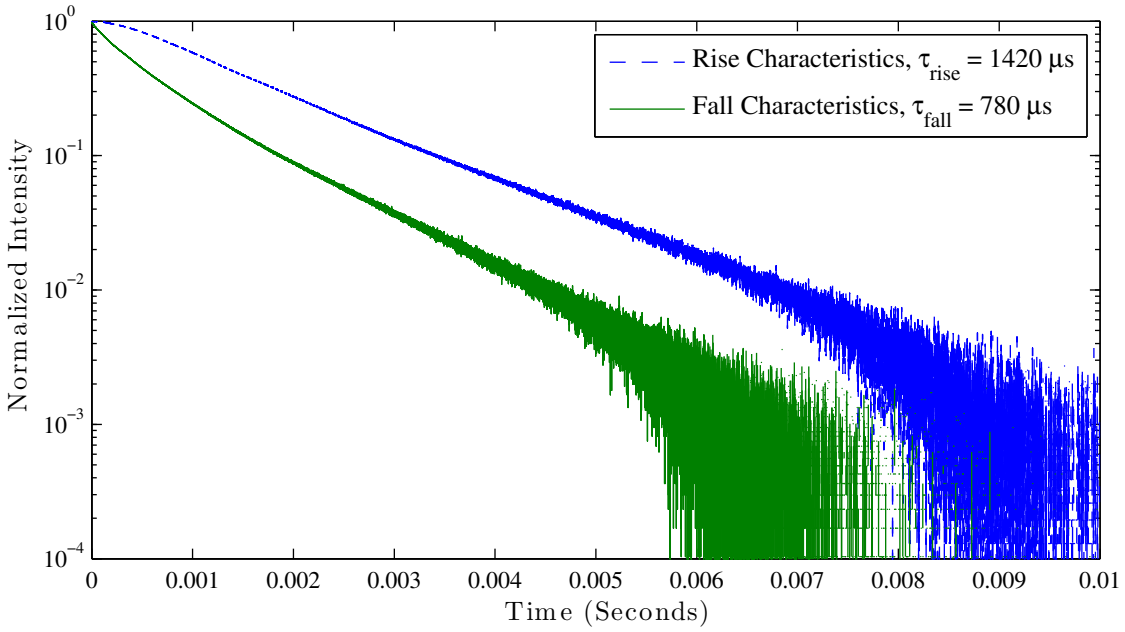

Figure 6.86: The dynamics of $^4S_{3/2}$ fluorescence intensity versus time for 15% Er:Y_2O_3 under 800 nm up to 1 kW/cm^2 intensity puming on semilog-y plot.

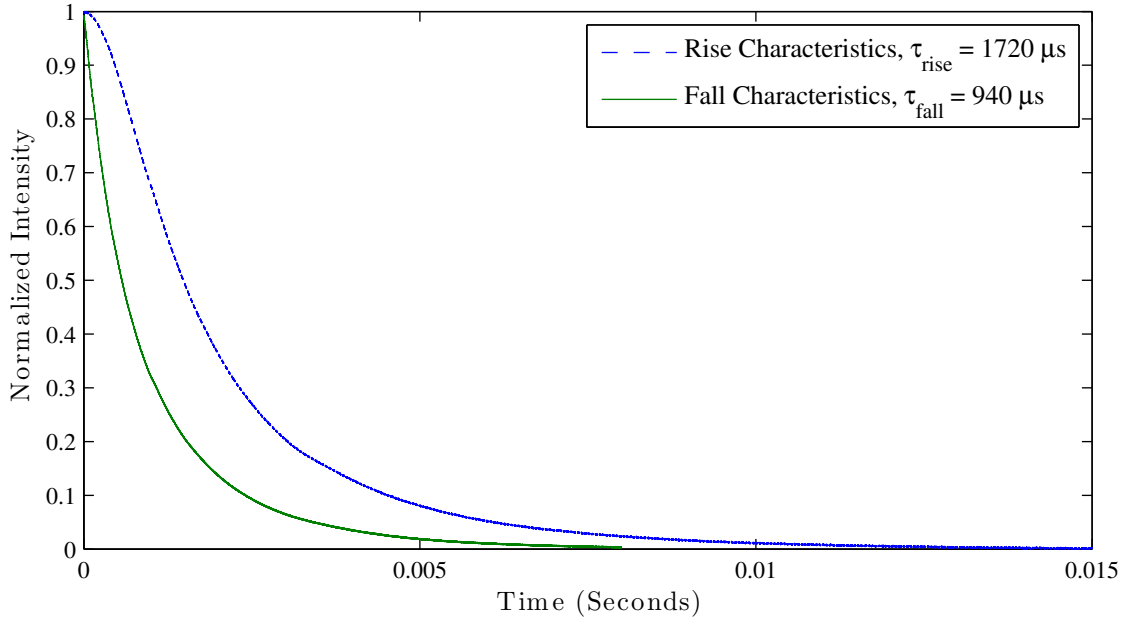

Figure 6.87: The dynamics of $^4F_{9/2}$ fluorescence intensity versus time for 15% Er:Y_2O_3 under 800 nm up to 1 kW/cm^2 intensity puming.

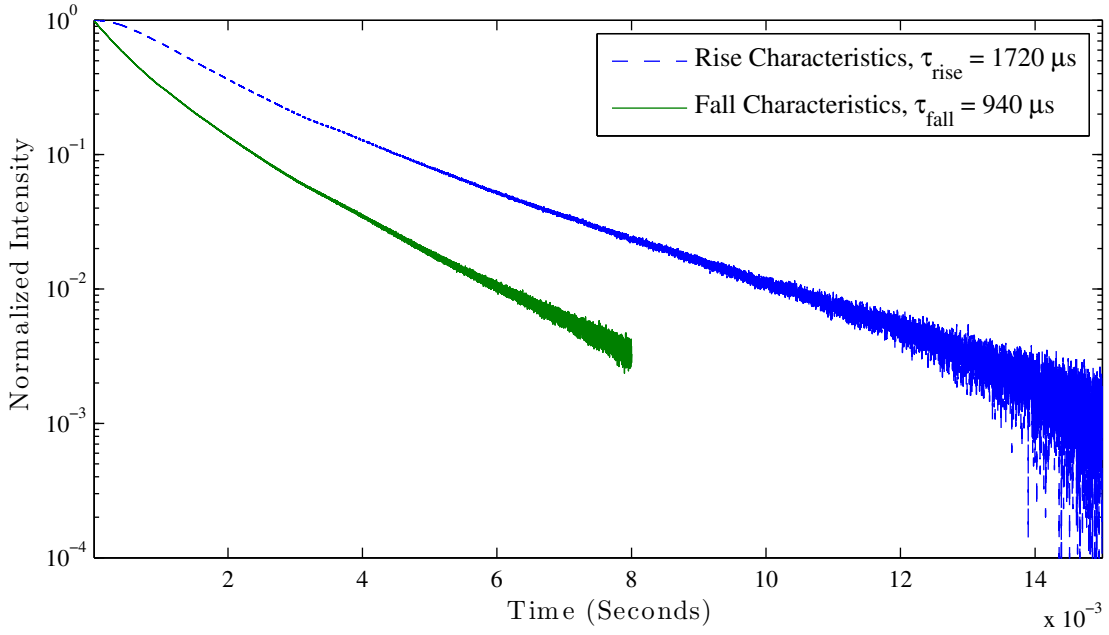

Figure 6.88: The dynamics of $^4F_{9/2}$ fluorescence intensity versus time for 15% Er:Y_2O_3 under 800 nm up to 1 kW/cm^2 intensity puming on semilog-y plot.

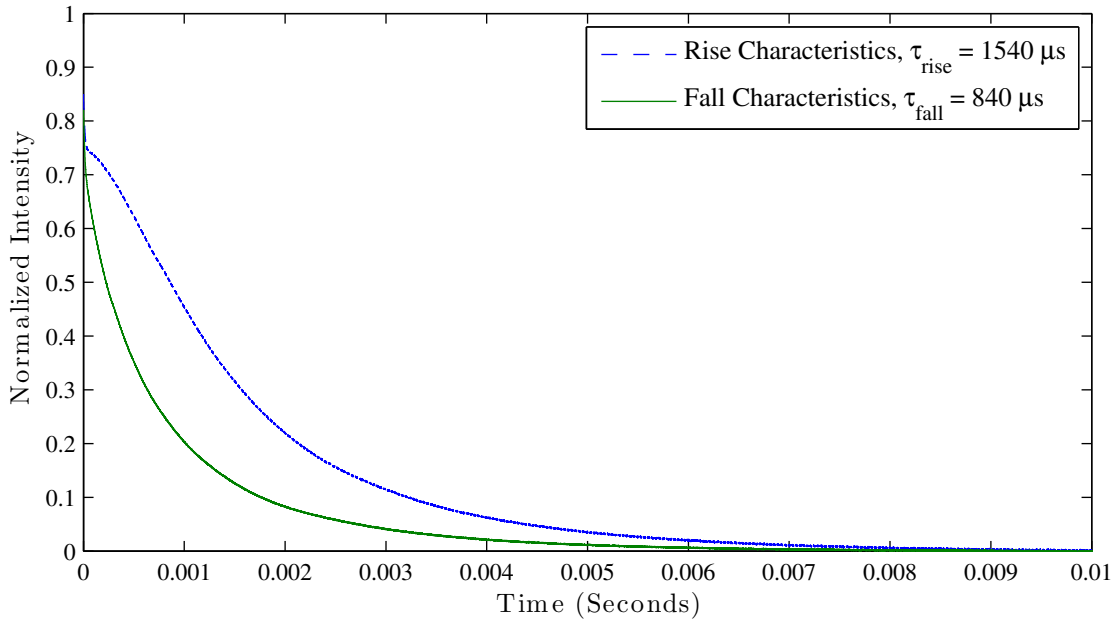

Figure 6.89: The dynamics of $^4I_{9/2}$ fluorescence intensity versus time for 15% Er:Y_2O_3 under 800 nm up to 1 kW/cm^2 intensity puming.

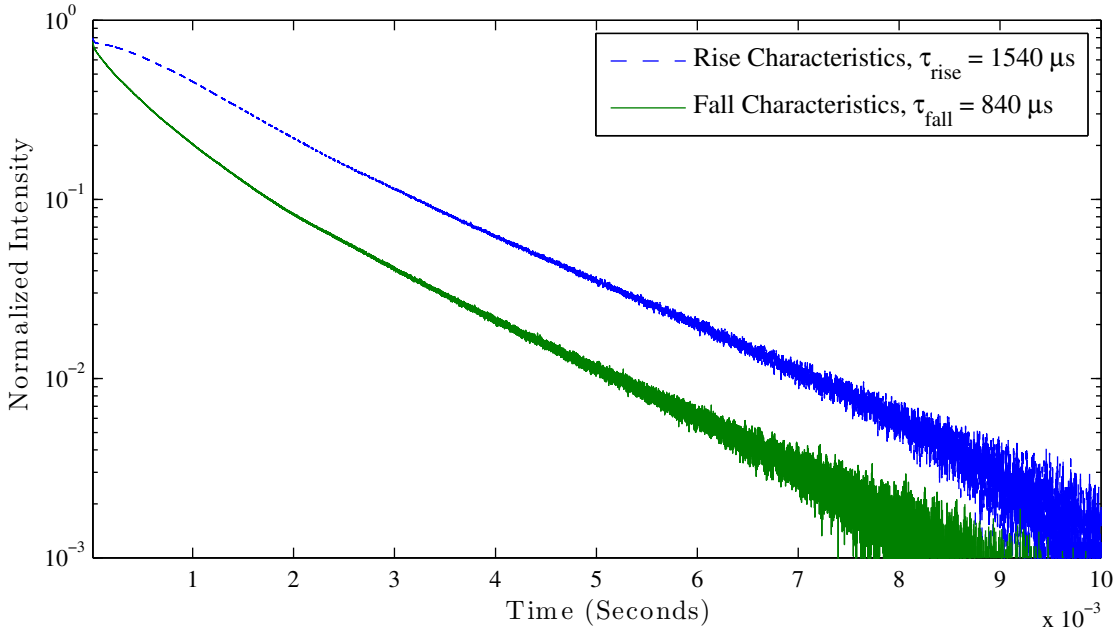

Figure 6.90: The dynamics of $^4I_{9/2}$ fluorescence intensity versus time for 15% Er:Y_2O_3 under 800 nm up to 1 kW/cm^2 intensity puming on semilog-y plot.

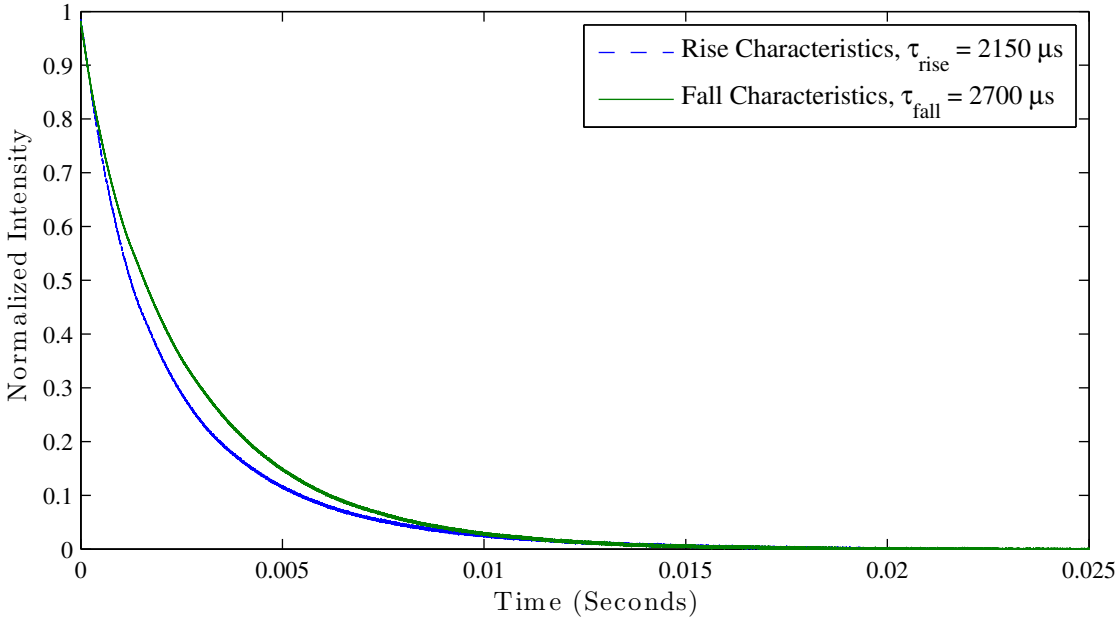

Figure 6.91: The dynamics of $^4I_{11/2}$ fluorescence intensity versus time for 15% Er:Y_2O_3 Er:YAG under 800 nm up to 1 kW/cm^2 intensity puming.

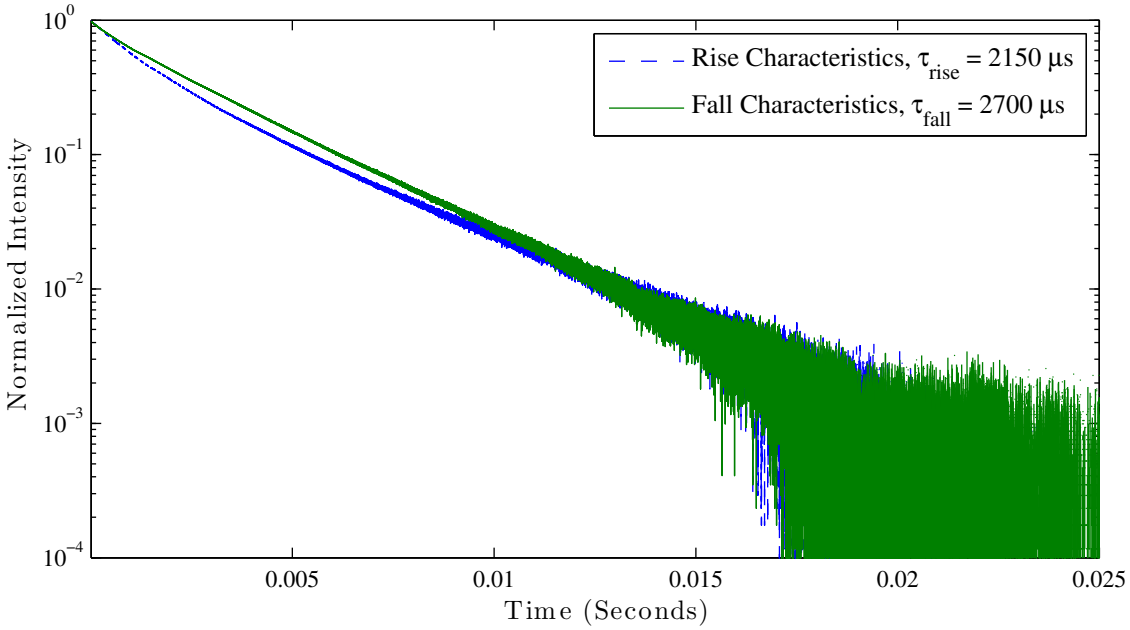

Figure 6.92: The dynamics of $^4I_{11/2}$ fluorescence intensity versus time for 15% Er:Y_2O_3 under 800 nm up to 1 kW/cm^2 intensity puming on semilog-y plot.

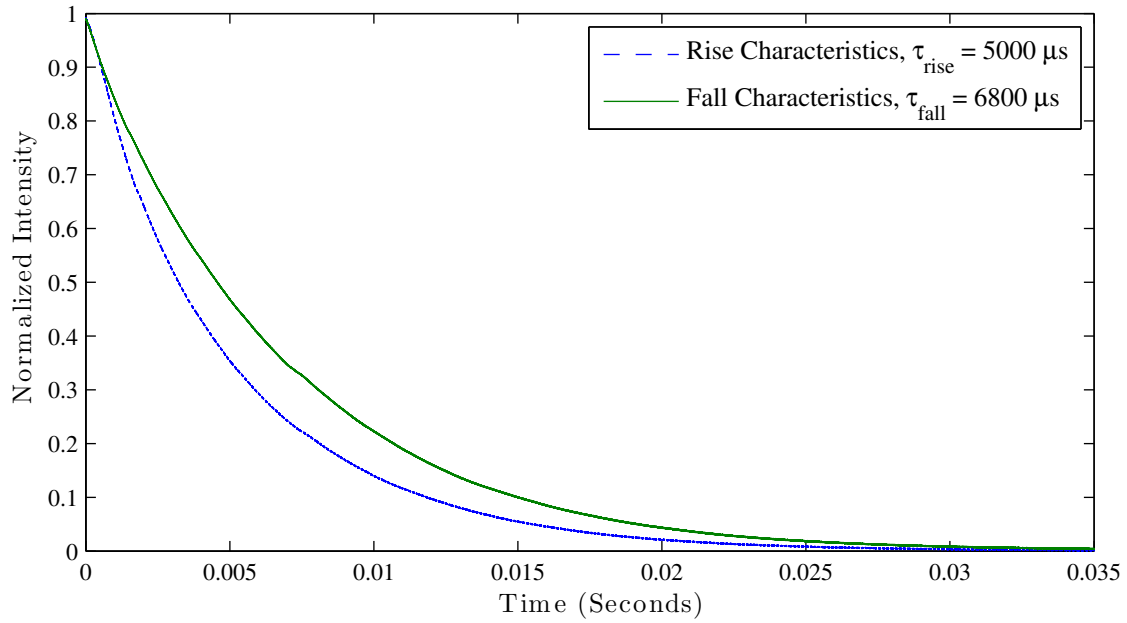

Figure 6.93: The dynamics of $^4I_{13/2}$ fluorescence intensity versus time for 15% Er:Y_2O_3 under 800 nm up to 1 kW/cm^2 intensity puming.

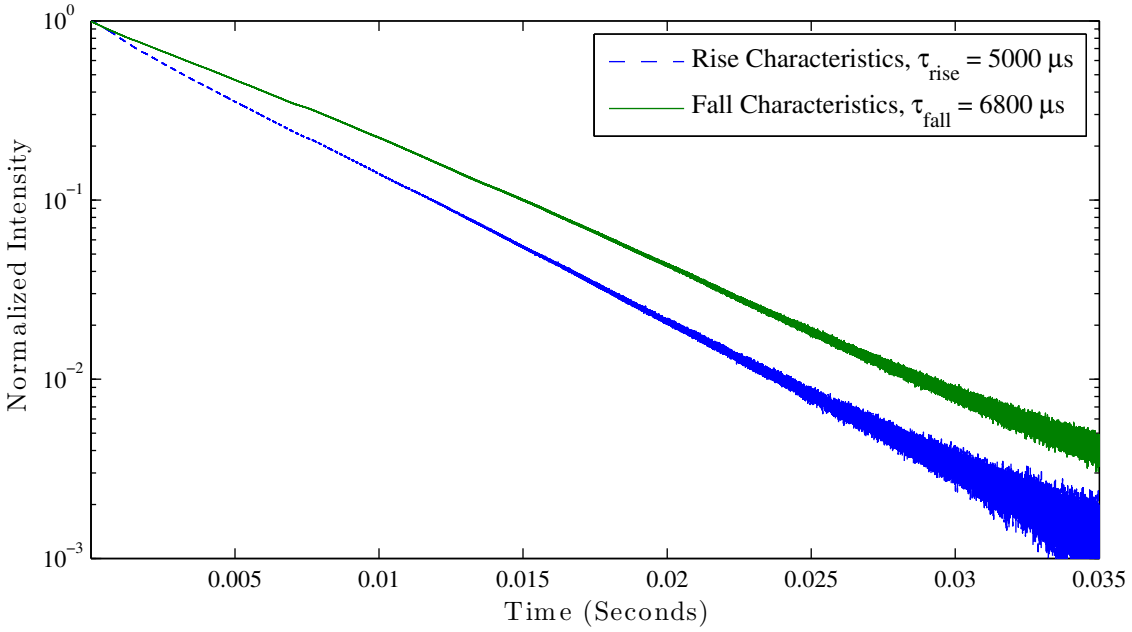

Figure 6.94: The dynamics of $^4I_{13/2}$ fluorescence intensity versus time for 15% Er:Y_2O_3 under 800 nm up to 1 kW/cm^2 intensity puming on semilog-y plot.

6.3.10 25% Er:Yttria under 800 nm Pump

The upper state for 25% Er:Yttria follows a similar trend as other Yttria samples under 800 nm pump. One interesting fact worth mentioning is that the upconversion from $^4I_{13/2}$ to $^4I_{9/2}$ actually drops as the doping increased from 15% to 25% even though from 1% to 15% an increase of the contribution to the $^4I_{9/2}$ from $^4I_{13/2}$ is observed.

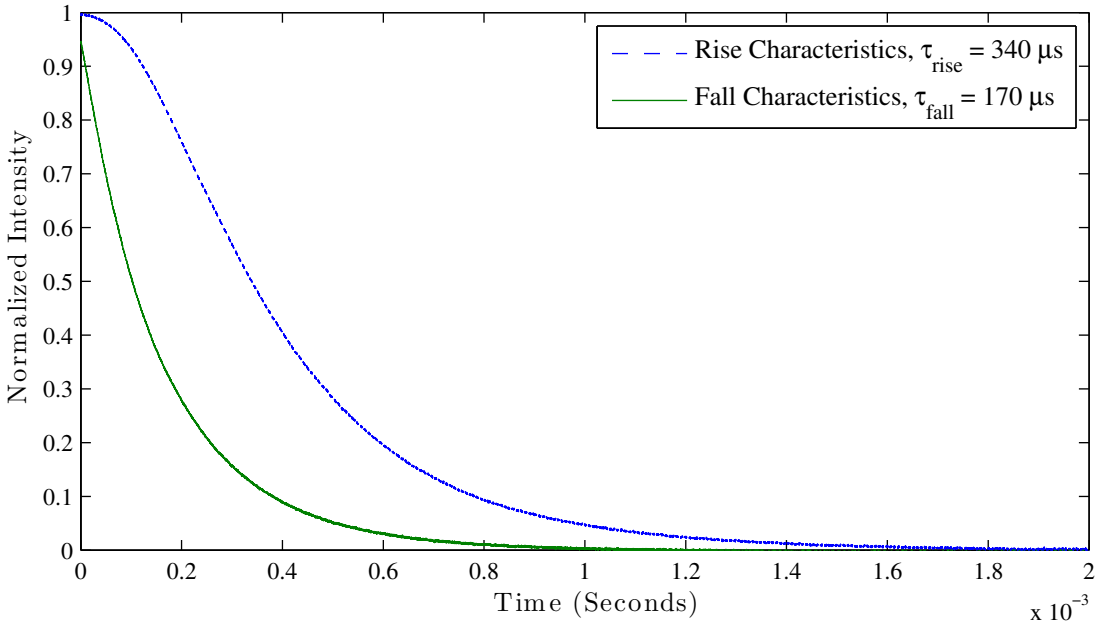

Figure 6.95: The dynamics of $^4S_{3/2}$ fluorescence intensity versus time for 25% Er:Y_2O_3 under 800 nm up to 1 kW/cm^2 intensity puming on linear plot.

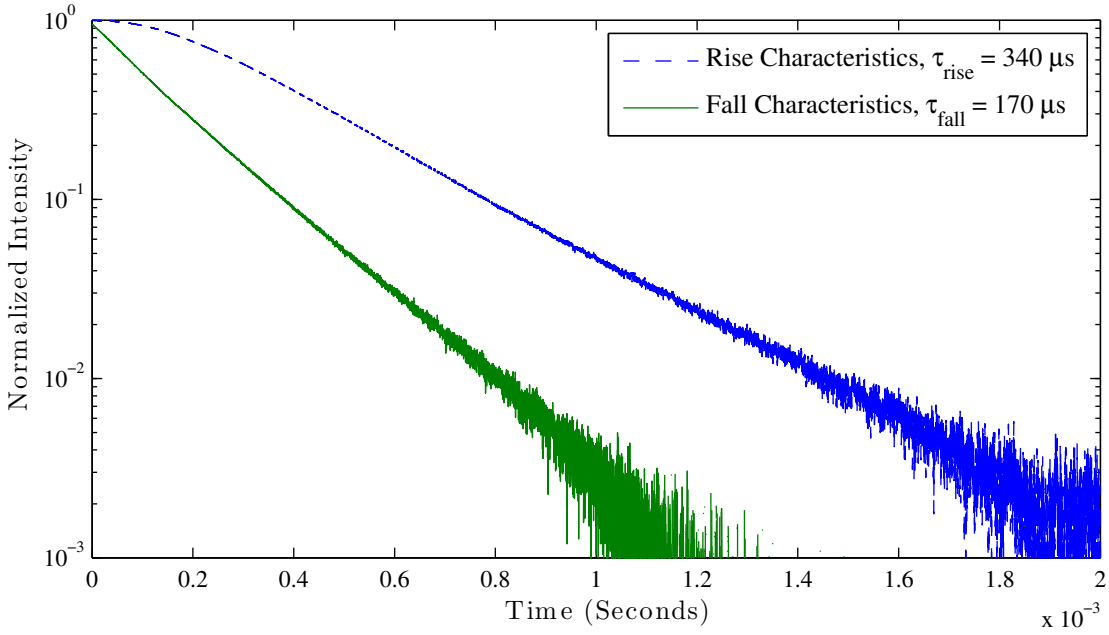

Figure 6.96: The dynamics of $^4S_{3/2}$ fluorescence intensity versus time for 25% Er:Y_2O_3 under 800 nm up to 1 kW/cm^2 intensity puming on semilog-y plot.

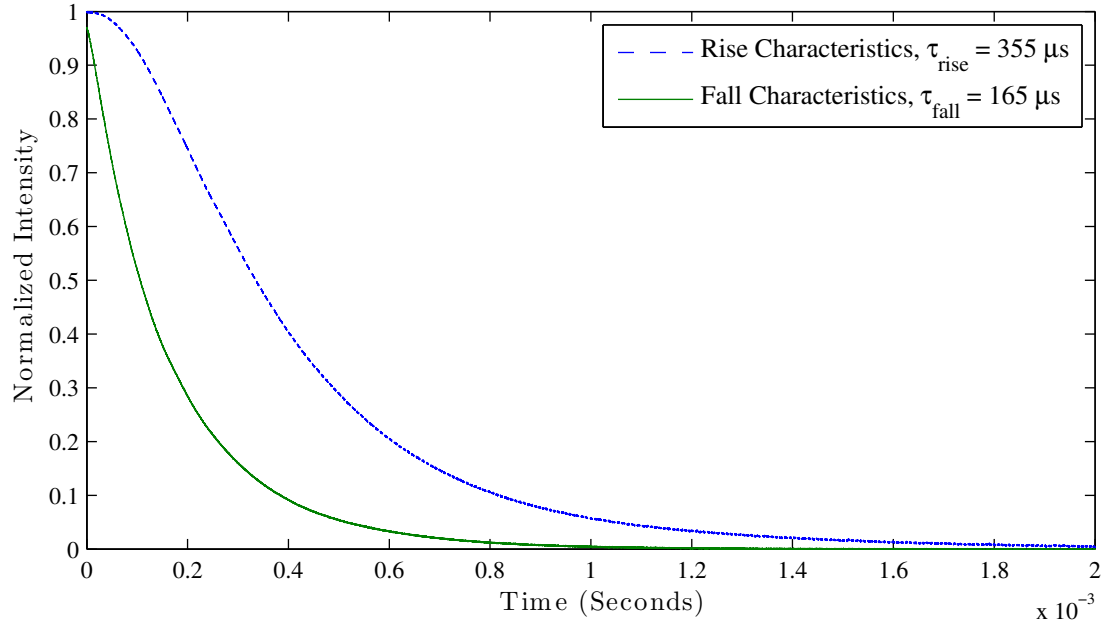

Figure 6.97: The dynamics of $^4F_{9/2}$ fluorescence intensity versus time for 25% Er:Y_2O_3 under 800 nm up to 1 kW/cm^2 intensity puming.

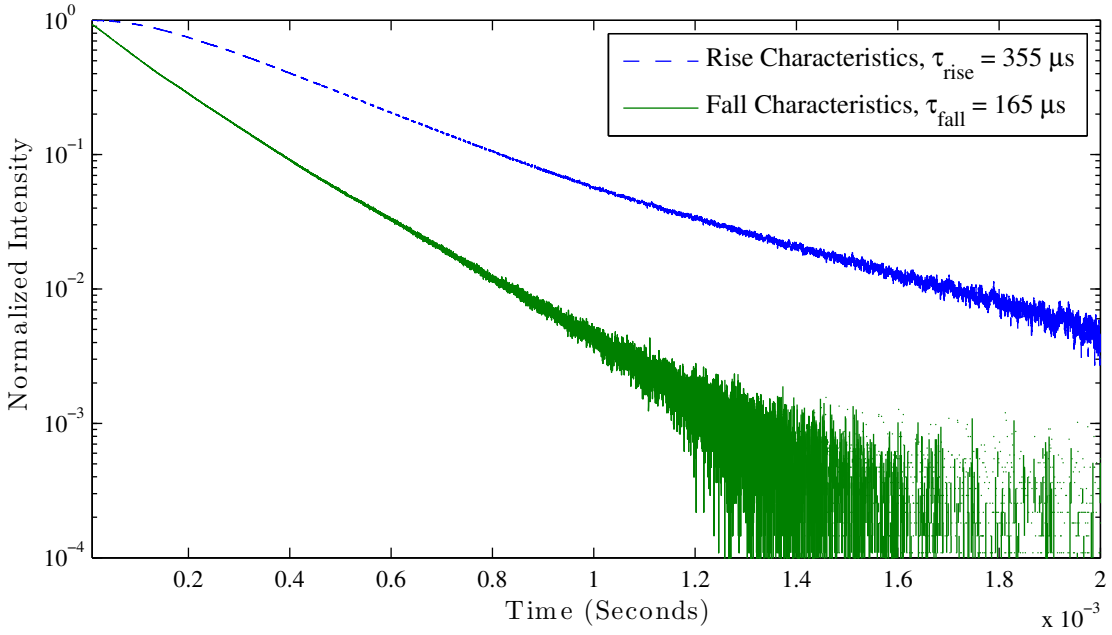

Figure 6.98: The dynamics of $^4F_{9/2}$ fluorescence intensity versus time for 25% Er:Y_2O_3 under 800 nm up to 1 kW/cm^2 intensity puming on semilog-y plot.

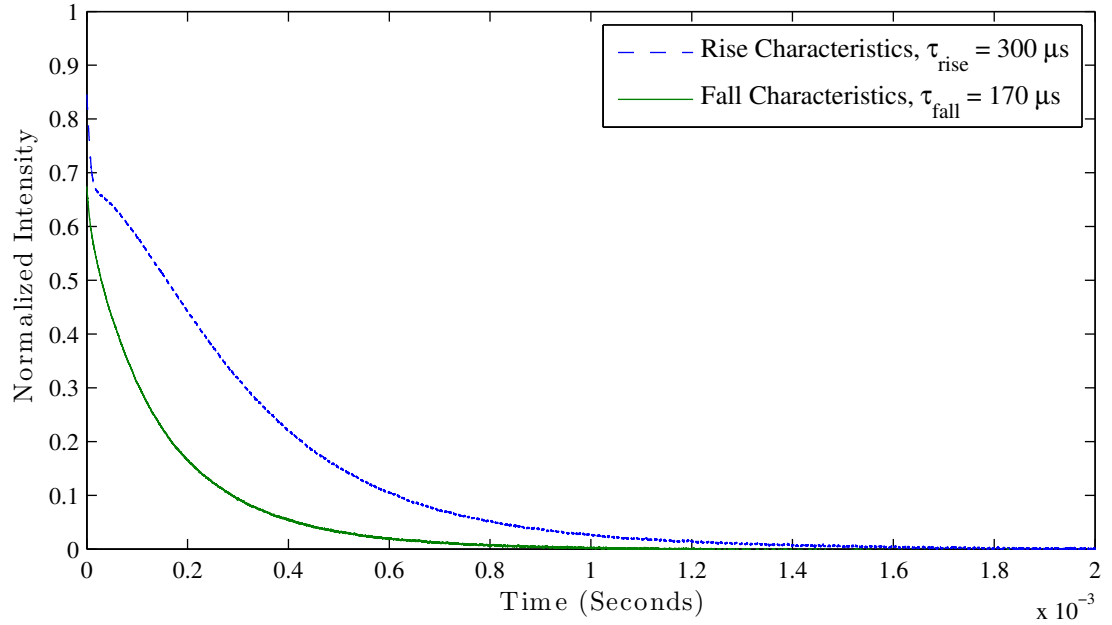

Figure 6.99: The dynamics of $^4I_{9/2}$ fluorescence intensity versus time for 25% Er:Y_2O_3 under 800 nm up to 1 kW/cm^2 intensity puming.

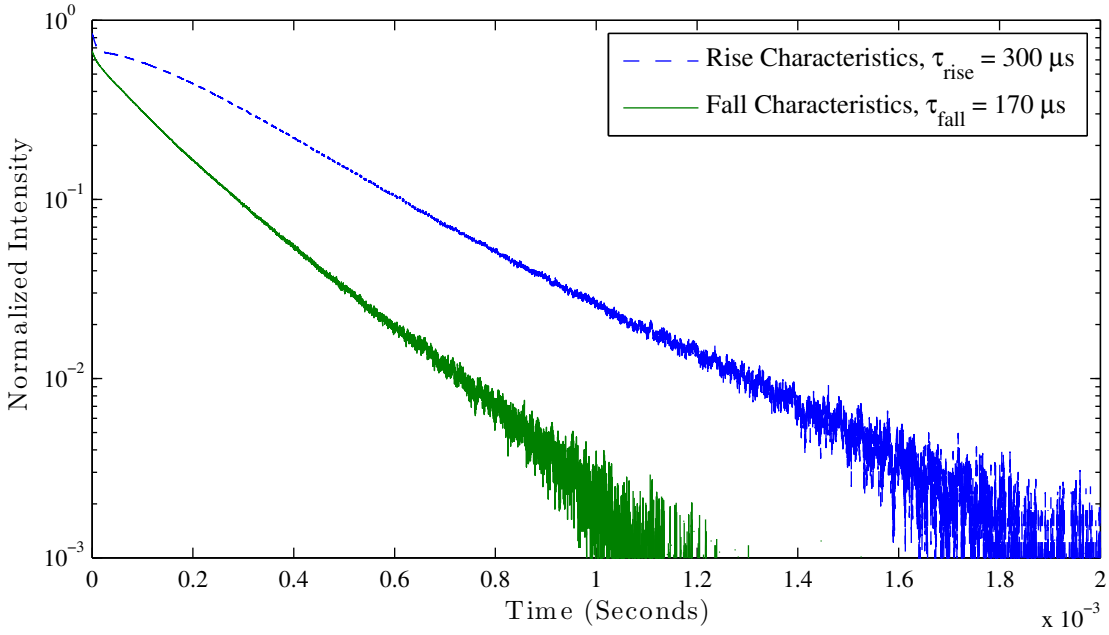

Figure 6.100: The dynamics of $^4I_{9/2}$ fluorescence intensity versus time for 25% Er:Y_2O_3 under 800 nm up to 1 kW/cm^2 intensity puming on semilog-y plot.

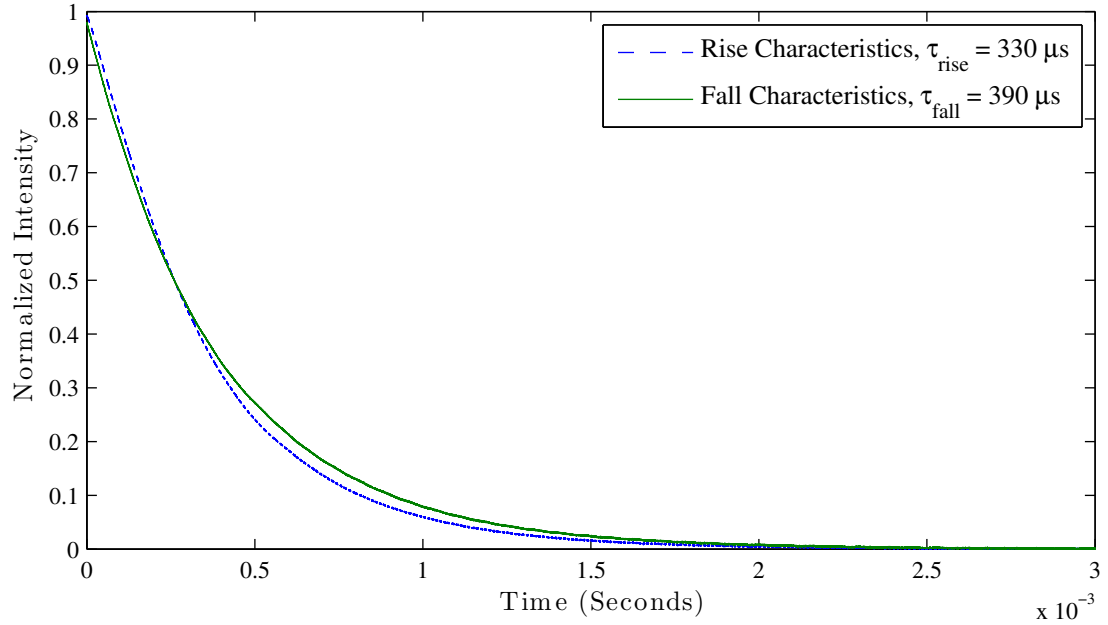

Figure 6.101: The dynamics of $^4I_{11/2}$ fluorescence intensity versus time for 25% Er:Y_2O_3 Er:YAG under 800 nm up to 1 kW/cm^2 intensity puming.

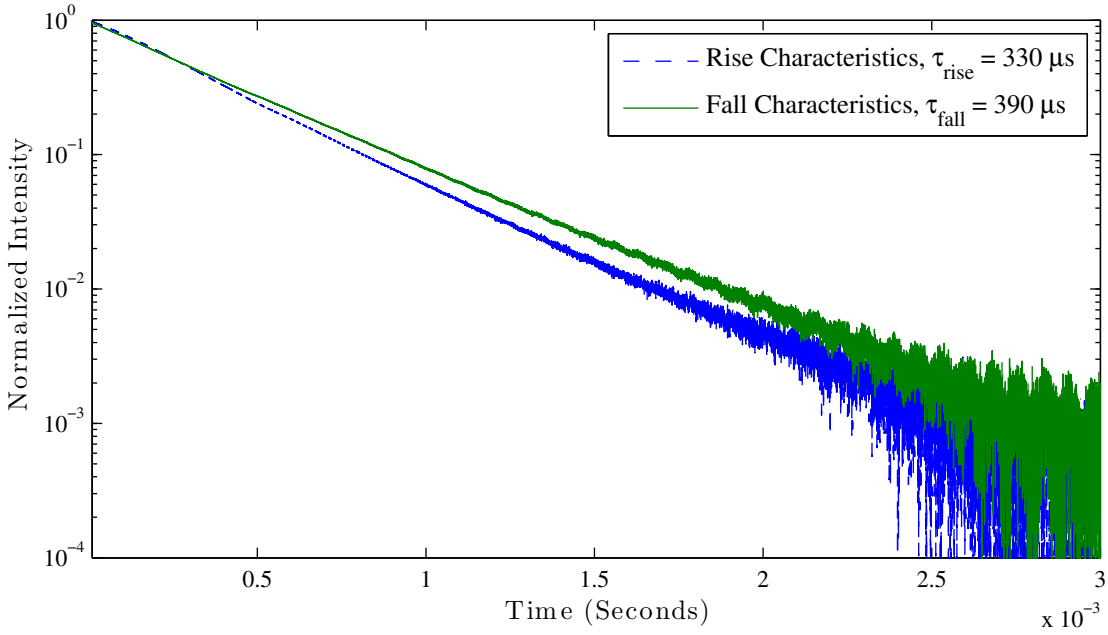

Figure 6.102: The dynamics of $^4I_{11/2}$ fluorescence intensity versus time for 25% Er:Y_2O_3 under 800 nm up to 1 kW/cm^2 intensity puming on semilog-y plot.

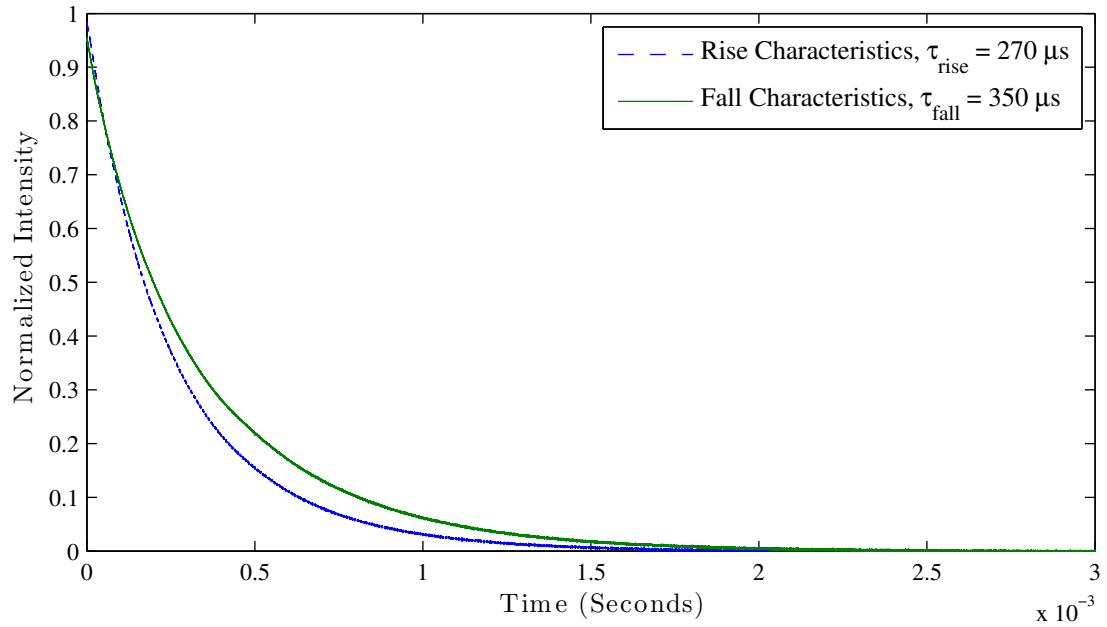

Figure 6.103: The dynamics of $^4I_{13/2}$ fluorescence intensity versus time for 25% Er:Y_2O_3 under 800 nm up to 1 kW/cm^2 intensity puming.

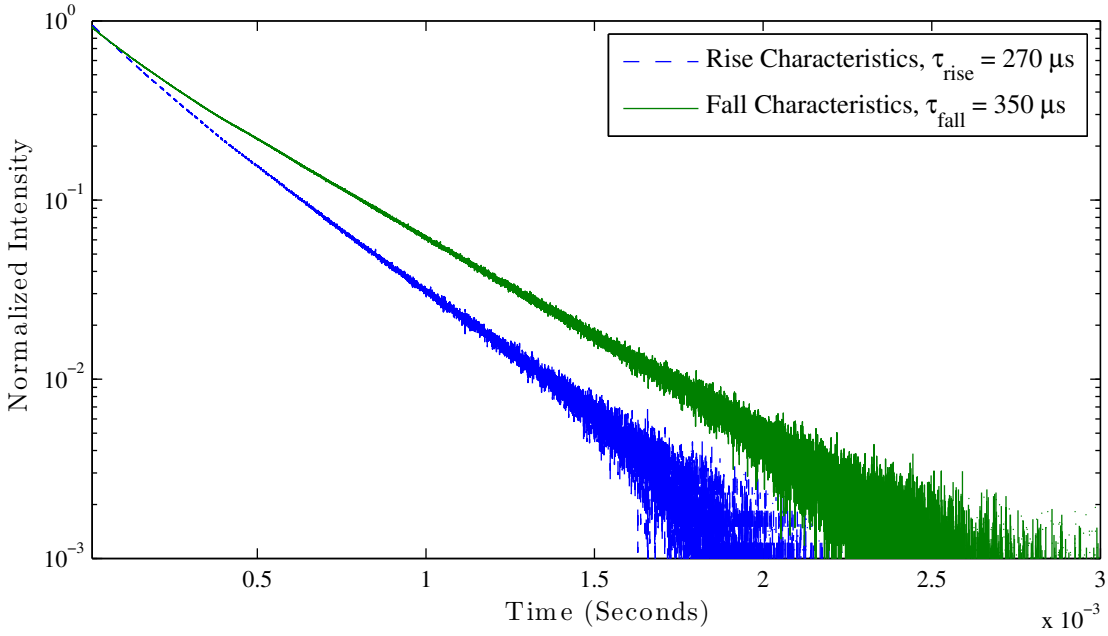

Figure 6.104: The dynamics of $^4I_{13/2}$ fluorescence intensity versus time for 25% Er:Y_2O_3 under 800 nm up to 1 kW/cm^2 intensity puming on semilog-y plot.

6.4 Rate Calculation

Here the ESA and ETU coefficients are estimated. The coefficients we calculate are the under-estimates of what they actually are, which is explained as follows. Looking at the rate equations (Equation 2.24) given on page 25, we can simplify the rate equation based on the data observed. Since mainly only the N^2 cooperative effects of ETU kind and not the XR kind are observed, we can remove all of the "weak" terms from the rate equations, and it becomes Equation 6.6 on page 128. We can perform direct rate estimation, which, as an example, is given in Equation 6.7 on page 129 for 50% Er:YAG under 965 nm pump. Figure 6.105 on page 130 reflects the removal of the unobserved processes. This computation is the lower limit of the rates since the sample is too thick to have uniform axial pump intensity due to strong erbium sample absorption. The up-conversion rate is both population density and pump intensity dependent. Therefore, the photodetector collects optical information from both the strongly pumped region and weakly pumped region. Furthermore, the method estimated introduces another underestimation. Since ETU on the fall is the strongest when the population is big, by the time we capture the e^{-1} time, the ETU rate has decreased by about a factor of 63%. Therefore, the ETU coefficients we calculate based on the data we collect would be smaller than what it actually is. On the rise, ETU does not become strong until population becomes big, therefore, it estimating the 63% point will only capture the lower part of ETU. In short, both the ESA and ETU results are estimated to be the lowerbounds and can only be stronger.

This method also allows the observation of relative changes of the laser state population. Using 50% Er:YAG under 965 nm pumping as an example, since the effective life time for the $^4I_{11/2}$ roughly doubled, the population roughly doubled. By the same token Since the effective life time of $^4I_{13/2}$ decreased by 63%, this means the population in the lower laser state of 3 μmhas decreased by about 63% had the ESA and ETU effects been missing.

$^4S_{3/2}$: $$\frac{dN_5}{dt} = -\frac{1}{\tau_5}N_5 + \alpha_{25}IN_2 + W_{22}N_2^2 \tag{6.6a}$$

$^4F_{9/2}$: $$\frac{dN_4}{dt} = \frac{1}{\tau_{54}}N_5 - \frac{1}{\tau_4}N_4 + \alpha_{14}IN_1 \tag{6.6b}$$

$^4I_{9/2}$: $$\frac{dN_3}{dt} = \frac{1}{\tau_{53}}N_5 + \frac{1}{\tau_{43}}N_4 - \frac{1}{\tau_3}N_3 + W_{11}N_1^2 \tag{6.6c}$$

$^4I_{11/2}$: $$\frac{dN_2}{dt} = \frac{1}{\tau_{52}}N_5 + \frac{1}{\tau_{42}}N_4 + \frac{1}{\tau_{32}}N_3 - (\frac{1}{\tau_2} + \alpha_{25}I)N_2 - 2W_{22}N_2^2 + \alpha_{02}IN_0 \tag{6.6d}$$

$^4I_{13/2}$: $$\frac{dN_1}{dt} = \frac{1}{\tau_{51}}N_5 + \frac{1}{\tau_{41}}N_4 + \frac{1}{\tau_{31}}N_3 + \frac{1}{\tau_{21}}N_2 - (\frac{1}{\tau_1} + \alpha_{14}I)N_1 + W_{50}N_5N_0 - 2W_{11}N_1^2 \tag{6.6e}$$

$^4I_{15/2}$: $$\frac{dN_0}{dt} = \frac{1}{\tau_{50}}N_5 + \frac{1}{\tau_{40}}N_4 + \frac{1}{\tau_{30}}N_3 + \frac{1}{\tau_{20}}N_2 + \frac{1}{\tau_1}N_1 - \alpha_{02}IN_0 + W_{22}N_2^2 + W_{11}N_1^2 \tag{6.6f}$$

$$\frac{1}{\tau_{fall}} = \frac{1}{\tau_1} + R_{ETU} \tag{6.7a}$$

$$\frac{1}{\tau_{rise}} = \frac{1}{\tau_1} + R_{ETU} + R_{ESA} \tag{6.7b}$$

$$\tau_{fall} = 800\,\mu\text{s} \tag{6.7c}$$

$$\tau_{rise} = 475\,\mu\text{s} \tag{6.7d}$$

$$R_{ETU} = 504\,\mu\text{s}^{-1} \tag{6.7e}$$

$$R_{ESA} = 809\,\mu\text{s}^{-1} \tag{6.7f}$$

$$R_1 = 769.2\,\mu\text{s}^{-1} \tag{6.7g}$$

$$R_{ETU} \equiv 2W_{11}N_1 \tag{6.7h}$$

$$R_{ESA} \equiv \alpha_{14}I \tag{6.7i}$$

$$R_1 \equiv \frac{1}{\tau_1} \tag{6.7j}$$

(6.7k)

10

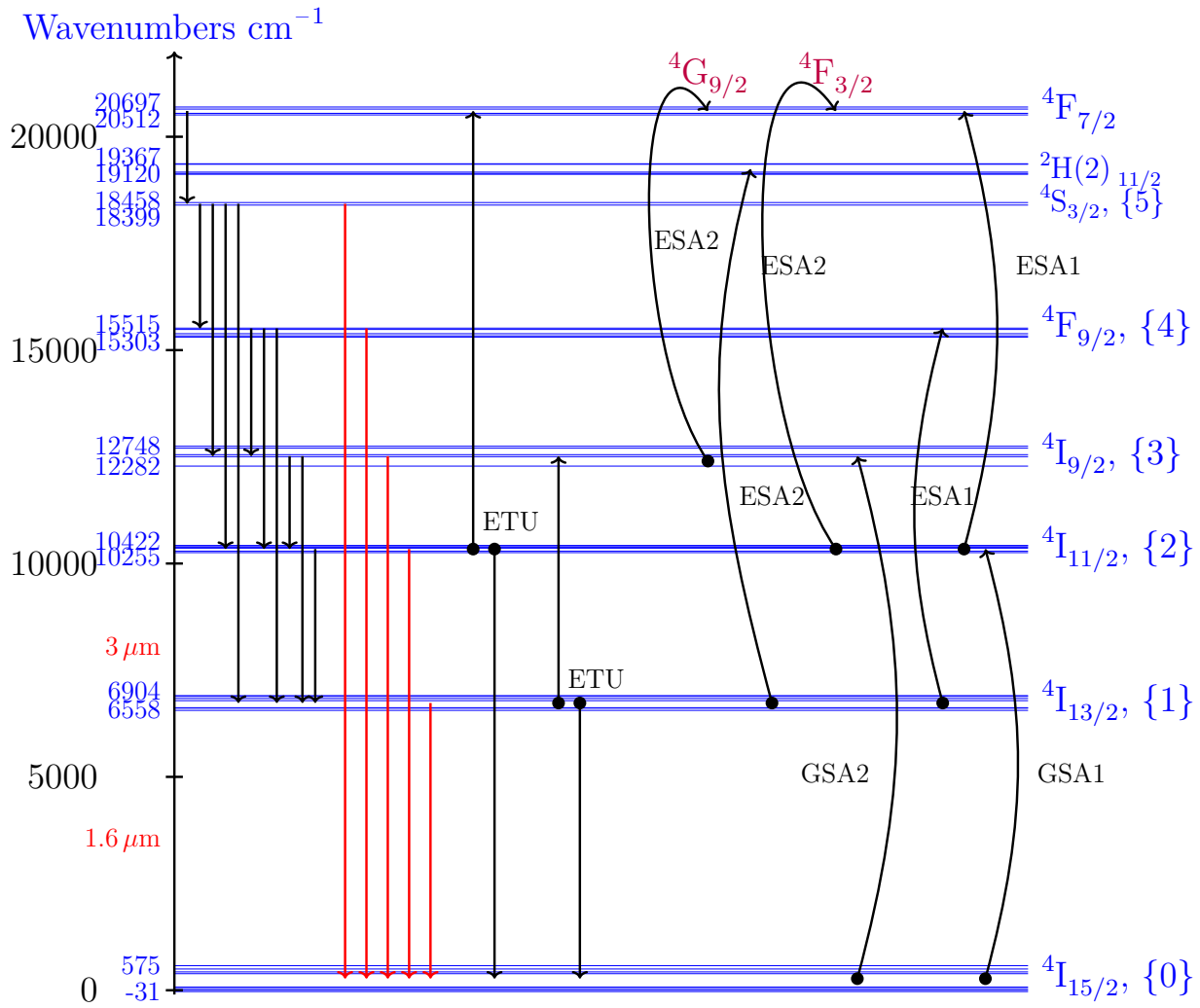

Figure 6.105: Calculated energy Levels of Er:YAG. Unobserved processes are removed from the diagram and replaced with 800 nm GSA and ESA effects. ESA1 and GSA1 correspond to the pump at 960 nm and ESA2 and GSA2 corresond to the pump at 800 nm.

Chapter 7

Conclusions & Suggested Future Studies

In this thesis, we demonstrated a simple technique that has allowed us to observe the following in both Er:YAG and Er:Y_2O_3.

- Possibility of some clumping or pairing of ions in low erbium-doped in YAG and in Y_2O_3 samples.
- The dominant path of the up-conversion in some of the states.
- Change of population due to ESA and ETU in the levels that are of particular interest for 1.6 μm and 3 μm lasers ($^4I_{11/2}$ and $^4_{I13/2}$) using erbium YAG and Yttria.
- The ESA and ETU rate of the erbium terminal laser level of 3 μm ($^4I_{13/2}$) without resorting to rate equation fitting and modeling (Direct Observation).

Since this dynamic fluorescent life time observation technique does not require rate equation model fitting as only the fluorescence information is collected, optical quality samples, which are expensive in both time and money, are unnecessary. Because this technique measures the dynamic behavioir (rise and fall times) of fluorescence, the samples does not need

to be of good optical properties. Powdered samples were measured and found that they exhibit similar behavior to crystalline and ceramic samples [28]. The only caviat with respect to the powdered samples is the necessity of not exposing them to water vapor. It is noted, however, that subsequent calcining at 600 °C or higher will remove measurable water quenching of fluorescence [28]. Cheap calcined powdered samples is all that is needed to observe this information. In addition, this method allows the observation of the "effectiveness" of a pump for a certain operation such as 1.6 μm or 3 μm. For example, we can easily compare the effectiveness of pumps such as 960 nm and 800 nm for 3 μm operation. Since we want to remove the terminal laser state and populate the upper laser state. ESA and ETU are both desired effects at the terminal laser level. If the intensity of both pumps are equal, this will allow easy comparison of the pump effectiveness in producing the ESA effects. Another example is we can observe that in 15% Er:Y_2O_3, over 75% of the population at $^4I_{9/2}$ comes from ESA of $^4I_{13/2}$ instead of ground state absorption. In short, this method is an efficient tool for laser designers to save money and time on determining the quality of crystal sample for laser operation and finding the optimal wavelength for pumping.

As indicated in the experimental setup, the samples are about 1 cm in thickness. However, the sample sizes would have been much better had the thickness been about one absorption length (for 960 nm pump, it would be $1/40\,\mathrm{cm}^{-1}$) so that the pump intensity is much more uniform axially for a better estimation on ESA and ETU. In addition, the simulated on-off switch is done by a two blade mechanical chopper at 100 Hz for the best rise time we could obtain. A better way to achieve faster rise and fall time without shifting the pump wavelength is desired. In this work, this method is only tested on erbium doped samples. However, all rare earths have ESA and ETU effects. Therefore, it would be interesting to suggest an investigation of this technique on other rare earth doped samples such as praseodymium and neodymium.

As observed from the rate equations given in Equation 2.24 on page 25, that the equations contain N^2 terms or higher order, and therefore, multiple possible steady state solutions are possible. This can potentially lead to chaos, which has been observed during the experiment

of high intensity 965 nm pumping on 50% Er:YAG. It would be interesting to investigate further in the future. Furthermore, since in this study, the population of $^4I_{11/2}$ and $^4I_{9/2}$ are dependent of which pump (800 nm or 965 nm) is used. The more fair study is to perform dual pump experiment. By that, we mean a study in which the sample is thin enough so that we can coaxially and contradirectionally pumped the sample from both sides. Even though the steady state[1] under 965 nm and 800 nm pump at the same time would be the same whether we turn the 800 nm on first or 965 nm on first, the dynamics or how the system reach that state would be different. Therefore, it would be interesting to turn one pump on as DC and observe the rise and fall times as we modulate the other pump at the other wavelength. Finally, this is less of an important experiment from the engineering perspective. However, since today the standard method in working in this field is still rate equation model fitting. It would be interesting and helpful to the community to obtain the "branching ratios" of each state. Since each upper level state will decay some to each lower level state, and we can only observe the total decay rate. We do not know what the decay rate to each state is exactly. With the advancement of optical filters that allows an optical density of OD8 just a few nanometers away from the pump now exist, we can pump into a stark level of the lowest excited state of some state and look at other stark level fluorescence and estimate the population using calculation. This allows us to correspond a certain intensity level of fluorescence to a certain population. Next we move up one excited state and pumping directly into that state's one stark level and estimate the population. We can then look at the intensity of the fluorescence from the lower state, which we have calibrated for population. Since we know the total rate of the upper-excited state. We know the population of the lower excited state. This allows us to actually calculate the branching ratio, which is used a lot in rate equation models. To get these constants, of course, a low pump intensity is required so cooperative effects can be ignored.

[1] As indicated in this paragraph, multiple possible steady states exist, and it is up to future investigation to determine that; however, assuming that it is true then this statement is correct.

The suggested future works coupled with this work would hopefully improve our understanding of rare earth energy transfer effects and efficiency in manufacturing rare earth laser systems.

Bibliography

[1] F. Auzel and D. Pecile. Comparison and efficiency of materials for summation of photons assisted by energy transfer. *Journal of Luminescence*, 8(1):32 – 43, 1973.

[2] F.E. Auzel. Materials and devices using double-pumped-phosphors with energy transfer. *Proceedings of the IEEE*, 61(6):758–786, June 1973.

[3] Norman P Barnes, Brian M Walsh, Farzin Amzajerdian, Donald J Reichle, George E Busch, and William A Carrion. Up conversion measurements in Er:YAG; comparison with 1.6 μm laser performance. *Optical Materials Express*, 1(4):678–685, 2011.

[4] John A. Caird, M. D. Shinn, T. A. Kirchoff, L. K. Smith, and R. E. Wilder. Measurements of losses and lasing efficiency in GSGG:Cr, Nd and YAG:Nd laser rods. *Appl. Opt.*, 25(23):4294–4305, Dec 1986.

[5] Robert G. DeLosh and Walter J. C. Grant. Electronic energy transfer via virtual-phonon processes. *Phys. Rev. B*, 1:1754–1765, Feb 1970.

[6] D. L. Dexter. A theory of sensitized luminescence in solids. *The Journal of Chemical Physics*, 21(5):836–850, 1953.

[7] D. L. Dexter. Cooperative optical absorption in solids. *Phys. Rev.*, 126:1962–1967, Jun 1962.

[8] Bradley J Dinerman and Peter F Moulton. 3-μm CW laser operations in erbium-doped YSGG, GGG, and YAG. *Optics letters*, 19(15):1143–1145, 1994.

[9] T. Förster. Zwischenmolekulare Energiewanderung und Fluoreszenz. *Annalen der Physik*, 437:55–75, 1948.

[10] Mario Furtado. Codoped erbium laser crystals, 2005. Copyright - Copyright ProQuest, UMI Dissertations Publishing 2005; Last updated - 2014-01-22; First page - n/a.

[11] S. Georgescu and V. Lupei. Q-switch regime of 3-µm Er:YAG lasers. *Quantum Electronics, IEEE Journal of*, 34(6):1031–1040, Jun 1998.

[12] S Georgescu, V Lupei, A Lupei, VI Zhekov, TM Murina, and MI Studenikin. Concentration effects on the up-conversion from the $^4I_{13/2}$ level of Er^{3+} in YAG. *Optics communications*, 81(3):186–192, 1991.

[13] S. Georgescu, V. Lupei, A. Petraru, C. Hapenciuc, C. Florea, C. Naud, and C. Porte. Excited-state-absorption in low concentrated Er:YAG crystals for pulsed and CW pumping. *Journal of Luminescence*, 93(4):281 – 292, 2001.

[14] S. Georgescu, V. Lupei, M. Trifan, R. J. Sherlock, and T. J. Glynn. Population dynamics of the threeâĂŘmicron emitting level of Er^{3+} in $YAlO_3$. *Journal of Applied Physics*, 80(12):6610–6613, 1996.

[15] S. Georgescu, O. Toma, and I. Ivanov. Upconversion from the $^4I_{13/2}$ and $^4I_{11/2}$ levels in Er:YAG. *Journal of Luminescence*, 114(1):43 – 52, 2005.

[16] Serban Georgescu. Mathematical modeling of 3-μm erbium lasers. In *Proceedings of The First French-Romanian Colloquium of Numerical Physics*, 2000.

[17] Serban Georgescu and Octavian Toma. Er : YAG three-micron laser: performances and limits. *Selected Topics in Quantum Electronics, IEEE Journal of*, 11(3):682–689, 2005.

[18] Serban Georgescu, Octavian Toma, and H Totia. Intrinsic limits of the efficiency of erbium 3-μm lasers. *Quantum Electronics, IEEE Journal of*, 39(6):722–732, 2003.

[19] Walter J. C. Grant. Role of rate equations in the theory of luminescent energy transfer. *Phys. Rev. B*, 4:648–663, Jul 1971.

[20] John B Gruber, Gary W Burdick, Sreerenjini Chandra, and Dhiraj K Sardar. Analyses of the ultraviolet spectra of Er^{3+} in Er_2O_3 and Er^{3+} in Y_2O_3. *Journal of Applied Physics*, 108(2):023109–023109, 2010.

[21] John B Gruber, Sreerenjini Chandra, Dhiraj K Sardar, Uygun V Valiev, Nafisa I Juraeva, and Gary W Burdick. Modeling optical spectra and van vleck paramagnetism in Er^{3+}: $YAlO_3$. *Journal of Applied Physics*, 105(2):023112–023112, 2009.

[22] John B Gruber, JR Henderson, M Muramoto, K Rajnak, and John G Conway. Energy levels of single-crystal erbium oxide. *The Journal of Chemical Physics*, 45(2):477–482, 1966.

[23] John B Gruber, William F Krupke, and John M Poindexter. Crystal-field splitting of trivalent thulium and erbium j levels in yttrium oxide. *The Journal of Chemical Physics*, 41(11):3363–3377, 1964.

[24] John B. Gruber, Kelly L. Nash, Dhiraj K. Sardar, Uygun V. Valiev, Nikolay Ter-Gabrielyan, and Larry D. Merkle. Modeling optical transitions of Er^{3+}(4f 11) in c2 and c3i sites in polycrystalline Y_2O_3. *Journal of Applied Physics*, 104(2):–, 2008.

[25] John B Gruber, John R Quagliano, Michael F Reid, Frederick S Richardson, Marian E Hills, Michael D Seltzer, Sally B Stevens, Clyde A Morrison, and Toomas H Allik. Energy levels and correlation crystal-field effects in Er^{3+}-doped garnets. *Physical Review B*, 48(21):15561, 1993.

[26] John B Gruber, Dhiraj K Sardar, Bahram Zandi, J Andrew Hutchinson, and C Ward Trussell. Spectra and energy levels of Er^{3+}(4f 11) in $Gd_3Ga_5O_{12}$. *Journal of applied physics*, 93(6):3137–3140, 2003.

[27] Mitio Inokuti and Fumio Hirayama. Influence of energy transfer by the exchange mechanism on donor luminescence. *The Journal of Chemical Physics*, 43(6):1978–1989, 1965.

[28] Abhijeet Joshi. The Er^{3+} : Y_2O_3 ceramic system, 2012.

[29] J. Koetke and G. Huber. Infrared excited-state absorption and stimulated-emission cross sections of Er^{3+}-doped crystals. *Applied Physics B*, 61(2):151–158, 1995.

[30] William F Krupke and John B Gruber. Energy levels of Er^{3+} in LaF_3 and coherent emission at 1.61 μ. *The Journal of Chemical Physics*, 41(5):1225–1232, 1964.

[31] Joseph R. Lakowicz. *Multiphotion Excitation of Molecular Fluorophores*, volume 5. Kluwer Academic Publishers, New York, Boston, Dordrecht, London, Moscow, 2002.

[32] V. Lupei, S. Georgescu, and V. Florea. On the dynamics of population inversion for 3 µm Er^{3+} lasers. *Quantum Electronics, IEEE Journal of*, 29(2):426–434, Feb 1993.

[33] Jack S. Margolis, Oscar Stafsudd, and Eugene Y. Wong. Fluorescence in mixed crystals of Ce:$PrCl_3$. *The Journal of Chemical Physics*, 38(8):2045–2046, 1963.

[34] E. Nakazawa and S. Shionoya. Cooperative Luminescence in $YbPO_4$. *Physical Review Letters*, 25:1710–1712, December 1970.

[35] M. Pollnau, Th. Graf, J. E. Balmer, W. Lüthy, and H. P. Weber. Explanation of the cw operation of the er^{3+} 3-μm crystal laser. *Phys. Rev. A*, 49:3990–3996, May 1994.

[36] Markus Pollnau and Stuart D Jackson. Energy recycling versus lifetime quenching in erbium-doped 3-μm fiber lasers. *Quantum Electronics, IEEE Journal of*, 38(2):162–169, 2002.

[37] Dhiraj K Sardar, Sreerenjini Chandrasekharan, Kelly L Nash, and John B Gruber. Optical intensity analyses of Er^{3+}:$YAlO_3$. *Journal of Applied Physics*, 104(2):023102–023102, 2008.

[38] Dhiraj K Sardar, Charles C Russell, John B Gruber, and Toomas H Allik. Absorption intensities and emission cross sections of principal intermanifold and inter-stark transitions of Er^{3+}(4f 11) in polycrystalline ceramic garnet $Y_3Al_5O_{12}$. *Journal of applied physics*, 97(12):123501–123501, 2005.

[39] Dhiraj K Sardar, Charles C Russell, Raylon M Yow, John B Gruber, Bahram Zandi, and Edvard P Kokanyan. Spectroscopic analysis of the Er^{3+}(4f 11) absorption intensities in $NaBi(WO_4)_2$. *Journal of applied physics*, 95(3):1180–1184, 2004.

[40] Gilbert. Strang. *Eigenvalues and Eigenvectors*. Wellesley - Cambridge Press Box 812060 Wellesley MA 02482, 2009.

[41] Octavian Toma and Serban Georgescu. Dynamics of an upconversion Er:YAG laser with reabsorption losses. *JOSA B*, 21(9):1630–1637, 2004.

[42] I. Ursu, A. Lupei, S. Georgescu, V. Lupei, A.M. Prokhorov, V.I. Zhekov, T.M. Murina, and M.I. Studenikin. Energy transfer characteristics of the $^4S_{3/2}$ level of Er^{3+} in YAG. *Optics Communications*, 72(3-4):209 – 213, 1989.

[43] F. Varsanyi and G. H. Dieke. Ion-pair resonance mechanism of energy transfer in rare earth crystal fluorescence. *Phys. Rev. Lett.*, 7:442–443, Dec 1961.

[44] Li Wang, Haitao Huang, Deyuan Shen, Jian Zhang, Hao Chen, Yong Wang, Xuan Liu, and Dingyuan Tang. Room temperature continuous-wave laser performance of LD pumped Er:Lu_2O_3 and Er:Y_2O_3 ceramic at 2.7 μm. *Opt. Express*, 22(16):19495–19503, Aug 2014.

[45] Colin E. Webb and Julian D. C. Jones. *Handbook of Laser Technology and Applications*, volume 2. Institute of Physics Publishing, Philadelphia, 2004.

[46] J. C. Wright. *Upconversion and excited state energy transfer in rare-earth doped materials*. Springer-Verlag, 1976.

[47] Evgenii V. Zharikov. Crystals of scandium garnets for solid state lasers. *Proc. SPIE*, 1839:46–68, 1992.

[48] Jonathan D Zuegel and Wolf Seka. Upconversion and reduced $^4F_{3/2}$ upper-state lifetime in intensely pumped Nd:YLF. *Applied optics*, 38(12):2714–2723, 1999.